NOVA SCHOOL OF SCIENCE & TECHNOLOGY

DEPARTMENT OF ELECTRICAL AND COMPUTER ENGINEERING

RECEIVER DESIGN FOR RELIABLE AND SECURE WIRELESS COMMUNICATIONS

JOÃO FALÉ DE CARVALHO MADEIRA

Master in Electrical and Computer Engineering

DOCTORATE IN ELECTRICAL AND COMPUTER ENGINEERING

NOVA University Lisbon
September, 2024

NOVA SCHOOL OF
SCIENCE & TECHNOLOGY

DEPARTMENT OF ELECTRICAL
AND COMPUTER ENGINEERING

RECEIVER DESIGN FOR RELIABLE AND SECURE WIRELESS COMMUNICATIONS

JOÃO FALÉ DE CARVALHO MADEIRA

Master in Electrical and Computer Engineering

Adviser: Rui Miguel Henriques Dias Morgado Dinis
Full Professor, Faculdade de Ciências e Tecnologia, Universidade NOVA de Lisboa

Co-adviser: João Francisco Martinho Lêdo Guerreiro
Assistant Professor, Faculdade de Ciências e Tecnologia, Universidade NOVA de Lisboa

Examination Committee

Chair: Paulo da Costa Luís da Fonseca Pinto
Full Professor, Faculdade de Ciências e Tecnologia, Universidade NOVA de Lisboa

Rapporteurs: Marko Beko
Associate Professor with Habilitation, Instituto Superior Técnico, Universidade de Lisboa

João Pedro Calado Barradas Branco Pavia
Assistant Professor, ISCTE, Instituto Universitário de Lisboa

Adviser: Rui Miguel Henriques Dias Morgado Dinis
Full Professor, Faculdade de Ciências e Tecnologia, Universidade NOVA de Lisboa

Members: Paulo da Costa Luís da Fonseca Pinto
Full Professor, Faculdade de Ciências e Tecnologia, Universidade NOVA de Lisboa

Luís Filipe Lourenço Bernardo
Associate Professor with Habilitation, Faculdade de Ciências e Tecnologia, Universidade NOVA de Lisboa

DOCTORATE IN ELECTRICAL AND COMPUTER ENGINEERING

NOVA University Lisbon
September, 2024

Receiver Design for Reliable and Secure Wireless Communications

This document was created with the (pdf/Xe/Lua)LaTeX processor and the NOVAthesis template (v7.1.18) [1].

Acknowledgements

I would like to thank my advisor Professor Rui Dinis and my co-advisor Professor João Guerreiro for all the help and support they provided during the PhD, as well as the teaching and non-teaching staff of the Department of Electrical Engineering at the Faculty of Sciences of the Universidade Nova de Lisboa. My thanks also go to the Instituto de Telecomunicações and the Fundação para a Ciência e Tecnologia for coordinating and funding my doctoral scholarship, with the reference doi:10.54499/UI/BD/150877/2021.

Finally, I want to thank my wife, Leonor Augusto, for supporting me and making these years happier, my parents, José Madeira and Célia Madeira, and my brother, Ricardo Madeira, for all the support they have given me and will continue to give me.

”

‘The single biggest problem in communication is the illusion that it has taken place.’ (George Bernard Shaw)

“

Abstract

Wireless networks have become so intrinsically linked with our daily lives to the point it is expected to be always available at any time and place, with high data rates. Due to services such as two factor authentication and remote working, a connectivity problem can severely impact individual productivity, not to mention the potential industrial impacts.

To achieve this level of connectivity and speed, many manufacturers compromise on the efficiency and cost of the hardware. In fact, Wi-Fi devices have been known to consume significant power due to the transmission scheme chosen in the protocol, which precludes the usage of saturated power amplifiers. Another challenge lies in the non-ideal nature of the hardware. Manufacturing hardware that operates closer to an ideal transceiver can be significantly more expensive or even impossible. Therefore, there is a large research interest into Digital Signal Processing (DSP) techniques that can provide benefits while still using cheap and efficient hardware.

In this thesis the author proposes nonlinear detection techniques that can cope with hardware impairments in the transmitter, or, in the limit, use these effects to achieve a better communication. Since in the current age it is impossible to ignore the security aspects of communication systems, this thesis also presents a study on how these techniques behave in the presence of malicious eavesdroppers.

Keywords: Nonlinear effects, Physical Layer Security, Hybrid Automatic Repeat Request (HARQ)

Resumo

As redes sem fios tornaram-se tão intrinsecamente ligadas às nossas vidas diárias ao ponto de se esperar que estejam sempre disponíveis em qualquer momento e lugar, com elevadas velocidades. Devido a serviços como autenticação de dois fatores e trabalho remoto, um problema de conectividade pode afetar severamente a produtividade individual, sem considerar os impactos industriais.

Para alcançar este nível de conectividade e velocidade, muitos fabricantes comprometem a eficiência e custo do hardware. De facto, dispositivos Wi-Fi são conhecidos por consumir uma quantidade significativa de energia devido ao esquema de transmissão escolhido no protocolo, o que impede o uso de amplificadores de potência saturados. Outro desafio reside na natureza não ideal do hardware. Fabricar hardware que opere mais próximo de um transceptor ideal pode ser significativamente mais caro ou até mesmo impossível. Portanto, existe um grande interesse de pesquisa em técnicas de Processamento Digital de Sinais (DSP) que possam fornecer benefícios enquanto utilizam hardware barato e eficiente.

Nesta tese, o autor propõe técnicas de detecção não lineares que podem lidar com imperfeições no hardware do transmissor ou, no limite, utilizar esses efeitos para alcançar uma comunicação melhor. Uma vez que na era atual é impossível ignorar o aspecto de segurança de um sistema de comunicação, o autor analisa como estas técnicas se comportam na presença de ouvintes maliciosos.

Palavras-chave: Efeitos não-lineares, Segurança no nível físico, Hybrid Automatic Repeat Request (HARQ)

Contents

List of Figures

List of Tables

Acronyms

3GPP 3rd Generation Partnership Project *(pp. 28, 172)*
5G 5th Generation *(pp. 1, 29, 127)*

ACK Acknowledgement *(p. 22)*
ADC Analog-to-Digital Converter *(pp. 3, 4, 36, 37, 64, 92, 139, 141, 143, 146, 172)*
AM/AM Amplitude-to-Amplitude Modulation *(pp. 39, 42, 43, 45)*
AM/PM Amplitude-to-Phase Modulation *(pp. 39, 42, 43)*
AMP Approximate Message Passing *(p. 92)*
API Application Programming Interface *(pp. 64, 132)*
APP A Posteriori Probability *(pp. 21, 74)*
ARQ Automatic Repeat Request *(pp. 3, 4, 18, 22, 156, 158–161, 172)*
ASK Amplitude Shift Keying *(pp. 10, 11)*
AWGN Additive White Gaussian Noise *(pp. 8–10, 18, 44, 50, 158, 161, 163, 166, 167, 169)*

BER Bit Error Rate *(pp. 5, 12, 18, 22, 23, 30, 34–37, 44, 45, 48, 52, 54, 56–59, 70–72, 74, 76, 82, 83, 88, 90, 92, 95, 97–100, 104, 106, 109, 110, 128, 129, 135–137, 141, 142, 153, 158)*
BNC Bussgang Noise Cancelling *(pp. 4, 5, 58, 70, 72, 74, 76, 90–92, 98, 99, 101, 137, 139, 141–143, 146, 171)*
BP Belief Propagation *(pp. 21, 52, 150)*
bps Bits-per-Second *(p. 151)*
BPSK Binary Phase Shift Keying *(p. 11)*

CA-BNC Code Assisted Bussgang Noise Cancelling *(p. 99)*
CathLab Catheterization Laboratory *(pp. 126–128, 172)*
CFA Cost Function Approximation *(p. 48)*
CFO Carrier Frequency Offset *(pp. 29–31, 34, 46–48, 52, 54)*
CIR Channel Impulse Response *(pp. 13, 14, 18, 39, 49, 54, 85, 127)*

CP Cyclic Prefix *(pp. 14, 17, 117)*
CPE Common Phase Error *(pp. 30, 31, 34, 48–50, 52)*
CRC Cyclic Redundancy Check *(p. 88)*
CSI Channel State Information *(pp. 52, 54, 82, 110, 114, 117, 146, 148)*

DAC Digital-to-Analog Converter *(pp. 3, 10, 64)*
DC Direct Current *(p. 35)*
DFT Discrete Fourier Transform *(pp. 13, 68, 70, 106, 137)*
DPD Digital Pre-Distortion *(p. 56)*
DSP Digital Signal Processing *(p. 64)*

EGC Equal-Gain Combining *(p. 26)*
EVM Error Vector Magnitude *(pp. 28–30, 34, 36, 37, 45, 54, 57, 58, 135, 136, 171)*

FDE Frequency Domain Equalization *(pp. 15, 50)*
FEC Forward Error Correction *(pp. 5, 22, 27, 76, 98, 103, 106, 161, 171, 172)*
FFT Fast Fourier Transform *(pp. 14, 17, 64, 85, 102, 105, 107, 108, 133, 152)*
flop Floating-Point Operation *(pp. 102, 105)*
FSK Frequency Shift Keying *(p. 11)*

GAMP Generalized Approximate Message Passing *(pp. 4, 5, 52, 67, 83–85, 88, 90–92, 94, 95, 97, 98, 103–107, 136, 137, 139, 141–143, 146, 154, 157, 158, 165, 167, 169, 171, 172)*
GLM Generalized Linear Model *(pp. 83–85)*
GS Guard Subcarriers *(pp. 47, 48)*
GTurbo Generalized Turbo *(pp. xvii, 4, 5, 67, 92, 95–98, 106, 107, 171, 172)*

HARQ Hybrid Automatic Repeat Request *(pp. 22, 23, 148, 150, 161–164, 166–169, 172)*
HARQ-CC HARQ - Chase Combining *(p. 22)*
HARQ-IR HARQ - Incremental Redundancy *(p. 23)*

IB-DFE Iterative Block - Decision Feedback Equalizer *(pp. 15, 67, 68, 70, 72, 79, 80, 171, 172)*
ICI Intercarrier Interference *(pp. 29, 30, 32, 47–49, 171)*
IDFT Inverse Discrete Fourier Transform *(pp. 17, 56)*
IFFT Inverse Fast Fourier Transform *(pp. 15, 17, 85, 102, 104, 105, 107, 108)*
IMP Inter-Modulation Product *(pp. 40, 41)*
IQ In-Phase and Quadrature *(pp. 34, 35, 52, 53, 90)*
ISI Inter-Symbol Interference *(pp. 13, 16, 17, 80)*

IVUS Intravascular Ultrasound *(pp. 126, 127)*

LBC Linear Block Coding *(p. 56)*
LDPC Low-Density Parity-Check *(pp. 3, 5, 21–23, 52, 98, 99, 104, 106, 143, 146, 148, 150–154, 161)*
LLR Log-likelihood Ratio *(pp. 15, 16, 20, 22, 74, 99, 103, 104, 106)*
LMMSE Linear Minimum Mean Square Error *(p. 52)*
LoS Line-of-Sight *(pp. 10, 112, 121, 123, 148, 151, 153, 154)*
LPF Low-Pass Filter *(p. 34)*
LS Least Squares *(pp. 51–54)*
LSB Least Significant Bit *(p. 36)*
LT Lower Triangular *(p. 21)*
LTE Long Term Evolution *(p. 47)*
LUT Look-Up Table *(pp. 56, 103, 105)*

M-QAM M-ary Quadrature Amplitude Modulation *(pp. 11, 16, 17, 42, 58, 68, 85, 95, 127, 133)*
MC Multi Carrier *(pp. 4, 5, 10, 16–18, 25, 42, 67, 171)*
MFA Multi-Factor Authentication *(p. 2)*
MIMO Multiple Input, Multiple Output *(pp. 3, 24–27, 51, 52, 54, 57, 60, 67, 68, 82, 109, 110, 117, 119, 127–130, 134, 171, 172)*
ML Maximum Likelihood *(p. 20)*
mMIMO Massive Multiple Input, Multiple Output *(p. 54)*
MMSE Minimum Mean Square Error *(pp. 15, 17, 21, 26, 27, 48, 80, 85)*
MRC Maximal-Ratio Combining *(pp. 25, 26)*
MSE Mean Squared Error *(p. 15)*
MU-MIMO Multi-User MIMO *(p. 54)*

NAK Negative Acknowledgement *(p. 150)*
NL-ARQ Nonlinear ARQ *(pp. 158, 159)*
NL-ARQ-EP Nonlinear ARQ with Enhanced Power *(pp. 156, 159, 161)*
NL-HARQ Nonlinear HARQ *(pp. 161, 162, 166)*
NL-HARQ-EP Nonlinear HARQ with Enhanced Power *(pp. 156, 162–164, 166–169)*
NOMA Non-Orthogonal Multiple Access *(pp. 2, 3, 5, 64, 76, 77, 79, 82, 114, 117, 171, 172)*
NR New Radio *(pp. 23, 29, 47, 67)*
NSR Noise-to-Signal-Ratio *(p. 15)*

OBO Output backoff *(pp. 57, 59, 99–102)*

OFDM Orthogonal Frequency-Division Multiplexing *(pp. 17, 18, 22, 23, 27–31, 33–35, 37, 39–41, 43, 46–48, 50–58, 67, 88, 91, 92, 99, 104, 106, 127, 128, 130, 133, 134, 136, 141, 143, 153, 156, 158, 159, 165, 171, 172)*

OFDM-IM OFDM - Index Modulation *(p. 52)*

OOB Out-of-Band *(pp. 3, 41, 43, 55, 90, 97, 98)*

PA Power Amplifier *(pp. 3, 39, 55, 56, 137, 156, 172)*

PAPR Peak-to-Average Power Ratio *(pp. xvii, 3, 42, 44, 55, 56, 68, 90, 91, 98, 104, 106, 136, 137, 154, 156, 158, 159, 161–163, 166, 172)*

PDF Probability Density Function *(pp. 27, 148)*

PER Packet Error Rate *(p. 5)*

PHY Physical *(pp. 2, 18, 59, 60, 172)*

PI Peak Insertion *(p. 56)*

PIM Patient Interface Module *(p. 127)*

PLL Phase-Locked Loop *(p. 34)*

PLS Physical Layer Security *(pp. 2, 3, 5, 60, 62, 64, 77, 109, 127, 171, 172)*

PN Phase Noise *(p. 3)*

POC Proof-of-Concept *(p. 172)*

PR Peak Reduction *(p. 55)*

PSD Power Spectral Density *(pp. 12, 33, 41, 43, 50, 137)*

PSK Phase Shift Keying *(p. 11)*

PTS Partial Transmit Sequence *(p. 56)*

QAM Quadrature Amplitude Modulation *(pp. 12, 29, 30, 34, 37, 43, 44, 48, 52, 54, 57–59, 72, 74, 76, 88, 90, 95, 98, 99, 101, 102, 135–137, 141–143, 146, 152, 156, 158, 166, 172)*

QPSK Quadrature Phase Shift Keying *(pp. 11, 22, 23, 29, 88, 90, 98, 117, 135, 136)*

RF Radio Frequency *(pp. 1, 3, 4, 10, 28, 32, 34, 37, 39, 43, 64, 132, 136, 139)*

RNS Remaining Null Subcarriers *(pp. 47, 48)*

SC Single Carrier *(pp. 4, 5, 10, 12, 18, 25, 29, 30, 35, 42, 50, 51, 67, 171)*

SC-FDE Single Carrier with Frequency Domain Equalization *(pp. 17, 27, 68, 109, 117)*

SDR Software Defined Radio *(pp. 5, 60, 64, 65, 132, 172)*

SER Symbol Error Rate *(pp. 99, 102, 143, 145, 146, 148, 161–163, 166, 167, 169)*

SIC Successive Interference Cancellation *(pp. 77, 79, 80)*

SIR Signal-to-Interference Ratio *(pp. 30, 91, 92, 99)*

SiSi Soft-input, Soft-output *(p. 20)*

SISO Single Input, Single Output *(pp. 39, 60, 119, 127)*

SLM Selective Mapping *(p. 56)*
SNDR Signal-to-Noise plus Distortion Ratio *(p. 71)*
SNR Signal-to-Noise-Ratio *(pp. 12, 15, 28, 53, 54, 57, 62, 76, 78, 80)*
SR Secrecy Rate *(pp. 5, 21, 63, 171, 172)*
SSB Single-Sideband *(p. 33)*
SSPA Solid State Power Amplifier *(pp. xvii, 42–45, 57, 58, 68, 70, 91, 94, 103)*
Super-QAM Super Quadrature Amplitude Modulation *(p. 28)*
SVD Singular Value Decomposition *(pp. 3, 26, 60, 61, 67, 68, 78–82, 109, 117, 127, 128, 130, 133, 136, 171, 172)*
SVM Support Vector Machine *(p. 62)*

TDD Time Division Duplexing *(pp. 54, 117, 133)*
TLS Total Least Squares *(p. 51)*
TR Tone Reservation *(p. 56)*
TWT Travelling Wave Tube *(pp. 43, 45)*

UAV Unmanned Aerial Vehicle *(pp. 62, 63)*
UHD USRP Hardware Driver *(p. 64)*
USRP Universal Software Radio Peripheral *(pp. 64, 130, 132–134)*
UT Upper Triangular *(p. 21)*

VEM Variational Expectation Maximization *(p. 52)*

ZF Zero Forcing *(pp. 15, 17, 26, 27, 103, 133, 137, 141, 142, 145)*

1 Introduction

Wireless communications devices have created a lasting impact in our society and daily lives. As the world enter the third decade of the 21st century, the number of Internet capable devices owned per household continues to steadily increase in developed countries, as new wearable devices and smart home appliances are launched. It is through wireless communications that connecting these devices to the Internet becomes practical, or even feasible for small form factor devices. The wide diversity of applications for these wireless devices and fierce competition between manufacturers have increased the demand for better optimised wireless protocols and hardware. These demands have lead to the development of several wireless standards, such as 5th Generation (5G) [2] and 802.11ax [3], and continue to be a driving force for innovation in wireless communications.

Although different standards are suited for different scenarios, and are therefore designed to maximise different parameters, the power consumption of the hardware has always been a concern. This is particularly important for mobile devices due to their limited battery capacity. In devices that are not practical to be charged every day, such as long distance sensors, the battery drain must be kept to an absolute minimum, which as lead to the development of very low power wireless communication standards such as LoRaWan and Zigbee [4]. This power efficiency generally comes at the cost of a much lower maximum data throughput, which limits the amount of data these devices can transmit reliably.

The inverse of this trade-off is present in 5G and Wi-Fi systems, where the high data rates are obtained by sacrificing power efficiency. The impact on the battery duration is reduced by employing bigger batteries, and fast charging schemes to make charging the device more practical. However, the sheer number of these devices, as well as the infrastructure supporting it in the case of 5G, result in a very large energy footprint. These factors have become the main driving force behind research into power efficient wireless communication technology.

Hardware cost is another large concern when designing wireless systems. The Radio Frequency (RF) chain is comprised of several individual components which have non ideal behaviour. In general, less ideal hardware is cheaper and more power efficient,

though they introduce undesirable effects in the communication. For this reason, there is significant research being done to design wireless systems that can function with cheap and efficient components.

Security has always been a concern in the telecommunications sector, due to the sensitive information that is often transmitted, whether in wired or wireless communications. In the case of wireless communications, however, there is an additional security concern of eavesdropping, where a malicious user tries to decode a transmission meant for another user. In such a scenario there is an inherent security flaw that is usually compensated with upper layer security schemes such as cryptographic encoding. However, this security may fail if the eavesdropper has access to private keys or very powerful computation capabilities.

For this reason, techniques that resist eavesdropping at the physical level, so called Physical Layer Security (PLS) schemes, are being extensively investigated. With an ideal technique, an eavesdropper would not be able to obtain any part of the transmitted signal, rendering it impossible to obtain the information being sent. There are several different approaches to PLS techniques, with a common approach being minimising the power that is received by the eavesdropper through beamforming [5].

A user access scheme that has gained traction is Non-Orthogonal Multiple Access (NOMA), which combines different user signals in a non-orthogonal fashion, such as in the time-domain [6]. In this type of scheme, security is a concern since an eavesdropper might have natural access to the signals transmitted over the air.

1.1 Motivation

The products and services made possible by digital communication have become inseparable from our current society. Such as the convenience offered by wireless mobile devices that provide an accessible method to access all the benefits of an Internet connection, in addition to the standard voice call and text messaging features. The reliability and data rates of modern wireless system have led to the development of innovative solutions in industrial, medical and even emergency applications.

This fact means that service failures and security breaches are more damaging than ever. In fact, mobile phone numbers are widely used as a part of Multi-Factor Authentication (MFA) in government and banking systems. An exploitable security flaw that permits a malicious user to impersonate someone else in the mobile network could lead to serious and irreversible damage to the affected users. Ensuring the maximum level of security is therefore desirable, which is particularly difficult to achieve in wireless systems due to the broadcast nature of the communication. Any wireless malicious user can receive and transmit signals to a legitimate system, opening up the possibility for a security failure at the Physical (PHY) layer.

As wireless systems become faster and more complex, the necessary power to operate the system also increases. In fact, the power consumed by the radio infrastructure can

represent up to 80% of the total network operation cost [7]. This has lead to power efficiency becoming a crucial concern of 5G and 6G systems [8]. One of the key aspects that greatly increase power consumption is the Power Amplifier (PA) backoff, which is when a PA is set to operate below saturation to ensure linearity. The amount of backoff is usually expressed as dBs below the saturation input power. If the backoff is not sufficient then the amplified signal will be nonlinearly distorted, resulting in in-band interference and Out-of-Band (OOB) emissions. To avoid this effect, the PA's backoff must be enough to accommodate the input signal's PAPR, which for high data rate systems is typically large.

There are also other sources of nonlinearities in wireless transceivers, such as low resolution Digital-to-Analog Converters (DACs)/Analog-to-Digital Converter (ADC) and Phase Noise (PN), which although may not have such a big impact on the power consumed, can lead to a significant degradation of the signal quality. These effects can be extremely detrimental for very high data rate systems.

The problem considered for this thesis is therefore divided into two parts, security and efficiency in wireless communication systems.

1.2 Research Question and Hypothesis

The challenges identified in the previous section have many proposed solutions, involving techniques at various points of the radio chains. In this thesis the author will look into making use of the physical characteristics of the RF chain to increase the security and efficiency of the system. For the security aspect this is commonly known as PLS, and is essential to solve the problems associated with malicious users in the wireless channel.

Instead of decreasing the impact of the nonlinear effects that arise from the radio chain, the author will seek to use these effects to improve system performance.

This PhD thesis therefore addressed the following research question: "Can the non-ideal physical characteristics associated with a wireless communication be used to improve the efficiency and security of the communication?".

The hypothesis that will be investigated by this thesis will be whether the hardware and channel characteristics can be used to improve security and performance. The channel propagation characteristics in Multiple Input, Multiple Output (MIMO) systems can be leveraged to achieve PLS, even for NOMA schemes that require transmitting partial keys. Although these schemes require low correlation between MIMO streams, it was shown that even in scenarios with non-ideal propagation conditions, the PLS aspect of Singular Value Decomposition (SVD) schemes is still sufficient to ensure confidentiality.

The reliability of wireless communication is heavily dependent on the quality of the wireless link. If this quality is degraded, then retransmission schemes such as Automatic Repeat Request (ARQ) are employed to salvage the communication. Although in an ideal system, there would be no need for retransmissions, this could come at a significant hardware and energy cost. Therefore, retransmission schemes should be improved to better perform in non-ideal scenarios. The use of concatenated Low-Density Parity-Check

(LDPC) codes was proposed as an alternative to code puncturing that can be scaled up using large parity matrices.

The nonlinear behaviour of RF hardware can be accurately modelled using appropriate definitions. These models were used to develop and test different algorithms that can cope with the distortion in the signal. The use of Bussgang Noise Cancelling (BNC) to reduce nonlinear distortion for Single Carrier (SC) and Multi Carrier (MC) systems was shown to be effective, at a relatively low complexity. For stronger nonlinear effects, Generalized Approximate Message Passing (GAMP) and GTurbo were found to be better options over BNC, though at a cost of higher complexity. A novel use case of nonlinear GAMP was proposed for scenarios with low-resolution ADCs, to achieve excellent performance over conventional receivers. Also, a novel ARQ scheme was developed that makes use of nonlinear clipping operations to improve retransmission reliability and efficiency.

1.3 Contributions

The main contributions of this thesis are the receiver algorithms developed for wireless systems with nonideal physical characteristics. Additionally, multiple applications were developed that benefit from the enhanced wireless reception algorithms. The work in this thesis was published in the following research papers.

- "On the physical layer security characteristics for MIMO-SVD techniques for SC-FDE schemes", published in MDPI Sensors, 2019 [9];
- "Iterative frequency-domain detection and compensation of nonlinear distortion effects for MIMO systems", published in Elsevier Physical Communication, 2019 [10];
- "A physical layer security technique for NOMA systems with MIMO SC-FDE schemes", published in MDPI Electronics, 2020 [11];
- "Physical Layer Security for High Data Rate Communications in the CathLab Environment", presented in IEEE VTC2021-Fall, 2021 [12];
- "A Scalable LDPC Coding Scheme for Adaptive HARQ Techniques", presented in IEEE VTC2022-Spring, 2022 [13];
- "A Software Defined Radio Implementation of Physical Layer Security Using MIMO-SVD", presented in YEF-ECE, 2022 [14];
- "LDPC assisted GAMP for PAPR reduction in Super-QAM OFDM", presented in ICFSP, 2023 [15];
- "Receiver Design for OFDM Schemes With Low-Resolution ADCs", published in IEEE Open Journal of Vehicular Technology, 2024 [16];

- "Nonlinearity-Aided Hybrid ARQ for Satellite Communications", presented in VTC2024-Fall, 2024 [17].

Additionally, a papers was submitted to IEEE Transactions on Communication, which is still awaiting decision. A patent entitled "A method and an apparatus for physical layer in NOMA based wireless communication systems" was registered and published with number WO2021154106A1.

The author of this thesis also collaborated in other research work that was not included in this thesis. The following publications were the result of this collaboration.

- "Increasing reliability on UAV fading scenarios", published in IEEE Access, 2022 [18];
- "A Least Squares Approach for Estimating Non-linearity Parameters for OFDM Signals with Bussgang Receivers", presented in VTC2023-Spring, 2023 [19];
- "Quasi-Optimum Detection of Nonlinear OFDM: Performance Bounds and Receiver Design", published in IEEE Transactions on Communications, 2024 [20].

1.4 Outline

This thesis is organized into five chapters. Chapter 2 contains an extensive literature review of wireless transmission systems. It includes the system characterization that serves as a basis for the proposed systems. The impact of non-ideal hardware is characterized, and several solutions already present in the literature are reviewed. The chapter also defines PLS, and how it can be quantified for comparison between different systems. It ends with a brief introduction to Software Defined Radio (SDR) prototyping based on GNURadio.

Chapter 3 provides a basis for the proposed wireless communication systems. It begins by defining novel BNC and power-domain NOMA schemes for SC systems. For MC, the novel nonlinear GAMP and GTurbo receivers that can handle severe nonlinear distortion are characterized. This characterization is further extended for scenarios using Forward Error Correction (FEC), such as LDPC coding.

Chapter 4 presents several applications where the algorithms from Chapter 3 are shown to exhibit performance improvements relatively to existing approaches. The performance of these applications is measured in terms of Bit Error Rate (BER)/Packet Error Rate (PER), and Secrecy Rate (SR) for PLS scenarios.

Chapter 5 concludes the thesis, summarizes the main findings, and discloses future work prospects.

2

Literature Review

2.1 Introduction

This chapter presents a comprehensive review on the state-of-art of wireless communications research and identify the knowledge gaps that currently exist in this field.

2.2 Digital Communication

In information theory, any digital communication system can be characterised by the following block elements:

- Information Source - The physical element that is producing the information to be transmitted
- Source Encoder - Encodes the information source into a digital word.
- Channel Encoder - Converts the digital word into a signal that can be sent over the channel.
- Channel - The physical element that connects the transmitter and the receiver, which can be wired or wireless.
- Channel Decoder - Decodes the received signal back into information bits.
- Source Decoder - Decodes the information bits back into the original information.
- Receiver - The intended target for the information.

If the channel is noiseless and the source encoding is lossless, then the information that was sent from the information source will arrive without errors at the receiver. However, since there are no noiseless electronic circuits, the channel will contain a certain level of noise, which will create errors in the information. This analysis considers lossless source coding and will therefore focus only on channel coding.

Let us define the digital output of the source encoder, which is a stream of information bits, as $p(t)$, for a particular time t. The channel encoder will then encode this word into a stream of symbols, $s(t)$, defined as

$$s(t) = \text{Enc}\left(p(t)\right). \tag{2.1}$$

For simplicity, it is assumed that an encoded symbol represents only one information bit, although, it can represent several information bits, depending on the choice of encoding. The encoder can also be thought of as a codebook that maps all M possible values of $p(t)$ into a unique $s(t)$. The resulting symbols are then sent through the physical channel, $\text{F}(\cdot)$, defined as

$$x(t) = \text{F}(s(t)), \tag{2.2}$$

where $x(t)$ is the signal arriving at the channel decoder. The decoding of the incoming signal is defined as

$$p(t) = \text{Dec}\left(x(t)\right). \tag{2.3}$$

It can be concluded that the channel decoder must be adapted to take into account how the physical channel affects the transmitted symbols. How the channel affects the symbols will depend on the physical medium used in the communication, and can be approximated using appropriate channel models. Let us consider a channel function that simply adds a noise $n(t)$ to the incoming symbols. The expression in (2.2) can be rewritten as

$$x(t) = s(t) + n(t). \tag{2.4}$$

If the noise is independent of the input symbols, and is characterized by a Gaussian distribution with variance σ_N^2, then this channel model is known as Additive White Gaussian Noise (AWGN). Under this model, the received symbol $x(t)$ can assume any value with a certain probability, including other possible values of $s(t)$. The difference between the received and transmitted symbols can be seen as the distance between the two symbols, which will be equal to the noise at time t, and is written as

$$n(t) = x(t) - s(t). \tag{2.5}$$

Since $x(t)$ may not be equal to any of the possible transmitted symbols, the channel decoder must decide which symbol was most likely transmitted, from the set of M possible symbols $\mathbf{s}_{sym}$. For the AWGN channel model, it follows that the most likely transmitted symbol is the symbol that is closest to the received symbol. The estimated symbol $\tilde{s}(t)$ is the symbol that is closest to $x(t)$, which satisfies

$$\tilde{s}(t) = \min\left(\mathbf{s}_{sym} - x(t)\right), \tag{2.6}$$

where $\tilde{s}(t)$ is the decoded symbol estimate, which is the symbol in $\mathbf{s}_{sym}$ that minimises the equation. This leads to a decoded information word defined as

$$\tilde{p}(t) = \text{Dec}\left(\tilde{s}(t)\right). \tag{2.7}$$

In this channel decoder it is plain to see that there is a probability that $s(t)$ will be incorrectly decoded, resulting in $\tilde{p}(t) \neq p(t)$. It is easy to deduce that $s(t)$ will be incorrectly decided when

$$n(t) > \frac{\min\left(\mathbf{s}_{sym} - s(t)\right)}{2}, \quad \forall s(t). \tag{2.8}$$

Such an error can be said to occur with a probability $p_e(m)$, for the symbol $s_{sym}(m)$, which depends on the characteristics of the chosen channel coder. The system's error rate, P_e, can be obtained by taking the average of all the individual p_e, weighted by the probability of each symbol being transmitted, $p_s(m)$, defined as

$$P_e = \frac{1}{M} \sum_{m=1}^{M} p_e(m) p_s(m). \tag{2.9}$$

Therefore, the distribution of $s(t)$ will also condition the average error probability.

2.2.1 Entropy and Channel Capacity

The information rate that can be achieved for a noisy channel is, according to Shannon's limit [21], equal to the mutual information between $s(t)$ and $x(t)$, defined as

$$I(s, x) = H(s) - H(s|x), \tag{2.10}$$

where $H(s)$ denotes the entropy of the random variable $s(t)$, and $H(s|x)$ is the conditional entropy. This entropy is a measure of the uncertainty of a certain random variable. Let us consider a binary encoding scheme where $\mathbf{s}_{sym} \in \{0, 1\}$. The amount of information that can be encoded using this scheme is defined as the entropy of $s(t)$ and is given by

$$H(s) = -p \log_2 p - (1 - p) \log_2 (1 - p), \tag{2.11}$$

where p is the probability of $s = 1$. By deriving $H(s)$, it can be deduced that the maximum occurs for $p = 0.5$, and therefore, for maximum entropy of a binary symbol alphabet, $p_s = 0.5$. It follows that the information rate is inversely proportional to the conditional entropy $H(s|x)$, which intuitively means that the more information about $s(t)$ is contained in $x(t)$, the more information is transmitted. At the limit it becomes $H(s) = H(x), H(s|x) = 0$.

Let us consider a set of symbols $\mathbf{s}_{sym}$ where each $\mathbf{s}$ is a binary valued vector, referred to as a codeword. Shannon showed that for a noisy channel there exists a $\mathbf{s}_{sym}$ that maximises (2.10), which is the maximum rate of information that can be transmitted, also referred to as the channel capacity. Despite being proven to exist, so far there are no transmission techniques that achieve capacity.

For an AWGN channel, the capacity can be defined analytically as

$$C_{cap} = B \log_2 \left(1 + \frac{\sigma_s^2}{\sigma_N^2}\right), \tag{2.12}$$

where B is the bandwidth and σ_s^2 is the transmission power.

In the case of wireless channels, signal reflections can also arrive at the receiver, sometimes at a different time instant from the main signal. This multipath propagation might lead to fading, and is a significant challenge for any wireless application. The capacity of the fading channel is given by

$$C_{cap} = \int_{\gamma} B \log_2 \left(1 + \frac{\gamma}{\sigma_N^2}\right) p(\gamma) d\gamma, \tag{2.13}$$

where $p(\gamma)$ is the distribution of the channel fading effects. It is proven that this capacity is always lower than the AWGN channel capacity [22].

In practice, it is nearly impossible to know the exact channel distribution, and as such approximations are often used. One such approximation is to consider that the channel follows a Rayleigh distribution, with several uncorrelated rays arriving with different delays at the receiver. This model is often used due to its simplicity and acceptable accuracy. Another often used model considers that the channel follows a Rician distribution, which consists in a single highly correlated component due to Line-of-Sight (LoS) with power K, plus a Rayleigh distributed component that models the remaining rays with power $1 - K$.

2.3 Transmission Techniques

Telecommunication systems can be classified as either SC, wherein the information is sent over a limited bandwidth at a given carrier frequency, or MC, where the bandwidth is split into several narrowband signals, centred at the carrier frequency. In this section, a brief characterization of both systems is presented.

2.3.1 Modulation

In order to transmit the digital bits over a physical medium, such as a wire or the vacuum, the bits must be converted into an electromagnetic wave. This conversion is performed by using a DAC to convert the digital bits to a baseband analogue signal, in conjunction with an RF mixer to upconvert the signal to a carrier frequency f_c. The resulting signal $s(t)$ can be defined generically as

$$s(t) = s_m \cos(2\pi f_c t + \phi_m), \tag{2.14}$$

where s_m and ϕ_m are the amplitude and phase modulation coefficients, respectively, for the mth symbol that is mapped to a set of digital bits. The data transmission rate for this system is given by $B \log_2(M)$, where B is the bandwidth of the baseband signal, which is the inverse of the symbol time T_s.

For $M = 2$, there are mapping techniques such as Amplitude Shift Keying (ASK), where $\max(s(t))$ is either 0 or 1, $\phi_m = 0$, and s_m is defined as

$$s_m = \begin{cases} 1, & b_m = 1 \\ 0, & b_m = 0 \end{cases}, \tag{2.15}$$

where b_m is the mth digital bit. Alternatively, only the phase of $s(t)$ may be shifted according to the input bits, referred to as Phase Shift Keying (PSK). In the case of $M = 2$ distinct phases, this technique is known as Binary Phase Shift Keying (BPSK), $s_m = 1$, and ϕ_m is defined as

$$\phi_m = \begin{cases} \pi, & b_m = 1 \\ -\pi, & b_m = 0 \end{cases} . \tag{2.16}$$

Another approach is Frequency Shift Keying (FSK), where the frequency of $s(t)$ can assume two different values, f_1 and f_2, according to the value of the input bit. This relationship can be expressed by setting $s_m = 1$, and ϕ_m as

$$s(t) = \cos(2\pi(f_m)t), \tag{2.17}$$

where f_m is the variable frequency that is mapped from the input bits, according to

$$f_m = \begin{cases} f_1, & b_m = 1 \\ f_2, & b_m = 0 \end{cases} \tag{2.18}$$

Each of these techniques can be extended for larger values of M by simply increasing the number of possible amplitudes, frequencies or phases for each technique, and adding the suffix "M-ary" to the name of the technique. They can also be combined in order to increase the number of possible symbols.

2.3.1.1 Quadrature Modulation

The data rate of a wireless system can be increased by employing a second carrier wave that is orthogonal to the original carrier, referred to as a quadrature modulation. The resulting signal is defined as

$$s(t) = s_I \cos(2\pi f_c t) - s_Q \sin(2\pi f_c t), \tag{2.19}$$

where s_I, s_Q, are the in-phase and quadrature amplitudes, respectively. Using phasors, the equation is rewritten as

$$\bar{s} = s_I + j s_Q. \tag{2.20}$$

Each of these symbols can be mapped independently using the techniques discussed previously. The data rate for this type of modulation is given by $2B \log_2(M)$, which is double the data rate of non-quadrature systems.

If PSK is combined with quadrature modulation it is known as Quadrature Phase Shift Keying (QPSK), where both the in-phase, s_I, and quadrature, s_Q, components implement a BPSK technique, as in (2.16).

It is also possible to combine both ASK and PSK techniques with quadrature modulation into a technique known as M-ary Quadrature Amplitude Modulation (M-QAM), where M is the constellation's order. As an example, the combination of a BPSK and ASK for each of the two components results in a modulation that has $M = 16$ possible symbols,

distributed over a complex-valued constellation, otherwise known as 16-Quadrature Amplitude Modulation (QAM). Each increase in the size of the constellation increases the BER at the same Signal-to-Noise-Ratio (SNR), due to a decrease in the symbol distance. It is possible to use Monte Carlo simulations to measure the impact of the reduced symbol distance on the BER of the system. Fig. 2.1 shows the simulated BER for various QAM orders.

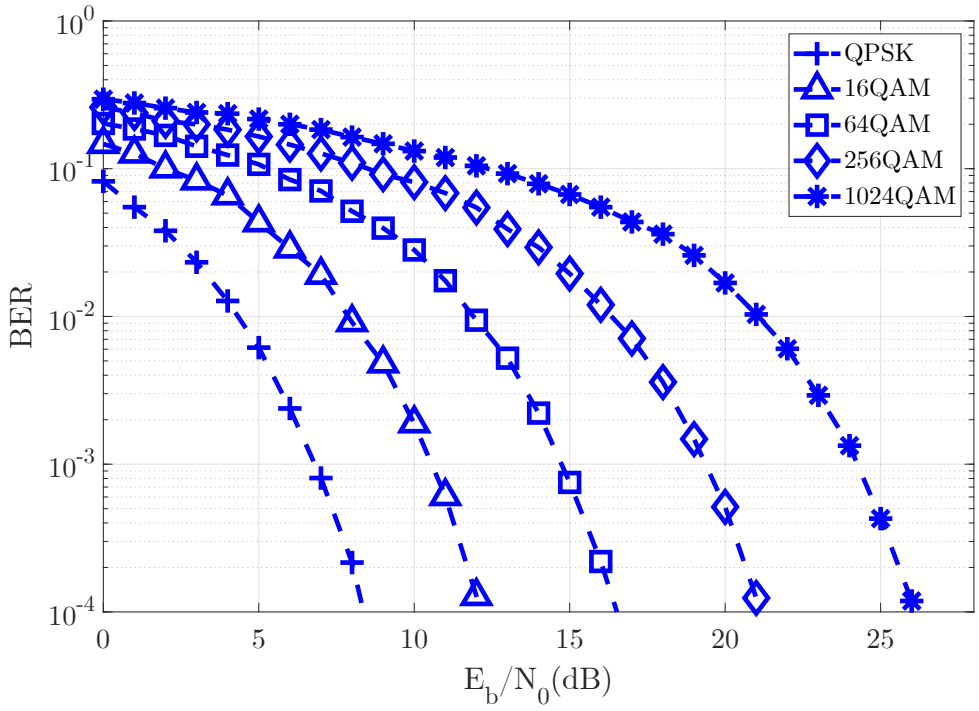

Figure 2.1: BER as a function of the E_b/N_0 for various orders of M-QAM.

For this result, the average bit energy ratio E_b/N_0 is used as an SNR metric, where E_b is the power associated to a single bit, and N_0 represents the noise Power Spectral Density (PSD). When the constellation size quadruples, the necessary E_b/N_0 also quadruples. Therefore, higher order constellations require additional power to function properly, which must be factored in during system design.

2.3.2 Single-Carrier

In an SC system, the complex envelope can be defined as

$$s_{sc}(t) = \sum_{n=0}^{N-1} \bar{s}_n r(t - nT_u), \tag{2.21}$$

where $\bar{s}_n$ is the nth transmitted symbol and $r(t)$ denotes the support impulse, which is defined as

$$r(t) = \frac{1}{T_u}\text{sinc}\left(\frac{t}{T_u}\right). \tag{2.22}$$

This sinc-like pulse is chosen for two reasons. The first is that it guarantees no Inter-Symbol Interference (ISI) if it is sampled perfectly at every T_u instant. The second is due to its frequency response being

$$R(f) = \text{rect}(fT_u), \tag{2.23}$$

which maximises the occupied bandwidth.

The signal is then transmitted over a noisy channel before arriving at a receiver. The received signal is therefore defined as

$$\bar{y}_{sc} = \bar{h} * \bar{s}_{sc} + \bar{n}, \tag{2.24}$$

where $*$ represents the convolution operation, $\bar{h}$ is the Channel Impulse Response (CIR) and $\bar{n}$ is a random noise term that follows a Gaussian distribution with variance σ_N^2. The number of taps in $\bar{h}$ will depend on the physical characteristics of the channel. For wireless environments, the propagation characteristics lead to a large amount of paths with varying length between transmitter and receiver. In such an environment a single transmitted signal may be received multiple times at different time instants, with varying power and phase, which can in the worst scenario cancel each other out. This effect is referred to as multipath fading. The received multipath signal with L paths is defined as

$$\bar{y}_{sc}(t) = \sum_{i=0}^{L} (A_i \bar{s}_{sc}(t - t_i)) + \bar{n}(t), \tag{2.25}$$

where A_i and t_i are amplitude and delay coefficients associated with the ith path, respectively.

The original signal can be recovered by equalizing the received signal, which requires inverting the effect of h by using a filter with the inverse impulse response. The equalized signal is defined as

$$\bar{z}_{sc} = \bar{f}_{sc} * \bar{y}_{sc}, \tag{2.26}$$

where $\bar{f}_{sc}$ is an equalization filter chosen to cancel the channel effects. This signal is then demodulated to recover the underlying bits with a certain error rate. The conditioning factors of the error rate are the noise power σ_N^2 and the choice of filter $\bar{f}_{sc}$.

2.3.2.1 Frequency Domain Equalization

The time-domain equalization presented in the previous subsection is difficult to implement, particularly for wireless channels that have long impulse responses. However, let us consider the frequency domain counterpart of the received signal which can be obtained using the Discrete Fourier Transform (DFT) and is written as

$$\bar{Y}_{sc} = \bar{H}S_{sc} + \bar{N}, \tag{2.27}$$

where the upper-case letters denote the frequency domain counterparts of the corresponding time domain variables. In this case, the equalization could be realised without the need for a high complexity filter. Unfortunately, this would only be accurate for an infinite number of samples, leading to an error proportional to the number of samples.

Alternatively, one can consider a block-based transmission scheme, where each block contains N time domain symbols and has a length T_b, defined as

$$\mathbf{s}_{sc} = [\bar{s}_{sc}(0), \bar{s}_{sc}(1), ..., \bar{s}_{sc}(N-1)]. \tag{2.28}$$

The symbol at the nth instant within the block is referred to as $s_{sc}(n)$. In this configuration, each block will be affected by the previous blocks, according to the length of the CIR. If a guard period of duration T_g, that is larger than the CIR, is considered between block transmissions, then each block would only be affected by replicas of itself, allowing us to simplify the received signal as

$$\mathbf{y}_{sc} = \mathbf{h} * \mathbf{s}_{sc} + \mathbf{n}. \tag{2.29}$$

Although this simplification allows for less strict filters, it still filters with long taps. Instead of not transmitting any signal during T_g, one can transmit the last samples of the next block, resulting in a window of $T_g + T_b$ where the block is cyclical, corresponding to $N_g + N$ samples, with N_g being the number of samples in T_g. The prepended sub block is known as a Cyclic Prefix (CP). Each transmitted sample $x_{sc}(n)$ can be expressed as the branch function

$$x_{sc}(n) = \begin{cases} s_{sc}(n + N - N_g) & n < N_g \\ s_{sc}(n) & n \geq N_g \end{cases}. \tag{2.30}$$

If the length of the CIR is smaller than T_g, then (2.29) becomes a circular convolution, given by

$$\mathbf{y}_{sc} = h \circledast \mathbf{s}_{sc} + n. \tag{2.31}$$

By taking advantage of the circular convolution, then it becomes possible to write Y_{sc} for the kth normalized frequency sample, or kth subcarrier, as

$$Y_{sc}(k) = H(k)S_{sc}(k) + N(k). \tag{2.32}$$

Under these conditions, the equalization of y_{sc} can be performed in the frequency domain by a single tap multiplication, which is significantly less complex than using a time domain filter with several taps. The frequency domain signal can be computed efficiently by using a Fast Fourier Transform (FFT).

The simplest equalization is defined as

$$\tilde{S}_{sc}(k) = \frac{Y_{sc}(k)}{H(k)}, \tag{2.33}$$

which is known as the Zero Forcing (ZF) criterion. Another equalizer that minimises Mean Squared Error (MSE) using the Minimum Mean Square Error (MMSE) criterion is defined as

$$\tilde{S}_{sc}(k) = \frac{H^*(k)Y_{sc}(k)}{|H(k)|^2 + \text{NSR}}, \tag{2.34}$$

where NSR is the Noise-to-Signal-Ratio (NSR), which is the inverse of the SNR. The time domain symbols are then obtained from $\tilde{S}_{sc}(k)$ using an Inverse Fast Fourier Transform (IFFT).

2.3.2.2 Iterative Equalization

In addition to the previously discussed advantages of Frequency Domain Equalization (FDE), it also enables a more robust iterative equalization technique known as Iterative Block - Decision Feedback Equalizer (IB-DFE) [23]. The equalized signal in this technique is defined as

$$\tilde{S}_{sc}^{(l)}(k) = F^{(l)}(k)Y_{sc}(k) - B^{(l)}(k)\hat{S}_{sc}^{(l-1)}(k), \tag{2.35}$$

where $\hat{S}_{sc}(k)$ is a detected symbol of the previous iteration, and $F^{(l)}(k)$ and $B^{(l)}(k)$ are the feedforward and feedback equalization factors for the kth subcarrier and lth iteration, respectively. The feedforward factor is defined as

$$F^{(l)}(k) = \frac{H^*(k)}{|H(k)|^2 + \text{NSR}}. \tag{2.36}$$

On the other hand, the feedback equalization factor is defined as

$$B^{(l)}(k) = F^{(l)}(k)H(k) - 1. \tag{2.37}$$

This technique enables significant performance gains even for a low number of equalization iterations. It is even possible to improve it by utilising soft decisions in the feedback loop. In this case, $\hat{S}_{sc}(k)$ is substituted by $\bar{S}_{sc}(k)$ in (2.35). Instead of outputting bits, the demodulator will output reliability of each bit, expressed as a Log-likelihood Ratio (LLR). The reliability of the mth bit at the nth symbol is given as

$$\begin{aligned} L_m^{(i)} \approx & \frac{1}{\sigma_i^2}(\text{Re}(\tilde{s}_n^{(l)} - \hat{s}_n^1) + \text{Im}(\tilde{s}_n^{(l)} - \hat{s}_n^1) \\ & - \text{Re}(\tilde{s}_n^{(l)} - \hat{s}_n^0) + \text{Im}(\tilde{s}_n^{(l)} - \hat{s}_n^0)), \end{aligned} \tag{2.38}$$

where $\hat{s}_n^1$ and $\hat{s}_n^0$ are the closest symbols to the received symbol with the bit in the mth position set to 1 and 0, respectively, and σ_i^2 is computed as

$$\sigma_i^2 = \frac{1}{2}\mathbb{E}\left[\left|s_n - \tilde{s}_n^{(l)}\right|^2\right] \approx \frac{1}{2N}\sum_{n=0}^{N-1}\left|\hat{s}_n - \tilde{s}_n^{(l)}\right|^2. \tag{2.39}$$

The LLRs then undergo a soft modulation that is defined according to the original modulation. For M-QAM the soft-modulated symbols can be obtained as

$$\mathrm{Re}(\bar{s}_n^{(l)}) = \sum_{m=1}^{\mu/2} 2^{\mu/2-m} \prod_{m'=0}^{m-1} \tanh\left(\frac{L_{(n+m')}^{(l)}}{2}\right), \tag{2.40}$$

and

$$\mathrm{Im}(\bar{s}_n^{(l)}) = \sum_{m=1}^{\mu/2} 2^{\mu/2-m} \prod_{m'=0}^{m-1} \tanh\left(\frac{L_{(n+m'+\mu/2)}^{(l)}}{2}\right), \tag{2.41}$$

where $\mu = \log_2 M$. The feedforward factor $F(k)$ can also be modified to take into account the reliability of the soft decisions as

$$F_k^{(l)} = \frac{H^*(k)}{\left(1 - \left|\rho^{(l-1)}\right|^2\right)|H(k)|^2 + \mathrm{NSR}}, \tag{2.42}$$

where $\rho^{(l)}$ is the reliability factor of the lth iteration, associated with the soft decisions. It can be divided into in-phase and quadrature reliabilities, which for M-QAM are calculated as

$$\rho_{n,I}^{(l)} = \sum_{m=1}^{\mu/2} 2^{\mu-2m} \prod_{m'=0}^{m-1} \tanh\left(\frac{|L_{(n+m')}^{(l)}|}{2}\right), \tag{2.43}$$

and

$$\rho_{n,Q}^{(l)} = \sum_{m=1}^{\mu/2} 2^{\mu-2m} \prod_{m'=0}^{m-1} \tanh\left(\frac{|L_{(n+m'+\mu/2)}^{(l)}|}{2}\right). \tag{2.44}$$

The combined reliability is then given by

$$\rho^{(i)} = \frac{\rho_{n,I}^{(l)} + \rho_{n,Q}^{(l)}}{4N\sigma_s^2}, \tag{2.45}$$

where σ_s^2 is the soft decided symbol variance given by

$$2\sigma_s^2 = \mathbb{E}[|s_n^2|]. \tag{2.46}$$

2.3.3 Multi-Carrier

In MC systems the bandwidth is divided into N narrower signals called subcarriers, spaced by Δ_f. The complex envelope is defined as

$$s_{mc}(t) = \sum_{m=0}^{N-1} s_m r(t) \exp\left(\frac{j2\pi mt}{pT_s}\right), \tag{2.47}$$

where T_s is the symbol length, and $p \geq 1$. The optimum support impulse $r(t)$ is chosen to maximise $\frac{N}{B}$, which is equivalent to minimising Δ_f, without ISI. Therefore, the optimum support impulse is defined as

$$r(t) = \mathrm{rect}\left(\frac{t}{T_s}\right), \tag{2.48}$$

which, in the frequency domain, is defined as

$$R(f) = \frac{1}{T_s}\text{sinc}\left(fT_s\right). \tag{2.49}$$

The frequency domain version of the signal is expressed as

$$S_{mc}(f) = \sum_{m=-\frac{N}{2}}^{\frac{N}{2}-1} S_m \frac{1}{T_s}\text{sinc}\left(fT_s - mp\right). \tag{2.50}$$

From the equation, it can be deduced that the spacing between subcarriers is defined as

$$\Delta_f = \frac{1}{pT_s}, \tag{2.51}$$

which is minimised when $p = 1$. This particular case is referred to as Orthogonal Frequency-Division Multiplexing (OFDM), and is the most common MC transmission technique.

2.3.3.1 Orthogonal Frequency Division Multiplexing

An OFDM system is a block-based MC scheme where there are N subcarriers that are spaced the minimum distance that ensures no ISI. Each subcarrier carries a modulated symbol, S_{mc}, of a specific modulation, such as M-QAM. The set of N symbols forms a vector defined as

$$\mathbf{S}_{mc} = \left[S_{mc}(0), S_{mc}(1), ..., S_{mc}(N-1)\right]. \tag{2.52}$$

Before transmission, however, this vector must be converted into the time domain by computing the Inverse Discrete Fourier Transform (IDFT), which can be achieved efficiently by using an IFFT.

Considering noisy channel transmission, and a proper CP length, the received frequency domain signal, obtained via FFT, at the kth subcarrier is given by

$$Y_{mc}(k) = H(k)S_{mc}(k) + N(k). \tag{2.53}$$

The equalization of the OFDM block can be performed using the equalizer as Single Carrier with Frequency Domain Equalization (SC-FDE), with ZF defined as

$$\tilde{S}_{mc}(k) = \frac{Y_{mc}(k)}{H(k)}, \tag{2.54}$$

and MMSE as

$$\tilde{S}_{mc}(k) = \frac{H^*(k)Y_{mc}(k)}{|H(k)|^2 + \text{NSR}}. \tag{2.55}$$

Since in conventional OFDM there is a high correlation between the equalized signal and the decided symbols, there is no added benefit from an iterative equalization scheme.

2.3.4 Automatic Repeat Request

In wireless communications there is a chance that the propagation conditions change abruptly, disrupting the communication and resulting in a failed transmission. When this occurs, mechanisms at the PHY layer might try to retransmit the signal. This type of retransmission scheme is referred to as ARQ, and is a widely adopted solution for many wireless standards [24]. For simplicity, the SC and MC notation is omitted, as it can be applied to either transmission technique. In ARQ, the rth received signal is denoted as

$$Y(k,r) = H(k,r)S(k) + N(k,r), \tag{2.56}$$

where $S(k)$ denotes the frequency-domain symbol or sample at the kth subcarrier, $N(k,r)$ is an independent noise term that follows a Gaussian distribution with variance $2\sigma^2_{N,r}$, and $H(k,r)$ is the CIR for the rth transmission attempt. The initial transmission is treated as $r = 0$, and the maximum number of attempts is written as R_T. As long as there is a chance of successful transmission, then the transmitter can continue to retransmit until it succeeds, or the delay exceeds what is allowed by the standard. This approach is considered less efficient, as it discards the previously received signals. On the receiver side, it is possible to optimize the chance of a successful reception by combining the information of all retransmitted symbols. The combination is expressed as

$$\hat{S}(k,r) = \frac{H(k)^H Y(k,r)}{|H(k,r)|^2 + \text{NSR}} + \tilde{S}(k,r-1), \tag{2.57}$$

where $\hat{S}(k,r)$ is the combined estimate that will be used in the decision process, for the rth retransmission attempt. If $r = 0$, then $\hat{S}(k,0) = \tilde{S}(k,0)$, the initial received symbol. Fig. 2.2 shows the BER of an OFDM system employing ARQ in an AWGN channel. It is clear that the performance improvement between retransmission attempts corresponds to the energy gain, as it decreases with each successive attempt due to all transmissions having the same power. From these results it is possible to determine how many retransmissions are necessary to achieve a certain BER, if the E_b/N_0 suddenly worsens.

Instead of retransmitting the same information, it is also possible to adjust transmission parameters based on the receiver's feedback as part of a process referred to as Adaptive ARQ [25].

2.4 Forward Error Correction

In the previous section it was shown that for a communication system with capacity C_{cap} and data rate R_b such that $R_b < C_{cap}$, there exists a block code with a set of codewords $\mathbf{C}$, with codeword length n, dimension k, and rate R_{code}, that can achieve an arbitrarily low bit error rate. However, although a coding scheme may exist, it may not be feasible to implement if the complexity or memory requirements are very high. In practical terms, a code can be characterised by its description, encoding and decoding complexities [26]. It

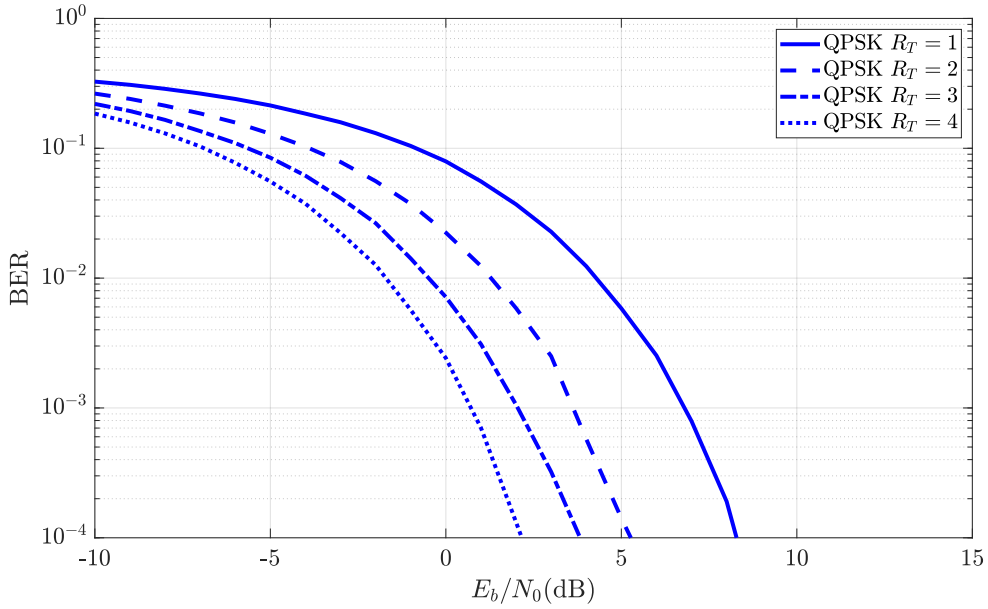

Figure 2.2: BER of QPSK employing ARQ.

is for this reason that most systems employ linear codes, which are codes that satisfy

$$c + c' \in \mathbf{C}, \quad \forall\, c, c' \in \mathbf{C}, \tag{2.58}$$

that is, any linear combination of codewords is also a codeword, including the all-zero codeword. The minimum distance, d_{min}, of a linear code is simply the minimum of the weight of all non-zero codewords. This type of code can be described by using a generator matrix, $\mathbf{G}$, which defines a codeword c_{word} as

$$c_{word} = b\mathbf{G}, \tag{2.59}$$

where b is a vector of n/R_{code} bits. The generator matrix is said to be in the systematic form when it is represented by $\mathbf{G} = [\mathbf{I}_k \quad \mathbf{P}]$, where $\mathbf{I}_k$ is the kth order identity matrix. If the generator matrix is systematic, then the codeword will be in the form $[\mathbf{b} \quad \mathbf{bP}]$, where the first part is the digital word containing the information bits, and the second part contains the parity bits.

In addition to the generator matrix, a second useful matrix can be defined called the parity check matrix, $\mathbf{H_p}$, which is a matrix that satisfies

$$\mathbf{H}_p c_{word}^T = 0^T. \tag{2.60}$$

The parity check matrix can also assume the systematic form $\mathbf{H}_p = [\mathbf{P} \quad \mathbf{I}_{n-k}]$. These matrices will be essential for defining the coding and decoding operations for linear block codes.

2.4.1 Encoding and Decoding

The encoding of a linear code is defined according to (2.59), and has a complexity of $O(n^2)$. This complexity can be lowered by using preprocessing techniques, which will be covered in the next sections.

For decoding a linear code, a Maximum Likelihood (ML) decision is used to find the most likely vector c_{word}^{ML} that solves (2.60), and is closest to the received signal vector y. The relationship between the two vectors can be expressed by an error vector $e_c = y + c_{word}$, which in $\mathbb{F}_2$, can be rearranged as

$$c_{word} = e_c + y. \tag{2.61}$$

It can then be substituted in (2.60) resulting in

$$\mathbf{H}_p e_c^T = \mathbf{H}_p y^T. \tag{2.62}$$

Let us define a syndrome vector s_{syn} that can be calculated at the receiver by

$$s_{syn}^T = \mathbf{H}_p y^T. \tag{2.63}$$

The syndrome can be substituted in (2.62) which leaves

$$s_{syn}^T = \mathbf{H}_p e^T, \tag{2.64}$$

in which a vector e that satisfies this equality is also the solution to the decoding process. Therefore, a ML decoding technique that finds e will also solve c_{word}^{ML}. However, this problem is known to be NP complete [27], which means that there is no known optimum and efficient algorithm to decode all linear codes. However, there may be efficient algorithms for specific subsets of all linear codes. The choice of which code to employ in a physical system will depend on whether the decoding of that particular code can be achieved efficiently with sufficient performance.

Conventional decoders use estimated received bits to compute ML estimation of the transmitted data. However, it is widely known that the optimum approach is to calculate the estimation based on the LLRs of the received bits using the so-called Soft-input, Soft-output (SiSi) decoders. This process can be understood as weighing each bit estimate by their reliability, in the updating phase of an iterative decoder. This approach is particularly effective when there are fading effects in the wireless channel.

2.4.2 Convolutional Codes

Convolutional codes are a widely used subclass of linear codes that can be efficiently decoded using the Viterbi algorithm [28], which exploits the structure of the code for high efficiency decoding. In a convolution encoder, k_0 information bits are coded into n_0 coded bits, for a rate of $R_{conv} = \frac{k_0}{n_0}$. In the previous analysed block codes, the coding efficiency is higher for larger block lengths, however, for convolutional codes k_0 and n_0 will assume

relatively low values, such as $k_0 = 1$ and $n_0 = 3$. The output bits are calculated through the convolution of the information bits with up to k_0 polynomial functions, hence the name of these codes.

A convolutional encoder consists of a series of shift registers that are fed with the information bits, with some of the registers' output being connected to a maximum of n_0 $\mathbb{F}_2$ adders. The adders are responsible for implementing the polynomial functions and are each connected to a different output, and if the code is systematic the latest information bit is connected directly to one of the outputs. The number of shift registers is defined as the constraint length, c_L, of the code. For example, a code with rate $1/2$ can be defined by the following equation

$$\begin{aligned} b_0(n) &= u(n) + u(n-1) + u(n-3) \\ b_1(n) &= u(n-1) + u(n-2), \end{aligned} \tag{2.65}$$

where $u(n)$ is the nth uncoded bit, $u(n-k)$ is the bit stored in the kth SR, and $b_0(n), b_1(n)$ are the first and second bits, respectively, associated with the nth uncoded bit. This code would have $c_L = 3$, requiring a total of 3 SR to implement, and for each uncoded bit there are two output bits, corresponding to the $1/2$ rate.

Although the encoding process is straightforward, decoding a convolutional code requires more complexity. In fact, these codes only surged in popularity with the development of the Viterbi decoder [28], named after its inventor. The BCJR decoder[29], named after its creators (Bahl, Cocke, Jelinek and Raviv), is another decoder that performs A Posteriori Probability (APP) decoding, which is also used for Turbo codes, which are convolutional codes with feedback bits.

2.4.3 Low-Density Parity Check Codes

An interesting set of block codes that have recently gained renewed interest are LDPC codes [30, 31]. The most important feature of this code family is the sparse parity and generator matrices used in the decoding and encoding [32]. These matrices must be sparse in order to take advantage of significantly large block lengths. The complexity of encoding and decoding grows exponentially with block length, unless, these processes can exploit the structure of the code to achieve lower complexities. In the case of LDPC codes, the encoding is simplified through pre-processing $\mathbf{G}$ into Upper Triangular (UT) or Lower Triangular (LT) form [26, 33], while the decoding is performed with Belief Propagation (BP).

The parity matrix represents a graph with N_{cbits} variable nodes, loosely connected to $V_{chk}s$ parity check nodes. Each variable node sends a message to the connected check nodes, and vice-versa for each check node. For optimum performance in MMSE, each check node sums the product of all received messages, known as the sum-product algorithm. In the first iteration ($i = 1$), the decoder computes the parity check operation for the qth connected check node, which is in turn connected to the dth variable node, defined for

the ith iteration as

$$R_j^{(i)}(d) = 2 \operatorname{atanh}\left(\prod_{d' \neq d} \frac{\tanh(V_{d'}^{(i-1)})}{2}\right), \tag{2.66}$$

where V_d' is the variable node operation of the d'th node, which must be computed for all variable nodes connected to the qth check node, except for the dth node. This operation is defined as

$$V_d^{(i)}(q) = L_d + \sum_{q' \neq q} R_{q'}^{(i)}, \tag{2.67}$$

where L_d is the LLR of the dth coded bit, and $R_{j'}^{(i)}$ are the parity checks of the connected check nodes, other than the jth one. In the first iteration $V_l^{(0)} = L_d$. The final step in the algorithm is to compute the output LLR values for the current iteration as

$$LU_b^{(i)} = LU_d + \sum_{q \in J_d} R_q^{(i)}(d), \tag{2.68}$$

where $LU_b^{(i)}$ is the LLR of the b uncoded bit at the ith iteration, and J_d contains the indices of the check nodes that are connected to the dth variable node. This process is repeated I times before a hard decision is performed on the decoded bits.

2.4.4 Hybrid ARQ

Although FEC can significantly increase the probability of a successful transmission, the high volatility of the wireless channel is still a problem. Abrupt changes in propagation conditions may still result in bit errors that exceed the code's error correcting ability. In such a situation, retransmitting the original data increases the odds of a successful transmission, as was the case for ARQ. When FEC is used in the original transmission, this scheme is referred to as Hybrid Automatic Repeat Request (HARQ).

During detection, the decoder attempts to decode the received codeword $\mathbf{L}$. If it succeeds, then the receiver uses a wireless feedback channel to transmit an Acknowledgement (ACK) [31]. On the other hand, if the transmission is deemed as failed, a retransmission is scheduled. If the retransmission contains the same bit data as the original transmission, then it is referred to as HARQ Type I. For each received retransmission, the receiver computes $\mathbf{L}$, which is then combined with the $\mathbf{L}$ from previous attempts to increase reliability. This process can be written as

$$\mathbf{L} = \sum_{r=0}^{N_t} \mathbf{L}^{(r)}, \tag{2.69}$$

where $\mathbf{L}^{(r)}$ refers to the soft decided bits of the rth transmission attempt, and N_t is the maximum number of possible retransmissions. The process of combining the energy of previous transmissions is also referred to as HARQ - Chase Combining (HARQ-CC).

Fig. 2.3 shows the BER of an OFDM system employing QPSK and LDPC coding, considering a Rayleigh fading channel. In the figure there is a noticeable difference

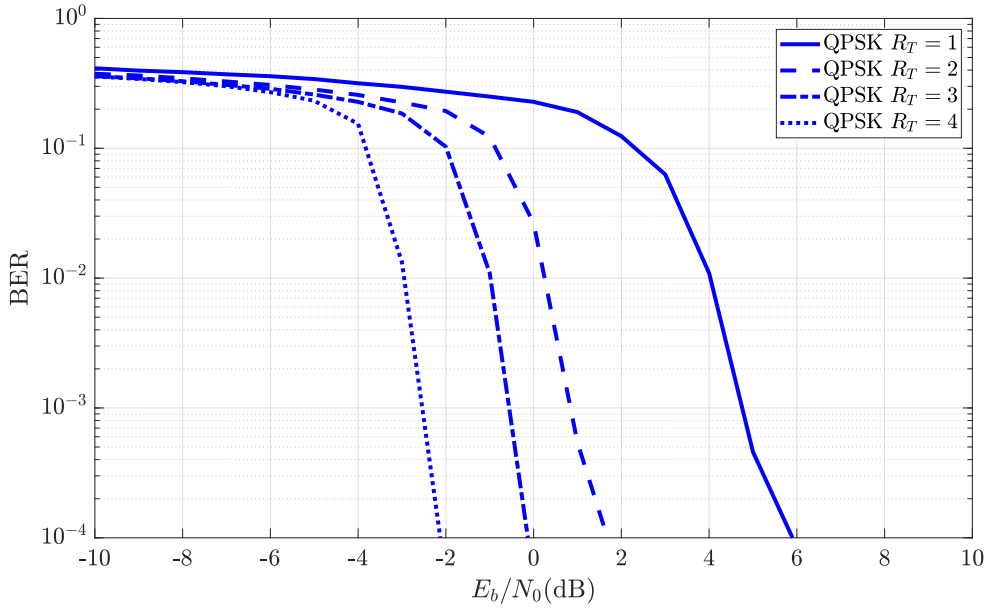

Figure 2.3: BER of an OFDM system using QPSK constellations and HARQ.

between first and second transmissions, as the code gain benefits from frequency diversity due to the varying channel between transmissions. Additional attempts achieve smaller gains, since the total energy is increased by the same amount each time.

2.4.5 HARQ Type II

In HARQ Type II, or HARQ - Incremental Redundancy (HARQ-IR), instead of transmitting the same data, additional parity bits are sent to the receiver to aid in decoding . This is the standard scheme for New Radio (NR) Release 17 [31], which consists in transmitting the parity bits that were punctured from the original codeword. For a certain transmission attempt, bits are selected to fill the OFDM symbol based on 4 different starting points in the codeword, named $rv_0 - rv_3$. rv_0 is the starting point for the initial transmission, and retransmissions follow a repeating pattern $rv_0, rv_2, rv3, rv1$ (including the initial transmission). Depending on bit space available in an OFDM symbol, there may be overlap between transmitted bits, with rv_0 and rv_2 contain the least possible overlap. The less overlap there is, the lower the code rate at the receiver, which is why rv_2 is a good choice for the first retransmission. In current applications, HARQ Type II significantly outperforms HARQ Type I.

Fig. 2.4 shows the BER of an OFDM system employing QPSK and NR LDPC coding, considering a Rayleigh fading channel. Compared to HARQ, there is a much larger performance gain with the first transmission attempt, which is consistent with the rv used in the NR standard. Successive transmissions do not have such a large gain, as this scheme was optimized for a low number of retransmissions. Although it would be possible to

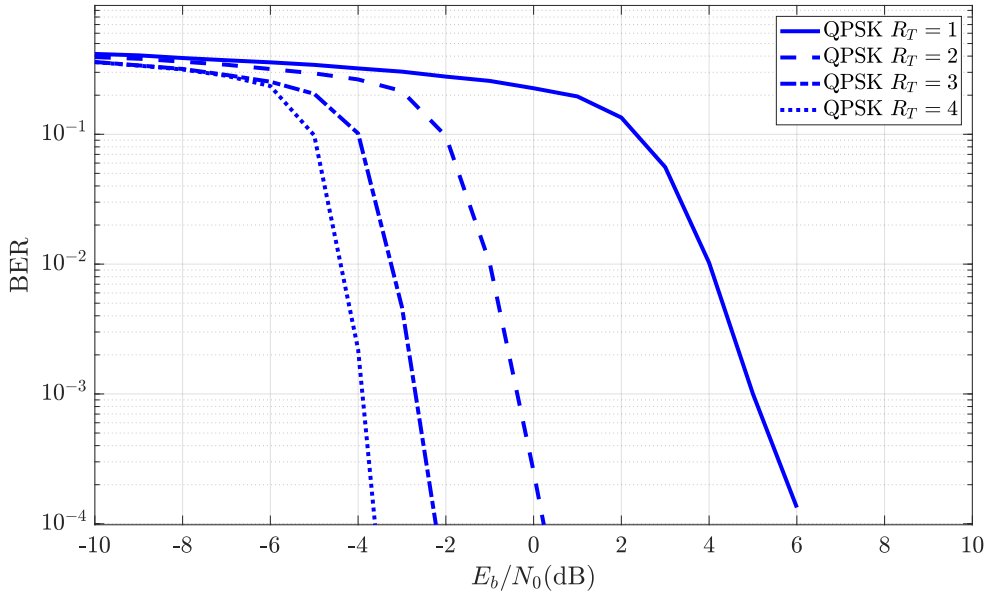

Figure 2.4: BER of an OFDM system using QPSK constellations and HARQ Type II.

have very large codewords that could be split into 4 or more chunks, it would be inefficient to encode such large blocks with each transmission.

2.5 Multi-Input Multi-Output

Increasing the data rates of a single antenna wireless system can be achieved with several different methods, such as larger bandwidths and modulations, each with an associated cost, such as larger spectral masks and transmissions power. An alternative method is to increase the number of available wireless channels by utilizing more antennas at the transmitter and receiver, known as MIMO [34]. Using T and R transmitting and receiving antennas, respectively, it can be shown that the system capacity can increase up to $\min(T, R)$ times, as it allows for independent data streams to be transmitted at the same time [35, 36]. The number of different data streams is referred to as C, and in the limit $C = \min(T, R)$. For notation simplicity, from this point on vector indices will be denoted as subscript, i.e. $S(k) = S_k$.

In a MIMO system, the channel at the kth subcarrier is given by

$$\mathbf{H}_k = \begin{bmatrix} H_k^{(1,1)} & H_k^{(1,2)} & \cdots & H_k^{(1,T)} \\ H_k^{(2,1)} & H_k^{(2,2)} & \cdots & H_k^{(2,T)} \\ \vdots & \vdots & \ddots & \vdots \\ H_k^{(R,1)} & H_k^{(R,2)} & \cdots & H_k^{(R,T)} \end{bmatrix}. \tag{2.70}$$

Similarly, the time domain SC symbol vector at the n timeslot is defined as

$$\mathbf{s}_n = \left[s_n^{(0)}, s_n^{(1)}, ..., s_n^{(C-1)} \right], \tag{2.71}$$

while in the case of MC transmission, the frequency domain symbol vector at the kth subcarrier is defined as

$$\mathbf{S}_k = \left[S_k^{(0)}, S_k^{(1)}, ..., S_k^{(C-1)} \right]. \tag{2.72}$$

The received signal at the kth subcarrier is therefore defined as

$$\mathbf{Y}_k = \mathbf{H}_k \mathbf{S}_k + \mathbf{N}_k, \tag{2.73}$$

where $\mathbf{N}_k$ is a matrix composed by the noise values at each channel.

Although MIMO can provide significant benefits, there are some drawbacks that should be mentioned. In fact, the maximum capacity gains are only achieved if the wireless channels are uncorrelated, which requires that the antennas be spaced by at least half the carrier wavelength, $\frac{\lambda_c}{2}$. This restricts the number of antennas that can be implemented in a mobile device. Another downside lies in the increased complexity of channel estimation and equalization. In both processes, the channel information at a certain subcarrier is now a matrix of size $T \times R$. As a result, inverting the channel now requires inverting a matrix, which is computationally more expensive.

2.5.1 Precoding and Decoding

Precoding and Decoding techniques consist in multiplying the outgoing or received signals by a precomputed matrix, respectively. In many applications, these techniques are utilized to reduce the computational complexity of the channel equalization process, or to perform the computation at the transmitter, instead of the receiver.

2.5.1.1 Maximum and Equal Gain Combining

The complexity of the equalization process can be significantly reduced on the condition that the receiver has many more antennas than the transmitter, $R \gg T$. In such a scenario, the equalization may not require the inversion of a $R \times T$ matrix, resulting in less computationally heavy equalization.

With $R >> T$ and low correlation between channels, a different equalization criterion must be used, such as Maximal-Ratio Combining (MRC). In MRC the received signals associated to a single stream are combined according to their channel power, which allows for the simplification

$$\mathbf{H}_k^H \mathbf{H}_k \approx R\mathbf{I}. \tag{2.74}$$

The equalization factor $\mathbf{F}_k$ for this criterion is simply

$$\mathbf{F}_k = \mathbf{\Psi} \mathbf{H}_k^H, \tag{2.75}$$

where $\mathbf{\Psi}$ is a matrix containing the appropriate normalization factors. This equalizer criterion requires no matrix inversion, when compared to MMSE and ZF. Another possible criterion is Equal-Gain Combining (EGC), wherein all signals associated to a certain stream are combined equally at the receiver, which results in

$$\mathbf{A}_k^H \mathbf{H}_k \tag{2.76}$$

being approximated as a diagonal matrix, where $\mathbf{A}_k$ is defined as

$$\mathbf{A}_k = \exp(j2(\mathbf{H}_k)). \tag{2.77}$$

The equalization factor of this criterion is defined as

$$\mathbf{F}_k = \mathbf{\Psi}\mathbf{A}_k^H, \tag{2.78}$$

where $\mathbf{\Psi}$ is the same normalization factor matrix as the one in MRC.

2.5.1.2 Singular Value Decomposition

This technique consists in combining precoding and decoding, and is commonly used in single point-to-point MIMO systems, where the channel interference cancellation is split between the transmitter and receiver [37]. The channel matrix $\mathbf{H}_k$ can be decomposed into three different matrices using SVD, which is defined as

$$\mathbf{H}_k = \mathbf{U}_k \mathbf{\Lambda}_k \mathbf{V}_k^H, \tag{2.79}$$

where $\mathbf{V}_k$ is the precoding matrix, $\mathbf{U}_k^H$ is the decoding matrix, and $\mathbf{\Lambda}_k$ is a diagonal matrix containing C singular values, provided that $\text{rank}(\mathbf{H}_k) = C$, which can be achieved by ensuring low correlation between antennas.

The precoded signal is obtained as

$$\mathbf{X}_k = \mathbf{V}_k \mathbf{S}_k, \tag{2.80}$$

which leads to the received signal

$$\mathbf{Y}_k = \mathbf{H}_k \mathbf{X}_k + \mathbf{N}_k. \tag{2.81}$$

The decoding is performed on the received signal as

$$\mathbf{W}_k = \mathbf{U}_k^H \mathbf{Y}_k, \tag{2.82}$$

where $\mathbf{W}_k$ is expanded as

$$\begin{aligned} \mathbf{W}_k &= \mathbf{U}_k^H \mathbf{H}_k \mathbf{X}_k + \mathbf{U}_k^H \mathbf{N}_k \\ &= \mathbf{U}_k^H \mathbf{H}_k \mathbf{V}_k \mathbf{S}_k + \mathbf{U}_k^H \mathbf{N}_k \\ &= \mathbf{U}_k^H \mathbf{U}_k \mathbf{\Lambda}_k \mathbf{V}_k^H \mathbf{V}_k \mathbf{S}_k + \mathbf{U}_k^H \mathbf{N}_k \\ &= \mathbf{\Lambda}_k \mathbf{S}_k + \mathbf{U}_k^H \mathbf{N}_k. \end{aligned} \tag{2.83}$$

The equalization is then simplified to inverting a diagonal matrix, which has trivial complexity. The ZF equalizer for this system is defined as

$$\mathbf{F}_k = \frac{1}{\boldsymbol{\lambda}_k}, \tag{2.84}$$

and the MMSE equalizer is defined as

$$\mathbf{F}_k = \frac{\boldsymbol{\lambda}_k}{\boldsymbol{\lambda}_k^2 + NSR}. \tag{2.85}$$

Although it is assumed in these definitions that all singular values exist, the generalization to other scenarios is straightforward.

The absolute value of the singular values may differ significantly, which will condition the performance of each stream. Fig. 2.5 shows the Probability Density Function (PDF) of each singular value in an 8×8 MIMO system. In this case, the strongest singular value can be more than 20 times greater than the weakest one.

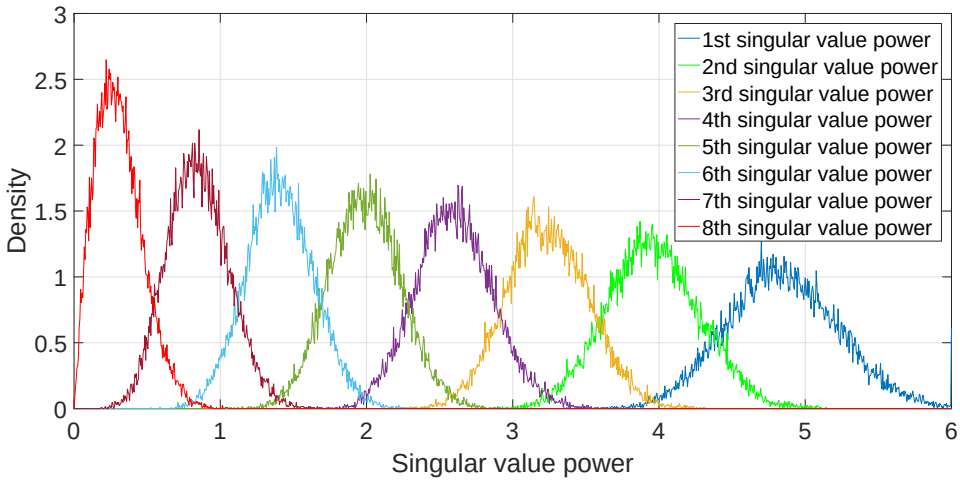

Figure 2.5: PDF of the singular values in an 8×8 MIMO system.

There are several compensation approaches such as water-filling power algorithms and adaptive modulations. An alternative low complexity solution is to interleave all streams in such a way that all streams are affected by all singular values, in equal proportions. An illustrative representation of this scheme is shown in Fig. 2.6.

In the case of SC-FDE, this interleaving is performed by the transmitter with the symbol blocks, and later the process is reversed by the receiver, before equalization, resulting in a significant improvement on the average performance over the conventional scheme. For OFDM, the interleaving is performed earlier at the bit blocks before modulation, and is deinterleaved after the equalization and demodulation. In this case the average performance does not show an improvement over the conventional scheme, however, if using a FEC scheme where the coded bits are interleaved, then there is a significant

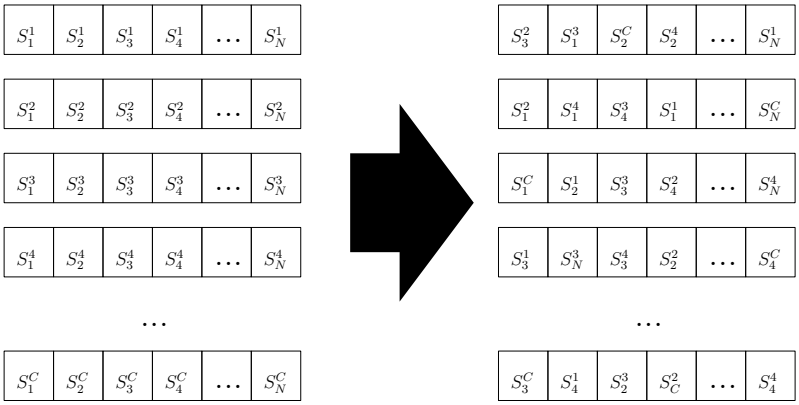

Figure 2.6: Example of the interleaving between C streams with N subcarriers.

improvement over the conventional scheme, with the added benefit that large codewords may be split among the different streams.

2.6 Non-Ideal Transceivers

Up to this point, only ideal systems have been considered, with perfect synchronization and hardware. Of course, in practice, this is not the case, and specific techniques may be required to cope with imperfect hardware. This section will outline several effects that arise due to non-ideal hardware and characterize their impact on the received signal. Since most of these effects are applied in the time domain, the impact on OFDM signals will be more complex and is therefore given further detail.

2.6.1 System Characterization

The linear requirements imposed on RF hardware have increased in step with higher system specifications. Particularly, the use of Super Quadrature Amplitude Modulation (Super-QAM) has been a significant motivator, as it allows higher data rates due to the increased spectral efficiency, compared to using larger bandwidths which may require purchasing spectrum. There are limits to the available bandwidth, and which carrier frequencies can be used, while modulation order largely depends on the available SNR at the receiver. However, the error threshold for Super-QAM detection is very low, due to the higher constellation density. In 3rd Generation Partnership Project (3GPP) documentation, this threshold is expressed as a limit to the transmitted symbols' Error Vector Magnitude (EVM), which, for simplicity, is defined as

$$\mathrm{EVM} = \sqrt{\frac{1}{N}\sum_{k=0}^{N-1}\frac{|X_k - S_k|^2}{2\sigma_s^2}}, \tag{2.86}$$

where X_k is the kth subcarrier of the transmitted signal, and $2\sigma_s^2 = \mathbb{E}[|S_k|^2]$. In the standard, the EVM is measured at the receiver with specific setup conditions, which

Modulation Scheme	EVM Requirement
QPSK	17.5%
16-QAM	12.5%
64-QAM	8%
256-QAM	3.5%
1024-QAM ($f_c \leq 4.2$GHz)	2.5%
1024-QAM ($f_c > 4.2$GHz)	2.8%

Table 2.1: EVM limits for different modulations in release 17 of 5G.

makes it difficult to characterize. The definition in (2.86) characterizes the minimum EVM that will be observed by a real system, and is therefore a useful metric for system design. Table 2.1 shows the EVM limits for different orders of QAM available in release 17 for 5G NR [38].

In the standard, the EVM is measured at each NR subcarrier averaged over a period of 10 ms, using all resource blocks. As will be shown in this section, hardware impairments contribute significantly to the resulting EVM.

2.6.2 Carrier Frequency Offset

A very common impairment in wireless systems occurs when the carrier frequency oscillator is not exactly tuned to the desired frequency, being off by an error, δ_f, normalized to the subcarrier spacing Δ_f. Under those conditions, the sampled distorted signal can be characterized in the time domain as [39]

$$s_n^{\text{cfo}} = s_n \exp\left(j2\pi\delta_f n/N\right). \tag{2.87}$$

For SC systems, the phase shift distorts the constellation and impairs the demodulator, though can be compensated fully by inverting the effect of (2.87). On the other hand, the Carrier Frequency Offset (CFO) effects in OFDM systems are not as simple, as one can define the impaired signal as [40]

$$S_k^{\text{cfo}} = \sum_{l=0}^{N-1} C_{l-k} S_l, \tag{2.88}$$

where

$$C_{l-k} = \frac{1}{N} \frac{\sin \pi(l-k+\delta_f)}{\sin \pi \frac{(l-k+\delta_f)}{N}} \exp j\pi \frac{(N-1)(l-k+\delta_f)}{N}. \tag{2.89}$$

It is clear that in this situation the frequency-domain signal suffers from Intercarrier Interference (ICI) due to the CFO, which cannot be compensated fully in the frequency domain. In practice the CFO can be greater than the subcarrier spacing Δ_f, such as in high mobility scenarios due to Doppler spread. Therefore, it can be normalized to Δ_f, and split into two parts: integer; and fractional. If a normalized offset of $\delta_f = 1$ is considered, then according to (2.89) it becomes $C_{-1} = 1$ and $C_{l-k\neq-1} = 0$, which corresponds to shifting all

subcarriers by 1. In the literature, it is considered simple to estimate and compensate an integer offset [41], leaving only a remaining fractional offset. This leads to rewriting (2.89) into a simpler form as

$$C_{l-k} = \frac{1}{N}\sum_{m=0}^{N-1} \exp\left(\frac{j2\pi m(l-k+\delta_f)}{N}\right). \tag{2.90}$$

For $l-k=0$, which corresponds to the desired subcarrier, it becomes

$$C_0 = \frac{1}{N}\sum_{m=0}^{N-1} \exp\left(\frac{j2\pi m\delta_f}{N}\right), \tag{2.91}$$

which is a phase shift of the wanted subcarrier that does not depend on the subcarrier index, i.e., it is constant for all subcarriers, referred to as the Common Phase Error (CPE). For $l \neq k$, the sum terms of (2.90) corresponds to the ICI due to all other subcarriers, which will depend on the subcarrier index and power. Therefore, rewriting S_k^{cfo} as

$$S_k^{\text{cfo}} = C_0 S_k + \sum_{m\neq k}^{N-1} C_{m-k} S_m, \tag{2.92}$$

where the second term's power will define the system's Signal-to-Interference Ratio (SIR).

2.6.2.1 Simulation Results

The impact of CFO on the BER is shown in Fig. 2.7 for an OFDM system with $N = 512$ and 256-QAM. From the figure, it can be noted that for relatively low values of CFO, the average BER increases significantly compared to a linear system without CFO. Although for $\delta_f = 0.009$ the system does not exceed the standard's maximum EVM for this constellation size, it already requires 6 dB more power to achieve the same performance as the linear receiver, for a target BER of 10^{-4}.

Fig. 2.8 presents the EVM as a function of δ_f. This figure shows us a clear linear relationship between EVM and CFO, which is to be expected as the interference power is linearly proportional to the CFO.

2.6.3 Phase Noise

Ideally, the oscillator responsible for generating the carrier wave will output a perfect sine wave. In practice, however, the period of the sine wave may vary slightly from the intended period. This fluctuation, referred to as jitter, creates phase noise around the carrier, which can be interpreted as a phase modulation of the carrier frequency [42]. The time-domain signal distorted by phase noise is defined as

$$s_n^{\text{pn}} = s_n \exp(j\phi_n), \tag{2.93}$$

where ϕ_n is the phase noise at the nth instant. The presence of this impairment can significantly degrade the system performance [43]. For SC systems, this effect cannot be

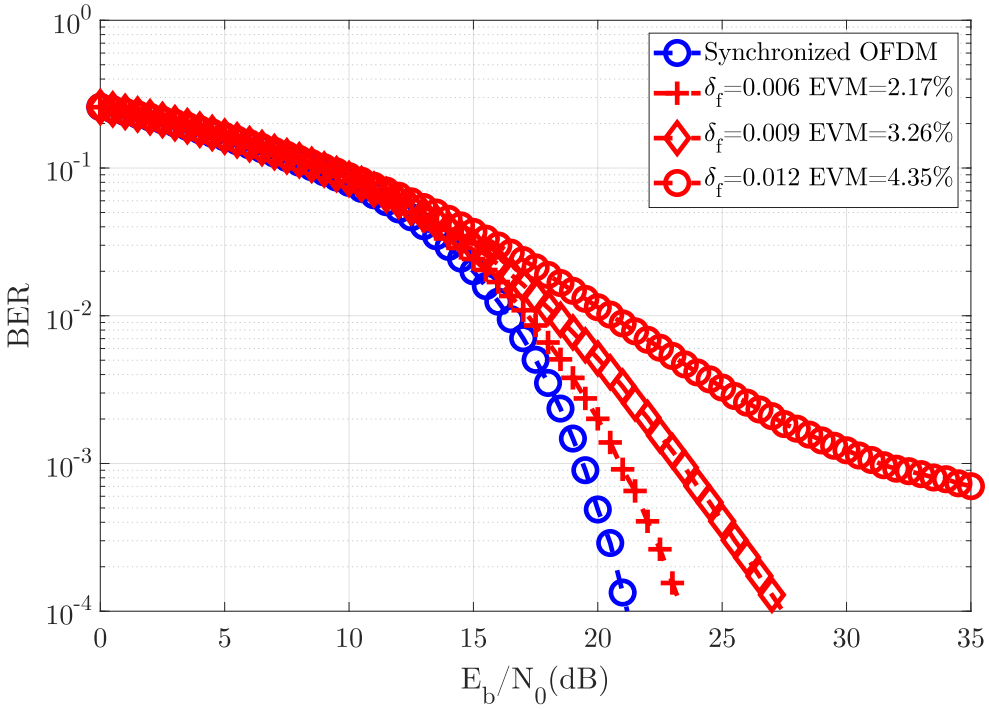

Figure 2.7: BER for an OFDM system with $N = 512$ and 256-QAM, with various levels of δ_f.

compensated fully without knowledge of ϕ_n, though it can be approximated to partially cancel out the phase noise [44].

For OFDM systems, the analysis must be done in the frequency domain. Note that for very low values of ϕ_n, the approximation $\exp(j\phi_n) \approx 1 + j\phi_n$ is tight. In the frequency domain, this becomes

$$S_k^{\text{pn}} = S_k + \frac{j}{N}\sum_{r=0}^{N-1} S_r \sum_{n=0}^{N-1} \phi_n \exp\left(j\frac{2\pi}{N}(r-k)n\right), \tag{2.94}$$

which can be interpreted as the signal plus an error term. The error term is divided in two parts, the first being for $r = k$, defined as

$$S_k \frac{j}{N}\sum_{n=0}^{N-1} \phi_n, \tag{2.95}$$

which, similarly to a CFO, referred to as the CPE. This part is simply the symbol at the kth subcarrier multiplied by the average of the phase noise, which can compensated at the receiver. The second part part of the error term, associated with subcarriers $r \neq k$, is given by

$$\frac{j}{N}\sum_{\substack{r=0 \\ r\neq k}}^{N-1} S_r \sum_{n=0}^{N-1} \phi_n \exp\left(\frac{j2\pi(r-k)n}{N}\right), \tag{2.96}$$

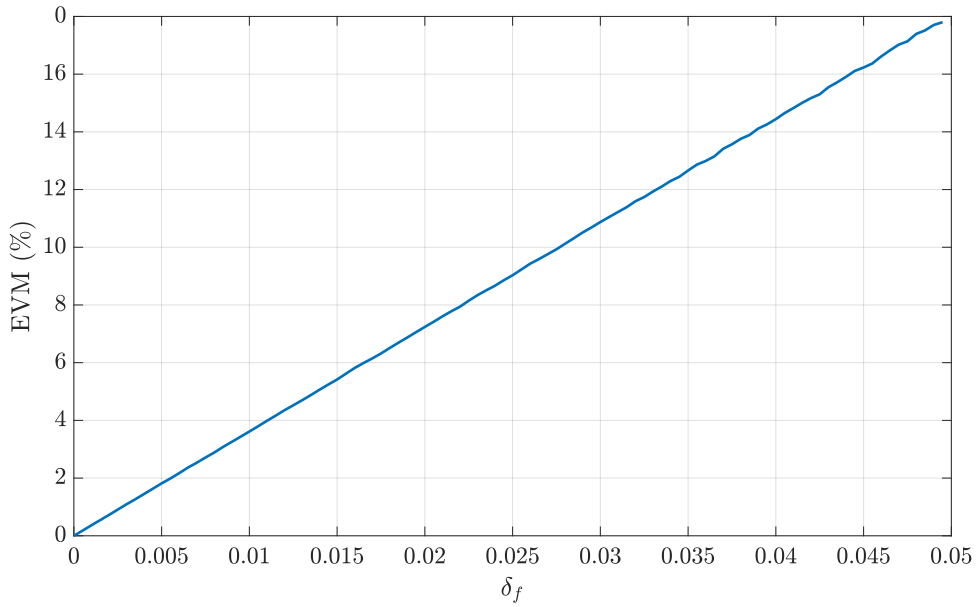

Figure 2.8: EVM as a function of δ_f, normalized to the subcarrier spacing.

which corresponds to interference from the other subcarriers, multiplied by the average phase noise shifted by a certain amount. Therefore, this is the factor that introduces ICI and, due to the random nature of the subcarriers, cannot be fully compensated.

It should also be noted that the characteristics of the phase modulation ϕ_n will depend on the underlying technology of the RF oscillator. Below, two types of phase modulation are described.

2.6.3.1 Free-Running Oscillator

The simplest RF oscillator is known as a Free-Running Oscillator, which is basically a circuit that outputs the desired RF carrier without needing an input clock. It has be shown in literature that the phase noise of this particular architecture can be modelled by a Wiener process [45] with $\mathbb{E}(\phi_n) = 0$ and

$$\phi_{n+1} = \phi_n + q^{\text{pn}}, \tag{2.97}$$

where q^{pn} is a Gaussian distributed random phase, with variance $\sigma_p(t) = 2\pi\beta_{LW}t$, and $\phi_0 = 0$. In this model, β_{LW} represents the linewidth between the two 3 dB points of the Lorentzian power spectrum of the phase noise, $\beta_{LW} = 2f_{3dB}$, where f_{3dB} is the phase noise 3 dB bandwidth. The quality of the oscillator is described by the parameter $c_{osc} = f_{3dB}\pi f_c^2$, where f_c is the carrier frequency, and it should be as low as possible. It is clear that for a carrier of $2f_c$ the 3 dB bandwidth must be $\frac{f_{3dB}}{4}$, to maintain the same quality factor, requiring a better oscillator.

The Single-Sideband (SSB) PSD of the phase noise around the first harmonic, $\mathcal{L}(f_m)$, is very useful in terms of describing the oscillator performance [46, 47]. For frequency offsets much lower than f_c, the SSB noise power spectrum can be approximated as

$$\mathcal{L}(f_m) \approx 10 \log_{10} \left(\frac{c f_c^2}{\pi^2 f_c^4 c^2 + f_m^2} \right). \tag{2.98}$$

The SSB for different subcarrier spacings, Δ_B, and f_{3dB} is shown in Fig. 2.9. As can

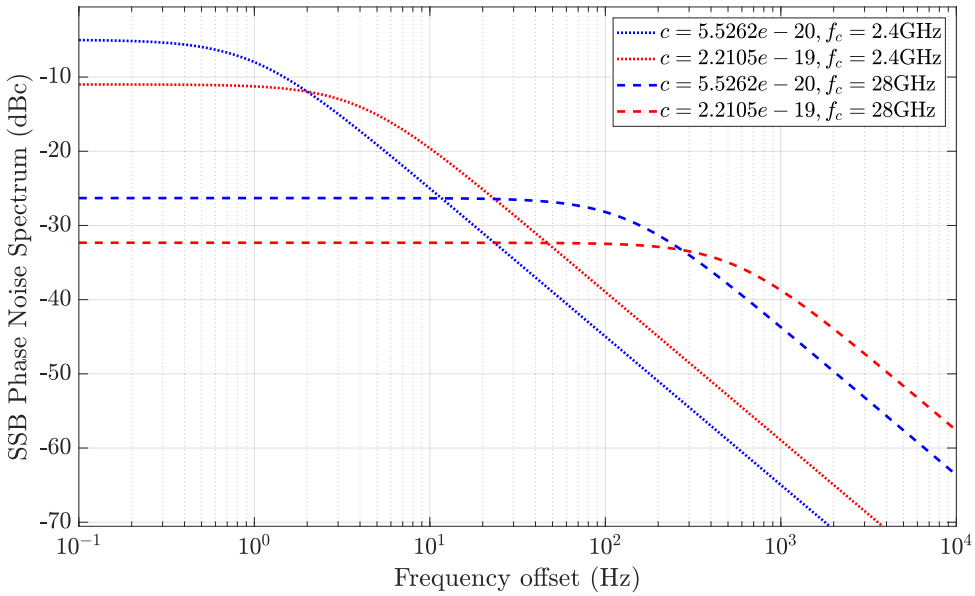

Figure 2.9: PSD of the SSB spectrum associated with the phase noise of a free running oscillator, with c designed for a bandwidth f_{3dB} of 1 and 4 Hz, respectively, for a carrier of 2.4 GHz (band n43 of 5G FR1), and 28GHz (band n257 of 5G FR2).

be observed, there are two regions, an initial constant region which will be centered on f_c, and a -20 dB/dec slope for frequencies beyond f_{3dB}. The second region is generally more important in OFDM due to subcarrier interference. Here, it can be noted that by halving f_{3dB}, the resulting phase noise power at each subcarrier is also halved, assuming that $\Delta_B < f_{3dB}$.

The Leeson model is a more accurate model for characterizing the phase noise spectrum of free running oscillators [48]. This model characterizes the spectrum near $f_m = 0$ with a decay of $1/f_m^3$, as opposed to the previous model's $1/f_m^2$, which transitions to a decay of $1/f_m^2$ for $f_m > f_{1/f_m^3}$. The SSB noise power spectrum is defined as

$$\mathcal{L}(f_m) = 10 \log_{10} \left[\frac{2FkT}{P_{\text{carr}}} \left(1 + \left(\frac{f_c}{2Qf_m} \right)^2 \right) \left(1 + \frac{f_{1/f_m^3}}{|f_m|} \right) \right], \tag{2.99}$$

where kT is the thermal noise, P_{carr} is the carrier power and Q is the resonator quality factor. In this model, both F and f_{1/f_m^3} are obtained empirically by measuring a specific oscillator.

2.6.3.2 Phase-Locked Loop Synthesizer

Another common RF oscillator architecture involves the use of a Phase-Locked Loop (PLL) to synthesize the RF frequency from an input reference signal, which can be provided by a free running oscillator [47]. This architecture is very appealing for systems that support multiple standards with different carriers. If it is considered that the reference signal is not ideal, and instead will drift with some time deviation $\alpha^{\text{in}}(t)$, which can be modelled by a Wiener process, then there will also be a time deviation at the output of the PLL, given by α_n^{VCO}. Therefore, the time deviation of the error signal at the input of the Low-Pass Filter (LPF) will be defined as

$$\beta_n^{\text{LPF}} = \alpha_n^{\text{VCO}} - \alpha_n^{\text{in}}. \tag{2.100}$$

Under these conditions α_n^{VCO} can be modelled by an Ornstein–Uhlenbeck process. The phase noise for this architecture is defined as

$$\phi_n = 2\pi f_c \alpha_n^{\text{VCO}}. \tag{2.101}$$

2.6.3.3 Simulation Results

In the following simulations, the free running oscillator model is used due to its simplicity, although the analysis and simulation can also be extended for PLL oscillators. Fig. 2.10 presents the simulated BER of an OFDM system with $N = 512$ and 256-QAM constellations, considering different levels of phase noise. From the figure, it can be noted that this system is particularly sensitive to phase noise, since the BER is severely degraded even when the considered value of f_{3dB} yields an EVM of 2.1%. In part, this can be explained by the constellation phase rotation from the CPE, which has a higher variance than a constant CFO. Moreover, the larger the constellation, the more important it is to compensate this phase shift. In Fig. 2.11 the EVM as a function of f_{3dB} is shown.

Naturally, the EVM does not scale linearly with f_{3dB}, since it is a factor that determines the variance of the Wiener process. Also, it can be noted that the required EVM threshold for 256-QAM constellations with unmitigated phase noise requires $f_{3dB} > 8$ Hz.

2.6.4 IQ Imbalance

In an In-Phase and Quadrature (IQ) architecture, there should be a 90 degree phase difference between the equal power in-phase and quadrature components. However, in practical systems it is difficult to ensure that phase difference and an exact equal distribution of the power among the two branches. This effect is known as IQ imbalance [49], and can be modelled in the time-domain as

$$s_n^{\text{IQ}} = \alpha s_n + \beta s_n^*, \tag{2.102}$$

with

$$\alpha = (\cos(\Delta\phi) - j\epsilon_g \sin(\Delta\phi)), \tag{2.103}$$

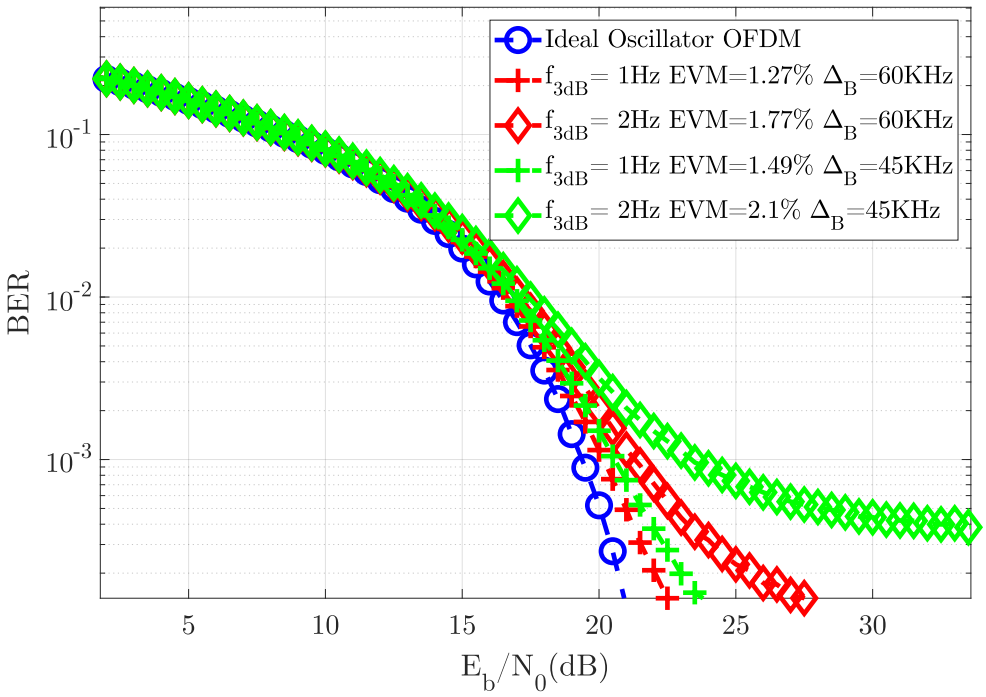

Figure 2.10: BER for a 256-QAM OFDM system with $N = 512$, considering different phase noise bandwidths f_{3dB} and subcarrier spacings Δ_f.

and

$$\beta = (\epsilon_g \cos\Delta\phi - j\sin(\Delta\phi)), \tag{2.104}$$

where ϵ_g is the amplitude imbalance and $\Delta\phi$ is the phase imbalance. In an SC system, this corresponds to a phase shift on the received symbols, which can be estimated and compensated. For OFDM systems, the effect must be analysed in the frequency domain, which becomes

$$S_k^{\text{IQ}} = \alpha S_k + \beta S^*_{(N-k-1)}, \tag{2.105}$$

which is simply the original signal scaled by a complex factor α, plus the interference of the mirrored subcarrier scaled by β. In the literature, it is sometimes considered that $k = 0, 1, ..., N/2 - 2$, because in direct conversion architectures the Direct Current (DC) subcarrier, $N/2$, does not carry data, which results in the $N/2 - 1$ subcarrier not suffering interference due to IQ imbalance.

2.6.4.1 Simulation Results

The IQ imbalanced system was tested under the same conditions as the previous simulations. Fig. 2.12 presents the BER for different levels of IQ imbalance. Since this impairment has two parameters, for this comparison they were varied in tandem. It can be observed

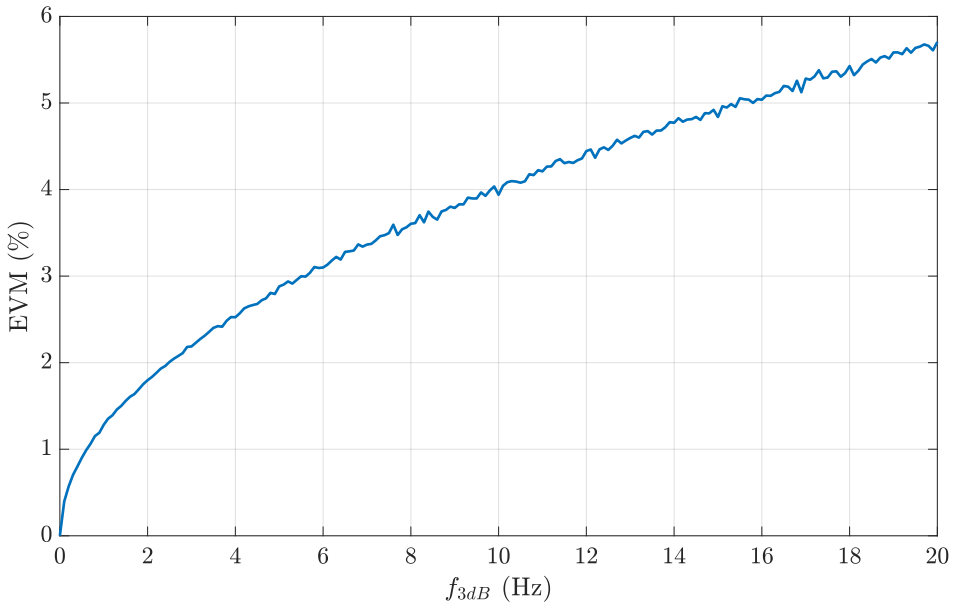

Figure 2.11: EVM as a function of f_{3dB}, with $\Delta_B = 60$ KHz.

that the BER is degraded by about 10 dB even for an imbalance of $\epsilon_g = 3\%$ and $\Delta\phi = 1.5°$, considering a target BER of 10^{-4}.

In Figs. 2.13 and 2.14 the EVM is shown as a function of each of the parameters. For each varying parameter the other was fixed at a nonzero value. If the impact on the EVM of each parameter is similar in magnitude, increasing only one parameter does not result in a linear increase of the EVM. If one parameter is much larger than the other, then increasing this parameter does result in a linear increase of the EVM. Therefore, it is important to reduce both amplitude and phase imbalance to minimise EVM.

2.6.5 Analog-to-Digital Converter

An essential component of any digital communication system is the ADC present at the receiver. This element is responsible for converting the arriving analog signal, into a set of digital samples. Ideally, the relationship would be perfectly linear, however, that would require an ADC with infinite resolution. A non-ideal ADC can be represented by the branch function

$$f(x) = \text{lfloor}\left(0.5 + \frac{x}{2^{R_{\text{bit}}-1}}\right) A_{\text{bit}}, \tag{2.106}$$

where the function lfloor$(\cdot)$ discards the fractional part of the argument, R_{bit} is the ADC bit resolution, and A_{bit} is the Least Significant Bit (LSB) amplitude, which depends on the ADC saturation range A_{adc}, and is defined as

$$A_{\text{bit}} = \frac{A_{\text{adc}}}{2^{R_{\text{bit}}-1}}. \tag{2.107}$$

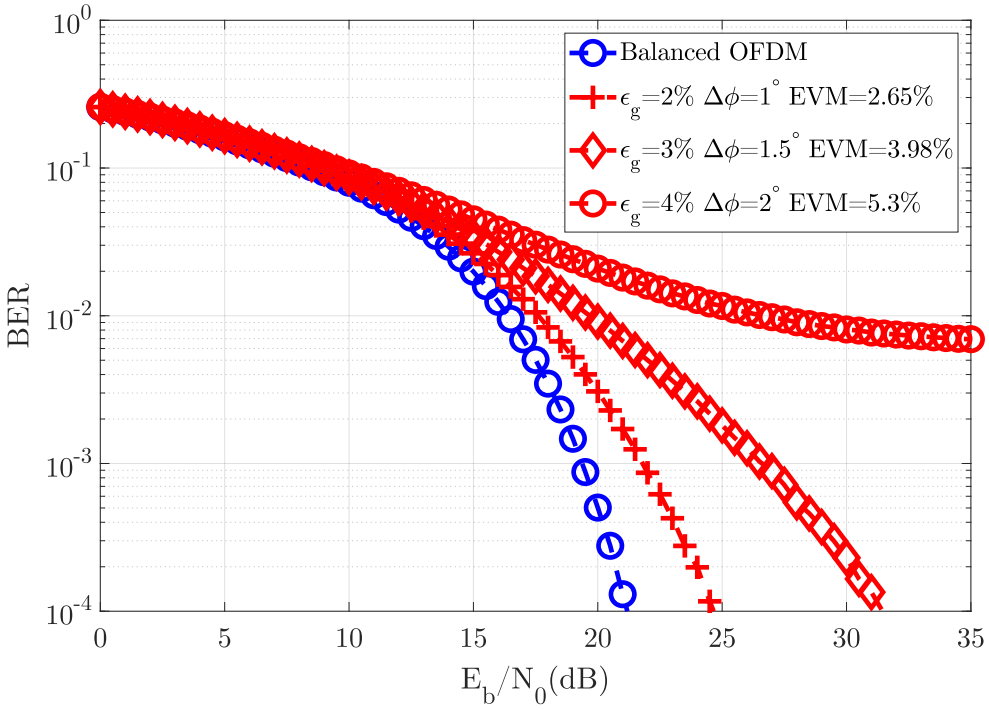

Figure 2.12: BER for an OFDM system with $N = 512$ and 256-QAM, with various levels of ϵ_g and $\Delta\phi$.

The ADC is applied independently to the in-phase and quadrature components, using the same R_{bit} and A_{bit} for both. The distortion associated with the ADC can be divided into two parts: a uniformly distributed quantization error with power inversely proportional to R_{bit}; and a nonlinear distortion term due to clipping that occurs if $s_n > A_{\text{adc}}$. Note that, if A_{adc} is set too high, then the effective resolution of the ADC is lower, since not all thresholds are used.

2.6.5.1 Simulation Results

Fig. 2.15 presents the simulated BER of an OFDM system with $N = 512$, and 256-QAM constellations, considering a non ideal ADC with $A_{\text{adc}} = 4\sigma_s$ and different resolutions. From the figure, it is clear how a low resolution can have a significant impact in performance. For 256-QAM, an ADC resolution of $R_{\text{bit}} = 6$ is the minimum to ensure compliance with EVM standards. It should also be noted how each bit decrease of the resolution doubles the EVM, which is expected since the quantization noise is also doubling in power.

2.6.6 Nonlinear Amplification

In a wireless application, the RF signal must be amplified to reach the desired distance. Ideally, amplifying an RF signal would be the same as scaling it by a large factor. However,

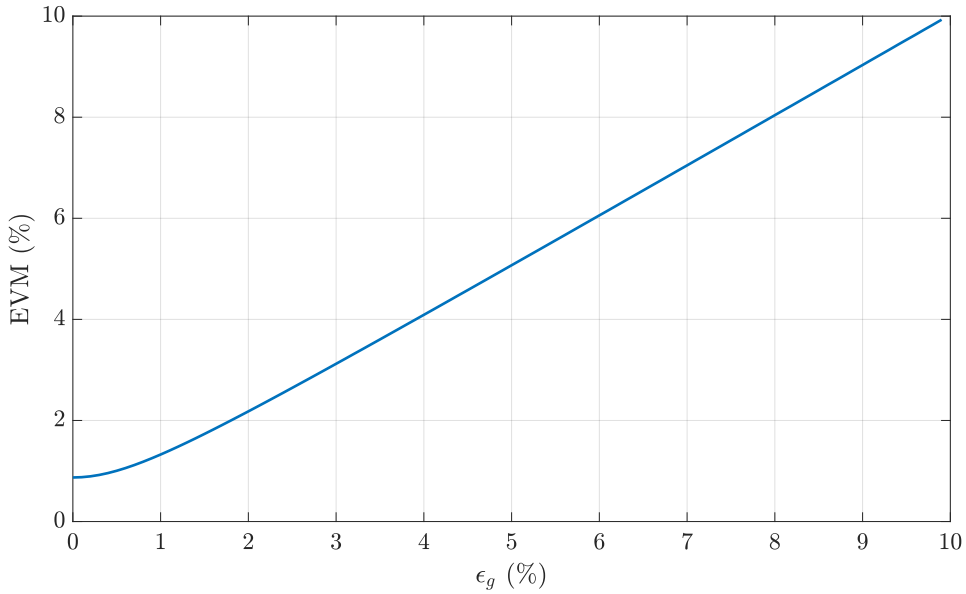

Figure 2.13: EVM as a function of ϵ_g, with $\Delta\phi = 0.5°$.

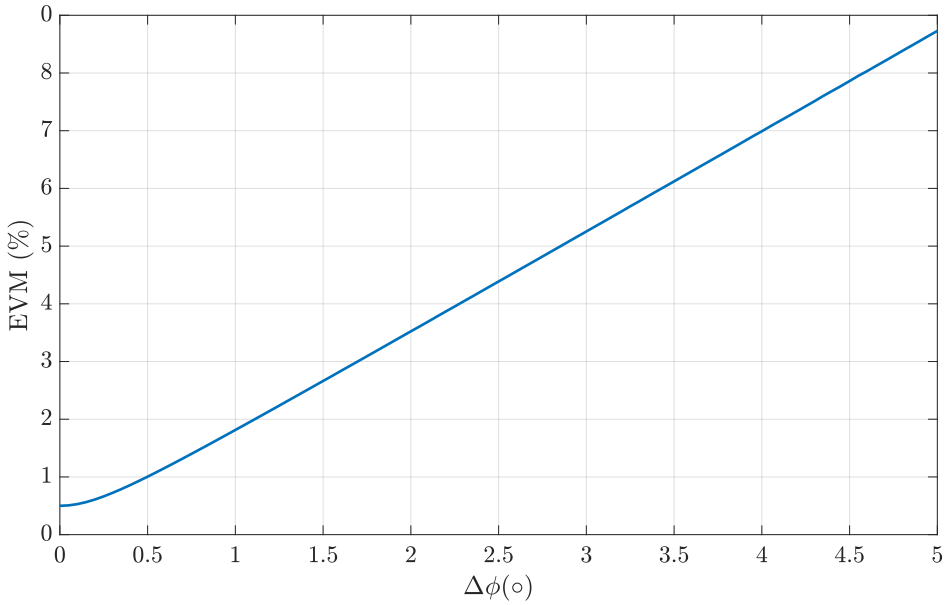

Figure 2.14: EVM as a function of $\Delta\phi$, with $\epsilon_g = 0.5\%$.

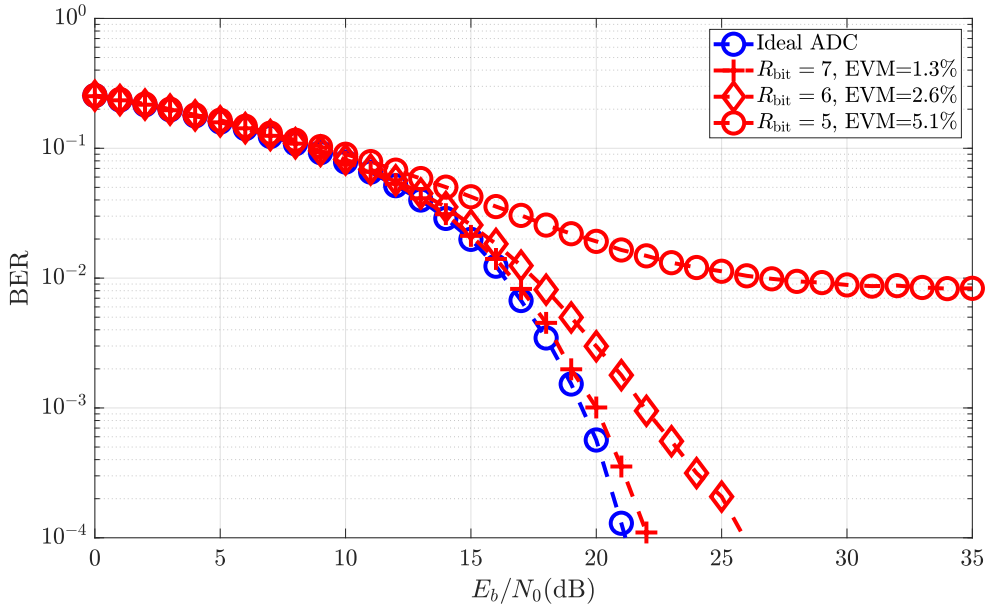

Figure 2.15: BER for an OFDM system with $N = 512$ and 256-QAM, with various ADC resolutions and $A_{\text{adc}} = 4\sigma_s$.

physical PAs do not have perfectly linear transfer functions, as they depend on the hardware architecture.

Let us consider a Single Input, Single Output (SISO) OFDM signal $\mathbf{S}$, with a time domain counterpart $\mathbf{s}$. Before each nth sample reaches the channel, h_n, it is affected by a nonlinear function, $f(\cdot)$, which represents the imperfections in the transmission chain. This is expressed in the time domain as

$$x_n = f(s_n), \tag{2.108}$$

where x_n is the distorted sample at the nth instant. In this case, the received frequency domain signal, Y_k, is defined as

$$Y_k = H_k X_k + N_k, \tag{2.109}$$

where X_K is the distorted symbol at the kth subcarrier and H_k is the kth subcarrier's CIR. The nonlinear distortion introduces an additional error source, besides the noise, which can significantly degrade the performance of the receiver.

Most RF PAs can be modelled as bandpass memoryless nonlinearities [50]. In general, a signal that has been nonlinearly distorted by a bandpass memoryless nonlinear characteristic is defined as

$$f(s_n) = f_A(|s_n|) \exp\left(j\left(f_\theta(|s_n|) + \arg(s_n)\right)\right), \tag{2.110}$$

where $f_A(\cdot)$ and $f_\theta(\cdot)$ are the Amplitude-to-Amplitude Modulation (AM/AM) and Amplitude-to-Phase Modulation (AM/PM) characteristics of the nonlinearity, respectively. This

type of nonlinearity can be expanded by the power series

$$f(s_n) = \sum_{m=0}^{\infty} \beta_m s_n^{m+1} (s_n^*)^m, \tag{2.111}$$

where each term of the series, aside from the first, will be associated to an Inter-Modulation Product (IMP) of the nonlinear distortion [51].

Characterizing the impact of these nonlinearities can be computationally complex, since it is usually done utilizing Monte Carlo simulations. However, in the case of OFDM with a high number of subcarriers, the time domain signal can be approximated by a Gaussian distribution with variance σ_s. In fact, Fig. 2.16 shows that even for $N = 256$ subcarriers, this Gaussian approximation is very tight. This allows us to analytically characterize an OFDM signal submitted to a nonlinear function [52–54].

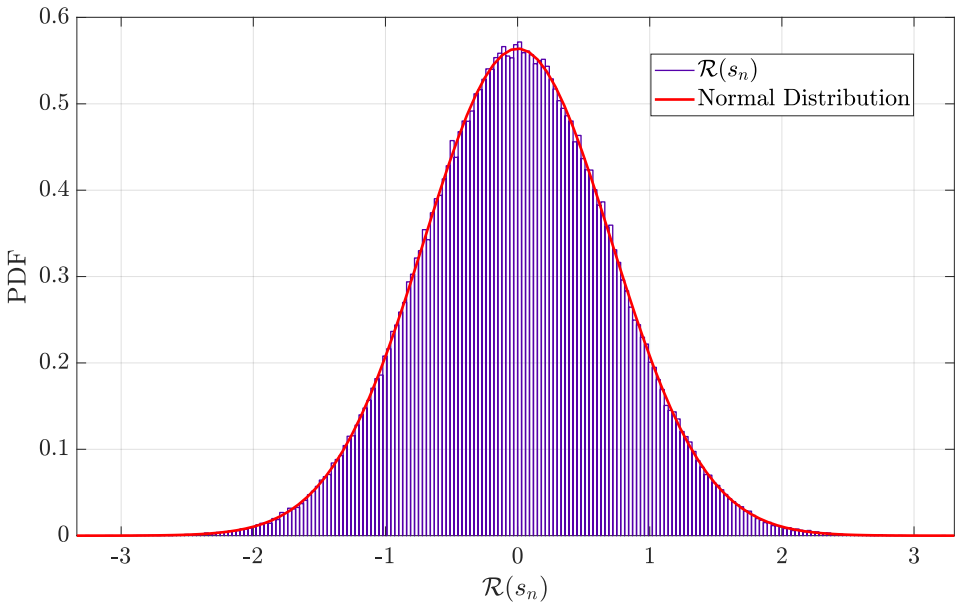

Figure 2.16: Histogram of the real part of s_n with normal distribution curve fit considering OFDM signals with $N = 256$ subcarriers and 256-QAM constellations.

In that context, an important analytical tool is the Bussgang's theorem [55], which states that the cross-correlation between two Gaussian signals, where one was submitted to a nonlinear distortion, is equal to the cross-correlation before distortion, scaled by a factor α_{bg}. Considering a single Gaussian signal that is submitted to a nonlinearity, by Bussgang's theorem it can be written as

$$\mathrm{R}_{sf(s)}(\tau) = \alpha_{\text{bg}} \mathrm{R}_{ss}(\tau), \tag{2.112}$$

where $\mathrm{R}_{sf(s)}(\tau)$ is the cross-correlation between s_n and $f(s_n)$ and $\mathrm{R}_{ss}(\tau)$ is the auto-correlation of s_n. Additionally, the Bussgang's theorem allows us to define the signal at the

output of the nonlinearity as [56, 57]

$$f(s_n) = \alpha_{\text{bg}} s_n + d_n, \tag{2.113}$$

where d_n is an uncorrelated self interference term that arises due to the distortion. The attenuation factor can be calculated a priori by

$$\alpha_{\text{bg}} = \frac{\mathbb{E}[s_n^* f(s_n)]}{\mathbb{E}[|s_n^2|]}, \tag{2.114}$$

which for a Gaussian input signal becomes

$$\alpha_{\text{bg}} = \frac{1}{\sqrt{2\pi}\sigma_s^3} \int_0^{+\infty} x f(x) \exp\left(-\frac{x^2}{2\sigma_s^2}\right) dx, \tag{2.115}$$

where x is a complex integration variable. The average power of the nonlinearly distorted signal is characterized by

$$P_x = \mathbb{E}[f^2(s_n)] = \frac{1}{\sqrt{2\pi}\sigma_s} \int_{\mathbb{C}} f^2(x) \exp\left(-\frac{x^2}{2\sigma_s^2}\right) dx, \tag{2.116}$$

which allows us to determine the effective output power. In the case of a nonlinearity that only affects the amplitude of the signal then (2.116) is rewritten as [58]

$$P_x = \mathbb{E}[f^2(s_n)] = \frac{1}{2\sigma_s^4} \int_0^{+\infty} f_A^2(r) r^{-\frac{r^2}{2\sigma_s^2}} dr, \tag{2.117}$$

where r is a real integration variable that models the absolute value of the OFDM time domain signal. The portion of power that is used for the useful component is given by

$$P_\alpha = |\alpha_{\text{bg}}|^2 \sigma_s^2, \tag{2.118}$$

while the self interference power is given by

$$P_D = P_x - P_\alpha. \tag{2.119}$$

The PSD of the nonlinearly distorted signal is given by [53]

$$\begin{aligned} G_{f(s)}(f) =& 2 \sum_{\gamma=0}^{+\infty} \frac{P_{2\gamma+1}}{\sigma_s^{2\gamma+1}} . \underbrace{[G_s(-f) * G_s(-f) * G_s(-f) ... * G_s(-f)]}_{\gamma} . \\ & . \underbrace{[G_s(f) * G_s(f) * G_s(f) ... * G_s(f)]}_{\gamma+1}, \end{aligned} \tag{2.120}$$

where $P_{2\gamma+1}$ is the PSD of the IMP of order $2\gamma + 1$. For $\gamma = 1$, it is simply the PSD of original signal s_n attenuated by α_{bg}, while the remaining terms ($\gamma > 1$) characterize the self interference from the distortion. It can be clearly seen that the nonlinear distortion is not limited to the original bandwidth B, which explains the OOB radiation in the distorted signal.

2.6.6.1 Solid State Power Amplifier

The transfer function of an amplifier can be characterized by its AM/AM and AM/PM conversion characteristics. There is a widely accepted model for characterizing an SSPA [59, 60], which is one of the most common type of PAs.

For a complex signal s_n, the AM/AM characteristic is given by

$$f_A(|s_n|) = \frac{|s_n|}{\sqrt[2q_{\text{sspa}}]{1 + \left|\frac{s_n}{s_{\text{sat}}}\right|^{2q_{\text{sspa}}}}}, \tag{2.121}$$

where s_{sat} is the saturation level, usually expressed as a multiple of the signal variance σ_s, and q_{sspa} defines the sharpness of the transition between linear and nonlinear saturated characteristic. The AM/PM characteristic of an SSPA is considered negligible [61], i.e. $f_\theta(|s_n|) \approx 0$. A plot of this model is shown in Fig. 2.17, where one can identify three distinct regions: an initial linear region; a second nonlinear transition region; and a nonlinear saturated region. The level at which the input enters the second region is defined by s_{sat}.

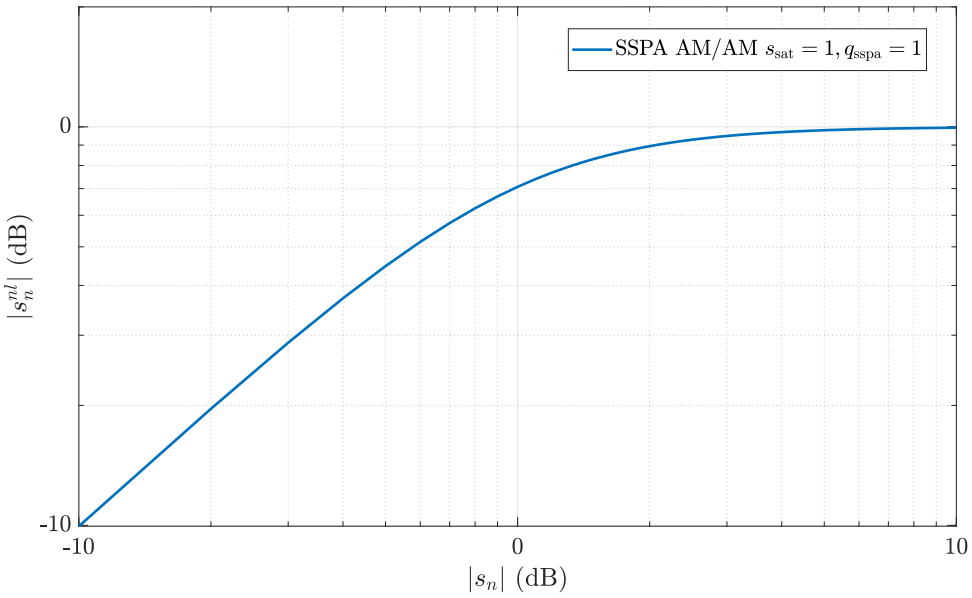

Figure 2.17: Plot of the AM/AM curve for an SSPA.

It is clear from this model that if an input signal has constant amplitude, then the output will simply be the scaled signal. However, the signal may have amplitude swings, which is the case for SC with M-QAM and MC modulations. These swings may be characterized by the signal's PAPR. In the SSPA model, a signal with high PAPR will be affected by a large stretch of the AM/AM characteristic, resulting in distortion. If the signal's amplitude could be made to fit in the linear region by adjusting s_{sat}, then there would be no distortion. The drawback is that the SSPA operates most efficiently

energetically at the saturation region, and increasing s_{sat} places the input farther away from saturation, reducing output power while maintaining the same consumed power.

In Fig. 2.18 the average PSD of an OFDM signal with $N = 512$ and 256-QAM is shown. In this case, the impairment function $f(\cdot)$ was set to be the SSPA model with $s_{\text{sat}} = 5\sigma_s$

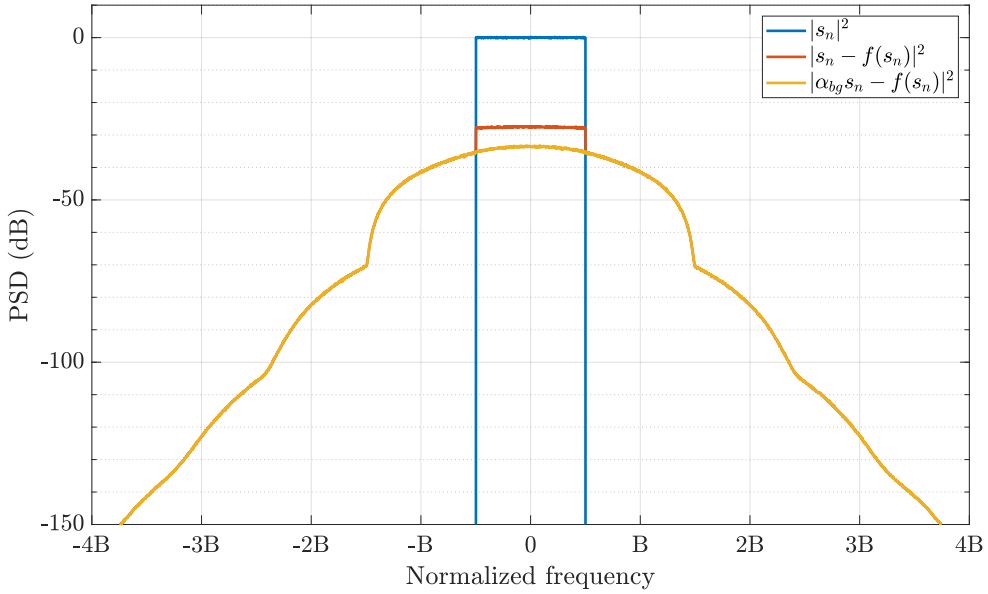

Figure 2.18: Average PSD of an OFDM signal with $N = 512$ and 256-QAM and nonlinear distortion factor.

and $q = 1$. From the figure, the OOB radiation of the nonlinear signal is clearly visible, and it can also be observed that the inband interference power P_D is only uncorrelated with $|s_n|^2$ if the attenuation factor α_{bg} is taken into account.

2.6.6.2 Travelling Wave Tube

Another common RF amplifier circuit is the Travelling Wave Tube (TWT). It is mainly used for high power applications such as satellite communications. It is not used in low power applications due to its large size compared with an SSPA. This amplifier can also be characterized by AM/AM and AM/PM characteristic that model the transfer function. In [62] a model for these characteristics is proposed, where the AM/AM and AM/PM are defined as

$$f_A(|s_n|) = 2s_{\text{sat}}^2 \frac{|s_n|}{|s_n|^2 + s_{\text{sat}}^2}, \tag{2.122}$$

and

$$f_\theta(|s_n|) = \frac{\pi}{3} \frac{|s_n|^2}{|s_n|^2 + s_{\text{sat}}^2}, \tag{2.123}$$

respectively. In these models s_{sat} is the saturation power level, which for maximum efficiency should be equal to the input amplitude. Fig. 2.19 shows the curves for both

characteristics with $s_{\text{sat}} = 1$. Similarly to the SSPA, a signal with non constant amplitude and average equal to s_{sat} will be significantly distorted. In those conditions s_{sat} must be significantly larger than the average signal amplitude, to accommodate the PAPR.

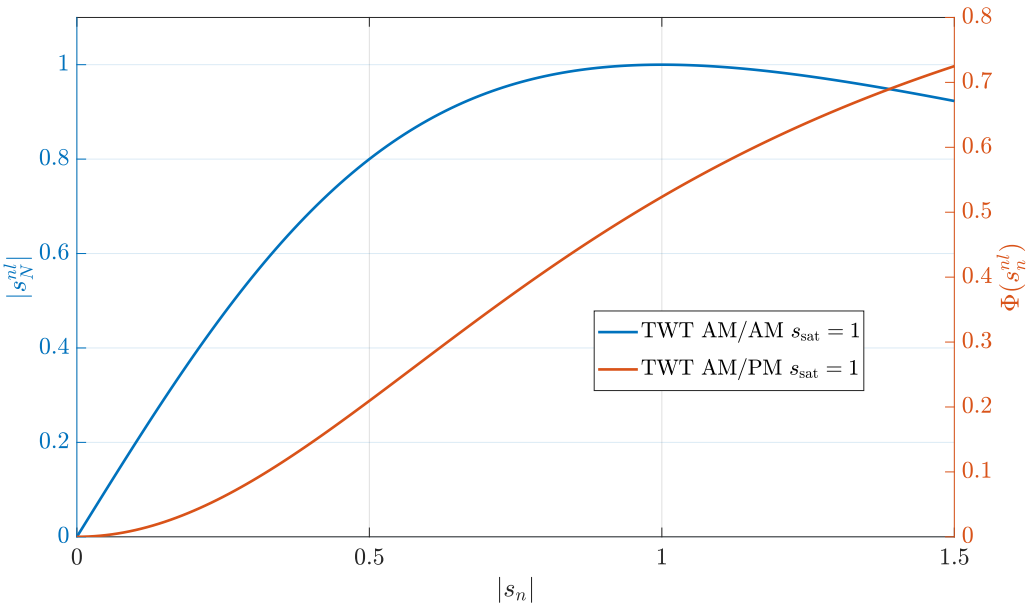

Figure 2.19: Plot of the AM/AM and AM/PM curves for a TWT amplifier.

2.6.6.3 Soft Clipping

In order to reduce the distortion that arises from nonlinear amplification it is possible to decrease the input signal's PAPR. There are many approaches, one such method is by "clipping" the maximum signal level to a certain threshold value s_{clip}, known as Soft Clipping. This is expressed as

$$f(s_n) = \begin{cases} -s_{\text{clip}}, & x < -s_{\text{clip}} \\ s_n, & -s_{\text{clip}} < x \leq s_{\text{clip}} \\ s_{\text{clip}}, & x > s_{\text{clip}} \end{cases}, \tag{2.124}$$

where s_{clip} is an appropriately selected threshold. Naturally, this operation introduces nonlinear distortion in the signal, though it can be easier to handle since the distortion is independent between I and Q components.

2.6.6.4 Simulation Results

Let us consider that $N = 512$ and a modulation order of 256-QAM for an AWGN channel. Fig. 2.20 shows the BER for various clipping levels of an SSPA model. From the figure, it can be observed that the BER is significantly dependent on the clipping level, which will

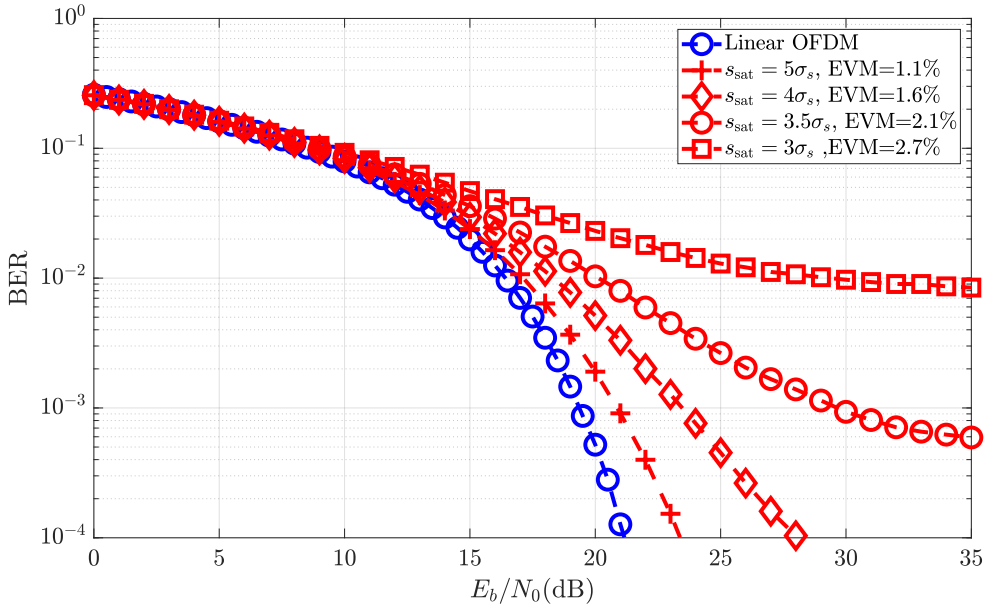

Figure 2.20: BER for an OFDM system using SSPA with $N = 512$ and 256-QAM, with various levels of s_{sat}.

define the SSPA operating point and efficiency. Even for large saturation levels such as $s_{\text{sat}}/\sigma_s = 7$, there is still a degradation of about 2 dB for a target performance of 10^{-4}. The EVM as a function of s_m/σ_s is plotted in Fig. 2.21.

From the figure, it is clear that there is a nonlinear relationship between the EVM and s_{sat}, which is due to the nonlinear characteristic of the AM/AM conversion for $q = 1$. As such, the EVM will be particularly sensitive for low levels of s_{sat}, at the cost of higher efficiency. Fig. 2.22 shows the BER for a system employing TWT amplifiers.

As was the case for SSPA, using a low saturation value s_{sat} results in worse performance, compared to using an SSPA. Fig. 2.23 shows the EVM as a function of the TWT saturation. From the figure, it can be seen how the EVM curve is similar to the one in Fig. 2.21. As was the case for SSPA, the TWT requires a large saturation s_{sat} in order to minimise the EVM. Fig. 2.24 shows the BER of a system employing clipping.

Since clipping is not an amplification operation, the results are significantly different. From the figure it can be observed that performance is highly sensitive to the clipping threshold s_{clip}. Fig. 2.25 shows the EVM as a function of the clipping threshold. Unlike the previous scenarios, the EVM curve for the clipping nonlinearity reaches 0 for a high enough s_{clip}, due to the nature of the branch function. For small variations of s_{clip}, there can be a large EVM variation.

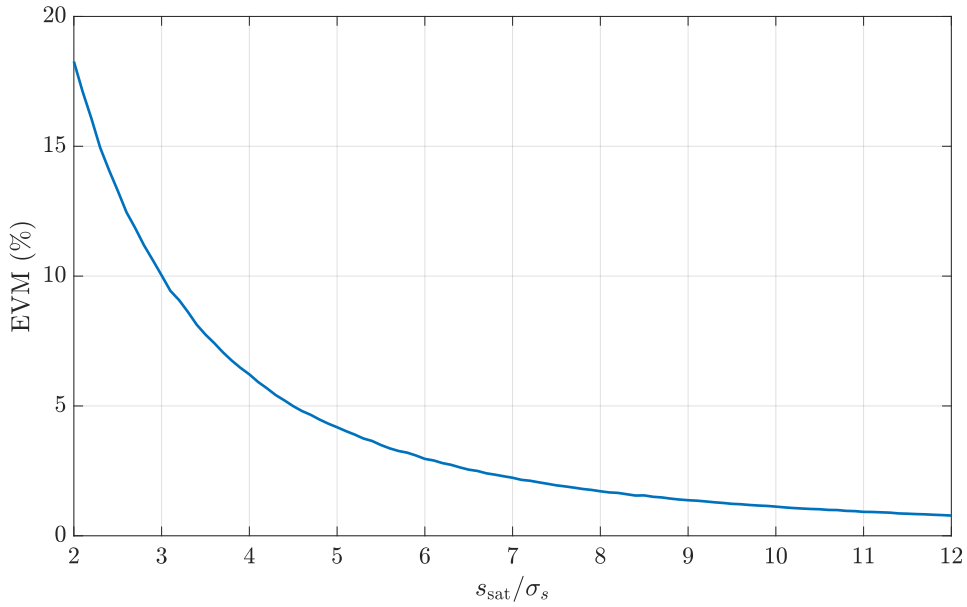

Figure 2.21: EVM as a function of SSPA s_{sat}.

2.7 State-of-the-Art Solutions to Cope with Hardware Impairments

This section presents several techniques available in the literature that aim to mitigate the impact of different sources of impairments.

2.7.1 Carrier Frequency Offset

In general, it can be assumed that any wireless telecommunication system will have CFO impairments, which will negatively impact performance [63]. That is why industry standards include specifications on how to achieve frequency synchronization between users. A very well known algorithm for frequency and timing synchronization in OFDM systems is the Schmidl and Cox algorithm [41]. This technique allows for synchronicity at the receiver if the transmitter considers a prefix of two OFDM symbols as preambles to each block transmission. The first preamble carries no data on the odd subcarriers, while the even subcarriers are modulated according to a pseudorandom sequence. This results in a preamble with two equal halves, in the time domain, and is used both for timing and frequency synchronization. Under these conditions, the frequency offset is estimated by

$$\hat{\delta}_f = \frac{1}{\pi T}\arg\left(\sum_{m=0}^{\frac{N}{2}-1} x^*_{n+m} x_{n+m+\frac{N}{2}}\right), \tag{2.125}$$

where $T = NT_s$, for a given time index n that must be found by the timing synchronization. Each time domain sample, including the preamble, is then phase adjusted by $\hat{\delta}_f$. There is

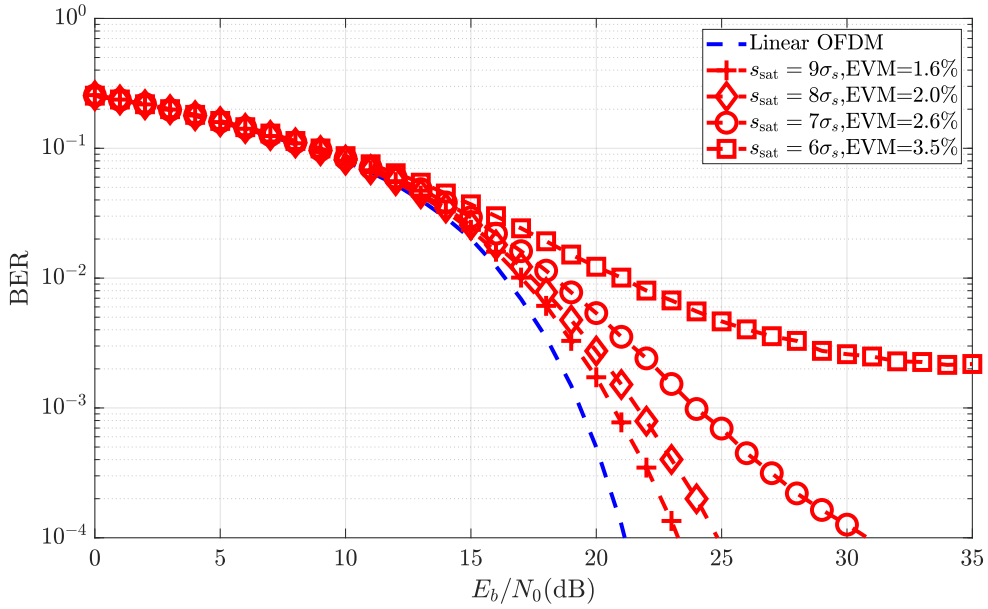

Figure 2.22: BER for an OFDM system with $N_u = 512$ and 256-QAM, with various levels of s_{sat}.

actually a phase ambiguity of $\frac{2l}{T}$, for a certain integer l, due to the integer part of the CFO. This ambiguity is resolved by estimating the integer δ_f^{in} in the frequency domain, using the second preamble symbol.

In [64], a joint time and frequency synchronization algorithm is proposed for full duplex OFDM systems. The CFO is split into an integer part δ_f^{in}, that is a multiple of the subcarrier spacing, and a fractional part δ_f^{fr}, which is the remainder, defined as

$$\delta_f = \delta_f^{\text{in}} + \delta_f^{\text{fr}}. \tag{2.126}$$

The integer CFO is estimated by correlating the received signal with the training sequence, similarly to the Schmidl and Cox algorithm, referred to as coarse frequency estimation. The fractional remainder is estimated using a repetitive time-domain preamble, and is referred to as fine frequency estimation. The authors of [65] analysed the performance and complexity of OFDM time and frequency synchronization for Long Term Evolution (LTE) and NR, and proposed a novel synchronization sequence with lower complexity and inter-cell interference.

In [66], a blind CFO estimation scheme for OFDM is proposed. In this technique each OFDM symbol reserves a certain number of null subcarriers at the start and end of the OFDM signal bandwidth. Each of these segments is split into a set of Guard Subcarriers (GS), adjacent to the symbol edges, and the Remaining Null Subcarriers (RNS). Since these subcarriers do not carry data, their energy will come only from the noise and the ICI, whereas if there is no CFO then it will only be noise. Therefore, the estimation consists

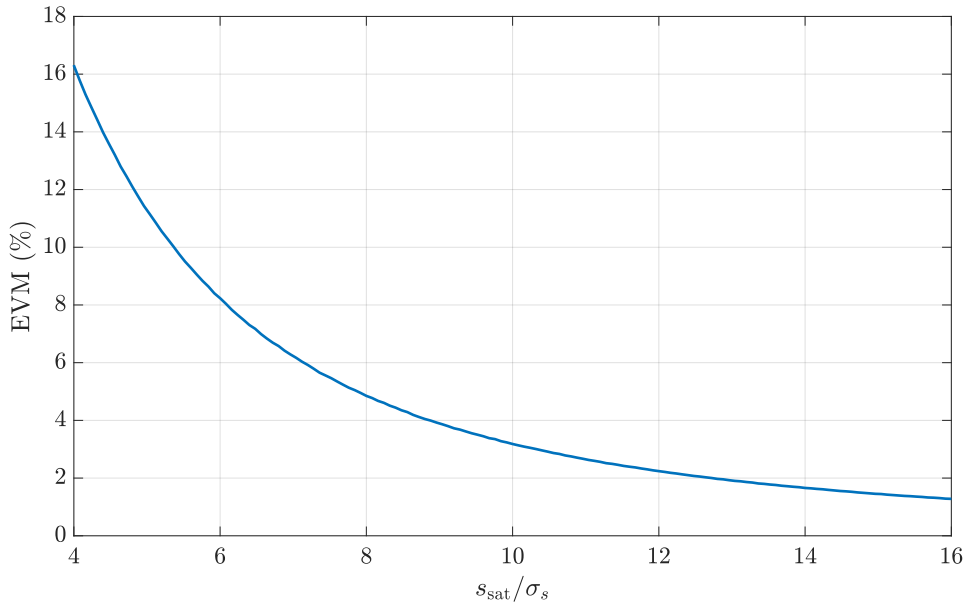

Figure 2.23: EVM as a function of TWT s_{sat}.

in finding an estimate $\hat{\delta}_f$ that minimises the energy in the RNS, represented by the cost function

$$C\{\hat{\delta}_f\} = \sum_{b=0}^{L-1} \sum_{k \in N_{ns}} ||y_{k,b}\{\hat{\delta}_f\}||^2, \tag{2.127}$$

where L and N_{ns} are the number of available OFDM symbols and set of null subcarrier indices, respectively. The factor $y_{k,b}\{\hat{\delta}_f\}$ is the received signal with compensated CFO using the estimate $\hat{\delta}_f$. The authors proposed a Cost Function Approximation (CFA) scheme that estimates $\hat{\delta}_f$ with lower complexity. An additional more complex scheme that makes use of the GS was also proposed and achieved a higher accuracy.

Compensation schemes that require training sequences decrease the spectral efficiency of the system. Contrarily, blind CFO estimation techniques do not have this drawback [67].

In Fig. 2.26 the BER curves of an OFDM 256-QAM system employing CPE correction are shown. The CPE is considered to be perfectly estimated, which can be achieved by averaging out the received pilot or data symbols. This compensation has low implementation complexity and withstands larger CFO levels. For more sophisticated schemes that compensate the ICI portion of the CFO, one can simply reduce the effective δ_f. In that scenario, δ_f becomes the remaining CFO that was not cancelled out.

2.7.2 Phase noise

A general phase noise mitigation technique is proposed in [68]. The authors used a MMSE equalizer that takes into account the ICI power and cancels out the CPE due to phase

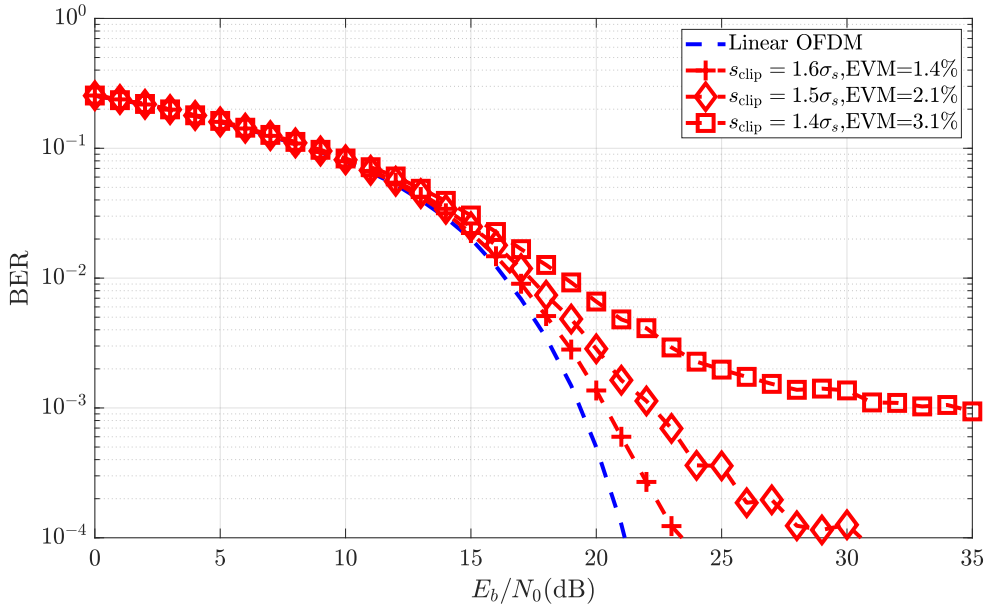

Figure 2.24: BER for an OFDM system with $N_u = 512$ and 256-QAM, with various levels of s_{clip}.

noise. The equalizer is defined as

$$F_k = \frac{I_0^* H_k^* \sigma_s^2}{\sigma_s^2 |I_0 H_k|^2 + \sigma_s^2 \sum_{p=1}^{N-1} \mathbb{E}\left[|I_p|^2\right] + \sigma_N^2}, \tag{2.128}$$

where I_0 corresponds to the CPE defined in (2.95), and I_p is the pth ICI term. This equalizer requires an estimate of I_0, which is computed as

$$\hat{I}_0 = \frac{Y_k H_k^* S_k^*}{\sum_{k \in \mathbf{S}_p} |H_k S_k|^2}, \tag{2.129}$$

where $\mathbf{S}_p$ is the set of pilot subcarriers.

In [69], a joint channel and phase noise estimation is proposed. This scheme considers the received signal as

$$\mathbf{Y} = \mathbf{A}\text{diag}(\mathbf{H})\mathbf{X} + \mathbf{N}, \tag{2.130}$$

where diag($\mathbf{H}$) is a diagonal matrix composed by the elements of $\mathbf{H}$, while $\mathbf{A}$ is a matrix that characterizes the interference due to phase noise. In the first step, the receiver estimates the time domain versions of $\mathbf{H}$, defined as $\mathbf{h}$. This is because $\mathbf{h}$ has a length L (i.e., its length is equal to the length of the CIR, and can be assumed that $N > L$. In the time domain ϕ_n can be estimated directly, however, in order to keep complexity low, the phase noise $\boldsymbol{\phi}'$ is only calculated for N_{int} points, with $N_{int} < N$, and is later interpolated for the remaining time domain samples. The problem is defined by the following minimization procedure

$$\min_{\mathbf{h},\boldsymbol{\phi}'} ||\mathbf{Y} - \mathbf{AHX}||^2. \tag{2.131}$$

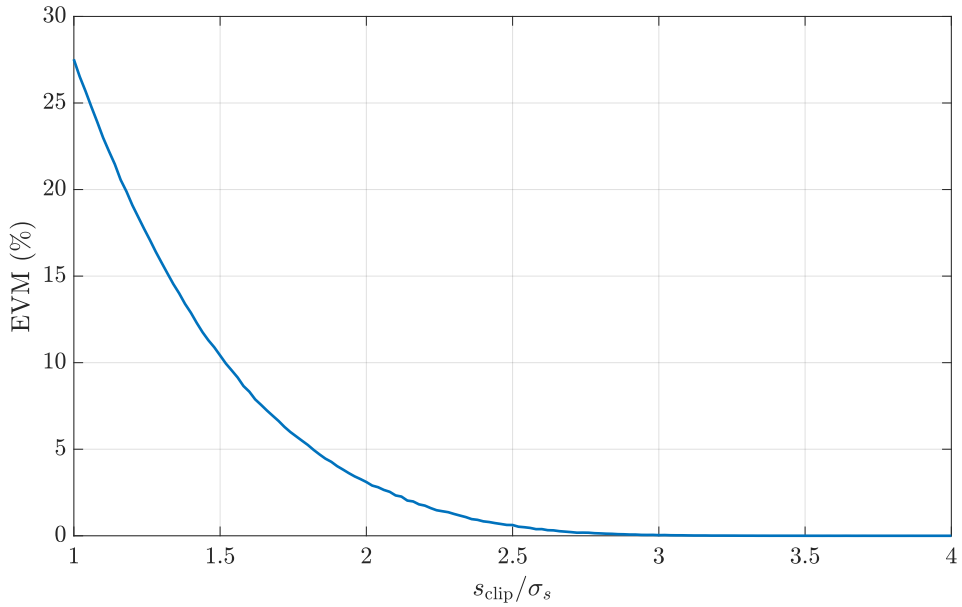

Figure 2.25: EVM as a function of clipping s_{clip}.

The authors make use of the short vector sizes to propose an iterative algorithm for suboptimal estimation of (2.131). The scheme begins by receiving an OFDM symbol containing only pilots, which is used for computing $\hat{\mathbf{h}}$, given the shortened $\hat{\boldsymbol{\phi}}$ of the previous iteration. The initial $\hat{\boldsymbol{\phi}}$ is set to a random guess, like a ones vector. In the next step the optimal $\hat{\boldsymbol{\phi}}'$ given $\hat{\mathbf{h}}$ is calculated. This process repeats until there is little change in the objective function.

After this initial estimation, the authors assume that the channel will vary slowly between symbols, while $\boldsymbol{\phi}$ may change drastically and must be estimated at each symbol. Therefore, it is assume that the next OFDM symbols contain data and pilots, modifying the estimation problem to

$$\min_{\mathbf{X}_{\text{data}},\boldsymbol{\phi}'} ||\mathbf{Y} - \mathbf{A}_{\text{data}}\mathbf{H}_{\text{data}}\mathbf{X}_{\text{data}} - \mathbf{A}_{\text{pilot}}\mathbf{H}_{\text{pilot}}\mathbf{X}_{\text{pilot}}||^2, \tag{2.132}$$

which can be solved using a similar solution to the previous problem. Before the iterative algorithm begins, the CPE of the signal is calculated and used as the initial estimate of $\hat{\boldsymbol{\phi}}$. The estimate obtained using the pilot symbols must be interpolated for the data subcarriers. If the PSD of the phase noise is unknown, then can be a simple linear interpolation, otherwise the interpolation matrix can be obtained a priori. In [70] this scheme is extended for IQ imbalance.

In [44], the authors combine FDE with phase noise mitigation for a SC system. The phase noise is modelled using a Wiener–Lévy model with AWGN affected observations, which poses a nonlinear filtering problem. The sequential Bayesian filtering distribution

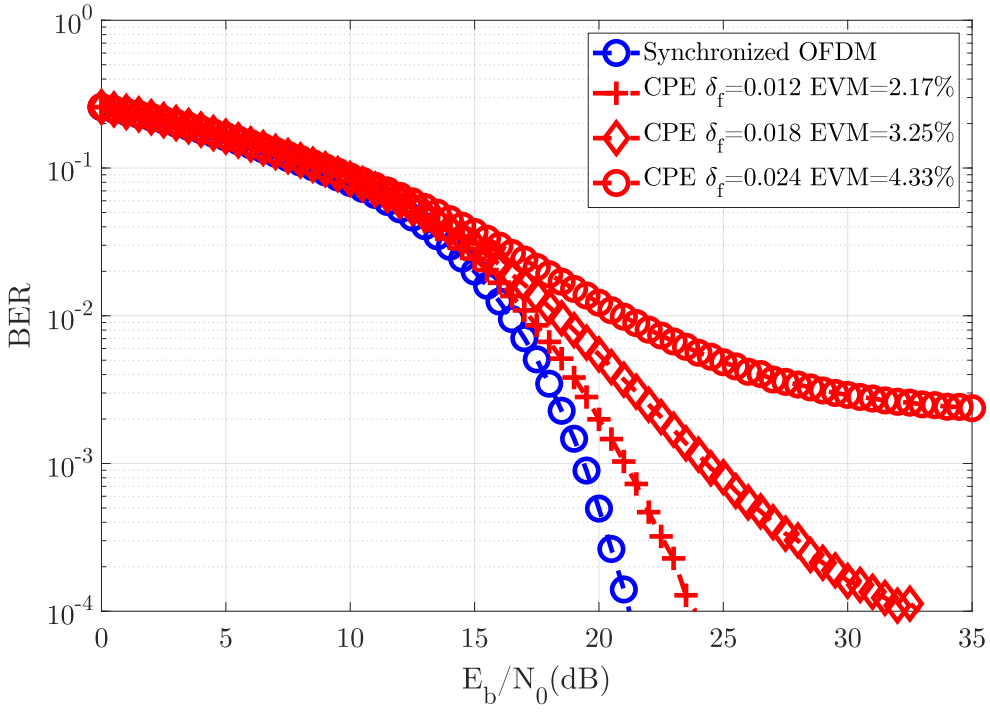

Figure 2.26: BER for a CFO impaired OFDM system with $N_u = 512$ and 256-QAM, using CPE compensation at the receiver.

is defined as

$$p(\phi_n|\tilde{s}_{0:n}) = \frac{p(\phi_n|\tilde{s}_{0:n-1})p(\tilde{s}_n|\phi_n)}{\int p(\phi_n|\tilde{s}_{0:n-1})p(\tilde{s}_n|\phi_n)d\phi_n}, \tag{2.133}$$

where $\tilde{s}_n$ is an equalized SC symbol, and $p(\phi_n|\tilde{s}_{0:n})$ is the filtering distribution at n of ϕ_n given n previous observations. The prediction distribution is given by

$$p(\phi_{n+1}|\tilde{s}_{0:n}) = \int p(\phi_{n+1}|\phi_n)p(\phi_n|\tilde{s}_n)d\phi_n \tag{2.134}$$

where $p(\phi_{n+1}|\tilde{s}_{0:n})$ is the prediction distribution at n of ϕ_N given the previous $n-1$ observations. Since these distributions are nonlinear, the authors propose recursive filtering as approximate solutions. The proposed techniques achieve a performance close to the posterior Cramér–Rao bound for the considered estimator.

In [71], the authors propose a time domain technique for handling phase noise at the receiver in OFDM systems. The phase noise is modelled using a filtered Gaussian distribution and estimated using a data-aided Least Squares (LS) estimator. In [72] the authors take into account the noise in the received signal and instead use a Total Least Squares (TLS) estimator, as well as extended the scheme for MIMO systems using a set of basis vectors based on the covariance of the phase noise.

In [73], the authors propose an OFDM pilot allocation scheme with low overhead that allows for non-iterative, low complexity phase noise compensation in the frequency

domain. The pilots are clustered into blocks inside the OFDM block and are used in the LS estimation of the complex phase noise exponential. The estimate is then applied in a deconvolution of the received signal to cancel out the phase noise effect. The authors of [74] consider a similar scheme for mmWave communications, and extend the analysis for a scenario with Linear Minimum Mean Square Error (LMMSE) estimation. A pilot allocation scheme for channel and phase noise estimation that takes into account the coherence bandwidth and time is proposed.

A phase noise and channel estimation scheme usingVariational Expectation Maximization (VEM) for MIMO systems was proposed by [75]. The system employs initial training OFDM symbols to estimate the channel and phase noise using an iterative algorithm. The resulting channel estimate is improved by the phase noise cancellation, and is used for detecting the OFDM data symbols. Since the phase noise varies significantly between successive OFDM symbols, it will have to be estimated for each data block as well. Therefore, the authors use a modified iterative algorithm to jointly estimate the data S_k and the phase noise interference, which is then compensated in the data detection.

Another interesting approach utilising GAMP for joint phase noise and symbol detection in OFDM with OFDM - Index Modulation (OFDM-IM) was proposed by the authors of [76]. They considered an LDPC coded system and combined BP decoding with GAMP symbol equalization and Mean-Field approximation for phase noise estimation in the same factor graph. An iterative decoder that implements this factor graph was simulated and compared with another factor graph implementation that does not consider GAMP. It was also shown that even for imperfect Channel State Information (CSI) and residual CFO the receiver still achieves a high performance. Fig. 2.27 shows the BER for an OFDM with 256-QAM system using two different phase noise compensation schemes.

The first scheme, shown in red as CPE, relies on compensating the known CPE in the distorted signal. Generally this factor is considered easy to estimate and offers a significant performance boost. The second scheme, portrayed by the green curves, not only compensates the CPE, but also estimates ϕ_n using a first order LS approximation. The resulting $\hat{\phi}_n$ is then used to compensate the phase noise in the time domain. As was discussed previously, this estimate can be obtained by interpolating between pilot symbols, and can reduce the phase noise distortion impact by about 5 dB.

2.7.3 IQ Imbalance

The presence of IQ imbalance can severely hamper the performance of modern systems [63, 77]. The authors of [78] define the effect of IQ imbalance and propose several compensation schemes, which are extended to MIMO in [79]. The authors define the received distorted signal $\mathbf{Y}$ as a set of equation pairs represented in matrix form by

$$\begin{bmatrix} Y_k \\ Y^*_{N-k+2} \end{bmatrix} = \mathbf{\Gamma}_k \begin{bmatrix} X_k \\ X^*_{N-k+2} \end{bmatrix} + \mathbf{N}_k \tag{2.135}$$

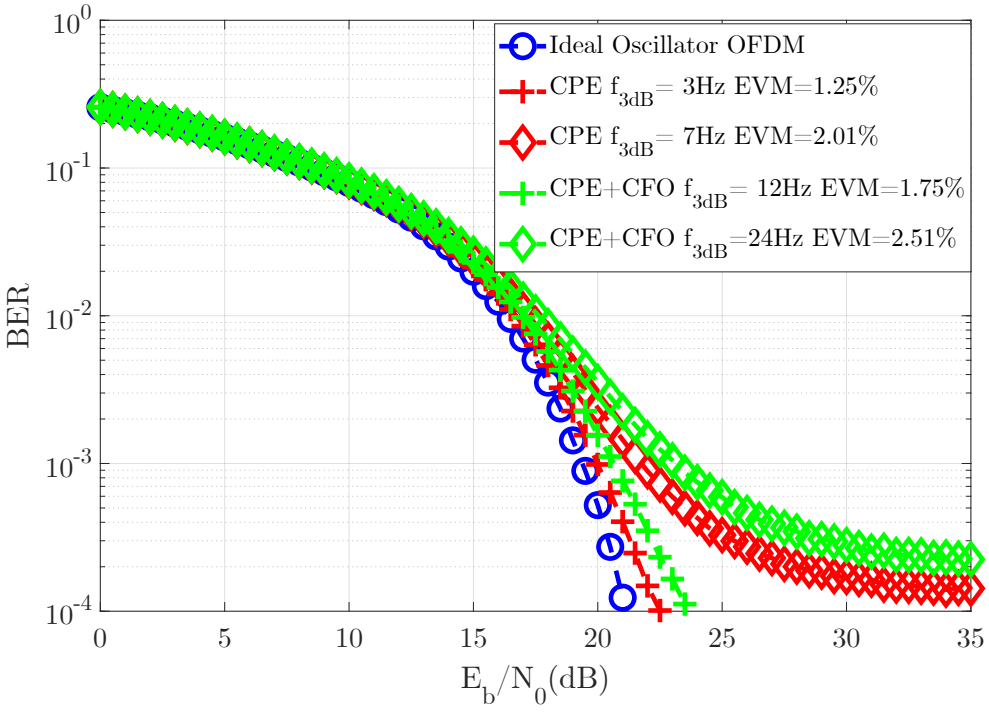

Figure 2.27: BER for a phase noise impaired OFDM system with $N_u = 512$ and 256-QAM, using CPE and CFO compensation at the receiver.

where $k = \{1, ..., N/2-1\}$ to simplify the analysis by discarding two indices, $\mathbf{N}_k$ is a matrix containing the noise terms defined similarly to the other matrices, and $\mathbf{\Gamma}_k$ is given by

$$\mathbf{\Gamma}_k = \begin{bmatrix} \alpha H_k & \beta H^*_{N-k+2} \\ \beta^* H_k & \alpha^* H^*_{N-k+2} \end{bmatrix}. \tag{2.136}$$

The authors propose LS and adaptive estimators for $\mathbf{\Gamma}_k$ based on observations from training symbols. The distorted signal in the time domain can be rearranged, based on (2.102), into the following format

$$x'_n \triangleq x_n - \frac{\beta}{\alpha^*} x^*_n = \left(\alpha - \frac{|\beta|^2}{\alpha^*}\right) s_n, \tag{2.137}$$

which is particularly useful for the receiver to develop a compensation scheme that only requires information on $\frac{\beta}{\alpha^*}$, instead of each parameter individually. If the receiver has perfect knowledge of $\frac{\beta}{\alpha^*}$, then the IQ imbalance interference can be cancelled out completely, leaving only a scale factor. In practice, however, the presence of noise after the distortion will lead to an amplification of the noise in the signal, reducing the available SNR.

In [70], a phase noise and channel equalization scheme was extended to include IQ imbalance. A full duplex OFDM system with IQ imbalance compensation was proposed in [80]. The authors developed a frequency domain LS estimator that combines channel

equalization and IQ imbalance mitigation, which is then improved by using the time domain CIR to improve the quality of the channel estimation.

A wideband application with IQ imbalance compensation was proposed in [81]. For large bandwidths, the IQ imbalance distortion becomes frequency dependent. This fact greatly increases the complexity of estimating and compensation the distortion. A MIMO system with CFO and IQ imbalance at the transmitter and receiver is considered, and an appropriate training symbol scheme is designed. The IQ imbalance at the transmitter is compensated via predistortion according to (2.137) by using a feedback link from the receiver to obtain information on $\frac{\beta}{\alpha^*}$. The receiver IQ imbalance is also compensated by (2.137), using an estimation from the training symbol. Each training symbol contains information only on half the subcarriers, which allows for simple measurement of the interference, and sent over alternating channels, i.e. for two channels a total of four training symbols are sent. The estimates for α and β are then found via two different LS estimators. In [82] a similar pilot design was proposed for compensating IQ imbalance without CSI.

In [77], the impact of IQ imbalance and phase noise in 802.11ax uplink Multi-User MIMO (MU-MIMO) was studied. Although phase noise did not result in a significant performance loss, IQ imbalance results in a severe degradation of system performance. The authors proposed an interesting compensation scheme that estimates the amplitude imbalance ϵ_g by computing the ratio between the average power of the I and Q components, and the phase imbalance $\Delta\phi$ is estimated by the cross-correlation between the I and Q components of the received signal. The receiver requires no additional training symbols, using only frames that are already present in the standard, and achieves excellent performance.

In [83], it is shown that IQ imbalance can destroy the channel reciprocity of Time Division Duplexing (TDD) systems. A TDD MIMO system is considered with IQ imbalance at both TX and RX chains for both uplink and downlink communications. It is shown that if the IQ imbalance parameters are known, then the reciprocity can be recovered by computing the appropriate inverse compensation matrices, which can be done with linear complexity scaling with the number of antennas.

A Massive Multiple Input, Multiple Output (mMIMO) scheme with IQ imbalance is considered in [84]. A scheduled adaptive pilot scheme is proposed that achieves a lower overhead than previous schemes, which is used to obtain an estimate of the equivalent channel, that combines CIR and IQ imbalance. A detector that takes into account the error in the channel estimation is shown and the sum rate is demonstrated.

The BER of the considered OFDM system with 256-QAM constellations using time domain compensation as described in [78] and (2.137) is shown in Fig. 2.28.

For this figure the EVM measurements have been omitted, since the drawback to this technique is the noise amplification, which would not be visible if x_n was compensated directly. If the ratio β/α^* is known, then this compensation does support much higher IQ imbalances than before. However, this technique is entirely reliant on the quality of ratio $\frac{\beta}{\alpha^*}$ estimation, and degrades the SNR due to the noise amplification.

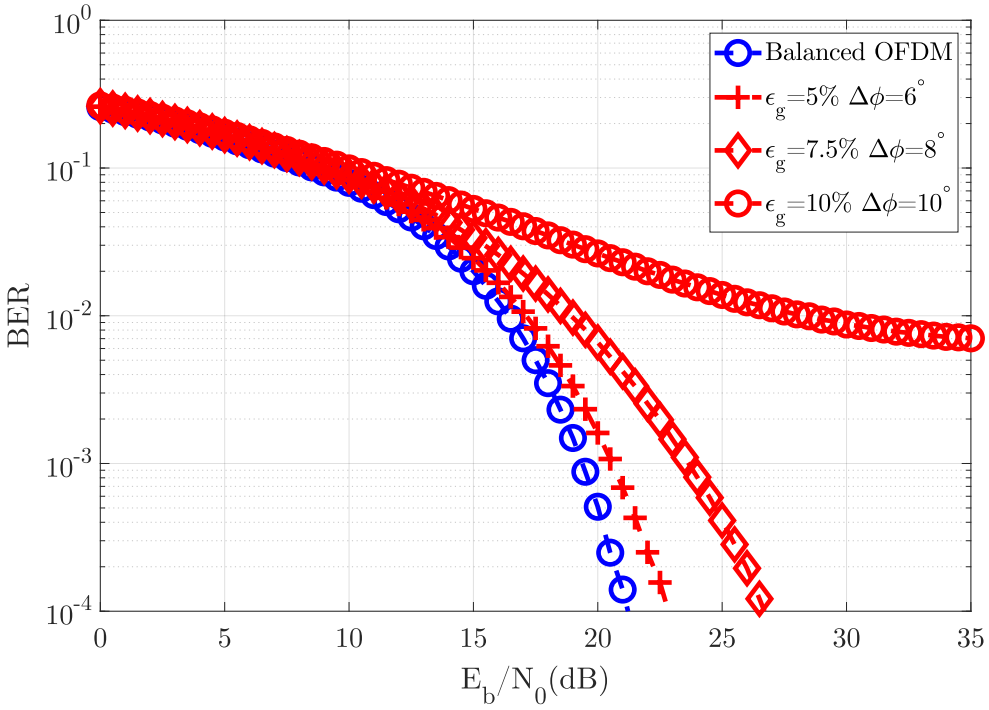

Figure 2.28: BER for an IQ imbalanced OFDM system with $N_u = 512$ and 256-QAM, using time domain compensation according to (2.137).

2.7.4 Nonlinear Amplification

The presence of distortion due to nonlinear amplification in the received signal can significantly limit the achievable performance of a system [58]. If the PAPR of the OFDM signal can be reduced, then the nonlinear distortion will also be lowered, or, alternatively, the PA can operate closer to saturation. The simplest technique is to simply reduce the average power of the signal, referred to as backoff. The energy efficiency of the system will suffer, at the benefit of less nonlinear distortion.

Other techniques attempt to reduce the PAPR with minimum impact on the average signal power [85]. Instead of reducing the entire signal power, one can simply limit the amplitude of the signal peak using soft clipping. Since this is a nonlinear process, there is both in-band and OOB radiation which degrade signal quality. The OOB emissions can be filtered out, however, the filter may also regrow the clipped signal peaks. A similar technique known as Peak Reduction (PR), is to fold the amplitude over the threshold limit, which can be represented by

$$|x_n| = \begin{cases} |s_n| & |s_n| \leq s_{clip} \\ 2s_{clip} - |s_n| & |s_n| > s_{clip} \end{cases}. \tag{2.138}$$

The clipped time sample indices may be transmitted to the receiver, which given the nature of the folding, can revert the clipping. In practice, the received signal is noisy, so

the receiver will struggle to reconstruct the original unclipped version without additional information. Another approach is called Selective Mapping (SLM). This technique consists in multiplying each subcarrier by a specific phase in order to decrease the PAPR of the OFDM block. Generally, this is achieved using only 90° phase shifts, to lower implementation complexity, and requires the transmission of the phase vector to the receiver as side information. A similar technique is known as a Partial Transmit Sequence (PTS), which instead of using a per subcarrier phase shift, it considers several sub-blocks within an OFDM block. Each sub-block is transformed by an IDFT and multiplied by a phase factor such that the combined signal has the lowest possible PAPR. A review on different PTS approaches was presented in [86]. The phase shifts are found by exhaustive search and must also be transmitted to the receiver for successful detection. Another technique is known as Linear Block Coding (LBC) which consists in adding bits to a codeword in order to reduce the PAPR of the symbol. This is particularly useful for codewords that have all odd and even bits equal to each other. Lastly, a technique known as Peak Insertion (PI) reduces PAPR by adding a peak in the frequency domain, which brings the mean energy of the signal up, thereby decreasing the PAPR in the time domain. All these techniques reduce the PAPR of the signal, but also negatively impact the BER, in addition to other complexity and implementation drawbacks.

In [87], a deep learning based scheme for PAPR reducing was developed. An autoencoder network that is capable of encoding and decoding OFDM signals was developed with a loss function designed to minimize the PAPR with minimum impact to the BER. The scheme was shown to achieve very large PAPR reductions while still maintaining an acceptable BER performance.

Another approach to avoid nonlinear amplification is to predistort the OFDM signal before the nonlinearity. This is generally referred to as Digital Pre-Distortion (DPD), and is widely used in power efficient amplification schemes [88]. The main objective of these techniques is to approximate the nonlinearity by a polynomial, such as a Taylor or Volterra series expansion for memoryless and memory nonlinearities, respectively. The DPD process consists on a multiplication of the input signal by the inverse polynomial of the approximation of the nonlinearity. Higher order approximations perform better, at the cost of more parameters to estimate via feedback loop. Another approach is to construct a Look-Up Table (LUT) with nonlinear observations, which can be used as a mapper and reverse mapper to reconstruct the original signal. In [89], a digitally intensive PA combined with adaptive DPD is proposed. The authors of [90] considered a combination of DPD and PAPR reduction to improve amplifier efficiency. The PAPR reduction was achieved using Tone Reservation (TR) that consists in reserving a certain number of subcarriers to carry specific signals to reduce the combined signal PAPR. The selection is optimized to reduce the size of the peaks in the time domain signal. For the DPD, the authors used an artificial neural network to find an additive signal $\mathbf{c}^{\text{dpd}}$ that satisfies

$$\mathbf{c}^{dpd} = f^{-1}(G_{\text{amp}})\mathbf{s} - \mathbf{s}, \tag{2.139}$$

where G_{amp} is the intended amplifier gain. The two techniques are combined in a "Ping-Pong" manner into an iterative process to find a signal with the intended performance.

In [91], it is shown that increasing the number of transmit antennas can reduce the power of the distortion component in MIMO systems. This analysis was extended to several precoding schemes and an analytical expression for the BER performance was derived in [92].

2.7.4.1 Bussgang Noise Cancelling

Consider the time domain OFDM signal $\mathbf{s}$ which has been distorted by an SSPA nonlinearity $\mathbf{x} = f(\mathbf{s})$. The received frequency domain signal at the kth subcarrier can be expressed as

$$Y_k = X_k H_k + N_k. \tag{2.140}$$

As shown previously, the time-domain OFDM signal is Gaussian in nature, and thus Bussgang's theorem can be applied to rewrite the received signal as

$$Y_k = (\alpha_{\text{bg}} S_k + D_k) H_k + N_k. \tag{2.141}$$

From the definition, it is clear that the received signal is simply an attenuated version of the original signal, plus noise and an additional distortion term that is affected by the channel H_k. This distortion does not depend on the SNR, and therefore cannot be mitigated by increasing transmit power. For an SSPA, it can be reduced by increasing the Output backoff (OBO), which consists in shifting the operating point of the amplifier gain below saturation. Since the SSPA gain is more linear the further away from saturation it is, the nonlinearity will be much less severe. The cost of this design choice is that the SSPA will consume a lot more DC power since the optimum amplification efficiency point occurs at saturation.

In this case, the OBO selection will impact the EVM of the transmitted signal. For instance, for a 256-QAM OFDM system with $N = 512$ subcarriers, a clipping level of $s_{\text{sat}}/\sigma_s = 7$, and $p = 1$, the average EVM over 1000 blocks is approximately 2.7%. This ensures that the system meets the EVM of 3.5% of 5G-NR Release 17 for this constellation size, leaving a 0.8% margin for other hardware impairments. Fig. 2.29 shows the simulated BER considering both linear and nonlinear OFDM systems with $N = 512$ subcarriers, highlighting the impact of the SSPA.

From the figure, one can note that an OFDM system distorted by an SSPA with $s_{\text{sat}}/\sigma_s = 7$, and $p = 1$ requires around 7 dB of extra transmit power to achieve a BER of 10^{-4} when compared with linear OFDM transmissions. This result can be drastically improved if the receiver takes advantage of Bussgang's theorem to estimate and cancel the nonlinear distortion D_k. Rewriting the Bussgang decomposition as

$$D_k = X_k - \alpha_{\text{bg}} S_k, \tag{2.142}$$

shows that this estimation requires knowing α_{bg}, which can be computed a priori, S_k, which is obviously not available at the receiver, and X_k, that can be estimated at the receiver

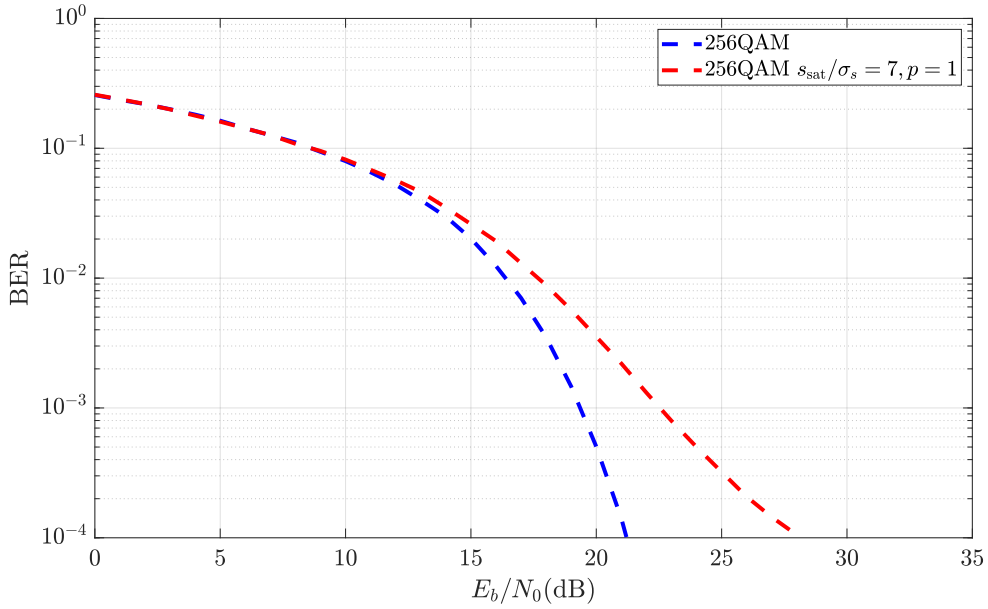

Figure 2.29: BER for linear and nonlinear OFDM systems.

if $f(\cdot)$ is known, either a priori or by pilot estimation [19]. The only unknown variable, S_k, can be estimated by an initial detection at the receiver, hence the algorithm can use an estimate of the transmitted data $\hat{S}_k$. Afterward, it is possible to perform a second detection while cancelling out the distortion factor D_k using an estimate $\hat{D}_k$. This process can be repeated up to $I_{\max}$ iterations to improve the estimation quality. This iterative process is referred to as BNC. At the ith iteration the signal for detection purposes is defined as

$$\tilde{S}_k^{(i)} = \begin{cases} \frac{Y_k + N_k}{\alpha_{\text{bg}} H_k}, i = 0 \\ \frac{Y_k + N_k - \hat{D}_k^{(i)}}{\alpha_{\text{bg}} H_k}, i > 0, \end{cases} \tag{2.143}$$

where $D_k^{(i)}$ is estimated as

$$D_k^{(i+1)} = f(\hat{S}_k^{(i)}) - \alpha_{\text{bg}} \hat{S}_k^{(i)}. \tag{2.144}$$

In (2.143), dividing by α_{bg} is crucial for larger constellations so that the static shift in the constellation can be corrected. Fig. 2.30 shows the BER of a BNC receiver with the same SSPA as the one used for the results of Fig. 2.29. It is considered an OFDM signal with $N = 512$ with different M-QAM constellations. The BNC receiver is parametrized with $I_{\max} = 4$.

From the figure, it is clear that the BNC technique can drastically improve performance when using a clipping level that meets the EVM requirements for 256-QAM. In fact, for this case, $\alpha_{bg} \approx 0.978$, which means that more than 90% of the signal power is used to transmit the useful component. Since α_{bg} is relatively high, it would be interesting to observe the impact of lower clipping levels on the achievable BER. For that purpose,

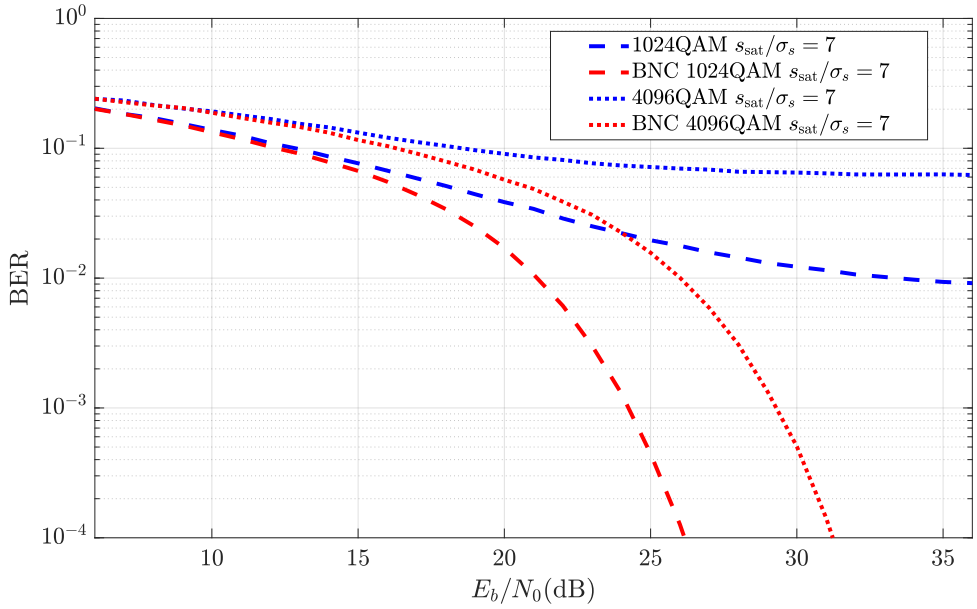

Figure 2.30: BER using the BNC receiver with $I_{\max} = 4$, considering different constellations.

a target BER of 10^{-4} was chosen, and the necessary E_b/N_0 to achieve it was simulated, considering various OBO levels. The OBO is defined as

$$OBO = 20 \log 10 \frac{s_{\text{sat}}}{\mathbb{E}[|s_n|^2]}. \tag{2.145}$$

Fig. 2.31 shows the results of these simulations.

From the figure, it is clear that there is an optimum OBO level that minimizes the transmitted power. For 1024-QAM, this occurs at an OBO of around 12.5 dB, while for 4096-QAMQAM it is approximately 14.5 dB.

2.8 Physical Layer Security

The confidentiality of information has always been a key concern in telecommunication systems. It is even more crucial in wireless systems, due to the broadcast nature of the wireless channel. Although historically this aspect was seen as a military concern, in modern times it has become a demand for commercially oriented telecommunication systems.

The general problem consists in how to ensure that data originating from a user Alice, or A for short, and intended for a recipient Bob, or B, does not fall into the hands of a malicious third user Eve, or E. Note that the main concern is the information itself, since Eve may be able to eavesdrop a signal without obtaining any information from it.

In most applications this security is achieved through cryptography and authentication techniques above the PHY layer of the OSI model, where the hardware is mostly abstracted.

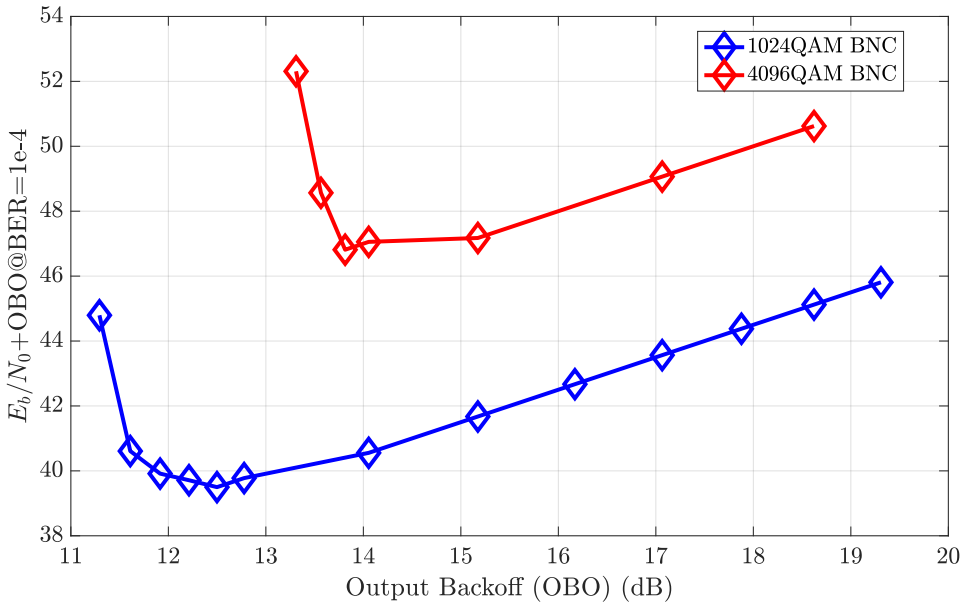

Figure 2.31: Required E_b/N_0+OBO using a BNC receiver with $I_{\max} = 4$ for a target BER of 10^{-4} considering different values of OBO and constellation orders.

This is important, since most eavesdropping attempts happen at higher layers as well. On the other hand, wireless systems are vulnerable to eavesdropping at the PHY layer, which generally has few or no security schemes. In fact, due to the development of more sophisticated SDR devices, eavesdroppers have increasingly more options at their disposal [93].

In this context, an area of research dedicated to the development of security schemes at the PHY layer has developed over the years, and is referred to as PLS [94].

2.8.1 Passive Eavesdropping

The simplest form of attack in a wireless communication consists in exploiting the broadcast signal to eavesdrop on information being transmitted. A malicious third party is considered a passive eavesdropper, if it only listens to the communication, without transmitting any signal. This makes the eavesdropper nearly undetectable, requiring the use of schemes that assume the presence of an eavesdropper. These schemes may not even require additional processing or power, such as the case of a MIMO beamforming system. The MIMO transmitter directs the power to the receiver, which has the added benefit of reducing power at other locations. An eavesdropper outside of the beam direction, would receive less power when compared to a SISO transmitter, resulting in better security. A survey detailing several beamforming based PLS techniques is available in [95].

Another example is the SVD scheme described in section 2.5.1.2. If an Eve with the same number of antennas, and knowledge of the modulation and interleaving is used,

then the eavesdropping capacity can be characterized using the channel definition. This eavesdropped channel can be viewed as the average between two physical channels, from Alice to Eve, and Bob to Eve, as

$$\mathbf{H}_{k_E} = \frac{\mathbf{H}_{k_{AE}} + \mathbf{H}_{k_{BE}}}{2}. \tag{2.146}$$

The real channel is then defined as

$$\mathbf{H}_k = \rho_E \mathbf{H}_{k_E} + \boldsymbol{\epsilon}_k. \tag{2.147}$$

where ρ_E is a correlation factor with the true channel, and $\boldsymbol{\epsilon}_k$ is an appropriate Gaussian distributed error with variance $\frac{\sigma_N^2}{\beta}$, where β_E is a scaling factor. The channels are equal when $\rho_E = 1$ and $\beta_E = \infty$. The SVD of the eavesdropper channel is defined as

$$\mathbf{H}_{k_E} = \mathbf{U}_{k_E} \boldsymbol{\Lambda}_{k_E} \mathbf{V}_{k_E}^H, \tag{2.148}$$

where $\mathbf{U}_{k_E}^H$ is the decoding matrix that will be used by the eavesdropper. This system is summarized in Fig. 2.32.

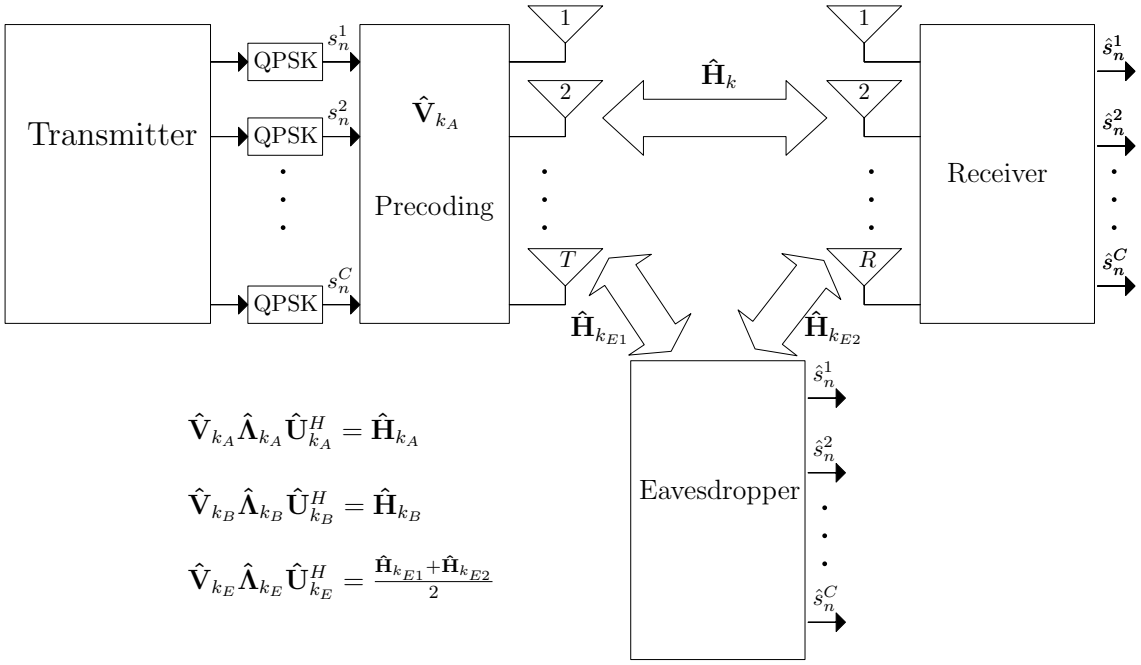

Figure 2.32: Diagram of the three user scenario for SVD MIMO.

At the eavesdropper, the received signal is defined as

$$\mathbf{Y}_{k_E} = \mathbf{H}_{k_E} \mathbf{X}_k + \mathbf{N}_{k_E}, \tag{2.149}$$

where $\mathbf{N}_{k_E}$ has the same variance as $\mathbf{N}_k$.

The decoding operation at the eavesdropper can be expressed as

$$\mathbf{W}_{k_E} = \mathbf{U}_{k_E}^H \mathbf{Y}_{k_E}, \tag{2.150}$$

which can be expanded as

$$\mathbf{W}_{k_E} = \mathbf{\Lambda}_{k_E} \mathbf{V}_{k_E}^H \mathbf{V}_k \mathbf{X}_k + \mathbf{U}_{k_E}^H \mathbf{N}_{k_E}. \tag{2.151}$$

Another technique is to add an artificial noise sequence to the transmitted signal [96, 97]. An example is shown in [96], where a transmitter employing T transmit antennas to a receiver with $R = 1$ receive antennas is being eavesdropped by multiple eavesdroppers with $R_E = 1$ antennas. The authors propose a precoding operation using the eigenvectors vectors of the matrix $\mathbf{H}_k^H \mathbf{H}_k$, defining the transmitted signal as

$$\mathbf{X}_k = \sqrt{a}\mathbf{t}\mathbf{S}_k + \sqrt{b}\nu, \tag{2.152}$$

where $\mathbf{t}$ is the eigenvector of $\mathbf{H}_k^H \mathbf{H}_k$ corresponding to the largest eigenvalue, and ν is an artificial noise vector constructed using the remaining eigenvectors, defined as

$$\nu = \frac{1}{\sqrt{T-1}} \sum_{i=1}^{T-1} \mathbf{t}_i \mu_i, \tag{2.153}$$

where $\mathbf{t}_i$ is the ith eigenvector of $\mathbf{H}_k^H \mathbf{H}_k$, and μ_i is a unitary complex scalar with random uniformly distributed phase. This results in a noise vector that is orthogonal to the equalization matrix, which can be cancelled out at the receiver. Since the eavesdropper does not have access to the exact same channel as the receiver, the orthogonality will be lost, and the signal will suffer from interference due to the noise vector, drastically lowering performance.

2.8.2 Active Attacker

Active PLS scenarios consider that the eavesdropper also participates in the communication, such as by impersonating another user or disrupting communication.

A common method of attack is described in [98]. The eavesdropper intervenes during the training phase by transmitting an identical pilot sequence at the same time as the intended receiver. This results in an incorrect channel estimate at the transmitter, which will reduce the transmitter's ability to allocate power to the receiver by precoding, thereby increasing the power available at the eavesdropper. During data transmission, the eavesdropper can also transmit a jamming signal to reduce the SNR available at the intended receiver, which the transmitter might try to compensate by increasing transmission power, inadvertently improving the SNR at the eavesdropper.

In order to counteract this type of attacks, additional measures must be adopted. One possibility is to increase the amount of information that is dependent on intrinsic characteristics of the intended transmitter or receiver, such as their location and paths [99]. Another approach relies on obfuscating the communication from the eavesdropper [100].

This problem has recently become an important focus in the field of Unmanned Aerial Vehicle (UAV) communication. In [101], the authors proposed an unsupervised Support Vector Machine (SVM) to detect when an eavesdropper was attempting to interfere

during the authentication phase of a UAV. In [102], the transmitter sends artificial noise sequences at the same time as data, which can be cancelled out by the receiver, to confuse the eavesdropper. An interesting approach that relies on knowing the trajectory of the UAV was proposed in [103]. Since it is difficult for the eavesdropper to mimic the trajectory of the UAV, this technique adds an appropriate security level.

2.8.3 Secrecy Rate

There are many methods to measure the security potential of a communication system, which makes it difficult to compare between different techniques. A commonly accepted metric is to compute the SR, which is the difference between the capacities of the intended and eavesdropped channels [104]. The capacity of the intended user can be calculated as

$$C_k = \sum_{c=1}^{C} \log_2 \left(1 + |\lambda_{k,c}|^2 \frac{\sigma_X^2}{\sigma_N^2} \right), \tag{2.154}$$

where σ_X^2 is the variance of $\mathbf{X}_k$, and $\lambda_{k,c}$ is the singular value of the cth branch. The capacity of the eavesdropped channel is defined as

$$C_k^E = \sum_{c=1}^{C} \log_2 \left(1 + |\rho_E \lambda_{k,c}|^2 \frac{\sigma_X^2}{\sigma_N^2 + \sigma_M^2} \right), \tag{2.155}$$

where σ_M is the interference power given by

$$2\sigma_M^2 = \mathrm{E}\left(\hat{\mathbf{\Lambda}}_{k_E} \hat{\mathbf{\Lambda}}_{k_E}^H \right), \tag{2.156}$$

and $\hat{\mathbf{\Lambda}}_{k_E}$ is the interference matrix defined as

$$\hat{\mathbf{\Lambda}}_{k_E} = \mathbf{U}_{k_E}^H \mathbf{H}_k \mathbf{V}_k - \mathrm{diag}(\mathbf{U}_{k_E}^H \mathbf{H}_k \mathbf{V}_k). \tag{2.157}$$

The sum-capacity of the proper MIMO channel, C_{AB}, can be computed as

$$C_{AB} = \sum_{k=1}^{N} C_k. \tag{2.158}$$

Likewise, the capacity of the eavesdropped channel is computed as

$$C_E = \sum_{k=1}^{N} C_k^E. \tag{2.159}$$

The secrecy rate SR is defined as

$$SR = C_{AB} - C_E. \tag{2.160}$$

2.9 Software Defined Radio

Developing prototypes to test new transceivers for wireless communications has always been expensive and time consuming, generally falling outside of the field of expertise of information theory researchers. Modern transceivers require custom made amplifiers, DACs/ADCs, filters, antennas, and low-level implementations of Digital Signal Processing (DSP), which may not be reusable for different prototypes due to varying carrier frequencies, bandwidths, transmission power, and others. An alternative that has been gaining traction in commercial solutions is to use SDRs, which are programmable RF devices that are designed to support several possible hardware configurations.

Currently, there are several different manufacturers of SDRs designed for different price points and use cases. One such manufacturer is Ettus Research[1], whom in addition to developing SDR platforms called Universal Software Radio Peripherals (USRPs), have also developed an open source Application Programming Interface (API) for interacting with USRPs via Python and C++, called USRP Hardware Driver (UHD).

2.9.1 GNURadio

GNURadio is a widely used open-source framework for developing signal processing applications [105]. It differs from Matlab's Simulink in that it utilizes a scheduling based approach that allows each block to process generic logical items independently, resulting in a large performance increase, particularly for multi-threaded systems.

Each application is structured in a flowgraph, which is a graphical representation of the connections between processing blocks that can be edited using the GNURadio Companion application. Each block can produce and consume samples at a certain ratio between input and output. If the ratio is 1, then they are called Synchronous blocks, while for ratios of $1/N$ and $N/1$ they are Interpolating and Decimation blocks, respectively. If a block only produces samples (i.e. no input) it is called a Source block. Inversely, if a block only consumes samples (i.e. no output) it is called a Sink block.

Each block can be implemented either as a combination of other blocks, or written directly in C++ or Python, with the former being more efficient in performance. GNURadio already includes a large set of blocks that implement commonly used functions such as the FFT, and even includes blocks that integrate the UHD API. Sending signals to a USRP is done using the USRP Sink block, while receiving uses the USRP Source block. Configuring the settings of each block allows changing the RF characteristics of the USRP (carrier frequency, amplifier gain, bandwidth filtering, etc.).

In the literature, SDR platforms are becoming common as a solution to evaluate the performance of new transceivers. An SDR implementation of a NOMA scheme was proposed by [43]. In [106], the author uses SDRs to implement two PLS schemes, verifying

[1] https://www.ettus.com/

their potential in a practical scenario. An SDR implementation of carrier and timing synchronization was shown in [107].

3

Nonlinear Receivers

3.1 Introduction

This chapter presents the proposed highly efficient receivers for nonlinear communications. It begins by characterizing distortion cancelling receivers for SC systems that use SVD for MIMO separation. For MC systems, distortion cancelling receivers based on Bussgang's theorem are analysed, and novel nonlinear distortion aided receivers based on GAMP and GTurbo are presented. The performance of all receivers is measured via simulation.

3.2 Nonlinear Receivers for Single-Carrier

This section shall cover advanced nonlinear receivers designed for SC systems. Although NR and 802.11 standards have moved away from SC, it is still an important research area for applications where MC schemes cannot perform adequately due to hardware constraints. The novel receiving schemes described in this section were published in [10, 108].

3.2.1 Bussgang SVD

As shown in subsection 2.7.4.1, Bussgang's theorem can be used to develop a receiver capable of mitigating nonlinear distortion present in the signal. The application of the theorem requires that the input signal follow a Gaussian distribution, as is the case for OFDM. However, for SC modulations, the time-domain signal distribution will depend on the constellation, and in most cases is not Gaussian.

An alternative scheme that makes use of SVD precoding to obtain a Gaussian distributed transmitted signal in the time-domain was developed for IB-DFE coded systems that achieved promising performance even for strong nonlinear effects.

As mentioned before, after the precoding operation, the signal associated to each transmit antenna will have substantial envelope fluctuations. This phenomena can be observed in Fig. 3.1, which shows the instantaneous power associated to a given precoded signal. Clearly, after the precoding operation, the time-domain signals present considerable

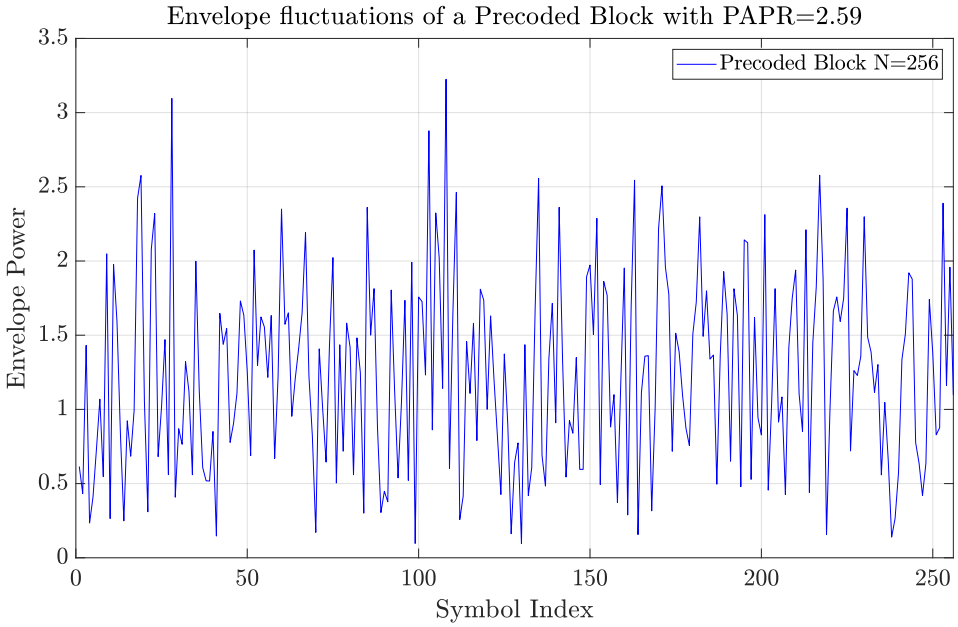

Figure 3.1: Instantaneous power associated with a time-domain precoded and interleaved signal.

PAPR. Under these conditions, it is very prone that the transmitted signal have nonlinear distortion effects, since the power amplifier characteristic cannot linearly accommodate signals with large envelope fluctuations. In fact, a nonlinear power amplification is almost unavoidable if an efficient power amplification is desired (since working in the linear region of the power amplifiers requires large backoffs, which substantially reduces the amplification efficiency).

3.2.1.1 Transmission

This wireless system employs SC-FDE transmission with M-QAM, transmitting up to C data streams using T transmit and R receive antennas. The time-domain symbols are aggregated by blocks, with the receiver employing IB-DFE to improve detection. The symbols at time instant n are represented by the $C \times 1$ vector $\mathbf{s}_n$, with the frequency-domain counterpart at the kth subcarrier, obtained via DFT, denoted by $\mathbf{S}_k$. To separate the different MIMO streams, the SVD scheme from sec. 2.5.1.2 is used, with the precoded symbols denoted as $\mathbf{x}_n$.

Consider that the precoded signal, which is obtained as in (3.17), is nonlinearly amplified by an SSPA, modelled by (2.121). The performance of this system will depend heavily on the normalized saturation level s_{sat}/σ_x, where σ_x is the variance of the real and imaginary parts of the precoded signal.

Although the data symbols $\mathbf{s}_n$ are not Gaussian, the precoded symbols $\mathbf{x}_n$ are approximately Gaussian, provided that the dimensions of the precoding matrix $\mathbf{V}_k$ are large and

the elements of the channel matrix have small correlation. Under these conditions, the precoded signal can be modelled by $x \sim \mathcal{N}(0, \sigma_x^2)$, where σ_x^2 is the variance of the real and imaginary parts of the precoded symbols $\mathbf{x}_n$, assumed to be the same for all streams. The tightness of this Gaussian approximation can be observed in Fig. 3.2, where the PDF of the real-part of the precoded symbols is shown. Thanks to this Gaussian approximation, it is

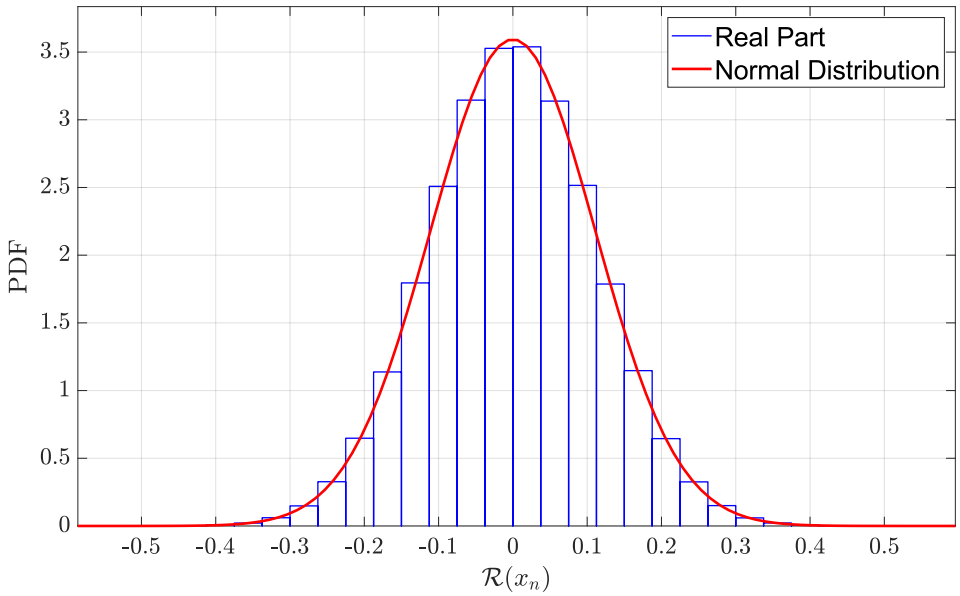

Figure 3.2: Distribution of the real part of the precoded interleaved signal when $C = T = R = 8$.

possible to take advantage of Bussgang's theorem to decompose the nonlinearly distorted Gaussian signal into two uncorrelated terms: a useful component that is a scaled replica of the input signal and a noisy term associated to the nonlinear distortion. For this scenario, the nonlinearly distorted signal at the output of the tth PA is written as

$$\mathbf{y}^{(t)} = \alpha_{\text{bg}}^{(t)} \mathbf{x}^{(t)} + \mathbf{d}^{(t)}, \tag{3.1}$$

where $\mathbf{d}^{(t)} = [d_1^{(t)}\ d_2^{(t)}\ \cdots\ d_N^{(t)}]$ is the set of nonlinear distortion terms of the tth branch and $\alpha_{\text{bg}}^{(t)}$ is the scale factor associated to the tth branch that can be obtained as

$$\alpha^{(t)} = \frac{\mathbb{E}\left[x_n^{(t)} y_n^{*(t)}\right]}{\mathbb{E}\left[\left|x_n^{(t)}\right|^2\right]} = \frac{\mathbb{E}\left[x_n^{(t)} f^*\left(x_n^{(t)}\right)\right]}{2\sigma_x^2}. \tag{3.2}$$

If it is assumed that the nonlinear characteristics of the PAs are equal and the power of precoded signals is the same for all the T transmit branches (the generalization to other cases is straightforward), the scale factor α is equal for all streams.

The DFT of (3.1) yields the frequency-domain version of the signal to be transmitted $\mathbf{Y}^{(t)} = \text{DFT}([y_1^{(t)}\ y_2^{(t)}\ \cdots\ y_N^{(t)}])$. Once again, from Bussgang's theorem, $\mathbf{Y}^{(t)}$ can be separated into two uncorrelated components, leading to

$$\mathbf{Y}^{(t)} = \alpha_{\text{bg}}\mathbf{X}^{(t)} + \mathbf{D}^{(t)}, \tag{3.3}$$

where $\mathbf{D}^{(t)} = \text{DFT}([d_1^{(t)}\ d_2^{(t)}\ \cdots\ d_N^{(t)}])$ represents the nonlinear distortion terms along the tth branch. Under these conditions, the nonlinearly distorted signal for the kth subcarrier is

$$\mathbf{Y}_k = \alpha\mathbf{X}_k + \mathbf{D}_k. \tag{3.4}$$

3.2.1.2 Reception

When there are nonlinear distortion effects, the received signal can be expressed as

$$\mathbf{Z}_k = \mathbf{H}_k\mathbf{Y}_k + \mathbf{N}_k. \tag{3.5}$$

After the decoding operation, it becomes

$$\begin{aligned}
\mathbf{W}'_k &= \mathbf{U}_k^H\mathbf{H}_k\mathbf{Y}_k + \mathbf{U}_k^H\mathbf{N}_k \\
&= \mathbf{U}_k^H\mathbf{H}_k(\alpha_{\text{bg}}\mathbf{X}_k + \mathbf{D}'_k) + \mathbf{U}_k^H\mathbf{N}_k \\
&= \alpha_{\text{bg}}\mathbf{U}_k^H\mathbf{H}_k\mathbf{V}_k\mathbf{S}'_k + \mathbf{U}_k^H\mathbf{H}_k\mathbf{D}'_k + \mathbf{U}_k^H\mathbf{N}_k \\
&= \alpha_{\text{bg}}\mathbf{U}_k^H\mathbf{U}_k\mathbf{\Lambda}_k\mathbf{V}_k^H\mathbf{V}_k\mathbf{S}'_k + \mathbf{U}_k^H\mathbf{H}_k\mathbf{D}'_k + \mathbf{U}_k^H\mathbf{N}_k \\
&= \alpha_{\text{bg}}\mathbf{\Lambda}_k\mathbf{S}'_k + \mathbf{U}_k^H\mathbf{H}_k\mathbf{D}'_k + \mathbf{U}_k^H\mathbf{N}_k.
\end{aligned} \tag{3.6}$$

Under these conditions, after applying the de-interleaving, it develops as

$$\mathbf{W}_k = \mathbf{\Lambda}'_k\mathbf{S}_k\alpha_{\text{bg}} + \mathbf{U}_k^{H\prime}\mathbf{H}'_k\mathbf{D}_k + \mathbf{U}_k'^H\mathbf{N}'_k. \tag{3.7}$$

If conventional IB-DFE concept, as described in sec. 2.3.2.2, was applied directly to the decoded signal, the nonlinear distortion component would be regarded as a simple additional noise component that will degrade the system's performance, imposing a BER floor that is higher for more severe nonlinear characteristics. In this work, however, a modified version of the conventional IB-DFE that includes a BNC technique was proposed. This technique requires an estimate of the transmitted signal $\mathbf{x}_n$, which for IB-DFE, can be obtained by applying the same transmission chain used by the receiver, to the estimated data symbols associated with the lth equalization iteration, $\hat{\mathbf{S}}_k^{(l)}$. Therefore, $\hat{\mathbf{S}}_k^{(l)}$ should be submitted to the interleaving, precoding, SSPA model, and de-interleaving operations. The estimate of the nonlinear distortion component associated to a given iteration is obtained by computing

$$\hat{\mathbf{d}}_n^{(l)} = f(\hat{\mathbf{x}}_n) - \alpha_{\text{bg}}\hat{\mathbf{x}}_n, \tag{3.8}$$

with $\hat{\mathbf{D}}_k^{(l)}$ being the frequency domain counterpart of the distortion term estimates. The equalized symbols are, therefore, computed by

$$\tilde{\mathbf{S}}_k^{(l)} = \mathbf{F}_k^{(l)}(\mathbf{W}_k - \mathbf{U}_k'^H\mathbf{H}'_k\hat{\mathbf{D}}_k'^{(l-1)}) - \mathbf{B}_k^{(l)}\bar{\mathbf{S}}_k^{(l-1)}, \tag{3.9}$$

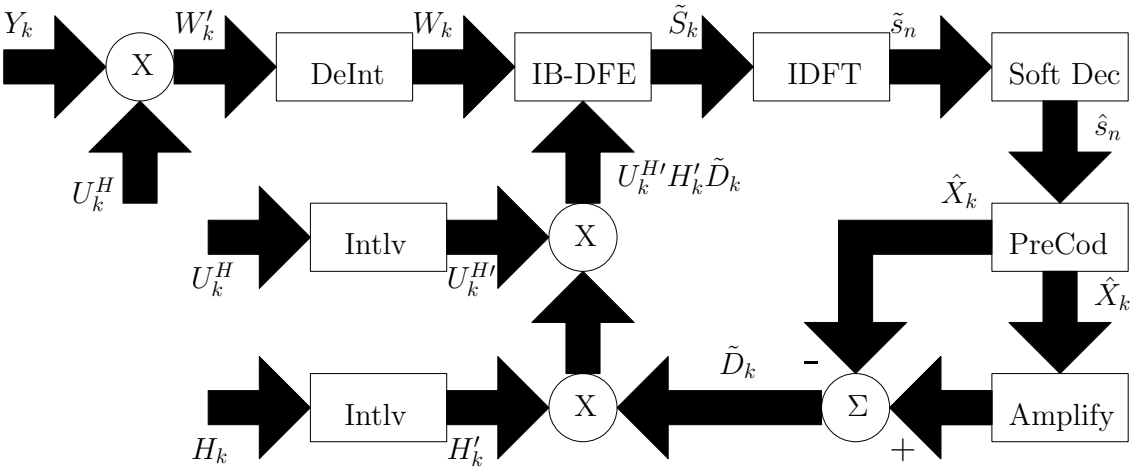

Figure 3.3: Block diagram of the proposed receiver. For simplicity's sake, the DFT operation is implied in the PreCod block, and the IDFT and subsequent DFT operations are implied by the Amplify block.

with $\hat{\mathbf{D}}_k^{\prime(0)} = 0$. A block diagram of the proposed receiver is shown in Fig. 3.3.

It should be noted that, in the first iteration ($l = 1$), there are no symbol estimates, and, therefore, the receiver is not able to compute an estimate of the nonlinear distortion component and perform its cancellation. However, it is possible to modify the feedforward equalization matrix to account for the nonlinear distortion component, which can be seen as an additional noise component [58]. This modification passes through change the effective SNR to account for the power of the nonlinear distortion noise, which gives rise to a "robust receiver". The Signal-to-Noise plus Distortion Ratio (SNDR) is defined as

$$\text{SNDR} = \frac{P_x}{\sigma_N^2 + P_D}, \tag{3.10}$$

where P_x is the signal power and P_D is the power associated with the distortion term. Under these conditions, the feedforward coefficient becomes

$$\tilde{\mathbf{F}}_k^{(l)} = \frac{\mathbf{\Lambda}'_k}{\mathbf{\Lambda}'^2_k + \frac{1}{\alpha_{\text{bg}}^2 \text{SNDR}}}. \tag{3.11}$$

By taking into account the power degradation due to the nonlinearity, performance can be improved for higher SNR. The same reasoning is applied to the calculation of the soft decisions in both coded and uncoded receivers, where an equivalent noise is defined as

$$\sigma_M^2 = \sigma_N^2 + P_D. \tag{3.12}$$

3.2.1.3 Simulation Results

This section presents a set of BER curves for the proposed reception scheme. Unless otherwise stated, each block contains $N = 512$ symbols. The channels between each

transmit and receive antenna are uncorrelated, (i.e., $\rho = 0$), and have 16 symbol-spaced multipath components with equal average power and uncorrelated Rayleigh fading.

Fig. 3.4 presents the impact of two levels of nonlinearity on the BER of a 16-QAM system with $R = T = 32$, at both the first and fourth iterations. When $s_{\text{sat}}/\sigma_x = 4.0$, there

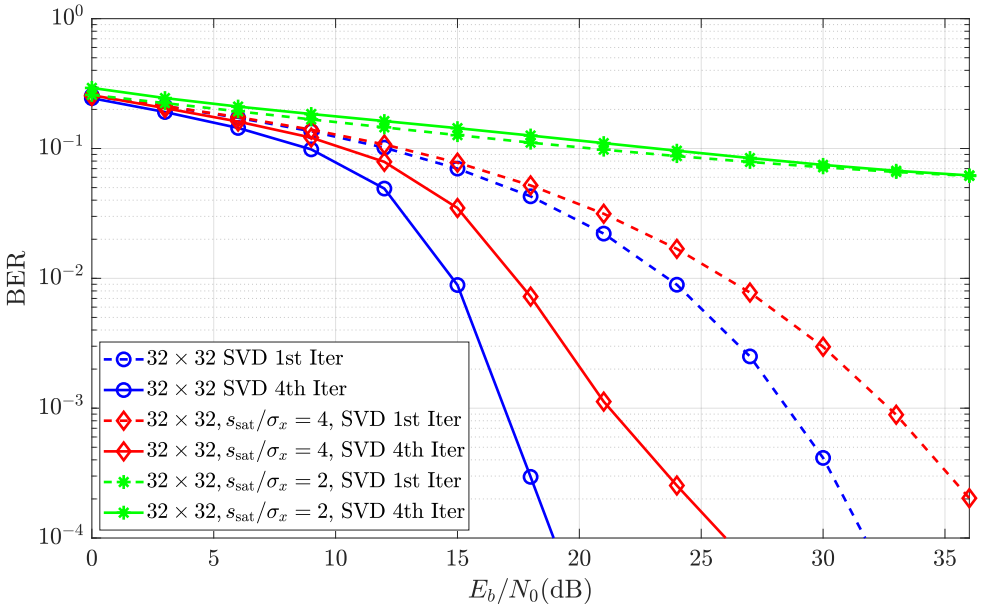

Figure 3.4: BER for a $R = T = 32$ SVD system employing 16-QAM, with various clipping levels.

is a degradation of about 7 dB for a target BER of 10^{-4}, compared to the linear case in the figure, while the gain from the IB-DFE iterations is the same even with the added distortion. However, for $s_{\text{sat}}/\sigma_x = 2.0$, the receiver's performance is significantly worse, and the BER floor is substantially higher in this case.

Fig. 3.5 compares the BER using BNC receivers. As can be observed in the figure, the addition of BNC provides a considerable improvement in the performance for systems with this type of distortion. The boost in performance of the BNC receiver for the first iteration is small, however, the iterative gain of this receiver is far larger. By comparing with the linear receiver, there is a gain of 6 dB when the BER is 10^{-4} and the clipping level is $s_{\text{sat}}/\sigma_x = 4.0$, and a lowered BER floor for a clipping level of $s_{\text{sat}}/\sigma_x = 2.0$. Since the back-off will be lower in the later case by 6 dB, this means a considerable performance gain.

Consider now a 64-QAM scheme. Fig. 3.6 concerns the linear case and Fig. 3.7 concerns the BNC receiver. Due to the larger constellation, the linearity requirements of the amplification process are much higher. This reflects in a severe performance degradation even for higher clipping levels than the ones considered with 16-QAM constellations. As such, the performance improvement of the BNC receiver is much higher. Particularly, for

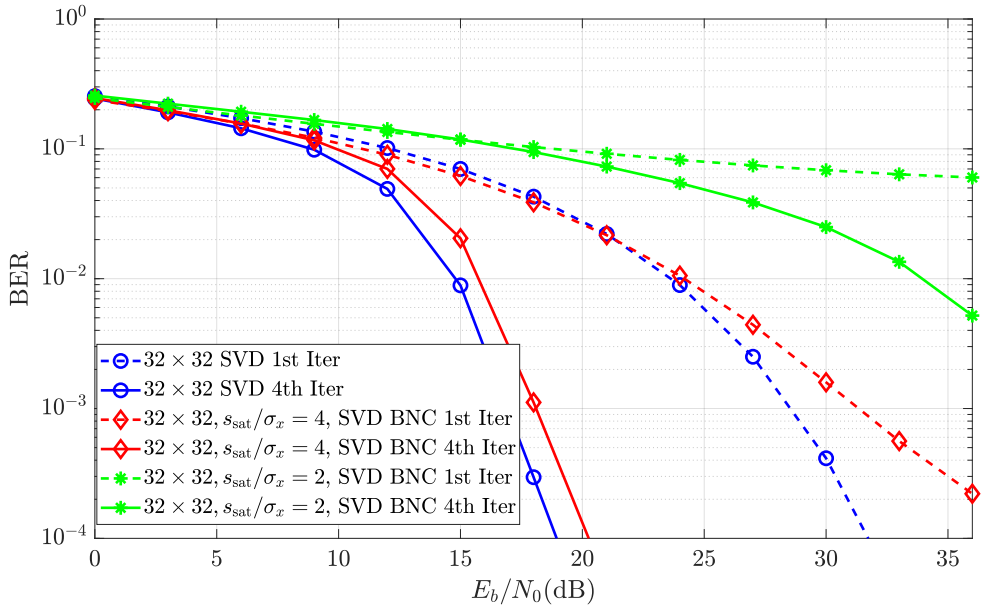

Figure 3.5: BER for a $R = T = 32$ SVD system with BNC, employing 16-QAM, for various clipping levels.

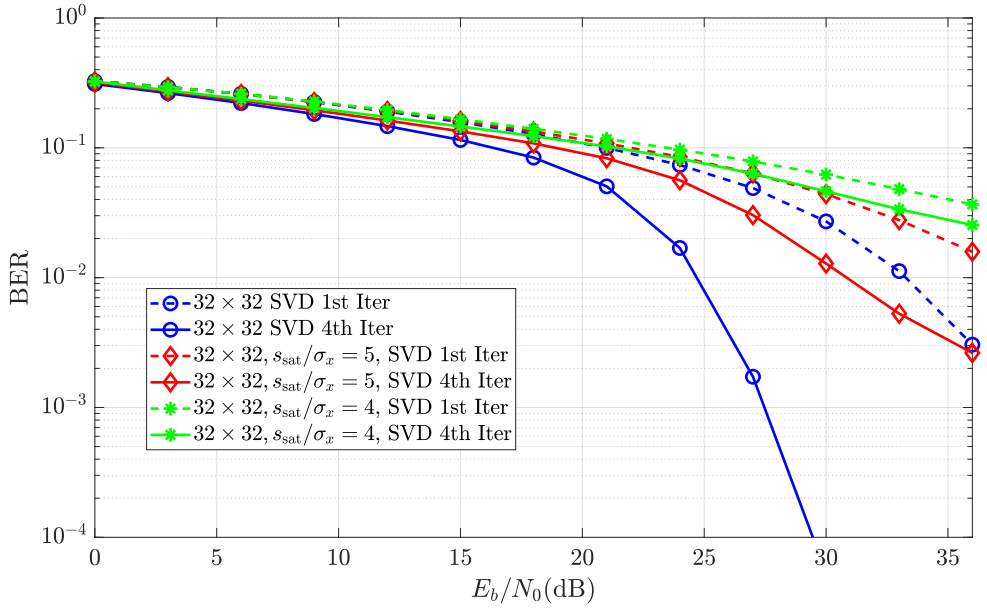

Figure 3.6: BER for a $R = T = 32$ SVD system employing 64-QAM, with various clipping levels.

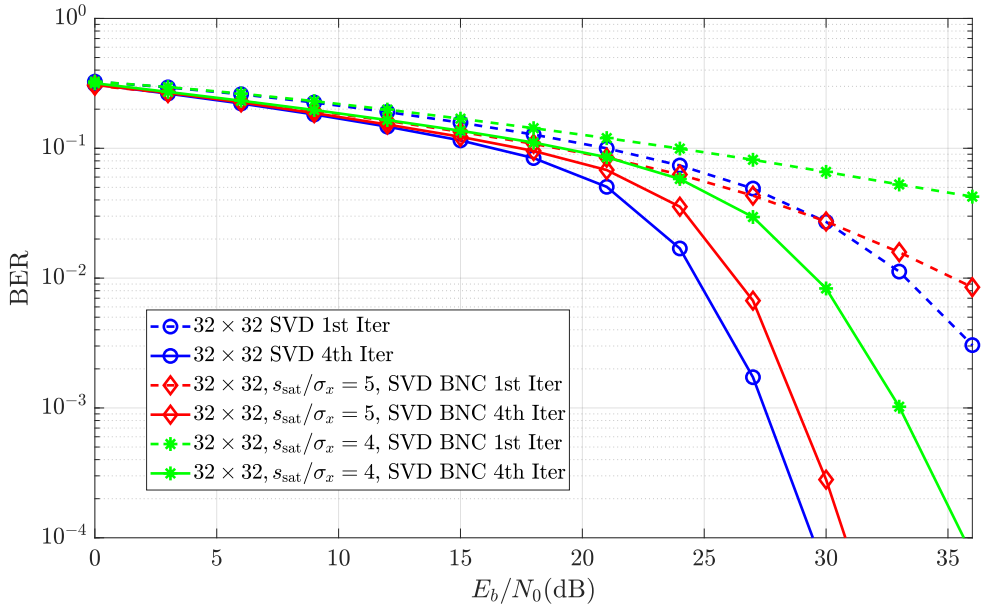

Figure 3.7: BER for a $R = T = 32$ SVD system with BNC, employing 64-QAM, for various clipping levels.

$s_{sat}/\sigma_x = 4.0$, the Bussgang-based receiver significantly outperforms the linear receiver, achieving only a 6.5 dB degradation over the ideal non-distorted receiver, for a target BER of 10^{-4}.

Under the same simulation conditions as before, a 64-state convolutional code was introduced. Due to the APP decoding making this receiver more robust, it is possible to employ lower clipping levels. Fig. 3.8 shows the BER considering 16-QAM. As can be seen in the figure, the addition of the APP decoder makes performance much better than the one associated with the non-coded receiver. Even with a clipping level of $s_{sat}/\sigma_x = 2.0$, the coded receiver outperforms the non-coded linear receiver. As is expected, a sudden drop in the BER is observed, as opposed to the smoother transition of the non-coded receiver, and the iterative gain is smaller as the decoder improves the results of the first iteration. In Fig. 3.10, a scenario with a 64-QAM constellation is considered. As can be observed, the performance increase is even larger, which can be explained by the larger noise and nonlinear sensitivity of this receiver. The same sharp drop and smaller iterative gain from the lower order system are also observed in this figure, though happening at higher

Fig. 3.9 shows the BER for the coded BNC receiver. With the same clipping levels as before, it can be observed that the distortion cancelling receiver outperforms the linear receiver by about 4 dBs, for a BER target of 10^{-4}, resulting in a performance that is much closer to a non-distorted receiver, while employing more energy efficient amplifiers. The change in the LLR calculation of this receiver results in a better performing first iteration, even though it does not perform any nonlinearity cancellation yet, and, for these clipping

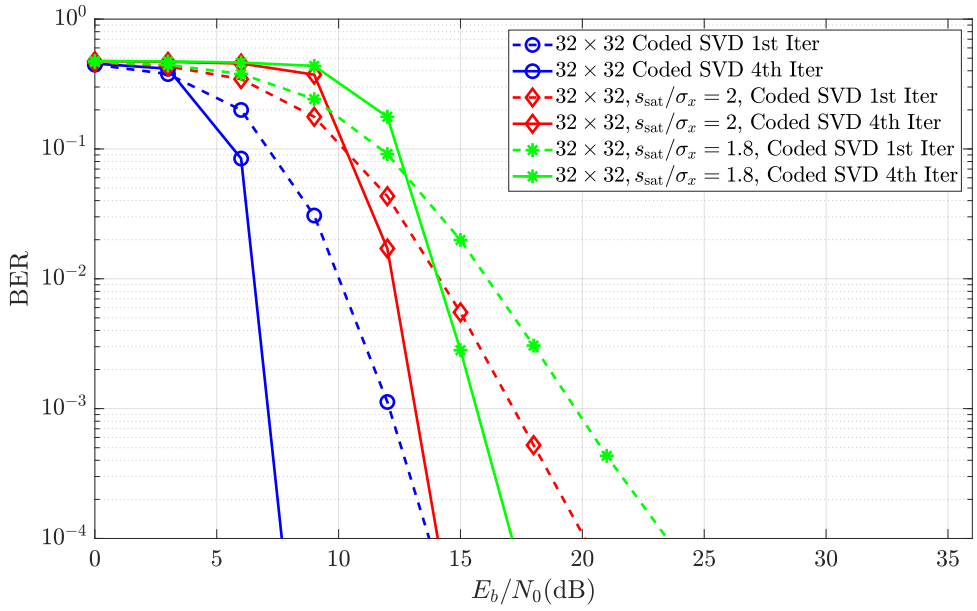

Figure 3.8: BER for a $R = T = 32$ coded SVD system employing 16-QAM, with various clipping levels.

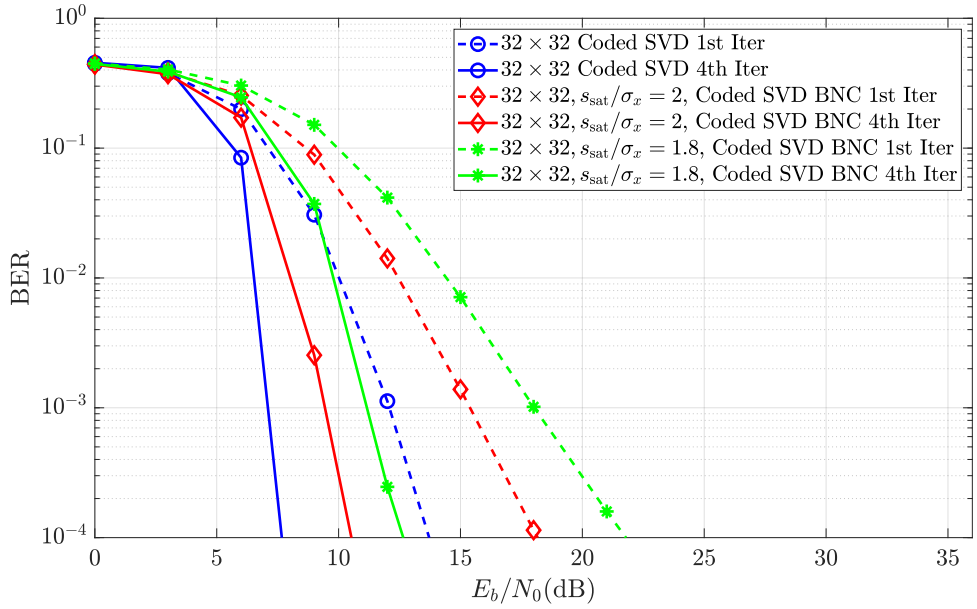

Figure 3.9: BER for a $R = T = 32$ coded SVD system with BNC, employing 16-QAM, with various clipping levels.

levels, removes the iteration degradation at low SNR that was present in the linear receivers. The iterative gain in this receiver is also larger than the linear receiver, as expected due to the nonlinear distortion cancelling of subsequent iterations.

Fig. 3.10 compares the BER for 64-QAM In this case, there is a larger performance

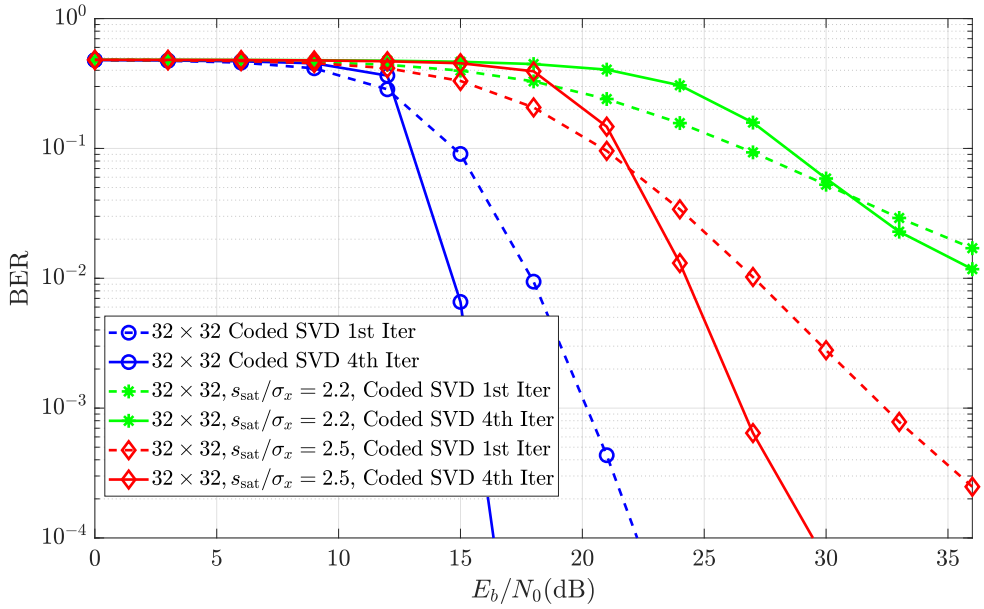

Figure 3.10: BER for a $R = T = 32$ coded SVD system employing 64-QAM, with various clipping levels.

degradation due to the nonlinear distortion, when compared to 16-QAM. Despite the use of FEC, it is still not sufficient to support more efficient amplification. Fig. 3.11 compares the BER for BNC receivers. In can be seen in the figure that there is a substantial performance gain of about 8 dB for a BER target of 10^{-4}. There is a much more noticeable performance difference in using larger constellations due to the higher sensitivity to nonlinear distortion effects, which allows for a much higher boost when the distortion is cancelled iteratively. This is visible in the large performance difference between iterations when compared to the 16-QAM case. Likewise, for these clipping levels, there is no performance degradation with the iterations for low SNR when the receiver design takes into account the power of nonlinear distortion.

3.2.2 NOMA SC-FDE

There is a growing demand for increasing user capacity in wireless systems. In conventional techniques, user communications are designed to be completely orthogonal, either in the time or frequency domains, or by using spread spectrum techniques. A novel alternative that has gained traction in the literature is to forgo this orthogonality entirely, and attempt to increase capacity by having superimposed user signals - so called NOMA

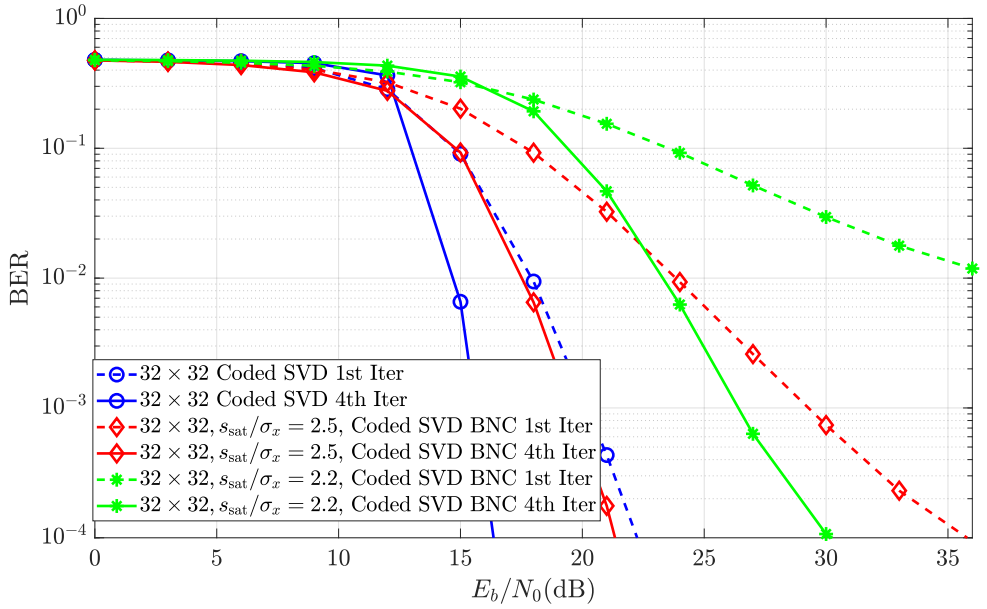

Figure 3.11: BER for a $R = T = 32$ coded SVD system with BNC, employing 64-QAM, with various clipping levels.

schemes. In this form, users can share the same resources which increases overall system capacity.

Naturally, there is a significant downside that warrants the use of orthogonal access schemes, and that is the difficulty in separating the different signals after being superimposed. In most NOMA applications, each user must detect and remove the signals belonging to other users from the received signal through an process of Successive Interference Cancellation (SIC), with the number of iterations depending on how many signals were combined. This has a negative impact on the system delay by increasing the time it takes to successfully receive data. Another concern, is that malicious eavesdroppers could also perform SIC to try and recover the data meant for legitimate users. As such, it is highly important to analyse the PLS of these schemes.

There are many methods to superimpose these signals. One such method is to simply transmit multiple user signals at the same time, with different transmission powers - power-domain NOMA. This type of scheme is particularly useful for scenarios where the distance to the transmitter is very different between receivers. This thesis considered a downlink power-domain NOMA system with two receivers, though the analysis can easily be extended for cases with more receivers.

3.2.2.1 Transmission

In a power-domain NOMA scheme, the data meant for each user is sent at the same time, and over the same channel, with differing transmitting power. For a scenario with one

transmitter, A, and two receivers, B and C, the power ratio between the two intended signals $\mathbf{S}_{k_B}$ and $\mathbf{S}_{k_C}$ is defined as α.

An interleaving scheme is used to average the power of all singular values, as shown in 2.5.1.2. The interleaving scheme can be different for each user, as it only affects the data symbols. Therefore, the interleaved symbols for users B and C are denoted as $\mathbf{S}'_{k_B}$ and $\mathbf{S}'_{k_C}$, respectively. Before transmitting data, there is an initial training sequence exchange between all users, so as to obtain the channel matrices with which to compute the SVD. The exchange begins with the farthest user, C, sending a training sequence meant for the transmitter, which is ignored by B. In the next step, B sends a training sequence meant for the transmitter as well. Lastly, the transmitter sends a training sequence, followed by the precoded data to all users. In all steps, there is an eavesdropper that listens to all of the exchanged sequences, and computes its own channel estimates.

The channel matrices associated to the kth subcarrier can be defined as

$$\mathbf{H}_{k_{AB}} = \rho_{A1}\hat{\mathbf{H}}_{k_{A1}} + \boldsymbol{\epsilon}_k, \tag{3.13}$$

and

$$\mathbf{H}_{k_{AC}} = \rho_{A2}\hat{\mathbf{H}}_{k_{A2}} + \boldsymbol{\epsilon}_k, \tag{3.14}$$

where $\hat{\mathbf{H}}_{k_A1}$ and $\hat{\mathbf{H}}_{k_A2}$ are the channel estimates used by the transmitter, ρ_{A1} and ρ_{A2} are correlation factors with the true channels, and $\boldsymbol{\epsilon}_k$ is the error associated to the channel estimation process. This error $\boldsymbol{\epsilon}_k$ is characterized as a complex variable with Gaussian distribution and variance $2\sigma_N^2/\beta$, where σ_N^2 is the noise variance for a specific SNR value and β is a scaling factor. For $\beta \to \infty$ and $\rho_{A1} = \rho_{A2} = 1$, there is a perfect channel estimation, i.e., $\hat{\mathbf{H}}_{k_{AB}} = \mathbf{H}_{k_{A1}}$ and $\hat{\mathbf{H}}_{k_{AC}} = \mathbf{H}_{k_{A2}}$. The SVD of the channel estimates is defined as

$$\hat{\mathbf{H}}_{k_{A1}} = \hat{\mathbf{U}}_{k_{A1}}\hat{\boldsymbol{\Lambda}}_{k_{A1}}\mathbf{V}^H_{k_{A1}}, \tag{3.15}$$

and

$$\hat{\mathbf{H}}_{k_{A2}} = \hat{\mathbf{U}}_{k_{A2}}\hat{\boldsymbol{\Lambda}}_{k_{A2}}\hat{\mathbf{V}}^H_{k_{A2}}. \tag{3.16}$$

Using the result of SVD, the transmitter performs the precoding operation defined as

$$\mathbf{X}_k = \hat{\mathbf{V}}_{k_A1}\mathbf{S}'_{k_B} + \sqrt{\alpha}\hat{\mathbf{V}}_{k_A1}\mathbf{S}'_{k_C}, \tag{3.17}$$

where $\mathbf{X}_k$ is the signal to be transmitted, and α is the ratio between the power transmitted meant for user C, and the power transmitted meant for user B. Since the precoding operation only utilises the channel estimate of the close user, additional information must be sent to allow the far user to complete the SVD process. The transmitter sends a partial key $\mathbf{Q}_k$ which is defined as

$$\mathbf{Q}_k = \mathbf{V}^H_{k_A1}\mathbf{V}_{k_A2}. \tag{3.18}$$

Since $\mathbf{Q}_k$ is a unitary matrix, then for the case of a system with $T = R = 2$, this matrix can be written as

$$\mathbf{Q}_k = \begin{bmatrix} a & b \\ -b^* \exp(j\phi) & a^* \exp(j\phi) \end{bmatrix}, \tag{3.19}$$

where a and b are complex coefficients such that $|a|^2 + |b|^2 = 1$, and the determinant of this matrix is given by

$$\det(\mathbf{Q}_k) = \exp(j\phi). \tag{3.20}$$

Under this decomposition, the transmitter must send four parameters that allow for the reconstruction of the original matrix. These parameters are $|a|$, $2(a)$, $2(b)$ and $\det(\mathbf{Q}_k)$, which are all real-valued quantities that can be quantized with a low resolution, so as to reduce the overhead associated to the transmission of the partial key.

3.2.2.2 Reception

The received signal at user B is

$$\mathbf{Z}_{k_B} = \mathbf{H}_{k_{AB}} \mathbf{X}_k + \mathbf{N}_k, \tag{3.21}$$

while the received signal at user C is given by

$$\mathbf{Z}_{k_C} = \mathbf{H}_{k_{AC}} \mathbf{X}_k + \mathbf{N}_k. \tag{3.22}$$

Before decoding the symbols, both receivers employ IB-DFE with soft decisions. However, it should be noted that this scheme must be slightly changed for the power-domain NOMA scenario, mainly due to the SIC and partial key requirements at each receiver.

3.2.2.3 Receiver B

As described earlier, user B also computes a channel estimation, with the training sequence transmitted by A. The channel can be expressed as

$$\mathbf{H}_{k_{AB}} = \rho_B \hat{\mathbf{H}}_{k_B} + \boldsymbol{\epsilon}_k, \tag{3.23}$$

where ρ_B is a correlation factor with the true channel. It is not unreasonable to assume that there is a high correlation between the estimate of the receiver B and the transmitter, therefore, it can be considered that $\rho_{A1} = \rho_B \approx 1$. For simplicity, it is also assumed that the error distribution of the channel estimate is the same for both A and B, though the generalization to other cases is straightforward. The SVD of the channel estimate at user B is written as

$$\hat{\mathbf{H}}_{k_B} = \hat{\mathbf{U}}_{k_B} \hat{\mathbf{\Lambda}}_{k_B} \hat{\mathbf{V}}_{k_B}^H, \tag{3.24}$$

with $\hat{\mathbf{U}}_{k_B}$, $\hat{\mathbf{\Lambda}}_{k_B}$ and $\mathbf{V}_{k_B}^H$ being the corresponding estimates of the matrices defined in (2.79). As in conventional SVD techniques, the decoding is performed by multiplying the signal by the decoding matrix $\mathbf{U}_{k_B}$, which is computed as

$$\mathbf{W}'_{k_B} = \hat{\mathbf{U}}_{k_B}^H \mathbf{Z}_{k_B}, \tag{3.25}$$

where $\mathbf{W}'_{k_B}$ is a $C \times 1$ column vector with the interleaved, decoded symbols. This operation can be expanded as

$$\begin{aligned} \mathbf{W}'_{k_B} &= \hat{\mathbf{U}}_{k_B}^H \mathbf{H}_{k_{AB}} \mathbf{X}_k + \hat{\mathbf{U}}_{k_B}^H \mathbf{N}_k \\ &= \hat{\mathbf{U}}_{k_B}^H \mathbf{H}_{k_{AB}} \mathbf{V}_{k_{A1}} (\mathbf{S}'_{k_B} + \sqrt{\alpha}\mathbf{S}'_{k_C}) + \hat{\mathbf{U}}_{k_B}^H \mathbf{N}_k \\ &= \hat{\mathbf{\Lambda}}_{k_{AB}} (\mathbf{S}'_{k_B} + \sqrt{\alpha}\mathbf{S}'_{k_C}) + \hat{\mathbf{U}}_{k_B}^H \mathbf{N}_k, \end{aligned} \tag{3.26}$$

with $\hat{\mathbf{\Lambda}}_{k_{AB}}$ corresponding to an estimate of the diagonal matrix composed by the singular values of the channel. Before performing equalization, however, the receiver must perform deinterleaving, to restore the original symbol order, yielding

$$\mathbf{W}_{k_B} = \hat{\mathbf{\Lambda}}'_{k_{AB}} (\mathbf{S}_{k_B} + \sqrt{\alpha}\mathbf{S}_{k_C}) + \hat{\mathbf{U}}'^H_{k_B} \mathbf{N}'_k. \tag{3.27}$$

Before user B can detect its intended symbols, it must perform the SIC reception on the symbols intended for user C. In order to do so, it first performs detection on the stronger signal, which has a much higher SNR) than the wanted signal, making the detection simple. The equalized signal is obtained by computing

$$\tilde{\mathbf{S}}_{k_C} = \mathbf{F}_{k_{B1}} \mathbf{W}_{k_B}, \tag{3.28}$$

where the equalization factor $\mathbf{F}_{k_{B1}}$ is defined according to MMSE criterion as

$$\mathbf{F}_{k_{B1}} = \frac{\hat{\mathbf{\Lambda}}'_{k_B}}{\hat{\mathbf{\Lambda}}'^2_{k_B} + \frac{1}{\sqrt{\alpha}\mathrm{SNR}}}. \tag{3.29}$$

Subsequently, the receiver computes the hard decisions $\hat{\mathbf{S}}_{k_C}$ of the symbols meant for user C, which consists in determining the closest constellation points to the received sample.Using this estimate, the receiver can perform detection on the intended symbols.

3.2.2.4 Iterative Equalization

To minimise the ISI, the receiver employs an iterative frequency domain equalization scheme based on the IB-DFE and MMSE criterion, which performs both feedforward and feedback equalization at a subcarrier level. This equalization process can be repeated up to L times, which was fixed at $L = 4$ for this scenario. The equalized symbols at the kth subcarrier and lth iteration are computed by

$$\tilde{\mathbf{S}}_{k_B}^{(l)} = \mathbf{F}_{k_{B2}}^{(l)} \left(\mathbf{W}_{k_B} - \sqrt{\alpha} \hat{\mathbf{\Lambda}}_{k_B}^{'} \hat{\mathbf{S}}_{k_C} \right) - \mathbf{B}_{k_{B2}}^{(l)} \bar{\mathbf{S}}_{k_B}^{(l-1)}, \tag{3.30}$$

where $\mathbf{F}_{k_{B2}}^{(l)}$ is the feedforward factor, $\mathbf{B}_{k_{B2}}^{(l)}$ is the feedback factor, and $\bar{\mathbf{S}}_{k_B}^{(l-1)}$ are the soft-decided symbols of the previous iteration (for $l = 1$ this is simply a null vector). The feedforward factor matrix is defined as

$$\mathbf{F}_{k_{B2}}^{(l)} = \frac{\hat{\mathbf{\Lambda}}_{k_B}^{'}}{\left(1 - \left|\rho^{(l-1)}\right|^2\right) \hat{\mathbf{\Lambda}}_{k_B}^{'2} + \frac{1}{\mathrm{SNR}}}, \tag{3.31}$$

where $\rho^{(l-1)}$ denotes the block-wise reliability associated to the data estimated in the $(l-1)$th iteration (for $l = 1$, $\rho^{(0)} = 0$). The feedback factor matrix, on the other hand, is defined as

$$\mathbf{B}_{k_B}^{(l)} = \mathbf{F}_{k_{B2}}^{(l)} \hat{\mathbf{\Lambda}}_{k_B}^{'} - \mathbf{I}. \tag{3.32}$$

3.2.2.5 Receiver C

The detection at user C is significantly different from the detection scheme employed in [9]. This is explained by the modifications required for the interleaving scheme and by the use of a partial key. As described earlier, user C also computes a channel estimation, with the training sequence transmitted by A. The frequency-domain channel response is expressed as

$$\mathbf{H}_{k_{AC}} = \rho_C \hat{\mathbf{H}}_{k_C} + \boldsymbol{\epsilon}_k. \tag{3.33}$$

where ρ_C is a correlation factor with the true channel. It is not unreasonable to assume that there is a high correlation between the estimate of the receiver C and the transmitter, therefore, it is considered that $\rho_{A2} = \rho_C \approx 1$. For simplicity, it is assumed that the error distribution of the channel estimate is the same for both A and C, though the generalization to other cases is straightforward. The SVD of the channel estimate at user C is written as

$$\hat{\mathbf{H}}_{k_C} = \hat{\mathbf{U}}_{k_C} \hat{\mathbf{\Lambda}}_{k_C} \hat{\mathbf{V}}_{k_C}^H, \tag{3.34}$$

with $\hat{\mathbf{U}}_{k_C}$, $\hat{\mathbf{\Lambda}}_{k_C}$ and $\hat{\mathbf{V}}_{k_C}^H$ being the corresponding estimates of the matrices defined in (4.6). As in conventional SVD techniques, the decoding is performed by multiplying the signal by the decoding matrix $\hat{\mathbf{U}}_{k_C}$, which is computed as

$$\mathbf{W}'_{k_C} = \hat{\mathbf{U}}_{k_C}^H \mathbf{Z}_{k_C}, \tag{3.35}$$

where $\mathbf{W}'_{k_C}$ is a $C \times 1$ column vector with the interleaved, decoded symbols. This operation can be expanded as

$$\begin{aligned}\mathbf{W}'_{k_C} &= \hat{\mathbf{U}}^H_{k_B}\mathbf{H}_{k_{AC}}\mathbf{X}_k + \hat{\mathbf{U}}^H_{k_C}\mathbf{N}_k \\ &= \hat{\mathbf{U}}^H_{k_C}\mathbf{H}_{k_{AC}}\mathbf{V}_{k_{A1}}(\mathbf{S}'_{k_B} + \sqrt{\alpha}\mathbf{S}'_{k_C}) + \hat{\mathbf{U}}^H_{k_C}\mathbf{N}_k \\ &= \hat{\mathbf{\Lambda}}_{k_{AC}}\mathbf{V}^H_{k_C}\mathbf{V}_{k_{A1}}(\mathbf{S}'_{k_B} + \sqrt{\alpha}\mathbf{S}'_{k_C}) + \hat{\mathbf{U}}^H_{k_C}\mathbf{N}_k,\end{aligned} \tag{3.36}$$

with $\hat{\mathbf{\Lambda}}_{k_{AC}}$ corresponding to an estimate of the diagonal matrix composed by the singular values of the channel. The received signal is then deinterleaved, so as to split the singular values amongst the streams, yielding

$$\mathbf{W}_{k_C} = \hat{\mathbf{\Lambda}}'_{k_{AC}}\mathbf{V}'^H_{k_C}\mathbf{V}'_{k_{A1}}(\mathbf{S}_{k_B} + \sqrt{\alpha}\mathbf{S}_{k_C}) + \hat{\mathbf{U}}'^H_{k_C}\mathbf{N}'_k. \tag{3.37}$$

As was the case with receiver B, this receiver performs the same iterative equalization, with the exception that it does not need to perform an initial first detection. The equalization is defined as

$$\mathbf{Y}^{(l)}_{k_C} = \mathbf{F}^{(l)}_{k_C}\mathbf{W}_{k_C} - \mathbf{B}^{(l)}_{k_C}\bar{\mathbf{Y}}^{(l-1)}_{k_C}, \tag{3.38}$$

where $\mathbf{Y}^{(l)}_{k_C}$ is the equalized received signal at the kth subcarrier and lth iteration, and $\bar{\mathbf{Y}}^{(l-1)}_{k_C}$ is the equalized signal estimate of the previous iteration (for $l = 1$ it is set to 0). However, unlike receiver B, this receiver cannot complete the SVD on its own. Therefore, it makes use of the partial key $\hat{\mathbf{Q}}_k$, which is computed from the received parameters as

$$\mathbf{Q}_k = \begin{bmatrix} \tilde{a}\exp j\tilde{\phi}_a & \tilde{b}\exp j\tilde{\phi}_b \\ -\tilde{b}\exp j(\tilde{\phi}-\tilde{\phi}_b) & \tilde{a}\exp j(\tilde{\phi}-\tilde{\phi}_a)\end{bmatrix}, \tag{3.39}$$

where $\tilde{a}$,$\tilde{\phi}_a$, $\tilde{\phi}_b$ and $\tilde{\phi}$ are the finite resolution quantized values transmitted by A, and $\tilde{b}$ is obtained from $\tilde{b} = \sqrt{1-\tilde{a}^2}$. Prior to applying the partial key, the equalized signal is interleaved, in order to match the SVD matrices. The equalized symbols estimates are expressed as

$$\tilde{\mathbf{S}}'^{(l)}_{k_C} = \mathbf{Q}_k\mathbf{Y}'^{(l)}_{k_C}, \tag{3.40}$$

which are then deinterleaved into the equalized symbol estimates $\tilde{\mathbf{S}}^{(l)}_{k_C}$.

3.2.2.6 Simulation Results

For these result, the frequency-selective channel is characterized by 16 multipath rays with uncorrelated Rayleigh fading. This analysis focuses on the achievable secrecy rate for various levels and sources of channel errors and different system considerations as well as on the BER of users B and C. Unless otherwise mentioned, the power ratio α is set to 18 dB. Fig. 3.12 shows the BER of the proposed NOMA scheme considering an 8×8 MIMO system with perfect CSI.

From the figure, it can be seen that user C requires an E_b/N_0 about 18 dB lower than user B in order to achieve the same BER in the first iteration, which corresponds to the

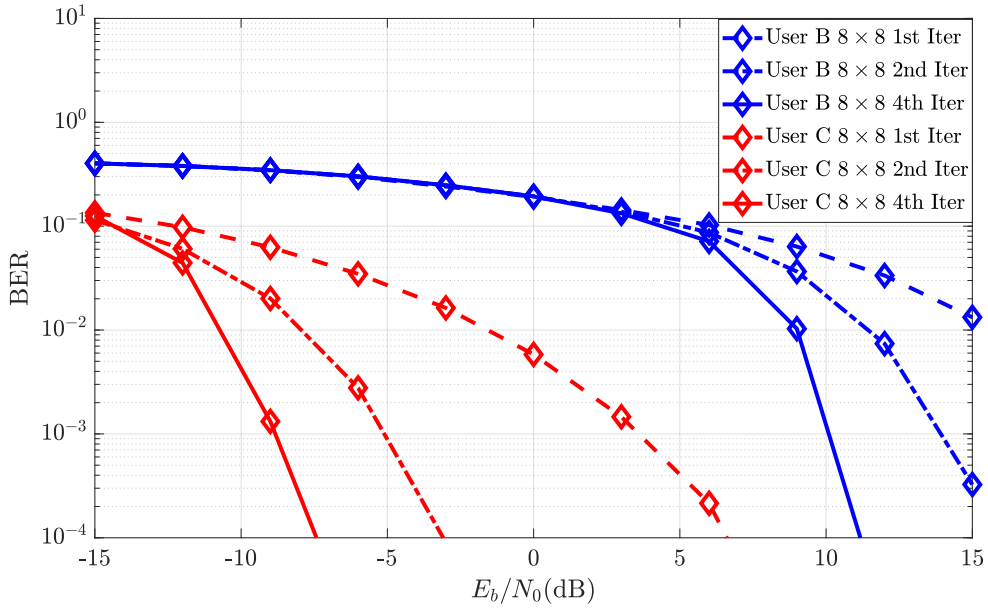

Figure 3.12: BER of both legitimate users for an 8×8 system.

gain due to the higher transmit power. As mentioned before, the partial key $\mathbf{Q}_k$ must be quantized using a finite resolution, before being transmitted. Fig. 3.13 shows the achievable BER results for a 2×2 system at user C for different quantization resolutions.

From the figure, it can be seen that this system requires at least 5 bits of quantization to reach a target BER of 10^{-4}. Since the matrix $\mathbf{Q}_k$ can be reconstructed based on 4 parameters, then the total overhead associated to the transmission of the partial key has a length of 20 bits.

3.3 Nonlinear Receivers for Multi-Carrier Schemes

As was discussed in the previous chapter, certain hardware impairments such as the amplifiers can introduce nonlinear effects in the transmitted signal. This leads to a degradation of the communication, and in the limit can make it impossible to use large constellations. In this section it is shown that it is possible to construct receivers that are aware of these nonlinear effects, and use that information to cope with the distortion and improve performance.

3.3.1 Generalized Approximate Message Passing

GAMP is a well known algorithm for estimating linearly transformed vectors from random observations [109], in a scenario referred to as the Generalized Linear Model (GLM). In this model, an input vector $\mathbf{q}$ is submitted through a Gaussian input channel, resulting in

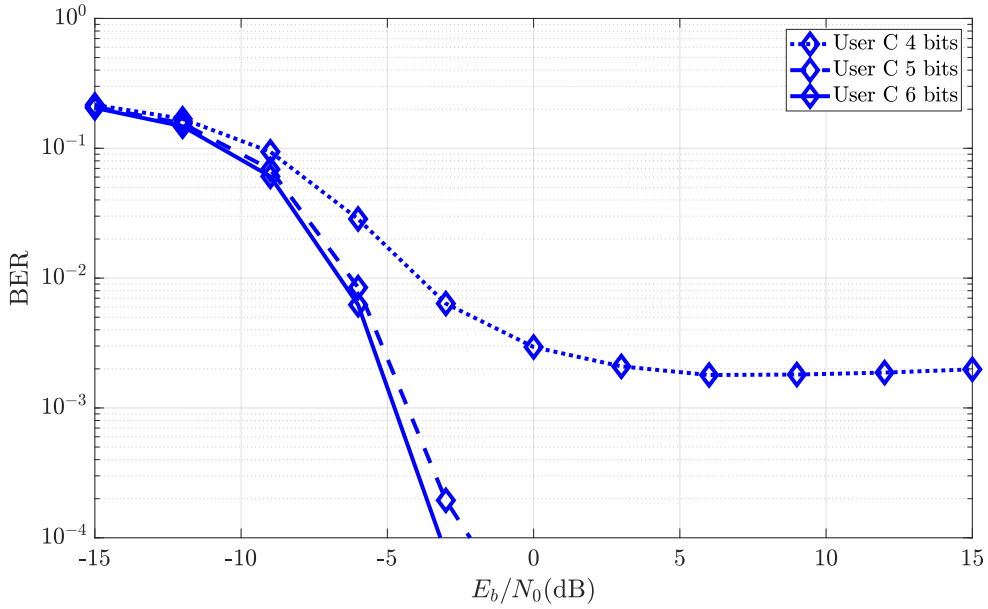

Figure 3.13: BER of a 2×2 system at user C, considering 4 IB-DFE iterations and different resolutions for quantization of the partial key $\mathbf{Q}_k$.

an output vector $\mathbf{x}$. This vector is then linearly transformed into $\mathbf{z}$ by

$$\mathbf{z} = \mathbf{A}\mathbf{x}, \tag{3.41}$$

where $\mathbf{A}$ is a known linear transform matrix. Lastly, $\mathbf{z}$ is submitted through a Gaussian output channel, resulting in the observation vector $\mathbf{y}$. Fig. 3.14 shows a block diagram that represents the GLM.

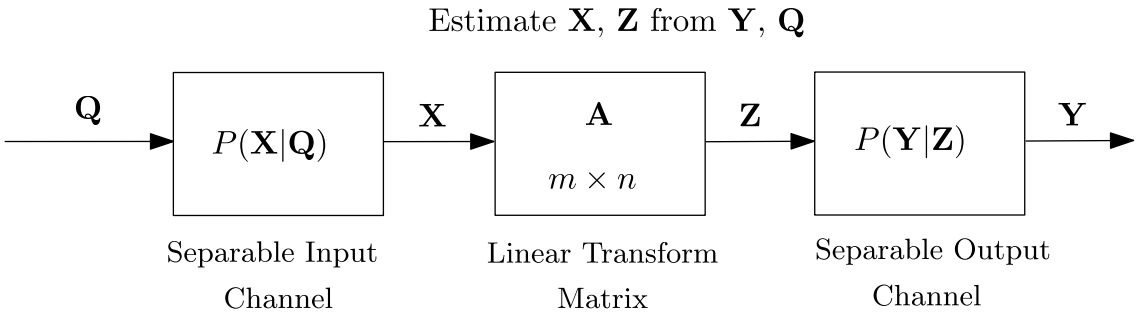

Figure 3.14: Block diagram of the GLM.

The goal of GAMP is to estimate the vectors $\mathbf{x}$ and $\mathbf{z}$, given the input and output vectors $\mathbf{q}$ and $\mathbf{y}$. If all elements of $\mathbf{x}$ follow the same distribution, then $\mathbf{q}$ can be replaced by a constant distribution in the algorithm.

The author of [110] proposed an adapted version of this algorithm for decoding a nonlinearly distorted signal, i.e., a nonlinear output channel. In the proposed system, a

frequency-domain signal is converted to the time-domain and nonlinearly distorted. It is then sent through a noisy channel to a receiver that knows the nonlinear function and CIR. In this particular case, the signal is considered to be real-valued in order to simplify calculations, and is characterized by NO_s samples, where O_s is an oversampling factor. Fig. 3.15 shows a block diagram of the nonlinearly distorted GLM.

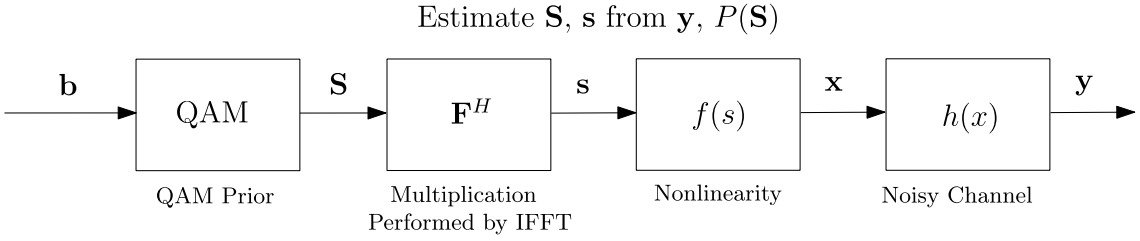

Figure 3.15: Block diagram of the nonlinearly distorted GLM.

In [111], a complex signal is considered, which significantly increases the complexity of the GAMP decoder. The decoder takes in the equalized time-domain signal $\mathbf{y}^{nl}$ and requires that the receiver knows the nonlinear function f, as well as the noise variance $2\sigma_N^2$. Since this is an iterative process, the output of the ith iteration shall be the symbol estimates $\hat{X}_k(i)$. The steps of each iteration are described in Algorithm 1. In step 1), the vectors requiring information from the previous iteration are initialized. Step 2) computes the matrix transform of the previous iteration's input signal estimate, which in this case can be implemented using the IFFT. Next, step 3) estimates the output signal using the nonlinear output function g_{out}. At step 4), the output signal estimate is matrix transformed, which once again may be implemented using the FFT. Lastly, step 5) estimates the input signal of the system using the nonlinear function g_{in}.

From this point on, the iteration indices from GAMP variables are omitted to simplify the notation. For MMSE estimation, the input nonlinear function g_{in} and its derivative g'_{in} are defined as [112]

$$g_{in}(\hat{V}_k, \mu^V) := \mathrm{E}[X_k|\hat{V}_k], \tag{3.42}$$

and

$$-\mu^V \frac{\partial}{\partial \hat{V}_k} g_{in} := \mathrm{var}[X_k|\hat{V}_k]. \tag{3.43}$$

The expectation for the M-QAM can be calculated by

$$\mathrm{E}[X_k|\hat{V}_k] = \sum_{i=0}^{M-1} D_i P(D_i|\hat{V}_k, \mu^V), \tag{3.44}$$

where D_i is the ith symbol of the constellation, and $P(D_i|\hat{V}_k\mu^V)$ is the likelihood of that symbol, defined as

$$P(D_i|\hat{V}_k, \mu^V) = \frac{\exp\left(-\frac{|D_i-\hat{V}_k|^2}{2\mu^V}\right)}{\sum_{j=0}^{M-1}\exp\left(-\frac{|D_j-\hat{V}_k|^2}{2\mu^V}\right)}. \tag{3.45}$$

Algorithm 1 GAMP Decoder

Given a nonlinearly distorted received signal in the time domain, $\mathbf{y}$, estimate the input vector $\mathbf{x}$.

1) Initialization

$$i = 1, \hat{\mathbf{x}}(1) = \mathbf{0}_{NO_s,1}, \hat{\mathbf{s}}(0) = \mathbf{0}_{NO_s,1}, \mu^X(1) = \mathbf{1}_{NO_s,1}$$

2) Output linear step

$$\mu^p(i) = \frac{1}{NO_s} \sum_{k=0}^{NO_s-1} \mu_k^X(i), \forall n$$

$$\hat{p}_n(i) = \sum_{k=0}^{NO_s-1} \left(F_{n,k}^H \hat{X}_k(i) \right) - \mu^p(i) \hat{s}_n(i-1), \forall n$$

3) Output nonlinear step

$$\hat{s}_n(i) = \left(1-\beta\right) \hat{s}_n(i-1) + \beta g_{out}(\hat{p}_n(i), \mu^p(i), y_n), \forall n$$

$$\mu_n^s(i) = \left(1-\beta\right) \mu_n^s(i-1) - \beta \frac{\partial}{\partial \hat{p}_n} g_{out}(\hat{p}_n(i), \mu^p(i), y_n), \forall n$$

4) Input linear step

$$\tilde{X}_k(i) = (1-\beta)\tilde{X}_k(i-1) + \beta \hat{X}_k(i), \forall k$$

$$\mu^V(i) = \left(\frac{1}{NO_s} \sum_{k=0}^{NO_s-1} \mu_n^s(i) \right)^{-1}, \forall k$$

$$V_k(i) = \tilde{X}_k(i) + \mu^v(i) \sum_{k=0}^{NO_s-1} F_{n,k} \hat{s}_k(i), \forall k$$

5) Input nonlinear step

$$\hat{X}_k(i+1) = g_{in}(\hat{V}_k(i), \mu^V(i)), \forall k$$

$$\mu_k^X(i+1) = -\mu^V(i) \frac{\partial}{\partial \hat{V}_k} g_{in}(\hat{V}_k(i), \mu^V(i)), \forall k$$

The variance of the distribution is calculated as

$$\mathrm{var}[X_k|\hat{V}_k] = \sum_{i=0}^{M-1}(D_i - \mathrm{E}[X_k|\hat{V}_k])^2 P(D_i|\hat{V}_k, \mu^V). \tag{3.46}$$

For $O_s > 1$, the unused subcarriers are set as $\hat{X}_k = 0$ and $\mu_k^X = 1$, for $O_s N > k > N$. The output nonlinear function g_{out} can be defined as

$$g_{out}(\hat{p}, \mu_n^p, y_n) = \frac{\hat{z}_0 - \hat{p}_n}{\mu^p}, z_0 := \mathrm{E}[z_n|\hat{p}_n, y_n, \mu^p]. \tag{3.47}$$

For a generic nonlinear function, the expectation can only be computed through complex numerical integration. The expectation is calculated as

$$\mathrm{E}[z_n|\hat{p}, y, \mu^p] = \frac{1}{C_n}\int_{-\infty}^{\infty} x \exp\left(-\frac{|y_n - f(x)|^2}{2\sigma_N^2} - \frac{|\hat{p}_n - x|^2}{2\mu_p}\right)\mathrm{d}x, \tag{3.48}$$

where C_n is the normalizing factor defined as

$$C_n = \int_{-\infty}^{\infty} \exp\left(-\frac{|y_n - f(x)|^2}{2\sigma_N^2} - \frac{|\hat{p}_n - x|^2}{2\mu_p}\right)\mathrm{d}x. \tag{3.49}$$

The partial derivative of g_{out} is defined as

$$-\frac{\partial}{\partial \hat{p}_n} g_{out}(\hat{p}_n, \mu^p, y_n) = \frac{1}{\mu^p}\left(1 - \frac{\mathrm{var}[z|\hat{p}, y_n, \mu^p]}{\mu^p}\right), \tag{3.50}$$

where the $\mathrm{var}[z|\hat{p}, y_n, \mu^p]$ variance is defined as

$$\begin{aligned}\mathrm{var}[z_n|\hat{p}_n, y_n, \mu^p] =& \frac{1}{C_n}\int_{-\infty}^{\infty} |x|^2 \exp\left(-\frac{|y_n - f(x)|^2}{2\sigma_N^2} - \frac{|\hat{p} - x|^2}{2\mu_p}\right)\mathrm{d}x \\ &- |\mathrm{E}[z_n|\hat{p}_n, y_n, \mu^p]|^2.\end{aligned} \tag{3.51}$$

However, if the nonlinearity is applied separately to the in-phase and quadrature components, then it is possible to divide the complex-valued double integral into two real-valued, single integrals. Under these conditions, the real component is calculated as

$$\mathrm{Re}\left(\mathrm{E}[z_n|\hat{p}_n, y_n, \mu^p]\right) = \frac{1}{C_n^R}\int_{-\infty}^{\infty} x \exp\left(-\frac{|\mathrm{Re}\,(y) - f(x)|^2}{2\sigma_N^2} - \frac{|\mathrm{Re}\,(\hat{p}_n) - x|^2}{2\mu_p}\right)\mathrm{d}x, \tag{3.52}$$

and the imaginary component as

$$\mathrm{Im}\left(\mathrm{E}[z_n|\hat{p}_n, y_n, \mu^p]\right) = \frac{1}{C_n^I}\int_{-\infty}^{\infty} xj \exp\left(-\frac{|\mathrm{Im}\,(y_n) - f(x)|^2}{2\sigma_N^2} - \frac{|\mathrm{Im}\,(\hat{p}_n) - x|^2}{2\mu_p}\right)\mathrm{d}x, \tag{3.53}$$

where C^R and C^I are normalization constants defined as

$$C_n^R = \int_{-\infty}^{\infty} \exp\left(-\frac{|\mathrm{Re}\,(y_n) - f(x)|^2}{2\sigma_N^2} - \frac{|\mathrm{Re}\,(\hat{p}_n) - x|^2}{2\mu_p}\right)\mathrm{d}x, \tag{3.54}$$

and

$$C_n^I = \int_{-\infty}^{\infty} \exp\left(-\frac{|\mathrm{Im}\,(y_n) - f(x)|^2}{2\sigma_N^2} - \frac{|\mathrm{Im}\,(\hat{p}_n) - x|^2}{2\mu_p}\right) \mathrm{d}x. \tag{3.55}$$

The variance is calculated as

$$\begin{aligned} \mathrm{var}[z|\hat{p}, y_n, \mu^p] = {} & \frac{1}{C_n^R} \int_{-\infty}^{\infty} |x|^2 \exp\left(-\frac{|\mathrm{Re}\,(y_n) - f(x)|^2}{2\sigma_N^2} - \frac{|\mathrm{Re}\,(\hat{p}) - x|^2}{2\mu_p}\right) \mathrm{d}x \\ & + \frac{1}{C_n^I} \int_{-\infty}^{\infty} |x|^2 \exp\left(-\frac{|\mathrm{Im}\,(y_n) - f(x)|^2}{2\sigma_N^2} - \frac{|\mathrm{Im}\,(\hat{p}) - x|^2}{2\mu_p}\right) \mathrm{d}x \\ & - |\mathrm{E}[z|\hat{p}, y_n, \mu^p]|^2. \end{aligned} \tag{3.56}$$

The integration variable lies in the range $[-A_x, A_x]$, with N_x points in between, for a total N_x^2 operations for polar nonlinearities, and a significantly lower value of $2N_x$ operations for nonlinearities that are independent between I and Q branches.

The algorithm will run $I_{\max}$ iterations, as it has no stopping condition. It is possible to include a Cyclic Redundancy Check (CRC) code in the OFDM symbol to function as a stopping condition, as well as correct leftover 1 bit errors. Another metric is to use the distance between the received signal and the estimation, expressed as

$$E(i) = \sum_{n=0}^{NO_s-1} y_n^{nl} - f\left(\sum_{k=0}^{NO_s-1} F_{n,k}^H \hat{X}_k(i)\right). \tag{3.57}$$

The $\mathbf{X}(i)$ with the lowest $E(i)$, or that passes the CRC check, is chosen as the best vector.

This algorithm can achieve promising performance, even exceeding the performance of ideal receivers [110]. Fig. 3.16 shows a BER comparison of the GAMP receiver with $N = 1024$ subcarriers averaged over 100 blocks. From the figure, it is clear that the GAMP receiver can achieve a target BER of 10^{-4} at an E_b/N_0 that is 3 dB lower than the linear transmitter system. This comes at a much higher complexity cost and requires a higher sampling rate ($O_s = 4$) at the receiver, not to mention the out-of-band radiation associated with the transmitted nonlinearly distorted signal. By comparing different integration resolutions, it is clear that increasing N_x brings an improvement to performance. In fact, for $N_x = 64$, the BER curve suffers a change in slope at 6 dB of E_b/N_0, which is resolved by increasing N_x.

Fig. 3.17 shows the BER results for 256-QAM. For larger constellations, higher values of N_x are required. As can be seen in the figure, the performance gain over the linear transmitter is much lower than the QPSK system. This can be attributed in part to a comparatively low value of N_x, which has a more noticeable impact on higher constellations. It also depends on the selected saturation level, which was not chosen as the optimum value. As previously mentioned, increasing N_x lowers the BER slope transition that occurs at 20 dB of E_b/N_0.

Fig. 3.18 shows the BER for a system using an IQ clipping nonlinearity at the transmitter. Considering an oversampling of $O_s = 4$, the performance is similar to the one in Fig.

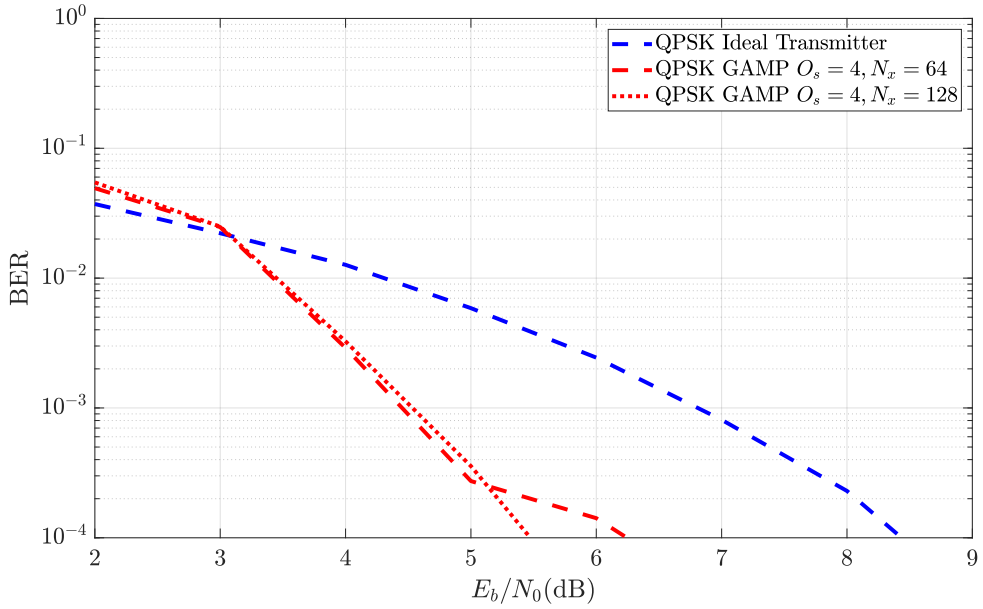

Figure 3.16: BER for the QPSK GAMP receiver with varying integral resolutions, using an SSPA nonlinearity with $q_{\text{sspa}} = 1, s_{\text{sat}}/\sigma_s = 0.42$.

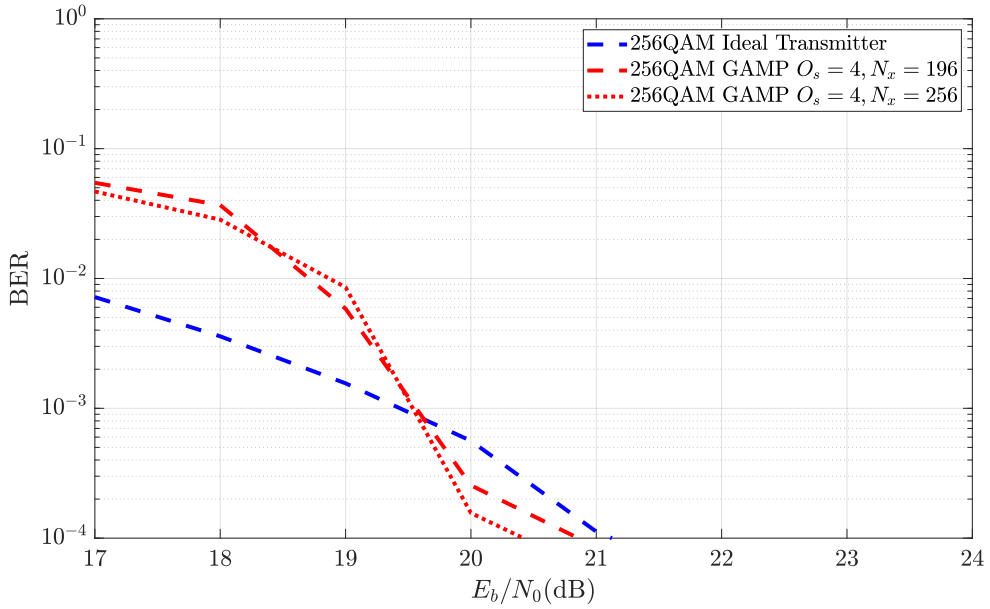

Figure 3.17: BER for the 256-QAM GAMP receiver, using an SSPA nonlinearity with $q_{\text{sspa}} = 1, s_{\text{sat}}/\sigma_s = 0.57$.

3.16, though this implementation has significantly less per iteration complexity. Even when considering no oversampling, performance is still superior compared to an ideal

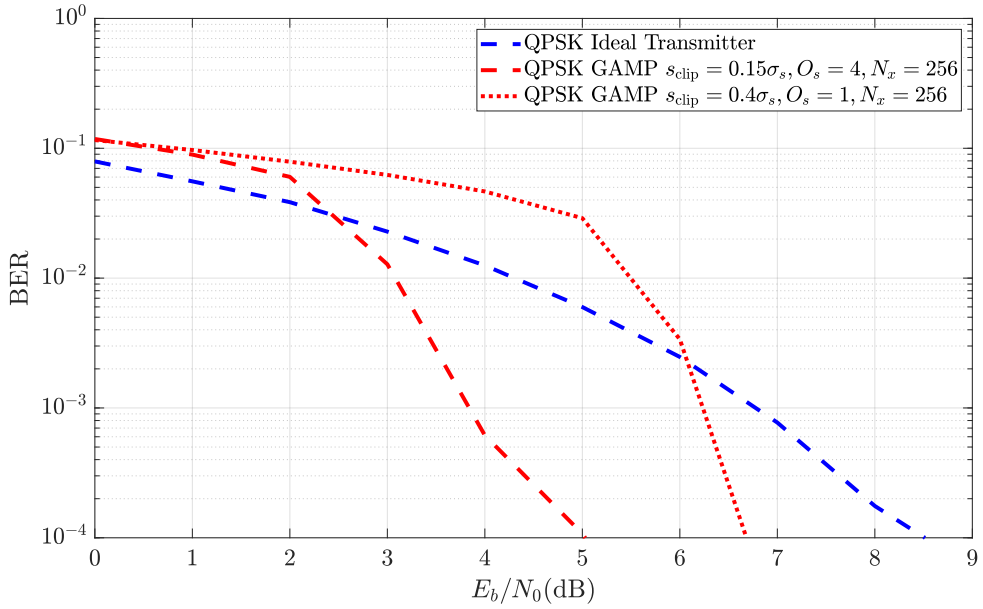

Figure 3.18: BER for the QPSK GAMP receiver with an IQ clipping nonlinearity.

transmitter. It should be noted that this type of nonlinearity can be implemented digitally, and has no OOB radiation, assuming it is linearly amplified.

For GAMP receivers, the OOB radiations due to the nonlinearity are used to improve detection, however, this means that the transmitted signal exceeds its allocated bandwidth. It is therefore important to characterize the performance of GAMP when the OOB radiation is filtered at the transmitter, resulting in a distorted signal fully contained within the original bandwidth. In this case a clipping IQ nonlinearity with oversampling can be used to obtain a distorted signal with OOB radiation. Fig. 3.19 presents the BER for ideal and filtered scenarios. In the figure, there is a clear degradation in performance for the filtered systems. This is due to the time-domain estimation that is performed within GAMP, that cannot take into account the filter's response without adding memory effects. In the filtered system, decreasing the clipping threshold has a negative impact on performance, and GAMP cannot outperform a linear system.

Fig. 3.20 shows the E_b/N_0+PAPR necessary to obtain a BER of 10^{-4}, with various GAMP configurations. This figure shows an important metric that further highlights the potential benefits of using GAMP. For QPSK, it can be seen that the performance of the unfiltered system is proportional to the strength of the nonlinearity, however, filtering the OOB radiation limits the level of distortion that is beneficial for performance at about 2 dB of PAPR. For 16-QAM, if there is no filtering there is an optimum PAPR of 1.4 dB. Removing the OOB radiation increase the optimum PAPR to 3 dB, reducing the possible energy efficiency gains.

Fig. 3.21 shows a BER comparison of the BNC and GAMP receivers with a nonlinear

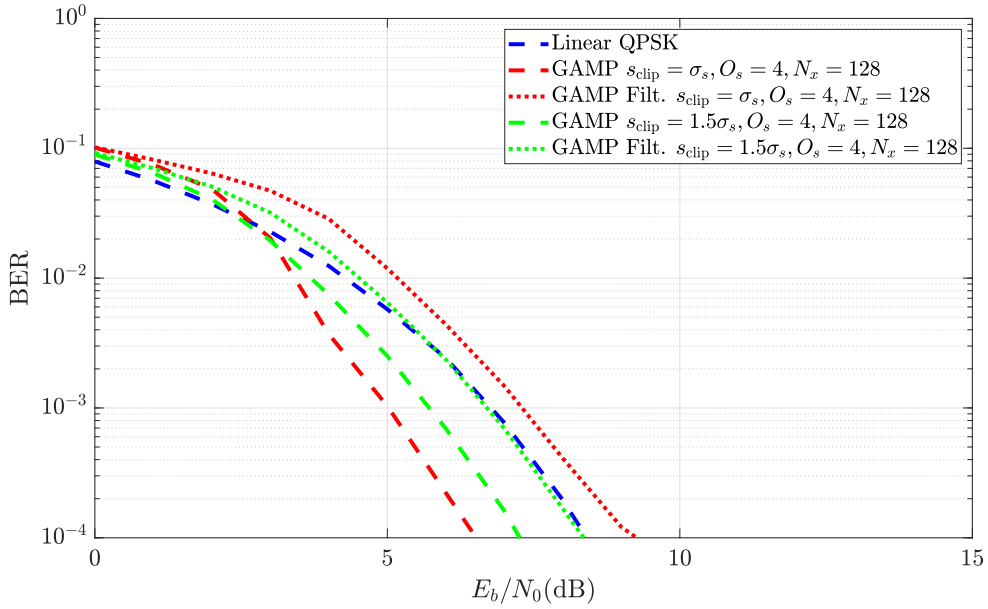

Figure 3.19: BER for the QPSK GAMP receiver with an IQ clipping nonlinearity and filtered bandwidth.

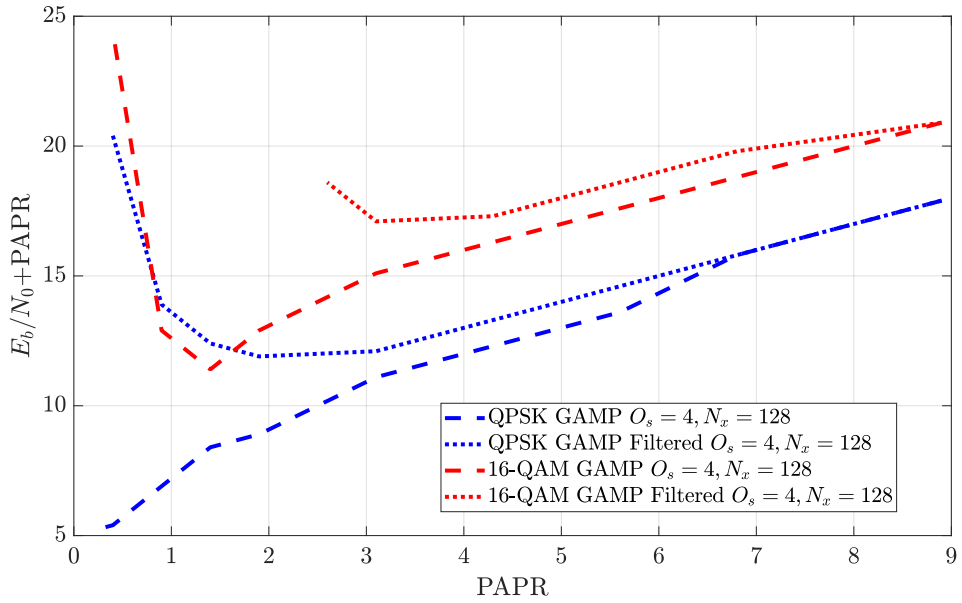

Figure 3.20: E_b/N_0+PAPR necessary to achieve a target BER of 10^{-4} with GAMP.

SSPA that results in a SIR of 25 dB, with $N = 512$, averaged over 50 OFDM blocks. The GAMP receiver has the following parameters $\beta = 0.5, O_s = 4, N_x = 256$. For this particular nonlinearity, the BNC receiver cannot cancel out the distortion with just 2 iterations, requiring at least 4 iterations in order to sufficiently cancel out the distortion, while still

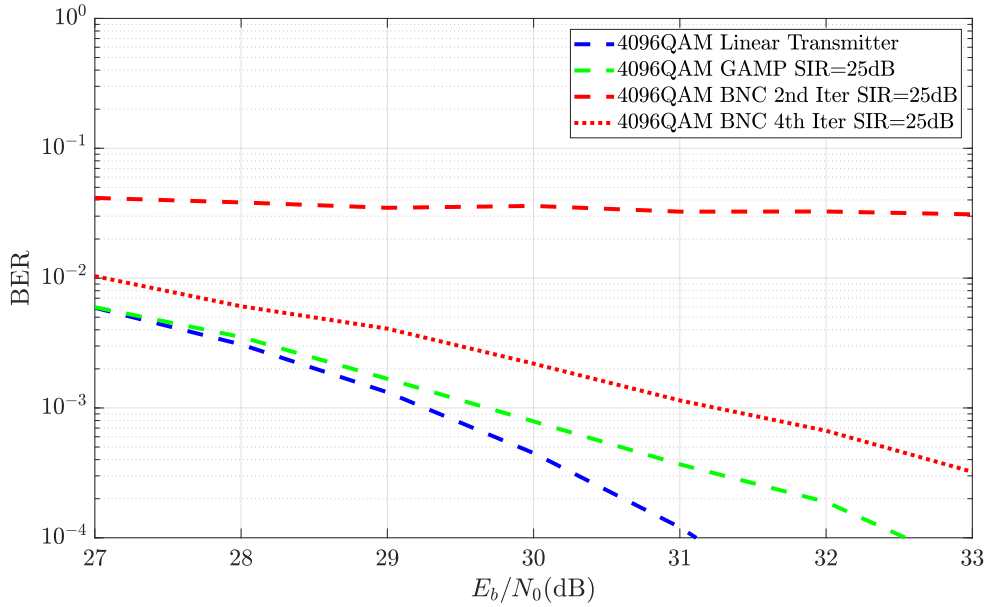

Figure 3.21: BER for 4096-QAM using different receivers, with an SSPA defined by $q_{\text{sspa}} = 1, A_{\text{sat}}/\sigma_s = 4.5$, for an effective SIR of 25 dB.

being significantly worse than the linear transmitter. The GAMP receiver can achieve a better performance, though the nonlinearity is not strong enough to outperform the linear OFDM performance.

Fig. 3.22 shows the BER for the same systems, but considering a stronger nonlinearity with a SIR of 18 dB. In this scenario, the BNC receiver does not cancel out the distortion even after 4 iterations. On the other hand, the GAMP receiver suffers only a small 0.5 dB degradation, which can be explained by the low value of N_x or by the low number of channel realizations.

3.3.2 GTurbo

GTurbo is a novel approach to approximate Bayesian estimation from nonlinear observations that is better suited than Approximate Message Passing (AMP) for orthogonal sensing matrices, like the Fourier matrix [113]. In the literature, it is often used to recover a signal that was submitted to a low resolution ADC [114]. This scheme is employed with a nonlinear operation at the transmitter, which is the same use case as GAMP. Alg. 2 presents the proposed GTurbo iterative algorithm based on [115, 116].

The expectation $\mathbb{E}[z_n|y_n]$ and variance $\mathbb{E}[z_n|y_n]$ are taken with regards to the distribution $P(z_n|y_n)$, which as was shown in GAMP can be defined as

$$\mathrm{E}[z_n|z_{n,A}^{\text{pri}}, y_k, \mu_A^{\text{pri}}] = \frac{1}{C_n}\int_{-\infty}^{\infty} x \exp\left(-\frac{|y_n - f(x)|^2}{2\sigma_N^2} - \frac{|z_{n,A}^{\text{pri}} - x|^2}{\mu_A^{\text{pri}}}\right)\mathrm{d}x, \tag{3.58}$$

Algorithm 2 GTurbo Decoder

Given a nonlinearly distorted received signal in the time domain, $\mathbf{y}$, estimate the input vector $\mathbf{x}$. **Initialization:** $\mathbf{z}_A^{\text{pri}} = \mathbf{0}_{NO_s,1}$, $\mu_A^{\text{pri}} = 1$

Module A

1) A Posteriori mean/variance of z

$$z_{n,A}^{\text{post}} = \mathbb{E}[z_n|y_n], \quad \mu_{n,A}^{\text{post}} = \text{Var}[z_n|y_n]$$

2) Extrinsic mean/variance of x

$$\mathbf{X}_A^{\text{post}} = \mathbf{F}\mathbf{z}_A^{\text{post}}, \quad \mu_A^{\text{post}} = \frac{1}{NO_s}\sum_{n=1}^{N}\mu_{n,A}^{\text{post}}$$

$$\mu_B^{\text{pri}} = \mu_A^{\text{ext}} = \left(\frac{1}{\mu_A^{\text{post}}} - \frac{1}{\mu_A^{\text{pri}}}\right)^{-1}$$

$$\mathbf{X}_B^{\text{pri}} = \mathbf{X}_A^{\text{ext}} = \mu_A^{\text{ext}}\left(\frac{\mathbf{X}_A^{\text{post}}}{\mu_A^{\text{post}}} - \frac{\mathbf{F}\mathbf{z}_A^{\text{pri}}}{\mu_A^{\text{pri}}}\right)$$

Module B

3) A Posteriori mean/variance of s

$$S_{k,B}^{\text{post}} = \mathbb{E}[S_k|X_{k,B}^{\text{pri}}], \quad \mu_{k,B}^{\text{post}} = \text{Var}[S_k|X_{k,B}^{\text{pri}}]$$

4) Extrinsic mean/variance of z

$$X_B^{\text{post}} = S_{k,B}^{\text{post}}, \quad \mu_B^{\text{post}} = \frac{1}{NO_s}\sum_{k=1}^{N}\mu_{k,B}^{\text{post}}$$

$$\mu_A^{\text{pri}} = \mu_B^{\text{ext}} = \left(\frac{1}{\mu_B^{\text{post}}} - \frac{1}{\mu_B^{\text{pri}}}\right)^{-1}$$

$$\mathbf{z}_A^{\text{pri}} = \mathbf{z}_B^{\text{ext}} = \mu_B^{\text{ext}}\left(\frac{\mathbf{F}^H\mathbf{X}_B^{\text{post}}}{\mu_B^{\text{post}}} - \frac{\mathbf{F}^H\mathbf{X}_B^{\text{pri}}}{\mu_B^{\text{pri}}}\right)$$

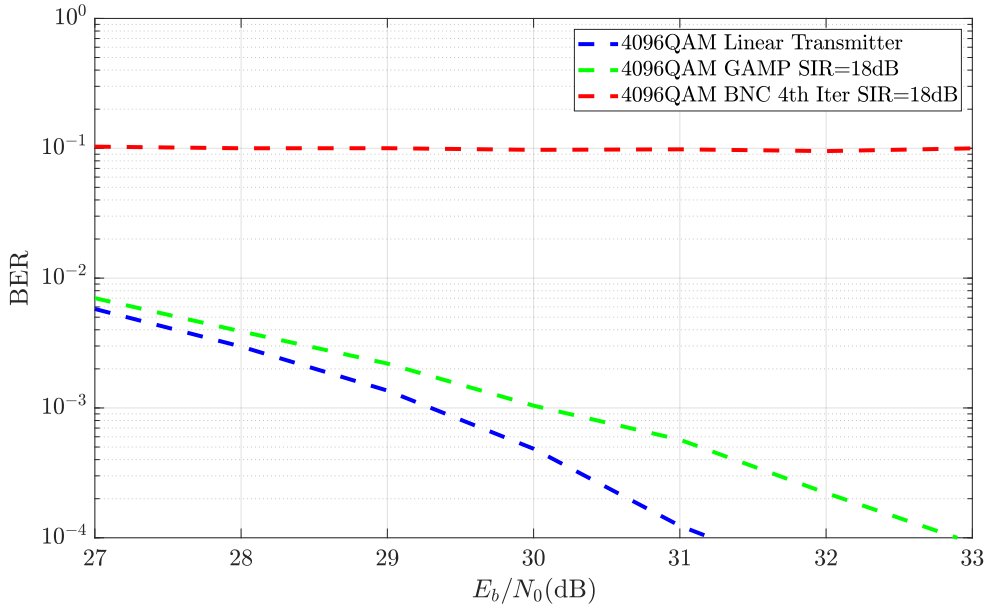

Figure 3.22: BER for 4096-QAM using different receivers, with an SSPA defined by $q_{\text{sspa}} = 1, A_{\text{sat}}/\sigma_s = 2.5$, for an effective SIR of 18 dB.

where C is the normalizing factor given as

$$C_n = \int_{-\infty}^{\infty} \exp\left(-\frac{|y_n - f(x)|^2}{2\sigma_N^2} - \frac{|z_{n,A}^{\text{pri}} - x|^2}{\mu_A^{\text{pri}}}\right) \mathrm{d}x. \tag{3.59}$$

The variance is defined as

$$\begin{aligned}\text{var}[z_n|z_{n,A}^{\text{pri}}, y_n, \mu_A^{\text{pri}}] = &\frac{1}{C_n}\int_{-\infty}^{\infty} |x|^2 \exp\left(-\frac{|y_n - f(x)|^2}{2\sigma_N^2} - \frac{|z_{n,A}^{\text{pri}} - x|^2}{\mu_A^{\text{pri}}}\right)\mathrm{d}x \\ &- |\text{E}[z_n|z_{n,A}^{\text{pri}}, y_n, \mu_A^{\text{pri}}]|^2.\end{aligned} \tag{3.60}$$

Similar to GAMP, this calculation can be split into two integrals for nonlinearities that are applied independently to I and Q. The real component is calculated as

$$\text{Re}\left(\text{E}[z_n|z_{n,A}^{\text{pri}}, y, \mu_A^{\text{pri}}]\right) = \frac{1}{C_n^R}\int_{-\infty}^{\infty} x \exp\left(-\frac{|\text{Re}\,(y) - f(x)|^2}{2\sigma_N^2} - \frac{|\text{Re}\,(z_{n,A}^{\text{pri}}) - x|^2}{\mu_A^{\text{pri}}}\right)\mathrm{d}x, \tag{3.61}$$

and the imaginary component as

$$\text{Im}\left(\text{E}[z_n|z_{n,A}^{\text{pri}}, y, \mu_A^{\text{pri}}]\right) = \frac{1}{C_n^I}\int_{-\infty}^{\infty} xj \exp\left(-\frac{|\text{Im}\,(y) - f(x)|^2}{2\sigma_N^2} - \frac{|\text{Im}\,(z_{n,A}^{\text{pri}}) - x|^2}{\mu_A^{\text{pri}}}\right)\mathrm{d}x, \tag{3.62}$$

where C_n^R and C_n^I are normalization constants defined as

$$C_n^R = \int_{-\infty}^{\infty} \exp\left(-\frac{|\text{Re}\,(y_n) - f(x)|^2}{2\sigma_N^2} - \frac{|\text{Re}\,(z_{n,A}^{\text{pri}}) - x|^2}{\mu_A^{\text{pri}}}\right)\mathrm{d}x, \tag{3.63}$$

and

$$C_n^I = \int_{-\infty}^{\infty} \exp\left(-\frac{|\mathrm{Im}\,(y_n) - f(x)|^2}{2\sigma_N^2} - \frac{|\mathrm{Im}\,(z_{n,A}^{\mathrm{pri}}) - x|^2}{\mu_A^{\mathrm{pri}}}\right)\mathrm{d}x. \tag{3.64}$$

The variance can be calculated as the sum of two real-valued integrals, i.e.,

$$\begin{aligned}\mathrm{var}[z_n|z_{n,A}^{\mathrm{pri}}, y_n, \mu_A^{\mathrm{pri}}] = \frac{1}{C_n^R}\int_{-\infty}^{\infty}|x|^2\exp\left(-\frac{|\mathrm{Re}\,(y_n) - f(x)|^2}{2\sigma_N^2} - \frac{|\mathrm{Re}\,(z_{n,A}^{\mathrm{pri}}) - x|^2}{\mu_A^{\mathrm{pri}}}\right)\mathrm{d}x \\ + \frac{1}{C_n^I}\int_{-\infty}^{\infty}|x|^2\exp\left(-\frac{|\mathrm{Im}\,(y_n) - f(x)|^2}{2\sigma_N^2} - \frac{|\mathrm{Im}\,(z_{n,A}^{\mathrm{pri}}) - x|^2}{\mu_A^{\mathrm{pri}}}\right)\mathrm{d}x \\ - |\mathrm{E}[z_n|z_{n,A}^{\mathrm{pri}}, y_n, \mu_A^{\mathrm{pri}}]|^2.\end{aligned} \tag{3.65}$$

As was the case for GAMP, the integration variable is defined to be between $[-A_x, A_x]$, with N_x points in between. The expectation for the M-QAM can be calculated by

$$\mathrm{E}[X_k|X_{k,B}^{\mathrm{pri}}] = \sum_{i=0}^{M-1} D_i P(D_i|X_{k,B}^{\mathrm{pri}}, \mu_B^{\mathrm{pri}}), \tag{3.66}$$

where D_i is the ith symbol of the constellation, and $P(D_i|X_{k,B}^{\mathrm{pri}}\mu^V)$ is the likelihood of that symbol, defined as

$$P(D_i|X_{k,B}^{\mathrm{pri}}, \mu_B^{\mathrm{pri}}) = \frac{\exp\left(-\frac{|D_i - X_{k,B}^{\mathrm{pri}}|^2}{2\mu_B^{\mathrm{pri}}}\right)}{\sum_{j=0}^{M-1}\exp\left(-\frac{|D_j - X_{k,B}^{\mathrm{pri}}|^2}{2\mu_B^{\mathrm{pri}}}\right)}. \tag{3.67}$$

The variance of the distribution is calculated as

$$\mathrm{var}[X_k|X_{k,B}^{\mathrm{pri}}] = \sum_{i=0}^{M-1}(D_i - \mathrm{E}[X_k|X_{k,B}^{\mathrm{pri}}])^2 P(D_i|X_{k,B}^{\mathrm{pri}}, \mu_B^{\mathrm{pri}}). \tag{3.68}$$

For $O_s > 1$, the unused subcarriers are set as $\mathrm{E}[X_k|X_{k,B}^{\mathrm{pri}}] = 0$ and $\mathrm{var}[X_k|X_{k,B}^{\mathrm{pri}}] = 1$, for $O_s N > k > N$.

Fig. 3.23 shows a BER comparison of the GTurbo receiver with $N = 512$ subcarriers averaged over 100 blocks. From the figure, the performance benefits of GTurbo over an ideal receiver can be observed clearly. The gain is similar to the gain associated with using GAMP.

Fig. 3.24 shows the BER for a 64-QAM system. Again, it can be seen that GTurbo achieves a similar performance to GAMP. In this case 64-QAM was used, since $N_x = 256$ was insufficient for 256-QAM to achieve a BER below 10^{-4}. It should be noted that GTurbo requires a larger resolution N_x than GAMP, for the same modulation.

Fig. 3.25 shows the BER for a system with an IQ clipping nonlinearity at the transmitter. It is clear from the figure that, compared to GAMP, GTurbo achieves a better performance with a gain of approximately 1 dB which can be a significant benefit for many applications.

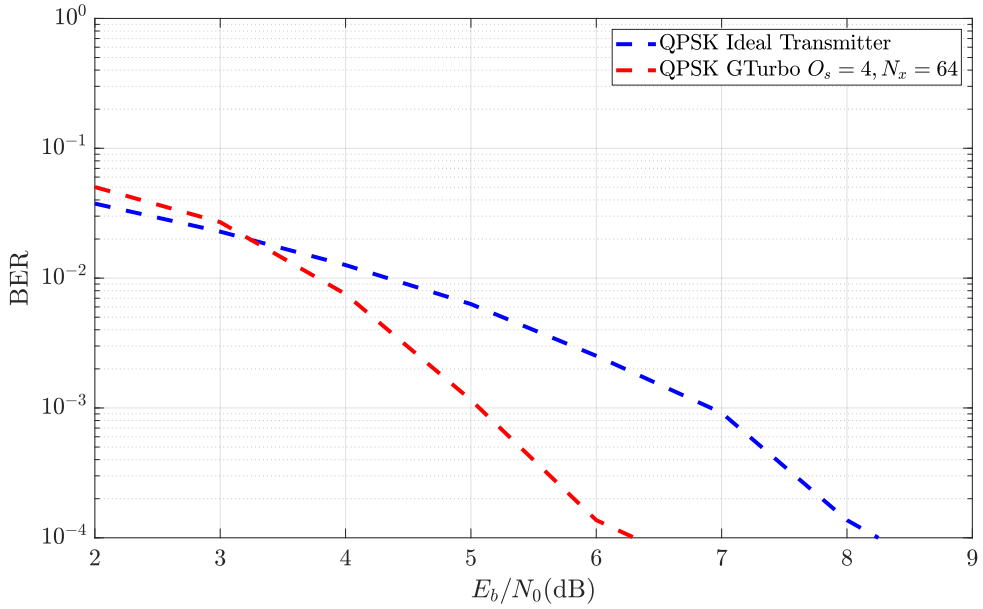

Figure 3.23: BER for the QPSK GTurbo receiver, using an SSPA nonlinearity with $q_{\text{ssspa}} = 1, s_{\text{sat}}/\sigma_s = 0.42$.

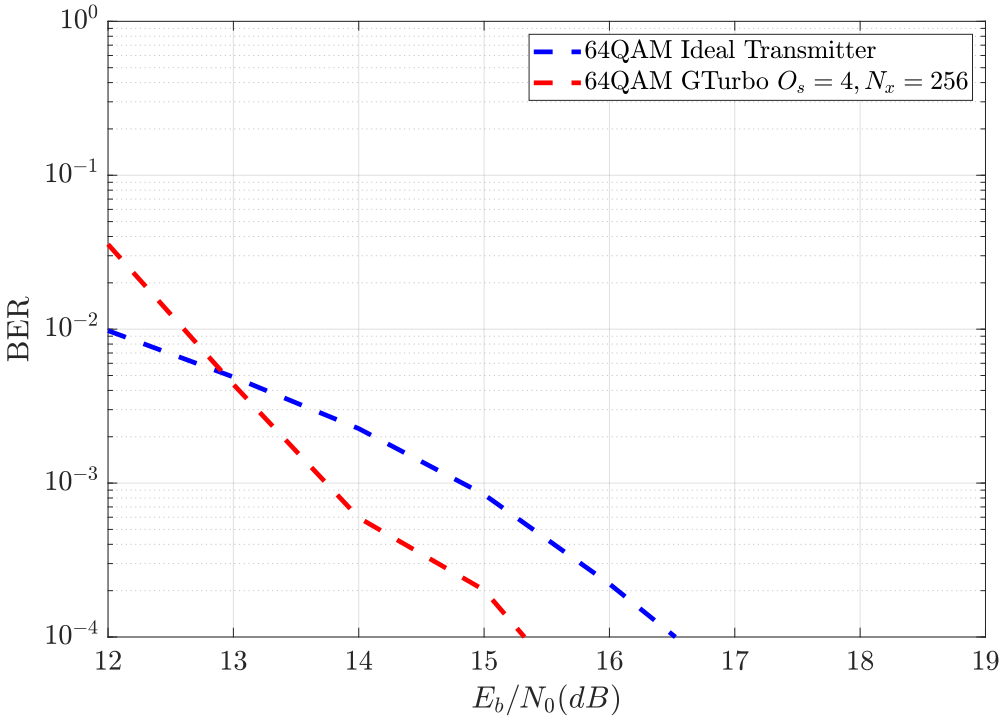

Figure 3.24: BER for the 64-QAM GTurbo receiver, using an SSPA nonlinearity with $q_{\text{sspa}} = 1, A_{\text{sat}}/\sigma_s = 0.57$.

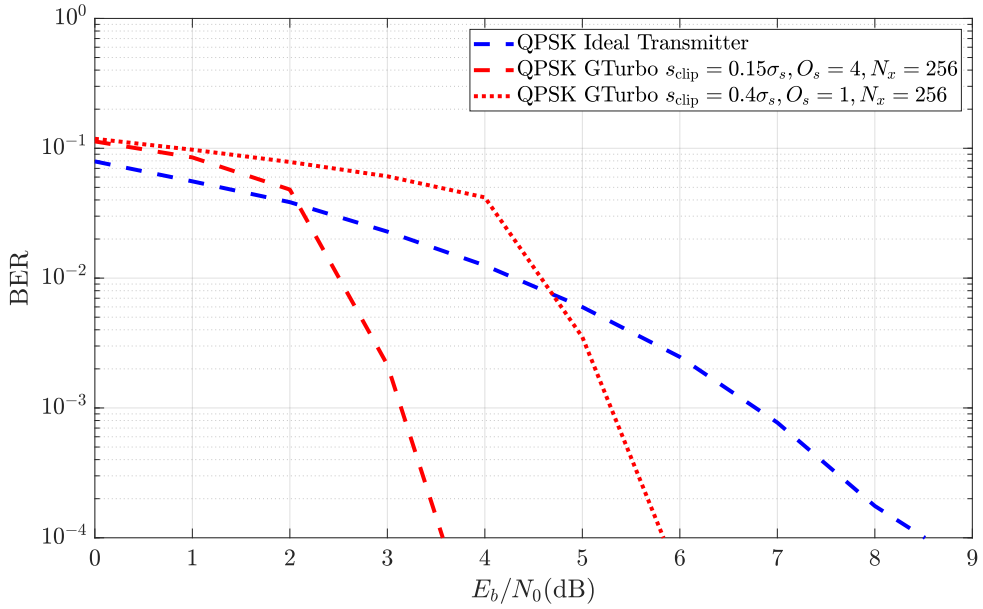

Figure 3.25: BER for the QPSK GTurbo receiver with an IQ clipping nonlinearity.

As was the case for GAMP, it is important to measure the performance of GTurbo in scenarios where there can be no OOB emissions. Fig. 3.26 presents the BER considered filtered and unfiltered scenarios. From the figure, there is a noticeable performance

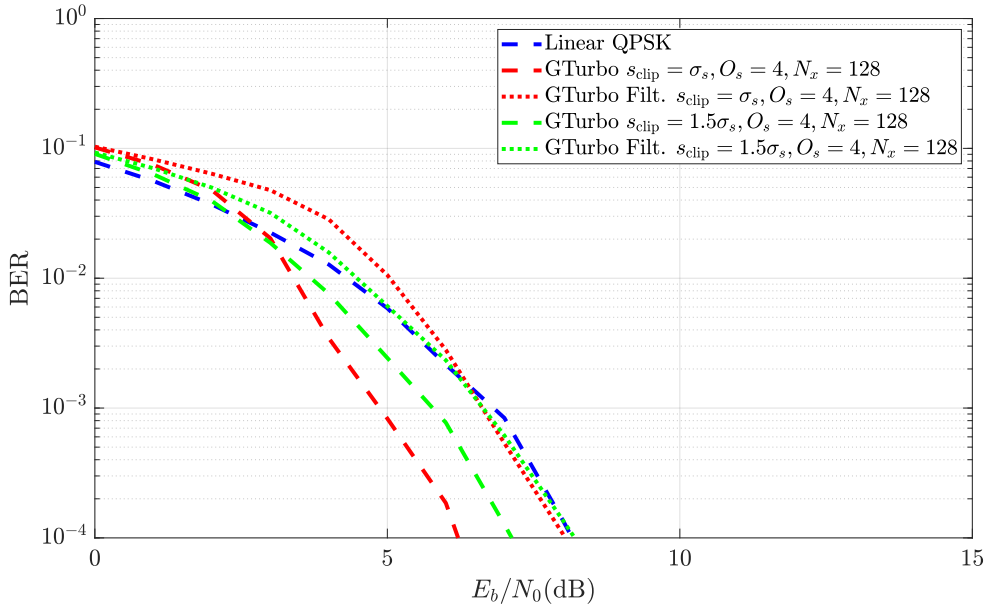

Figure 3.26: BER for the QPSK GTurbo receiver with an IQ clipping nonlinearity and filtered bandwidth.

penalty associated with filtering the OOB emissions. It is interesting to note that GTurbo can achieve a better performance than GAMP in the filtered scenarios, though it cannot outperform a linear system. This fact makes GTurbo better suited at mitigating distortion without increasing signal bandwidth.

Fig. 3.27 shows the E_b/N_0+PAPR necessary to obtain a BER of 10^{-4}, with various GTurbo configurations. As was the case for GAMP, it can be seen that unfiltered QPSK

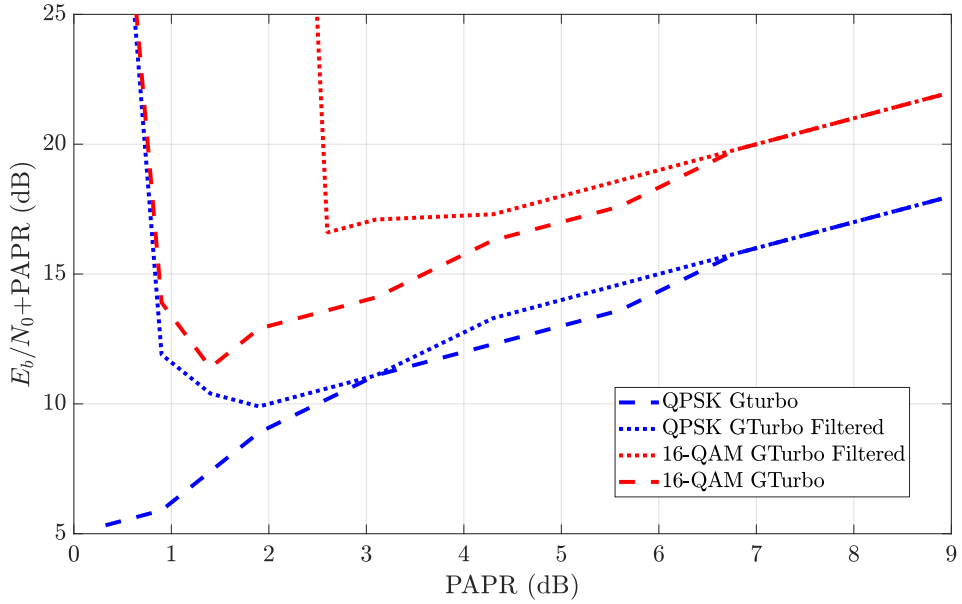

Figure 3.27: E_b/N_0+PAPR necessary to achieve a target BER of 10^{-4} with GTurbo.

performs best with the lowest possible PAPR. If the OOB radiation is filtered, then the optimum PAPR for GTurbo QPSK is 2 dB. For 16-QAM, unfiltered GTurbo performs best with 1.4 dB of PAPR, the same as GAMP, though it achieves an E_b/N_0+PAPR around 2 dB lower than GAMP, which means it requires less E_b/N_0 to reach the target BER. On the other hand, filtered GTurbo 16-QAM performs best with a PAPR of 2.6 dB, and achieves an E_b/N_0+PAPR about 1 dB lower than GAMP.

3.4 Coded Nonlinear Receivers

This section presents nonlinear receiver algorithms that were adapted to make use of FEC schemes. Specifically, LDPC coding was considered and implemented, as it is a widely adopted method of FEC.

3.4.1 Coded Bussgang Receiver

The BNC receiver can be greatly improved by adding channel coding, which can be done in two different configurations. The first and simplest configuration is to simply decode

the signal after the BNC process is complete. For a soft input decoder, the LLR of each bit can be approximated by

$$\begin{aligned} L_m^{(i)} \approx & \frac{\alpha_{\text{bg}}^2}{\sigma_N^2}(\text{Re}\,(\tilde{S}_k^{(i)} - \hat{S}_k^1) + \text{Im}\,(\tilde{S}_k^{(i)} - \hat{S}_k^1) \\ & - \text{Re}\,(\tilde{S}_k^{(i)} - \hat{S}_k^0) + \text{Im}\,(\tilde{S}_n^{(i)} - \hat{S}_k^0)), \end{aligned} \tag{3.69}$$

where $\hat{S}_k^1$ and $\hat{S}_k^0$ are the closest constellation symbols to $\tilde{S}_n^{(i)}$ where the mth bit is 1 and 0, respectively. The result is used as the soft input to the channel decoder, which can use any coding scheme.

The successful decoding likelihood can be improved by taking into account the power of the distortion factor in the LLR calculation, rewriting (3.69) as

$$\begin{aligned} L_m^{(i)} \approx & \frac{\alpha_{\text{bg}}^2}{\sigma_N^2 + P_D} \left(\left(\text{Re}(\tilde{S}_k^{(i)} - \hat{S}_k^1)^2 + \text{Im}(\tilde{S}_k^{(i)} - \hat{S}_k^1)^2 \right) \right. \\ & \left. - \left(\text{Re}(\tilde{S}_k^{(i)} - \hat{S}_k^0)^2 + \text{Im}(\tilde{S}_n^{(i)} - \hat{S}_k^0)^2 \right) \right), \end{aligned} \tag{3.70}$$

where P_D can be computed a priori by

$$P_D = P_x - \alpha_{\text{bg}}^2 2\sigma_S^2. \tag{3.71}$$

Implementing these modifications results in a more robust receiver that does not suffer from incorrect decoding at very high SNR due to incorrect SIR information. Fig. 3.28 shows a BER comparison of a 1024-QAM OFDM system using a clipping level of $s_{\text{sat}}/\sigma_S = 2.8$. As can be observed, the improved BNC achieves a slightly better performance after 2 iterations, though a significant gain is seen after 4 iterations. The conventional BNC becomes worse with successive iterations because the estimation quality does not improve significantly between iterations if it is not decoded by the LDPC. Therefore, for achieving maximum efficiency in a coded system, these modifications of the conventional BNC are necessary.

In the same fashion as the uncoded system, Fig. 3.29 shows the necessary E_b/N_0+OBO for a target BER of 10^{-5}, considering various OBO levels.

From the figure, it can be observed that at $I_{\text{max}} = 4$ there is an optimum OBO around 9 and 10 dB, for 1024-QAM and 4096-QAM, respectively. For $I_{\text{max}} = 8$, the required power increases, due to error propagation in the iterative process. Fig. 3.30 simulated the same conditions, but for a target Symbol Error Rate (SER) of 2%.

In this case, the optimum OBO for both modulations is around 9dB, at $I_{\text{max}} = 4$. There is no benefit to increasing I_{max} in this scenario, leading only to worse performance.

The coded BNC receiver can be improved by taking advantage of the decoder to better approximate the transmitted signal at each Bussgang iteration. This requires re-encoding and modulating the decoded bits at the end of each Bussgang iteration, increasing delay and complexity. This scheme is referred to as Code Assisted Bussgang Noise Cancelling

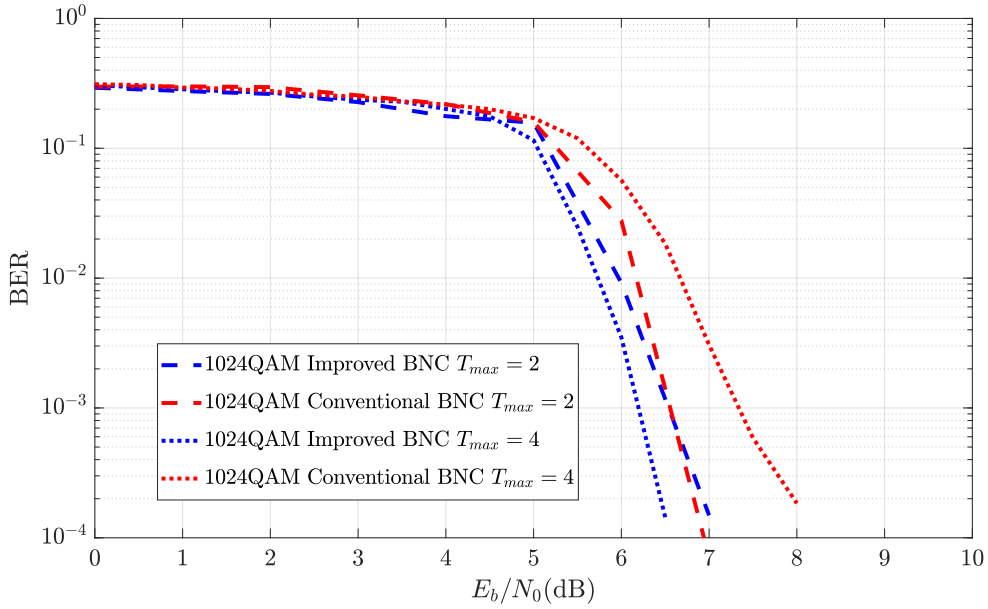

Figure 3.28: BER for 1024-QAM with $s_{\text{sat}}/\sigma_S = 2.8$ using conventional and improved coded BNC receivers.

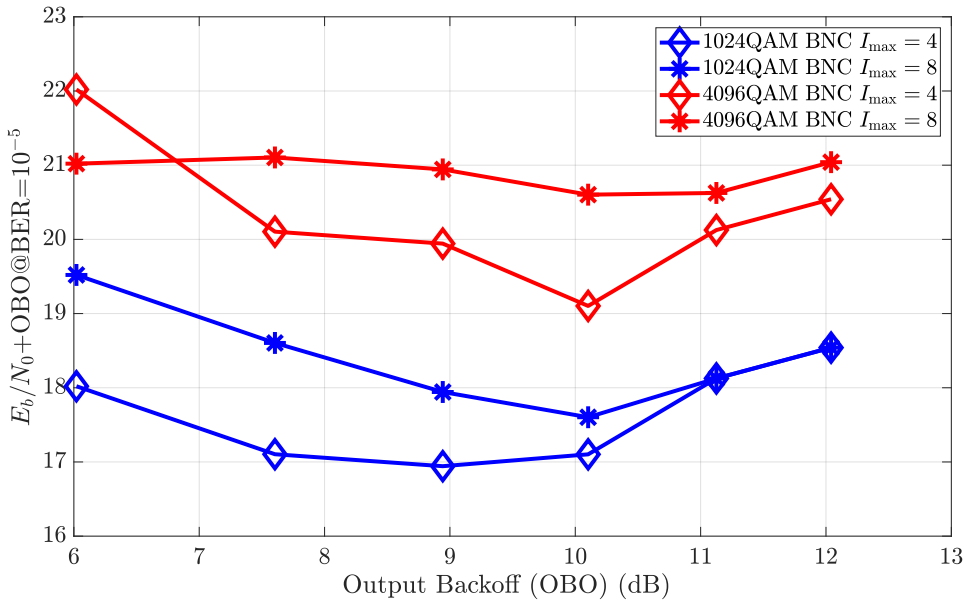

Figure 3.29: Required E_b/N_0+OBO for a target BER of 10^{-5} as a function of the OBO, for different constellations.

(CA-BNC). The benefit lies in the increased robustness to lower clipping levels. Fig. 3.31 shows the necessary E_b/N_0+OBO for a target BER of 10^{-5}, for various OBO levels.

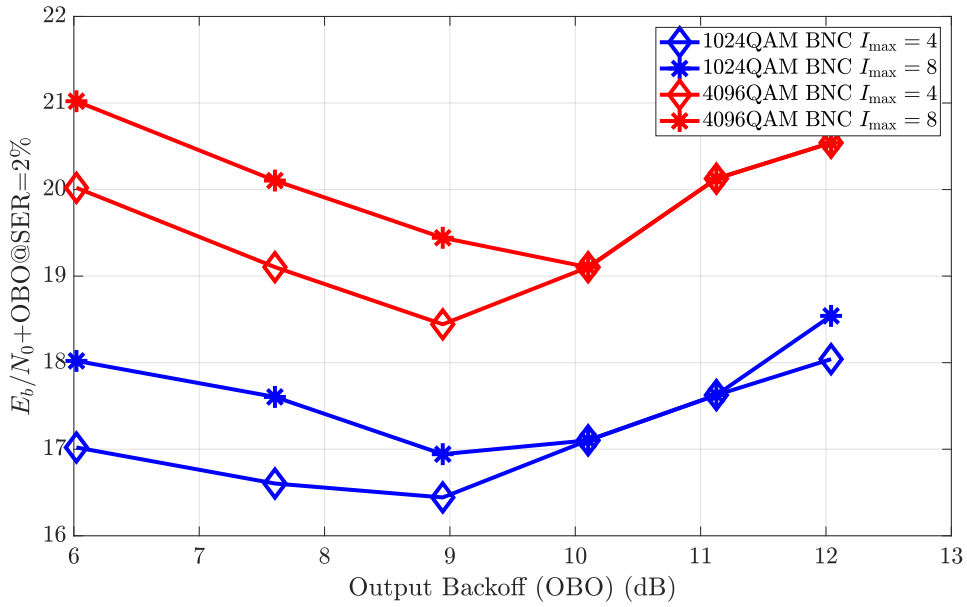

Figure 3.30: Required E_b/N_0+OBO for a target SER of 2% as a function of the OBO, for different constellations.

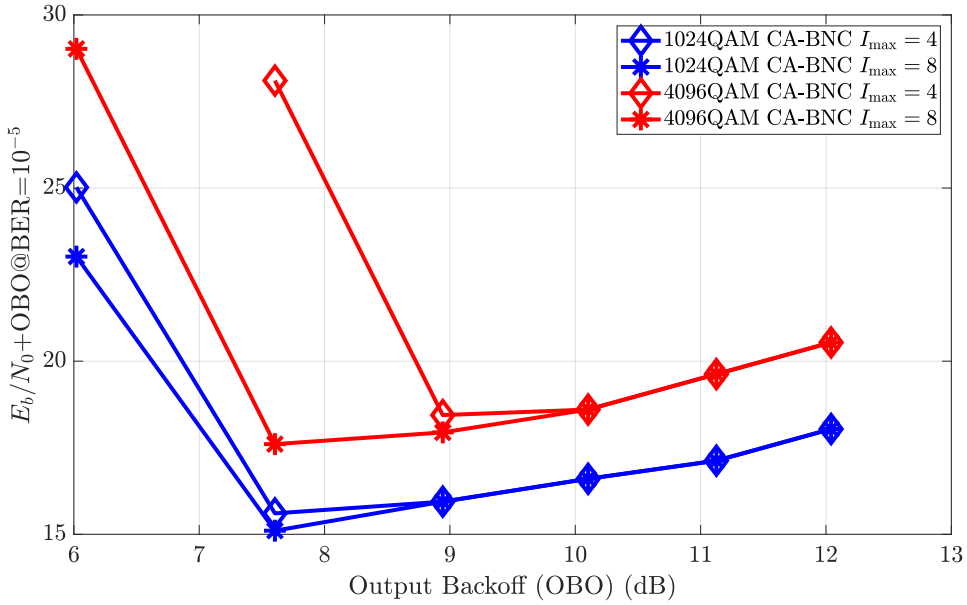

Figure 3.31: Required E_b/N_0+OBO of CA-BNC, for a target BER of 10^{-5} as a function of the OBO, for different constellations.

At $I_{\max} = 4$, the optimum OBO for 1024-QAM and 4096-QAM is 7.6 and 9 dB, respectively. For $I_{\max} = 8$ the optimum OBO for 1024-QAM does not change significantly, whereas for 4096-QAM the optimum OBO is 7.6 dB. Compared with regular BNC, there is

an approximate total power decrease of around 1.5 dB, at the optimum OBO for 1024-QAM and 4096-QAM. Fig. 3.32 simulated the same conditions, but for a target SER of 2%.

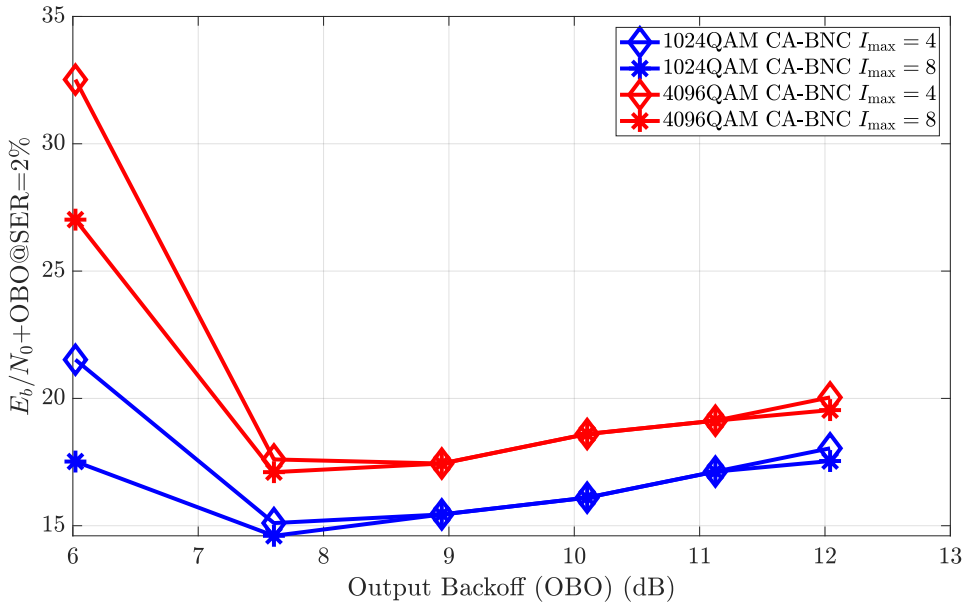

Figure 3.32: Required E_b/N_0+OBO of CA-BNC, for a target SER of 2% as a function of the OBO, for different constellations.

The optimum OBO in this scenario does not change significantly, for 1024-QAM, though it improves to 7.6dB for 4096-QAM. In this case, increasing the number of iterations does not have a noticeable impact on the necessary power.

Regardless of the constellation order, it can be seen that the coding scheme tolerates much lower clipping levels when compared to the uncoded system, achieving an optimum OBO of 7.6 dB.

3.4.1.1 Complexity Analysis

This section characterizes the computation complexity of an iteration of the proposed Bussgang receiver. Only the steps that are not part of a conventional receiver were considered, namely initial equalization and decoding. For simplicity, it is considered that an arithmetic operation between two real variables consumes 1 Floating-Point Operation (flop), whereas complex variables require 2 flops.

An iteration of Bussgang first calculates the distortion factor D_k in (2.142), from the previous iteration's symbol estimate. This step consists in computing the IFFT of the previous symbol estimate, applying the NL function to the resulting vector, computing the FFT to obtain the frequency domain symbols, and lastly subtracting the attenuated signal. Computing the attenuated signal consumes $2NO_s$ flops, and the subtraction another $2NO_s$ flops. The FFT and IFFT depend on the architecture of available, and the

Table 3.1: Summary of the complexity in each Bussgang iteration.

Bussgang Step	Complexity (flops)
First Iteration	FFT+IFFT+NL+$4NO_s$
Following Iterations	FFT+IFFT+NL+$8NO_s$

nonlinear function can vary significantly. For an SSPA, a specific implementation might use LUTs to implement the function, as it will be very expensive computationally.

The second step of a Bussgang iteration, which is only performed after the first iteration, is to subtract the D_k from the received signal, and perform equalization once again. For ZF, this requires $4NO_S$ flops, though more complex equalization schemes will have significant impact. Table 3.4.1.1 summarizes the per iteration complexity of Bussgang receivers. It is clear that the total flops of a Bussgang iteration depend heavily on the specific application, and should be analysed for specific scenarios. Each iteration can also decode the error correcting code, for better performance at the cost of higher complexity, depending on the decoder.

3.4.2 Coded GAMP

Similarly to Coded BNC, GAMP can also be improved by introducing FEC within each GAMP iteration. This modification can significantly improve GAMP convergence, thereby reducing the need for more iterations. This work was published in [15].

Each GAMP iteration computes the LLR, defined as

$$L_m = \frac{\sum^{S\in\mathbf{S}^0} \exp\left(-\frac{\left(\mathrm{Re}\,(\hat{V}_k)-\mathrm{Re}\,(S)\right)^2+\left(\mathrm{Im}\,(\hat{V}_k)-\mathrm{Im}\,(S)\right)^2}{2\sigma_N^2}\right)}{\sum^{S\in\mathbf{S}^1} \exp\left(-\frac{\left(\mathrm{Re}\,(\hat{V}_k)-\mathrm{Re}\,(S)\right)^2+\left(\mathrm{Im}\,(\hat{V}_k)-\mathrm{Im}\,(S)\right)^2}{2\sigma_N^2}\right)}, \tag{3.72}$$

which is then used as the input for decoding. It is possible to approximate the LLR using a lower complexity calculation, defined as

$$\begin{aligned} L_m^{(i)} \approx & \frac{1}{\mu_k^{v^2}}(\mathrm{Re}\,(\hat{V}_k - S_k^1) + \mathrm{Im}\,(\hat{V}_k - S_k^1) \\ & - \mathrm{Re}\,(\hat{V}_k - S_k^0) + \mathrm{Im}\,(\hat{V}_n - S_k^0)), \end{aligned} \tag{3.73}$$

however, this approximation may not be enough for very large constellations. It is necessary to modify the probabilities $P(D_i|\hat{V}_k, \mu^v)$ to use the LLR of each bit, defined as

$$P(D_i|\hat{V}_k, \mu^v) = \prod_{j=0}^{M_{bits}-1} \frac{1}{2}\left(1 + \tilde{b}_j \tanh\frac{L_j^c}{2}\right), \tag{3.74}$$

where $\tilde{b}_j$ is defined as

$$\tilde{b}_j := \begin{cases} 1, & b_j = 0 \\ -1, & b_j = 1 \end{cases}, \tag{3.75}$$

where b_j is the jth bit of the symbol. The rest of the algorithm does not require modifications, while the LLR is obtained from the output of the decoder, which in the case of ecoding does not require additional processing.

Coded GAMP can achieve promising results, even for high order modulations. Fig. 3.33 presents the BER of a system employing a 1/2 rate LDPC code, with $N_x = 512$, $O_s = 4$, $I_{\max} = 20$, $\beta = 0.85$.

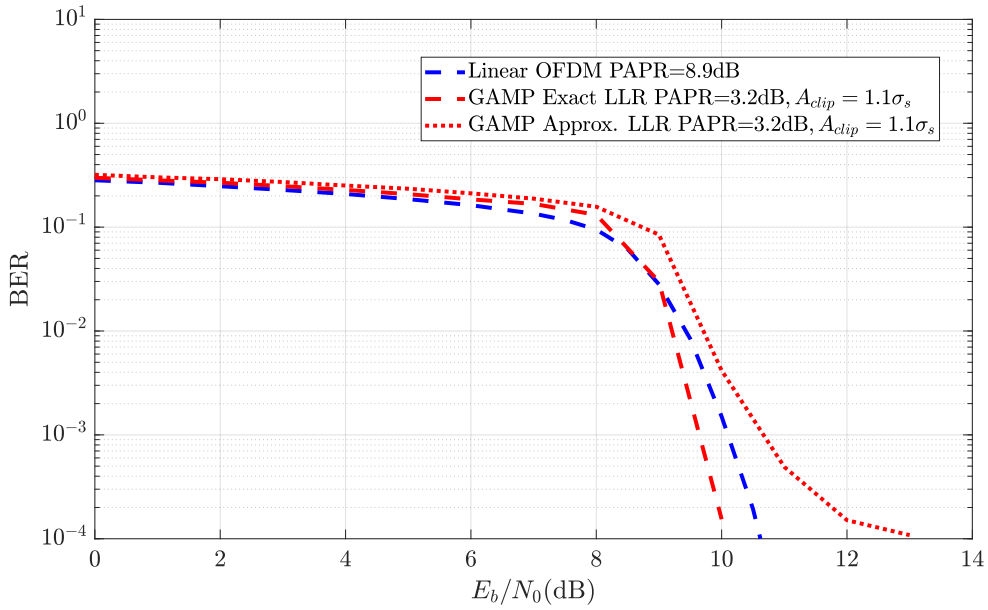

Figure 3.33: BER for 1024-QAM for linear and Coded GAMP receivers.

In this scenario, GAMP is being used to recover a signal that has been clipped to reduce the PAPR and amplified by a linear amplifier. As can be noted from the figure, with exact LLR calculation, GAMP can outperform a linear system by almost 1 dB, while supporting a PAPR that is 5.7 dB lower, allowing for much more efficient amplification. On the other hand, using approximate LLR calculation degrades performance, as certain OFDM symbols cannot be recovered due to the approximation error.

3.4.2.1 Complexity Analysis

The complexity of GAMP can be characterized per iteration, with total complexity depending on the expected number of iterations. An iteration is divided into 4 steps, as was previously shown, numbered between 2 and 5, since step 1 is the initialization.

Step 2 requires computing a real average, which costs NO_s flops, performing an IFFT of length NO_s, with complexity depending on the architecture, and a complex vector wise multiplication and subtraction, which cost an addtional $4NO_s$ flops. The total for this step is $7NO_s$.

Table 3.2: Summary of the complexity in each step of GAMP, per iteration.

GAMP Step	Complexity (flops)
Step 2	IFFT+$7NO_s$
Step 3	$NO_s(5 + 18N_x + 3N_x^2)$
Step 3 IQ	$NO_s(5 + 24N_x)$
Step 4	FFT+$1 + 11NO_s$
Step 5	$N(28M - 4)$
Total	$1 + 28NO_s + NO_s(3 + 18N_x + 3N_x^2) + N(28M - 4)$
Total IQ	$1 + 28NO_s + NO_s(5 + 24N_x) + N(28M - 4)$

Step 3 requires several computations. The complex integral in (3.49) requires computing $NO_sN_x^2$ flops, of which each term is the result of an exponential, that can be sourced from a LUT. The exponent is made up of a sum of two similar terms, with each parcel consisting of a square, subtraction and division, for a total of $6N_x$ flops per exponent term. The total amount of flops for the normalization factor is therefore $NO_s(14N_x + N_x^2)$. For (3.48), the exponential is the same, therefore it does need to be computed. The integral requires $NO_s(2 + 2N_x + N_x^2)$ flops. Calculating (3.47) requires an additional $4NO_s$ flops. The integral in (3.51) requires $NO_s(3 + 2N_x + N_x^2)$ flops, since part of the expression was already calculated in the previous calculation. Lastly, (3.50) requires $3NO_s$ flops. In total, calculating step 3) requires $NO_s(3 + 18N_x + 3N_x^2)$.

If a rectangular nonlinearity is used, then the complexity is lower. The normalization (3.54) requires NO_sN_x for the integration, and $6N_x$ flops to calculate the exponential. Taking into account (3.55), this step requires $2NO_s(8N_x)$ flops. The expectations (3.52) and (3.53) require $2NO_s(2 + 2N_x)$ flops in total. The nonlinear output step (3.47) requires the same number of flops. The variance (3.56) requires $NO_s(3 + 4N_x)$. The total number of flops in this step is $NO_s(5 + 24N_x)$, a significant reduction in flops.

Step 4 is similar to step 2, with an additional damping calculation, which consumes $6NO_s$ flops. The average requires $1 + NO_s$, due to the inversion, and the updated probability requires an FFT of size NO_s and an additional $4NO_s$ flops. The total for this step is $1 + 11NO_s$.

In step 5, the complexity of calculating the likelihood depends on which definition is used. For (3.45), it requires computing M exponents, each requiring 6 operations, and a sum of M complex terms in the denominator. The total is $8M$, assuming that the exponential requires no flops. The expectation in (3.44) requires $N(12M - 2)$ flops, since subcarriers beyond N do not carry data, and the variance (3.46) requires $N(16M - 2)$, where M is the constellation size. In total this step requires $N(28M - 4)$ flops.

Table 3.2 summarised the complexity of each GAMP iteration.

From this analysis, it is clear how certain variables define the computational complexity of each GAMP step. The heaviest step is clearly step 3, due to a factor $NO_sN_x^2$, which scales quadratically with the integral resolution that must be high for large constellations. For rectangular nonlinearities, the complexity is much lower, since it does not scale

quadratically with N_x. The term M in step 5 should also be noted, as for very large constellations it may exceed the complexity of step 3, for low oversampling or rectangular nonlinearities. The other steps are fairly simple to calculate, excluding the complexity of the DFT. Each iteration must also decode the codeword, which has a complexity that depends on the chosen coding scheme and decoder. Compared to a conventional receiver, performing I GAMP iterations will require I times more decoding operations.

3.4.3 Coded Generalized Turbo

GTurbo can also be improved using FEC, as was the case for GAMP. Each GTurbo iteration computes the LLR, defined as

$$L_m = \frac{\sum\limits^{S\in\mathbf{S}^0} \exp\left(-\frac{\left(\mathrm{Re}\,(X^{\mathrm{pri}}_{k,B})-\mathrm{Re}\,(S)\right)^2+\left(\mathrm{Im}\,(X^{\mathrm{pri}}_{k,B})-\mathrm{Im}\,(S)\right)^2}{2\sigma_N^2}\right)}{\sum\limits^{S\in\mathbf{S}^1} \exp\left(-\frac{\left(\mathrm{Re}\,(X^{\mathrm{pri}}_{k,B})-\mathrm{Re}\,(S)\right)^2+\left(\mathrm{Im}\,(X^{\mathrm{pri}}_{k,B})-\mathrm{Im}\,(S)\right)^2}{2\sigma_N^2}\right)}, \tag{3.76}$$

which is then used as the input for decoding. The approximate LLR is given by

$$\begin{aligned} L^{(i)}_m \approx & \frac{1}{\mu_k^{v^2}}(\mathrm{Re}\,(\mathrm{var}[X_k|X^{\mathrm{pri}}_{k,B}]-S^1_k)+\mathrm{Im}\,(X^{\mathrm{pri}}_{k,B}-S^1_k) \\ & -\mathrm{Re}\,(X^{\mathrm{pri}}_{k,B}-S^0_k)+\mathrm{Im}\,(X^{\mathrm{pri}}_{k,B}-S^0_k)), \end{aligned} \tag{3.77}$$

however, this approximation may not be enough for very large constellations. The probability $P(D_i|X^{\mathrm{pri}}_{k,B},\mu^{\mathrm{pri}}_B)$ is rewritten as

$$P(D_i|X^{\mathrm{pri}}_{k,B},\mu^{\mathrm{pri}}_B) = \prod_{j=0}^{M_{bits}-1}\frac{1}{2}\left(1+\tilde{b}_j\tanh\frac{L^c_j}{2}\right), \tag{3.78}$$

where $\tilde{b}_j$ is defined as

$$\tilde{b}_j := \begin{cases} 1, & b_j = 0 \\ -1, & b_j = 1 \end{cases}, \tag{3.79}$$

where b_j is the jth bit of the symbol.

As was the case for GAMP, Coded GTurbo can achieve excellent results, even for high order modulations. Fig. 3.34 presents the BER of a system employing a 1/2 rate LDPC code, with $N_x = 512$, $O_s = 4$, $I_{\max} = 20$.

In these results, the signal sent to the GTurbo receiver was submitted to a PAPR reducing clipping nonlinearity. With exact LLR calculation, GTurbo can outperform linear OFDM by almost 1 dB, similar to GAMP, with the added benefit of a 5.7 dB lower PAPR. Unlike GAMP however, GTurbo can still achieve nearly the same performance using approximate LLR calculation, due to the increased robustness to accumulated error over GAMP.

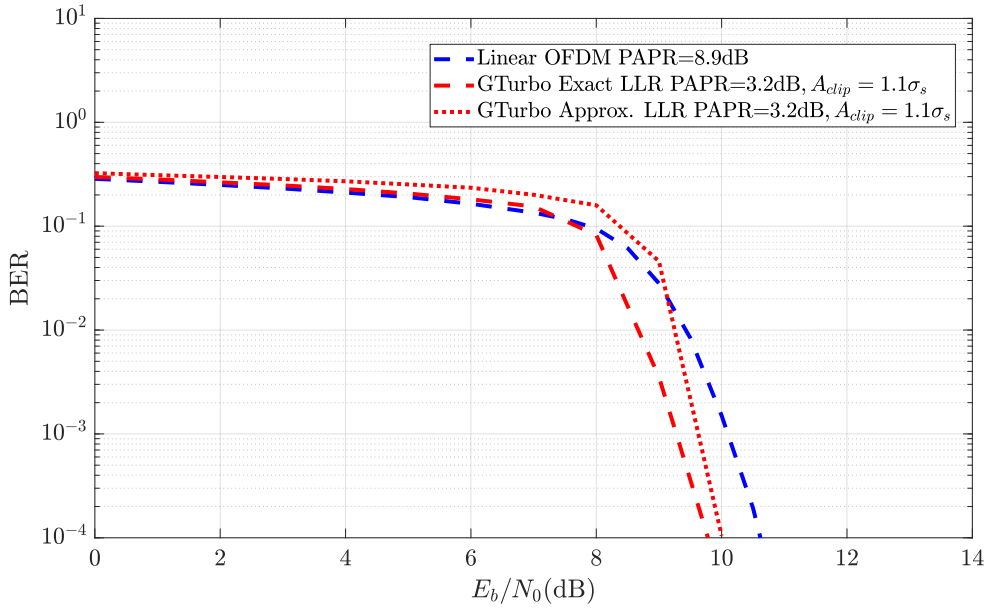

Figure 3.34: BER for 1024-QAM for linear and Coded GTurbo receivers.

3.4.3.1 Complexity Analysis

The complexity of GTurbo can also be characterized per iteration, with total complexity depending on the expected number of iterations. An iteration is divided into 4 steps, as was previously shown, numbered between 1 and 4.

Step 1 requires computing the a posteriori probabilities, which are computationally similar to GAMP. The normalization factor (3.59) computes a complex integral that consumes $NO_sN_x^2$ flops. Calculating the expression inside the integral requires $14N_x$ flops, for a total $NO_s(14N_x+N_X^2)$ flops. The expectation (3.58) consumes $NO_s(2+2N_x+N_x^2)$, and the variance (3.60) consumes $NO_s(3+2N_x+N_x^2)$ flops. In total, computing this step requires $NO_s(5+18N_x+3N_x^2)$.

For rectangular nonlinearities, computing (3.63) and (3.64) requires $2NO_s(8N_x)$, the expectations (3.61) and (3.62) consume $2NO_s(1+N_x)$, and the variance (3.65) requires $2NO_s(3+N_x)$. The total computing cost for IQ nonlinearities is $2NO_s(4+10N_x)$.

Step 2 requires an initial FFT, and an average requiring $1+NO_s$ flops. The following calculations for μ_B^{pri} and $\mathbf{X}_B^{\text{pri}}$ require another FFT, plus $4+4NO_s$ flops. The complexity of step 3 is identical to GAMP, with a change in variables. Lastly, step 4 is similar to step 2, requiring 2 IFFTs, and an additional $5+5NO_s$.

Table 3.3 summarised the complexity of each GTurbo iteration.

The complexity of a GTurbo iteration achieves a similar scale to GAMP iterations, with the exception of the additional FFTs requires by GTurbo. The choice between GAMP and GTurbo should therefore depend on the architecture and expected performance for both algorithms, as the expected number of iterations will be a deciding factor.

Table 3.3: Summary of the complexity in each step of GTurbo, per iteration.

GTurbo Step	Complexity (flops)
Step 1	$NO_s(5 + 18N_x + 3N_x^2)$
Step 1 IQ	$2NO_s(4 + 10N_x)$
Step 2	2 FFT $+5 + 5NO_s$
Step 3	$N(28M - 4)$
Step 4	2 IFFT $+5 + 5NO_s$
Total	$10 + 10NO_s + NO_s(5 + 18N_x + 3N_x^2) + N(28M - 4)$
Total IQ	$10 + 10NO_s + NO_s(4 + 10N_x) + N(28M - 4)$

4

Applications for Nonlinear Receivers

4.1 Introduction

This section presents several applications that were developed using the algorithms defined in Chapter 3. The work developed in this chapter was published in conference papers [12–15], journal papers [9, 11, 16, 18], and a patent [117]. Additionally, a conference paper was submitted to the conference "IEEE VTC 2024 (Fall)". Moreover, a journal paper was submitted to the journal "IEEE Transactions on Communications".

4.2 SVD Physical Layer Security

This section covers the work developed in PLS aspects of nonlinear receivers for MIMO systems. These schemes take advantage of the wireless MIMO channel to decrease the effective capacity of the eavesdropped channel, allowing for secure communications at the lowest layer. This work was published in [9, 11, 12, 14] and a patent was registered [117].

4.2.1 SC-FDE

This section analyses the PLS potential of the MIMO SVD scheme combined with SC-FDE techniques from [108], that can be achieved by exploiting the wireless channel characteristics. It is shown that an Eavesdropper will have a significantly degraded channel, hampering its ability to recover the eavesdropped signal. This degradation is shown to be proportional to the distance between legitimate users and eavesdropper.

The following results show the BER and secrecy rate of the considered point-to-point MIMO system with, unless otherwise mentioned, $T = 8$ transmit and $R = 8$ receive antennas. These performance results involve scenarios with Rayleigh and Rician fading, and were obtained by simulation. Unless otherwise stated, the block size is $N = 256$.

4.2.1.1 Rayleigh Fading

This analysis begins with the impact of the ρ_E factor in the receiver's BER performance. This can be observed in Fig. 4.1, where the BER of the eavesdropper is shown for different ρ_E values.

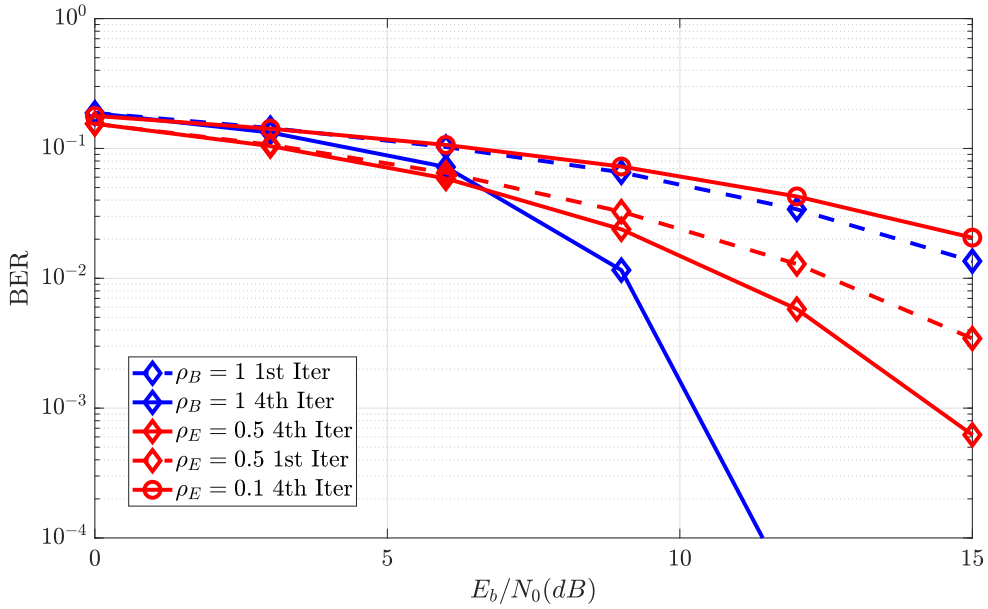

Figure 4.1: Comparison of BER for different values of ρ_E, with $\beta_N = \beta_M = \infty$.

From the figure, it can be observed that the system performance can be severely degraded at low levels of ρ_E. In accordance with the system definition, it is not unreasonable to assume that the eavesdropper will operate with small values of ρ_E. The next set of results show the simulated secrecy rate of the system under different conditions. Fig. 4.2 shows the secrecy rate as a function of ρ_E, considering different MIMO configurations.

From the figure it can be concluded that, with perfect CSI, the maximum attainable secrecy rate increases with the number of antennas of both users. Fig. 4.3 shows the secrecy rate of an 8×8 system, considering different values of β_N (i.e., considering different channel estimation errors on both receivers), at an SNR of 12 dB.

As expected, the addition of a channel estimation error negatively impacts the secrecy rate of the system, particularly for lower values of ρ_E. In Fig. 4.4, channel mismatch error was introduced, represented by β_M, in addition to the channel estimation error and SNR of the previous simulations.

From the figure, it can be seen that when the channel estimation error assumes low levels, the secrecy rate increases. It should also be noted that even for high values of ρ_E, the secrecy rate is higher than in a scenario with no channel mismatch error. This is expected due to the mismatch error affecting only the eavesdropper's capacity. In addition, a relatively small difference between the theoretical and simulated results can be observed.

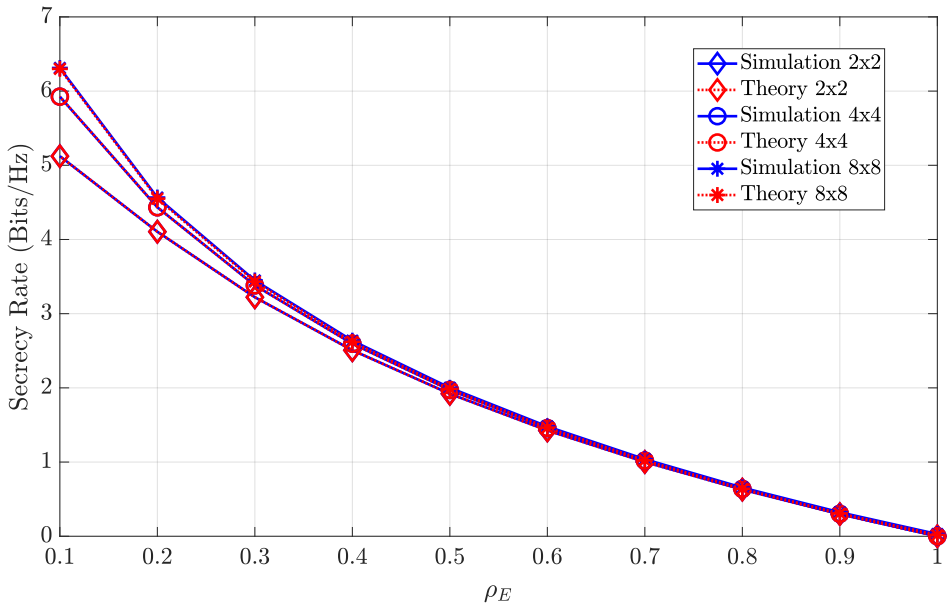

Figure 4.2: Secrecy rate of the system for an SNR of 12 dB and different MIMO configurations.

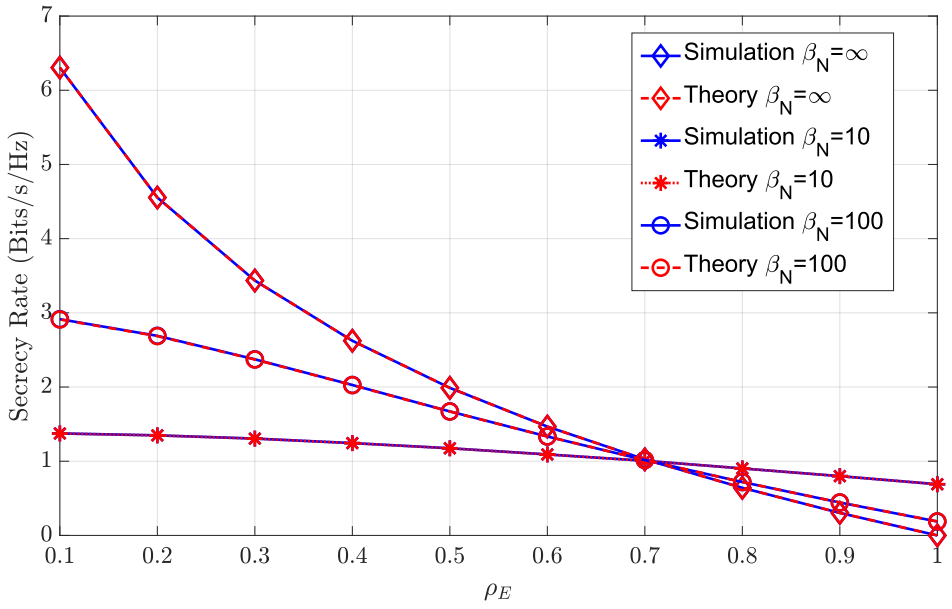

Figure 4.3: Secrecy rate of the system for an SNR of 12 dB and various levels of channel estimation error on both sides.

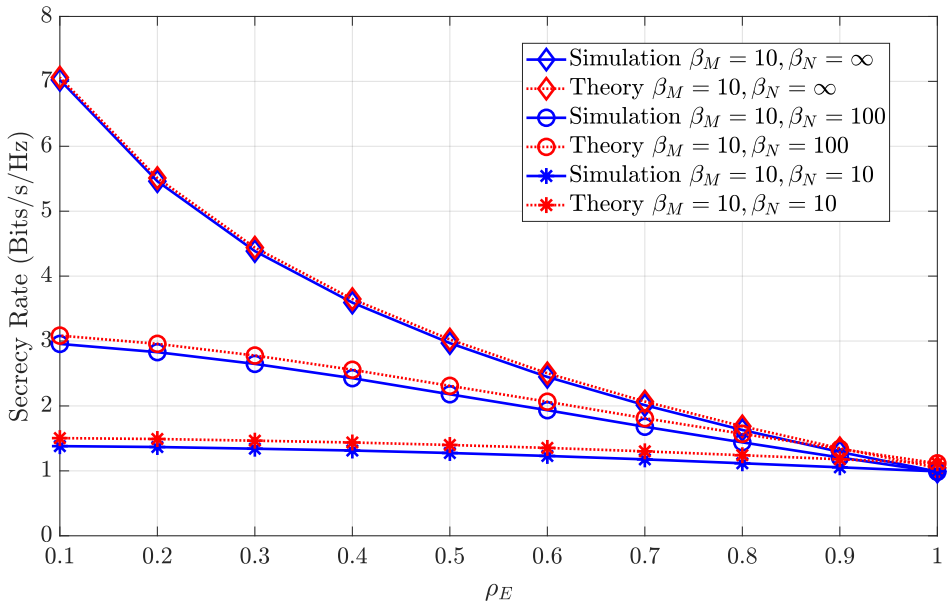

Figure 4.4: Secrecy rate of the system for an SNR of 12 dB and $\beta_M = 10$ with various levels of channel estimation error.

This arises due to the residual error of the Gaussian approximation. Fig. 4.5 combines various levels of SNR for the same levels of channel estimation and mismatch errors.

From the figure, it can be noted that a higher SNR leads to a higher secrecy rate, as expected, with the secrecy rate gain increasing further for smaller values of ρ_E.

4.2.1.2 Multiple eavesdroppers

An interesting scenario involves the existence of K eavesdroppers performing joint estimation and equalization. As mentioned before, this scenario is approximated by a single eavesdropper employing KR antennas, for $K > 1$. Fig. 4.6 shows the secrecy rate of the system for $K = 1, 2$ and 4.

From the figure, it can be seen that increasing the number of eavesdroppers leads to a lower attainable secrecy rate. This fact is not limited to the scenario without errors, as can be observed in the scenario with channel mismatch in Fig. 4.7.

From this figure, it can be noted that by considering more eavesdroppers and/or antennas, the impact of the channel mismatch error can be reduced (or even eliminated).

4.2.1.3 Rician Fading

In addition to varying ρ_E and the error factors, the ray power ratio between multipath component and main LoS component can also be varied. For coherence with paper notation, in this section the ray power in the Rician channel is denoted by α_{RP}, with an LoS component power of $1 - \alpha_{\text{RP}}$. Fig. 4.8 shows the secrecy rate with no errors, considering

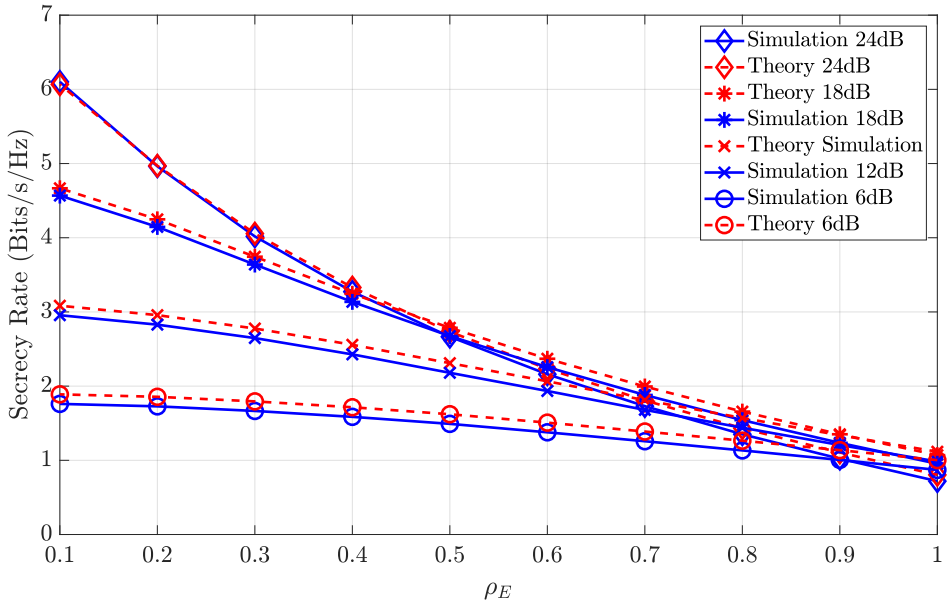

Figure 4.5: Secrecy rate of the system for different levels of SNR and with $\beta_N = 100$ and $\beta_M = 10$.

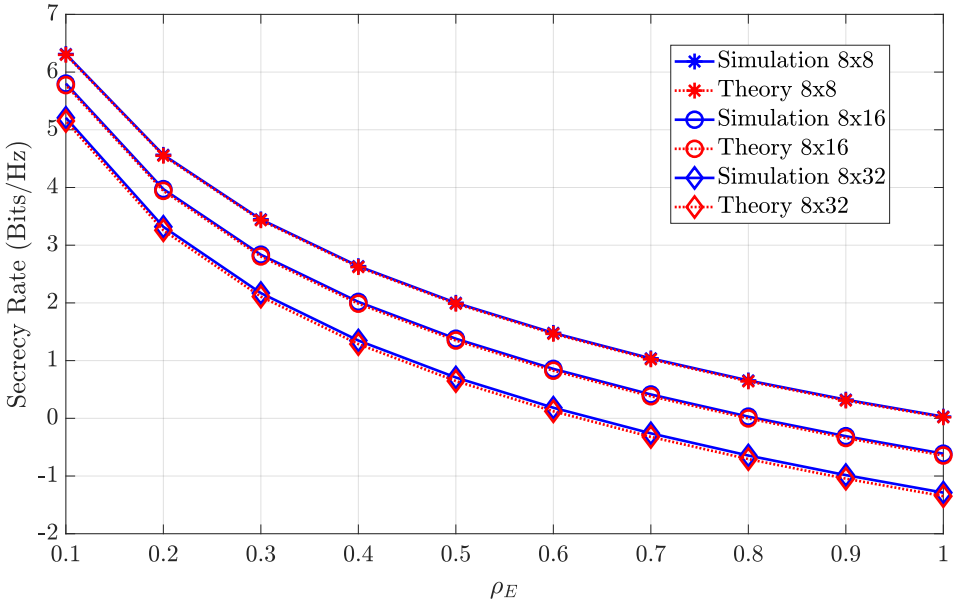

Figure 4.6: Secrecy rate of the system for various numbers of eavesdroppers, at 12 dB SNR.

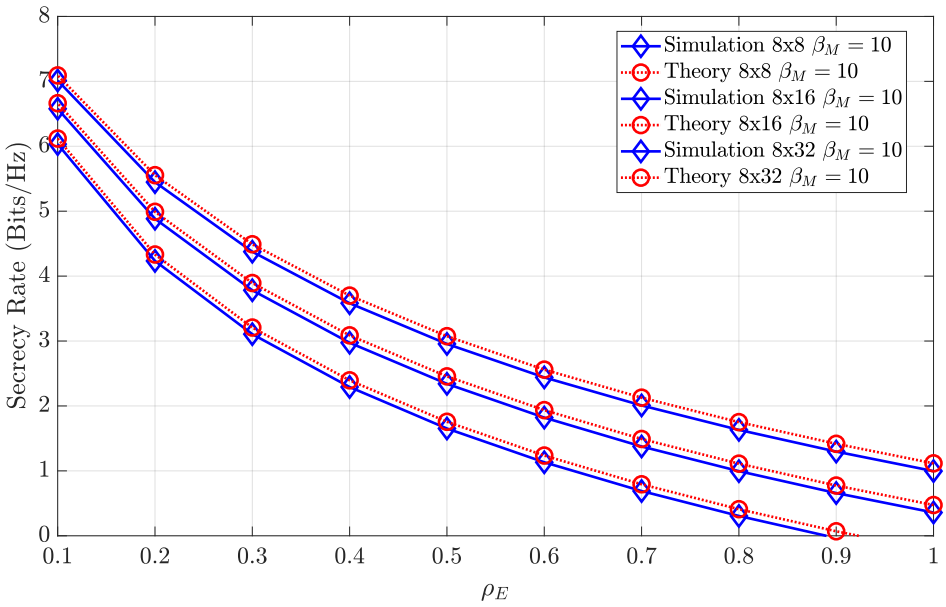

Figure 4.7: Secrecy rate of the system for various numbers of eavesdroppers and $\beta_M = 10$, at 12 dB SNR.

different values of ρ_E and different ray power coefficients α_{RP}. From the figure, it can be observed that the higher the ray power ratio, the higher the achievable secrecy rate. In fact, this is somewhat expected, since the component that the eavesdropper can estimate contributes less to the total channel power. Let us now consider a scenario with imperfect CSI.

Fig. 4.9 shows the secrecy rate when the SNR is 12 dB and different values of α_{RP} are considered. The unknown multipath component introduces a permanent error in the eavesdropper, which accounts for the higher secrecy rate at $\rho_E = 1$, similar to the mismatch error.

In Fig. 4.10, the mismatch error was introduced to the previous scenario. It is clear that the mismatch error leads to an overall increased secrecy rate at all power ratios, since by varying this ratio, only the eavesdropper's channel estimate and the corresponding capacity is affected.

4.2.2 NOMA-SVD

Let us now consider a three user system, where one user, the transmitter A, attempts to communicate with the other two users, receivers B and C. The receivers are separated by a large distance, d, with one receiver, B, being close to the transmitter, while C is placed far from the transmitter. The transmitter employs a power-based NOMA scheme, and transmits both users' signals at the same time. In addition, there is an eavesdropper near each user, attempting to listen to the messages being transmitted. An illustration of this

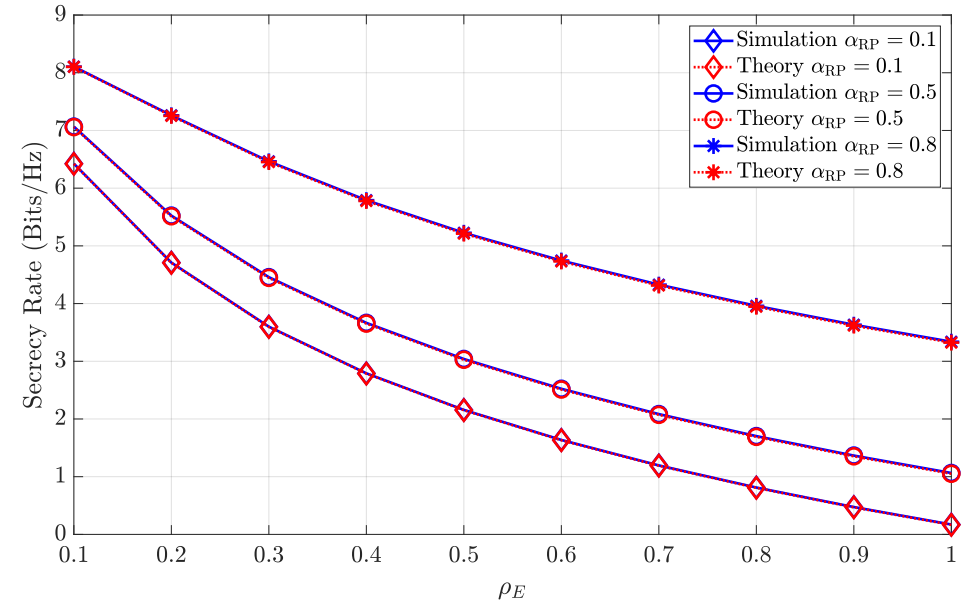

Figure 4.8: Secrecy rate of the system for various ray power ratios with $\beta_N = \infty$.

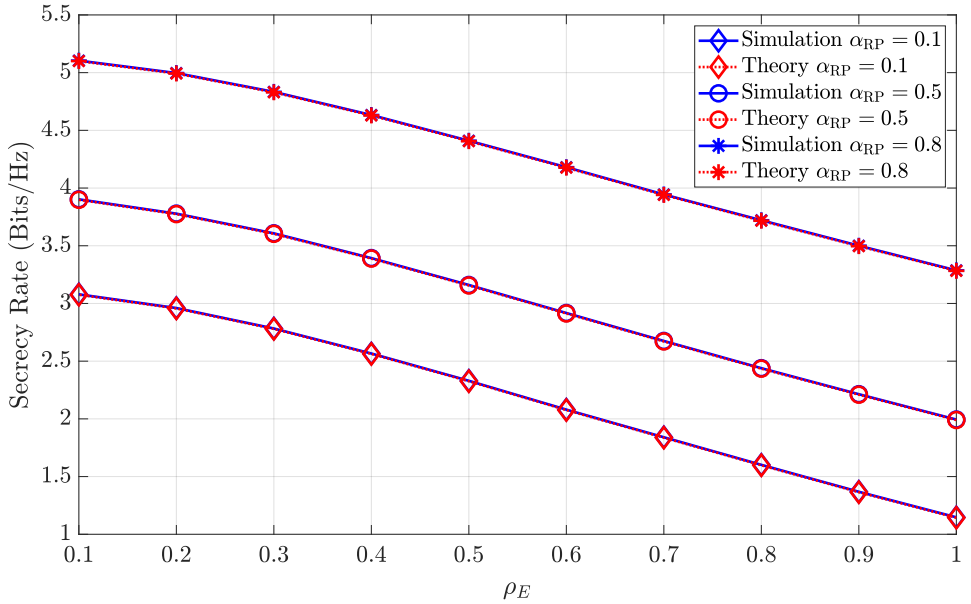

Figure 4.9: Secrecy rate of the system for various ray power ratios with $\beta_N = 100$ at 12 dB SNR.

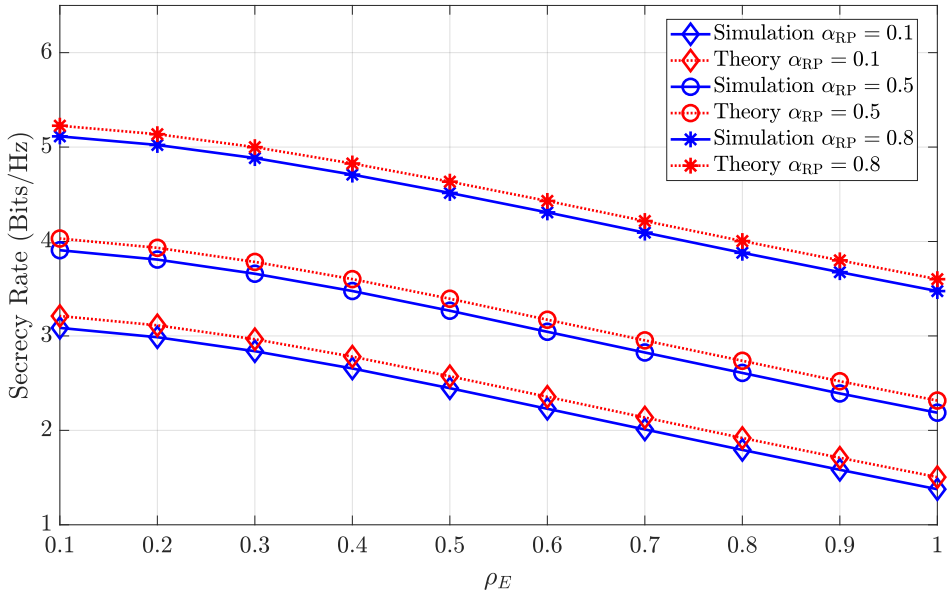

Figure 4.10: Secrecy rate of the system for various ray power ratios with $\beta_N = 100$ and $\beta_M = 10$ at 12 dB SNR.

communication scenario can be seen in Fig. 4.11.

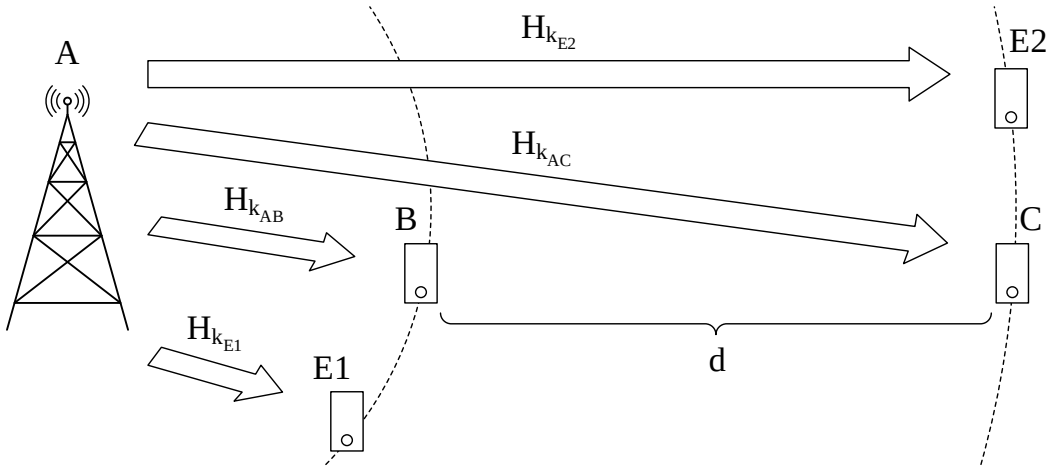

Figure 4.11: A diagram of the proposed NOMA scenario, with three users, 1 transmitting user and 2 receiving users, and 2 eavesdroppers.

Although the transmitter's position may vary, it is assumed that the distance to all other users is always much greater than the wavelength of the transmitted signal. The transmitter employs T antennas, while the receivers and eavesdropper employ R antennas. In order

to handle the highly frequency-selective channel, an SC-FDE technique is employed, combined with an appropriate CP larger than the maximum overall channel impulse response.

The transmitter sends C data blocks, with $C \leq R$, and each data block is composed by the sum of two blocks of N QPSK symbols with differing power. Contrarily to the single-user system studied in [9], the power-domain NOMA scenario of this application requires defining the symbols to be transmitted for both users. The data symbols transmitted for user B are denoted by the $C \times N$ matrix $\mathbf{s}_B$, with each data stream defined as $N \times 1$ vector $\mathbf{s}_B^{(c)} = [s_{1_B}^{(c)}\ s_{2_B}^{(c)}\ \cdots\ s_{N_B}^{(c)}]$. In that context, $s_{n_B}^{(c)}$ represents the QPSK symbol at the nth time instant of the cth data stream. The frequency-domain counterpart of the data to be transmitted is denoted by $\mathbf{S}_B$. The group of symbols associated to the kth subcarrier are defined as $\mathbf{S}_{k_B} = [S_{k_B}^{(1)}\ S_{k_B}^{(2)} \ldots S_{k_B}^{(C)}]$. The symbols for user C are defined identically to the symbols for user B, and denoted by $\mathbf{s}_C$, $\mathbf{s}_C^{(c)}$, $\mathbf{S}_C$ and $\mathbf{S}_{k_C}$, respectively. Under these conditions, the transmitted data at nth time instant is defined as

$$\mathbf{s}_n = \mathbf{s}_B + \mathbf{s}_C, \tag{4.1}$$

with a frequency-domain counterpart defined as

$$\mathbf{S}_k = \mathbf{S}_{k_B} + \mathbf{S}_{k_C}. \tag{4.2}$$

As the two receivers are not co-located, two channels can be defined, one from A to B and another from A to C. The frequency response for the kth subcarrier of the channel from A to B is defined as

$$\mathbf{H}_{k_{AB}} = \begin{bmatrix} H_{k_{AB}}^{(1,1)} & H_{k_{AB}}^{(1,2)} & \cdots & H_{k_{AB}}^{(1,T)} \\ H_{k_{AB}}^{(2,1)} & H_{k_{AB}}^{(2,2)} & \cdots & H_{k_{AB}}^{(2,T)} \\ \vdots & \vdots & \ddots & \vdots \\ H_{k_{AB}}^{(R,1)} & H_{k_{AB}}^{(R,2)} & \cdots & H_{k_{AB}}^{(R,T)} \end{bmatrix}, \tag{4.3}$$

and the frequency response for the kth subcarrier of the channel from A to C is written as

$$\mathbf{H}_{k_{AC}} = \begin{bmatrix} H_{k_{AC}}^{(1,1)} & H_{k_{AC}}^{(1,2)} & \cdots & H_{k_{AC}}^{(1,T)} \\ H_{k_{AC}}^{(2,1)} & H_{k_{AC}}^{(2,2)} & \cdots & H_{k_{AC}}^{(2,T)} \\ \vdots & \vdots & \ddots & \vdots \\ H_{k_{AC}}^{(R,1)} & H_{k_{AC}}^{(R,2)} & \cdots & H_{k_{AC}}^{(R,T)} \end{bmatrix}. \tag{4.4}$$

For separating the different MIMO streams, the system employs SVD for precoding and decoding. Calculating the SVD of the channel matrix requires CSI at both receivers and at the transmitter. This CSI can be obtained through the exchange of pilot sequences at the start of the transmission. In a TDD system, this process is greatly simplified due to the reciprocity of the channel.

The SVD of each channel matrix is defined as

$$\mathbf{H}_{k_{AB}} = \mathbf{U}_{k_{AB}} \mathbf{\Lambda}_{k_{AB}} \mathbf{V}_{k_{AB}}^{H}, \tag{4.5}$$

and

$$\mathbf{H}_{k_{AC}} = \mathbf{U}_{k_{AC}} \mathbf{\Lambda}_{k_{AC}} \mathbf{V}_{k_{AC}}^{H}. \tag{4.6}$$

For simplicity's sake, t the channel identifier (i.e., AB or AC) is omitted when referring to any channel. The $R \times R$ decoding matrix is denoted as $\mathbf{U}_k$, $\mathbf{V}_k$ is the $T \times T$ precoding matrix and $\mathbf{\Lambda}_k$ as a $C \times C$ diagonal matrix composed by the singular values of $\mathbf{H}_k$, which are sorted in descending order according to their power.

4.2.2.1 Eavesdropper

In the scenario where there is a nearby eavesdropper, E, attempting to listen to the message being sent to B, then it must attempt to estimate the channel between A and B. Since an eavesdropper cannot attempt to estimate this channel, it estimates two different channels, namely

$$\mathbf{H}_{k_{EB1}} = \rho_{EB1} \hat{\mathbf{H}}_{k_{EB1}} + \xi_k + \epsilon_k, \tag{4.7}$$

and

$$\mathbf{H}_{k_{EB2}} = \rho_{EB2} \hat{\mathbf{H}}_{k_{EB2}} + \xi_k + \epsilon_k, \tag{4.8}$$

where $\mathbf{H}_{k_{EB1}}$ is the channel between A and E, $\mathbf{H}_{k_{EB2}}$ is the channel between B and E, ρ_{EB1} and ρ_{EB2} are correlation coefficients with the true channels, and ξ_k being an appropriate Gaussian distributed error term with variance σ_N^2/β_M, where β_M is a scaling factor. Since the eavesdropper does not know the channel, it can be assumed that $\rho_{EB1} = \rho_{EB2} < 1$. For simplicity's sake, it is considered that $\rho_{EB1} = \rho_{EB2} = \rho_{EB}$.

If the eavesdropper is attempting to listen to signals sent to user C, then these expressions can be written as

$$\mathbf{H}_{k_{EC1}} = \rho_{EC1} \hat{\mathbf{H}}_{k_{EC1}} + \xi_k + \epsilon_k, \tag{4.9}$$

and

$$\mathbf{H}_{k_{EC2}} = \rho_{EC2} \hat{\mathbf{H}}_{k_{EC2}} + \xi_k + \epsilon_k, \tag{4.10}$$

where $\mathbf{H}_{k_{EC1}}$ is the channel between A and E, $\mathbf{H}_{k_{EC2}}$ is the channel between B and E, and ρ_{EC1} and ρ_{EC2} are correlation coefficients with the true channels. As was the case for user B, it can be assumed that $\rho_{EC1} = \rho_{EC2} < 1$. For simplicity's sake, it is considered that $\rho_{EC1} = \rho_{EC2} = \rho_{EC}$.

In order to increase the accuracy of the channel estimate, the receiver can compute the average of both intermediate channels, i.e.

$$\mathbf{H}_{k_{AB}} = \frac{\mathbf{H}_{k_{EB1}} + \mathbf{H}_{k_{EB2}}}{2}, \tag{4.11}$$

if eavesdropping user B, and

$$\mathbf{H}_{k_{AC}} = \frac{\mathbf{H}_{k_{EC1}} + \mathbf{H}_{k_{EC2}}}{2}, \tag{4.12}$$

for user C.

4.2.2.2 Secrecy Rate Results

Fig. 4.12 shows a comparison of the secrecy rate for both channels considering both a SISO and MIMO configuration.

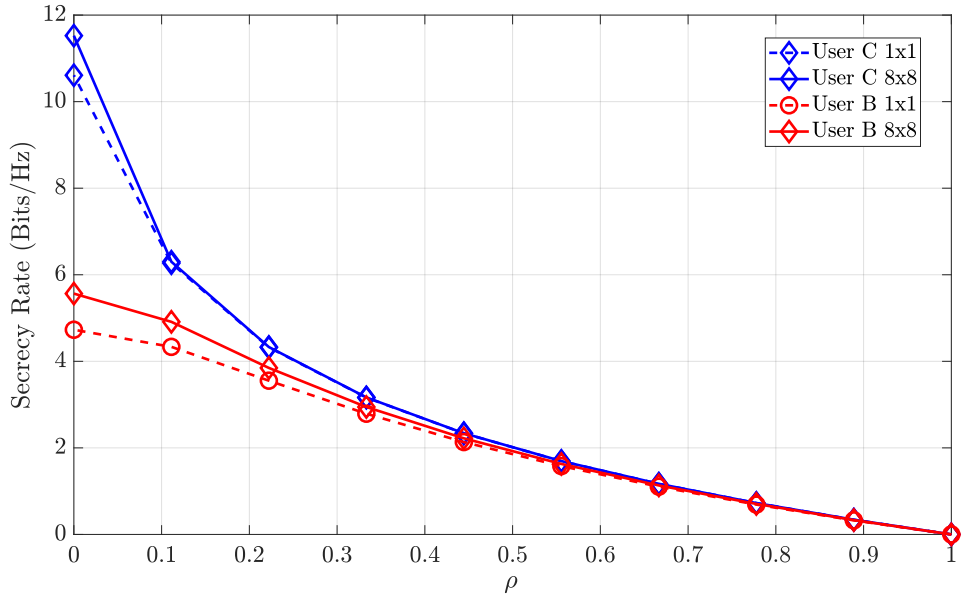

Figure 4.12: Secrecy rate for SISO and MIMO configurations considering perfect channel estimation. In this graph, ρ refers to either ρ_{EB} or ρ_{EC}, according to the user in question.

From the figure, it can be concluded that employing MIMO leads to a higher achievable secrecy rate at lower values of ρ_{EB} and ρ_{EC}.

User B Results The following results analyse the secrecy rate of the nearest user. Beginning with Fig. 4.13, which depicts the secrecy rate of user B under various channel estimation errors. It can be seen that minimising the channel estimation error in the receiver is crucial to ensuring a high secrecy rate. For low values of ρ_{EB}, this receiver achieves significant levels of secrecy rate.

In Fig. 4.14, the channel mismatch error is introduced. It is observed that maximum achievable secrecy rate, for low values of ρ_{EB}, increases as the channel estimation error decreases. It should be noted that in this scenario, since the channel mismatch error does not affect the intended receiver, the secrecy rate for high values of ρ_{EB} is also higher and cannot be compensated by decreasing the channel estimation error.

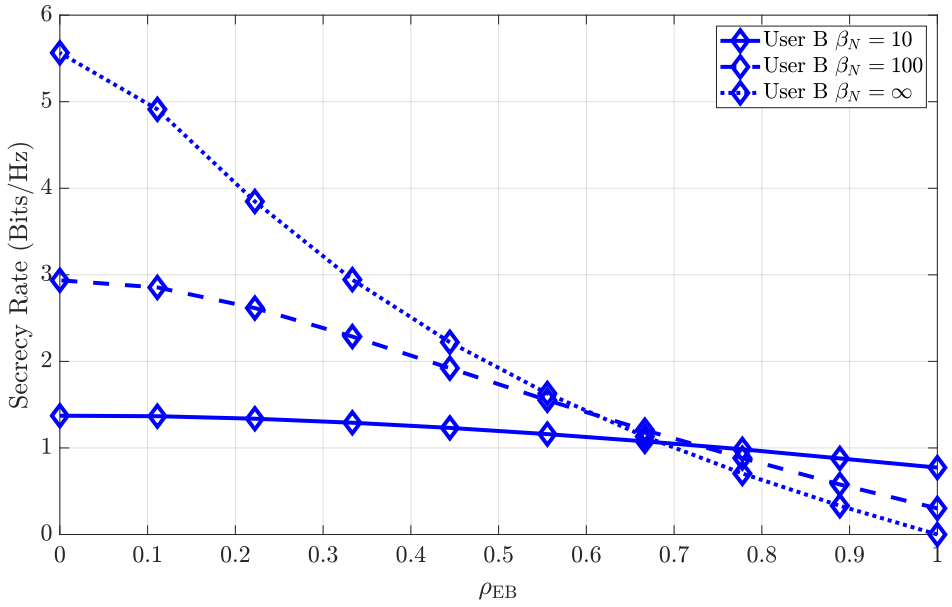

Figure 4.13: Secrecy rate of the 8×8 receiver B with different channel estimation errors.

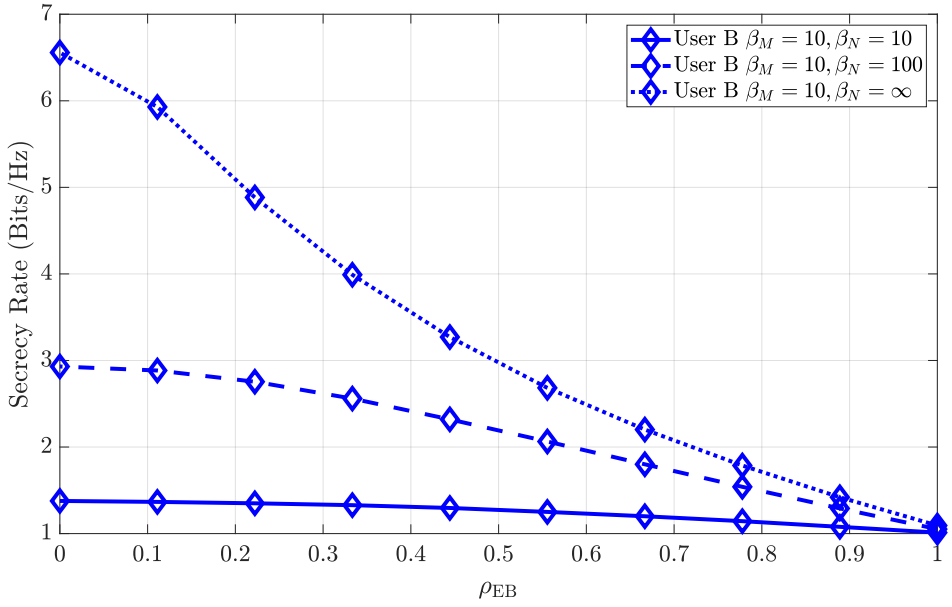

Figure 4.14: Secrecy rate of the 8×8 receiver B with different channel estimation errors and a permanent channel mismatch error.

Line-of-Sight at User B In this scenario there is a LoS with all users. Therefore, the impact of the power ratio α_{RP} on the attainable secrecy rate was analysed. In Fig. 4.15 the secrecy rate for various values of α_{RP} is shown for user B. As expected, since the

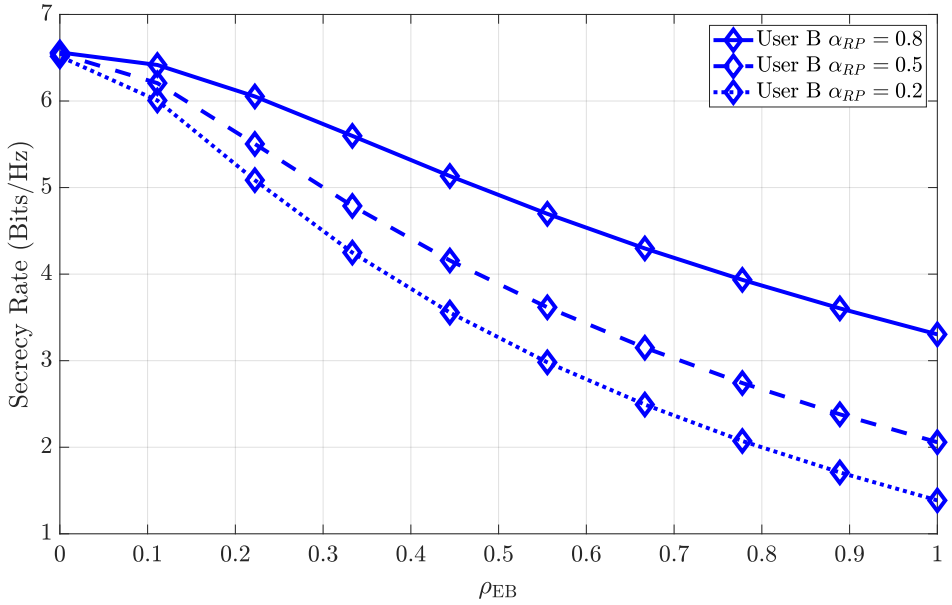

Figure 4.15: Secrecy rate of the 8×8 LOS receiver B with perfect channel estimation and varying ray power coefficient.

eavesdropper cannot estimate the multipath component, the greater the value of α_{RP} the more secure the system can be.

Fig. 4.16 shows the secrecy rate in a scenario where there is imperfect channel estimation. It can be observed that the channel estimation severely degrades the secrecy rate, however, even for high values of ρ_{EB} and ρ_{EC}, the secrecy rate remains high, when compared with the non LoS scenario, due to the multipath component. Fig. 4.17 shows the impact of a channel mismatch error in the secrecy rate. It can be concluded that the permanent channel mismatch error increases the secrecy rate for high values of ρ_{EB}, albeit the increase is relatively small, when compared with the non LoS scenario. Since the lack of a multipath estimation produces a much more significant effect on the secrecy rate, then a further channel mismatch error has a smaller impact on the secrecy rate.

User C Results The following results analyse the secrecy rate at the farthest user. Fig. 4.18 shows the secrecy rate of user C under different levels of channel estimation error. In this case, the maximum achievable secrecy rate is higher than the one of user B, due to the increased capacity of the channel with higher transmit power. The effect of minimising the channel estimation error of the receiver is significantly more noticeable in this scenario, at low values of ρ_{EC}.

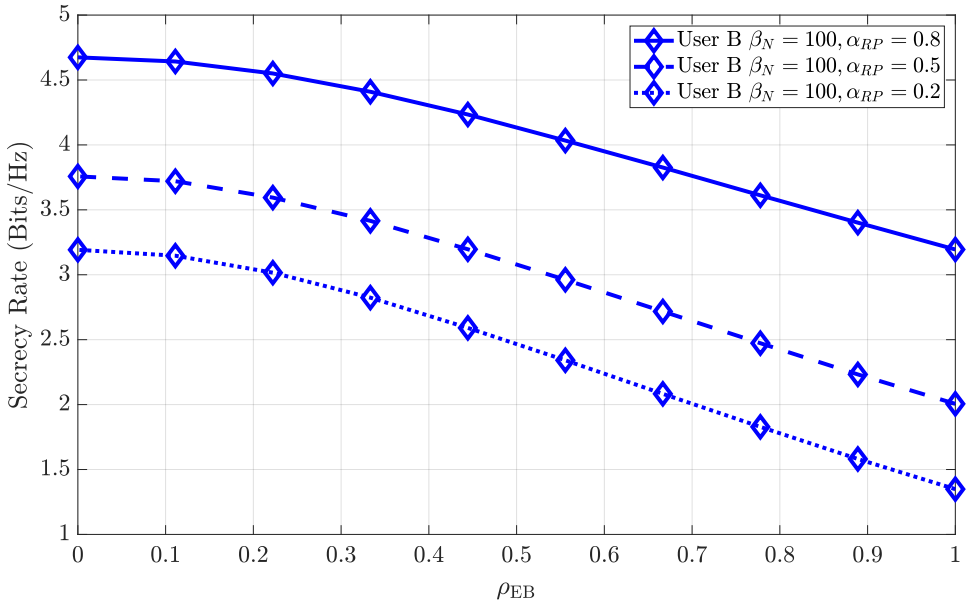

Figure 4.16: Secrecy rate of the 8×8 receiver B with channel estimation errors on both receiver and eavesdropper, for various ray power coefficients.

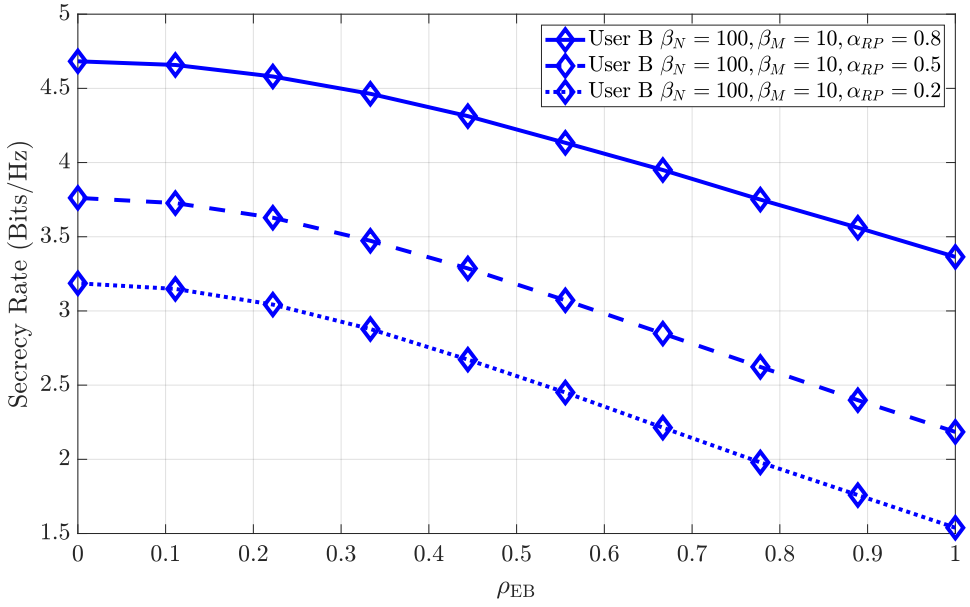

Figure 4.17: Secrecy rate of the 8×8 receiver B with channel estimation errors on both receiver and eavesdropper, as well as a permanent channel mismatch error, for various ray power coefficients.

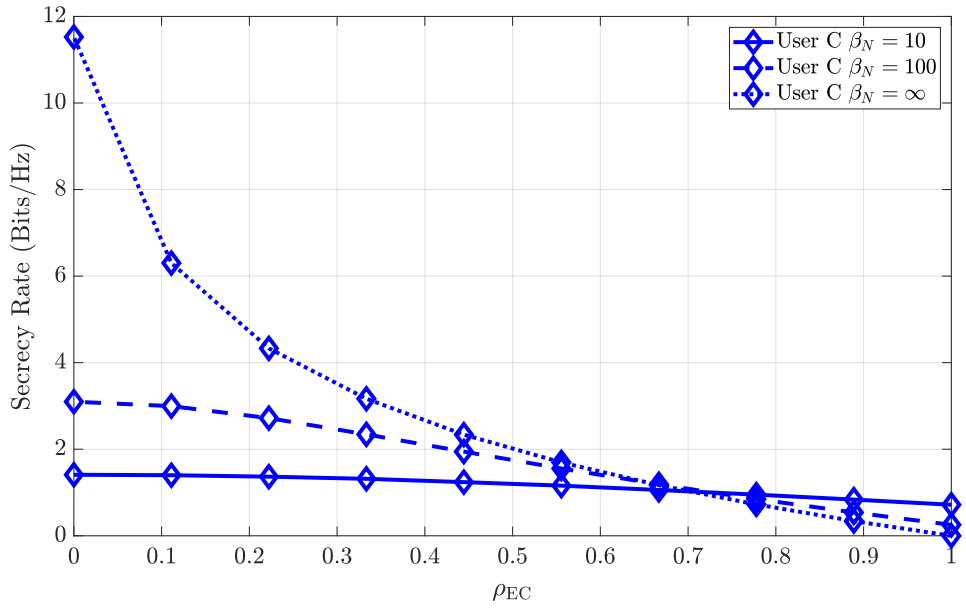

Figure 4.18: Secrecy rate of the 8×8 receiver C with different channel estimation errors.

In Fig. 4.19, the secrecy rate of user C is simulated under imperfect channel estimation, as well as a channel mismatch error at the eavesdropper. It can be seen that, similarly to user B, this system achieves a higher maximum secrecy rate, at low values of ρ_{EC}, and a higher secrecy rate, even for high values ρ_{EC}.

Line-of-Sight at User C The LoS scenario analysed the impact of the power ratio α_{RP} on the attainable secrecy rate for user C. In Fig. 4.20 the secrecy rate for various values of α_{RP} is shown. Similarly, for a higher contribution of the multipath component, the achievable secrecy increases. Since in this case there is perfect channel estimation, then user C achieves a much higher maximum secrecy rate than user B, due to its higher channel capacity.

Fig. 4.21 shows the secrecy rate for various values of α_{RP}, in the presence of channel estimation errors. In this case, the channel estimation error lowers the overall secrecy rate, however, the degradation is less severe for higher power multipath components. Moreover, it should be noted that user C's secrecy rate is degraded much more than user B's, as user C requires very precise channel estimation.

Fig. 4.22 shows the secrecy rate for various values of α_{RP} and various sources of channel estimation errors. As is the case for user B, the increase in the secrecy rate at high ρ_{EC} is relatively small, compared to the no LoS scenario, as the LoS component contributes less in this scenario.

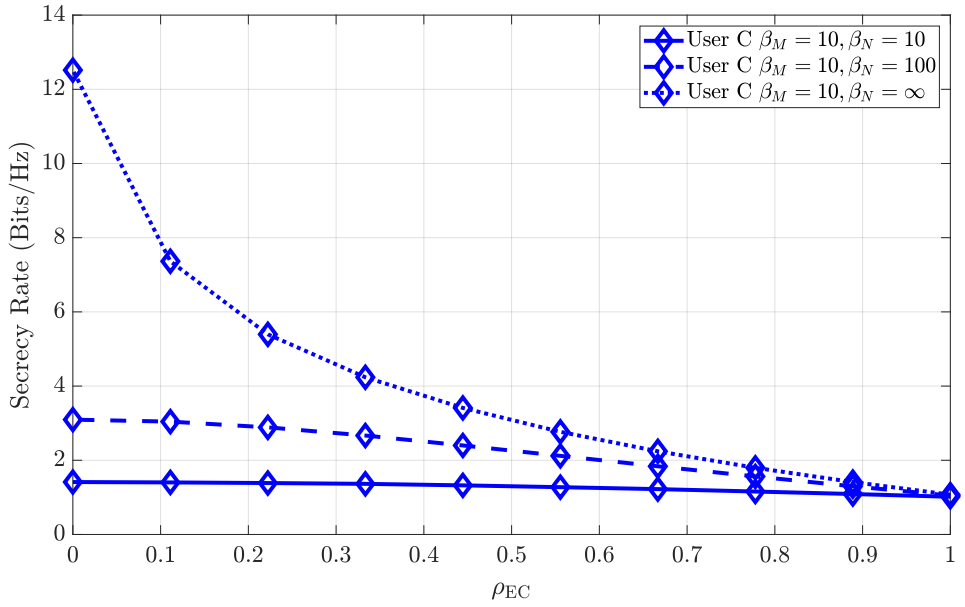

Figure 4.19: Secrecy rate of the 8×8 receiver C with different channel estimation errors and a permanent channel mismatch error.

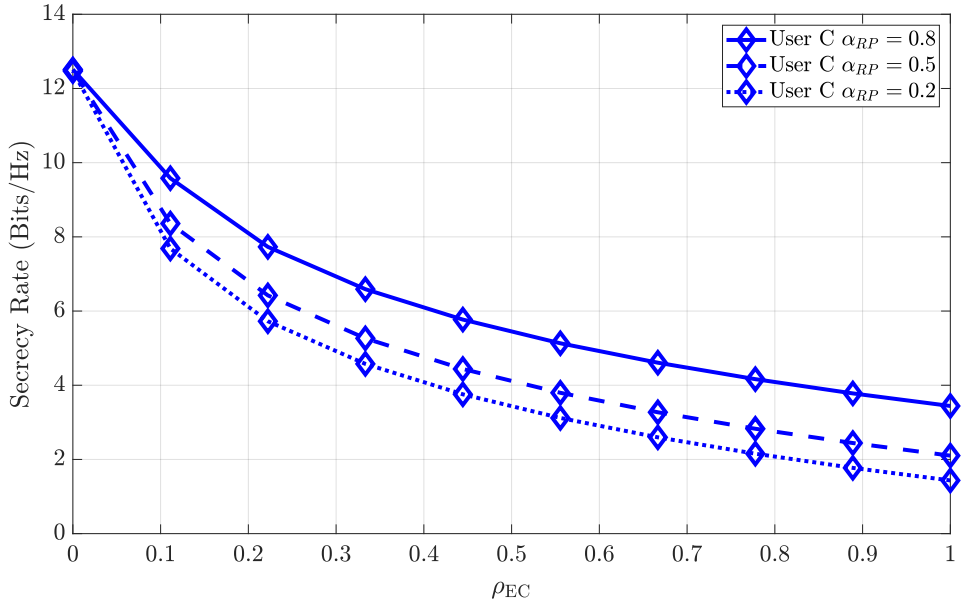

Figure 4.20: Secrecy rate of the 8×8 LOS receiver C with perfect channel estimation and varying ray power coefficient.

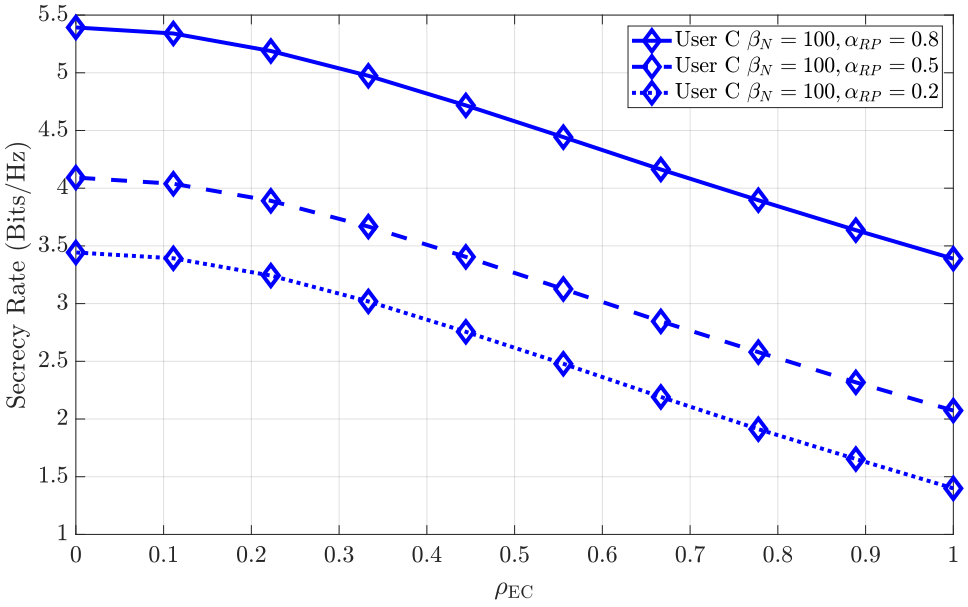

Figure 4.21: Secrecy rate of the 8×8 receiver C with channel estimation errors on both receiver and eavesdropper, for various ray power coefficients.

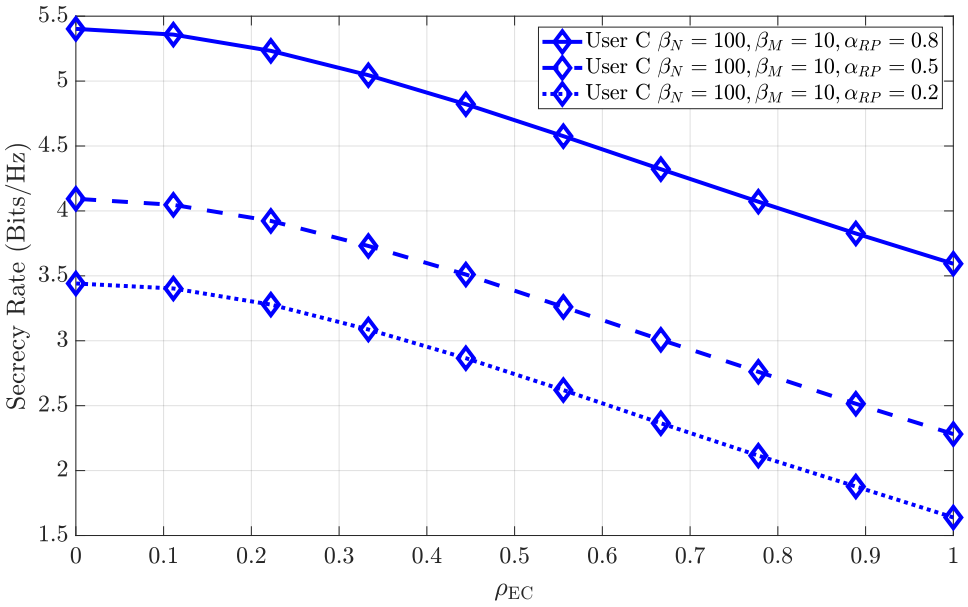

Figure 4.22: Secrecy rate of the 8×8 receiver C with channel estimation errors on both receiver and eavesdropper, as well as a permanent channel mismatch error, for various ray power coefficients.

4.2.3 Cathlab

The evolution of medical imaging technology has allowed for the diagnosis and treatment of pathologies that could not be properly observed before these techniques. One such example are the Intravascular Ultrasound (IVUS) techniques employed in the Catheterization Laboratory (CathLab) [118]. The IVUS provides high resolution images of the arteries and chambers of the heart through a very small camera that is inserted in the patient's arteries through a catheter. In current IVUS implementations, the image obtained from the sensors is then transmitted through a wired communication to the central device that displays the image to the medical personal [119]. In the general case, the sensors are terminated by a connector that is plugged to a cable which is then plugged to the central device. The wired nature of the communication raises severe problems, since it reduces the mobility and flexibility, not to mention the associated sterilization difficulties. An example of a conventional CathLab is shown in Fig. 4.23. To overcome these difficulties, there is a desire to have a wireless CathLab, with the wireless IVUS presenting the most difficult challenge

Figure 4.23: Picture of a wired CathLab, courtesy of Philips.

In practice, since the wireless devices will be powered by batteries, the transmitter must be highly power efficient [120]. Moreover, the highly miniaturized nature of the IVUS means limited signal processing capabilities, especially on the transmitter side, which precludes the use of video encoding hardware, and leads to signals with very high data rate, from 300 Mpbs to 1Gbps or more. Additionally, the IVUS requires a reliable, secure and low latency communication, which begets a wireless link with highly demanding QoS.

These rates could be achieved by employing OFDM techniques in a MIMO system [121]. The channel capacity gains of MIMO systems over traditional SISO systems [35], are the main reason why they are being widely employed in wireless communication standards, such as 5G and 802.11. However, the MIMO capacity gain from using MIMO requires channels with small correlation [122], which may be difficult to achieve in the CathLab environment, as shown in [121]. Therefore, it might be necessary to employ high order constellations such as M-QAM to further increase the spectral efficiency.

On the other hand, the wireless nature of the channel poses an additional security problem. In fact, an eavesdropper in an adjacent room could tap the wireless signal and view the image results of the test, raising problems of patient confidentiality. Since the sensors have low computational capabilities due to their size, PLS schemes are preferred [94]. And, due to the high data rates needed, a scheme that does not decrease the effective data rate is required.

This scenario considers the design of a communication system for a wireless IVUS. A MIMO system is employed, with an SVD technique to separate the different MIMO streams. It is shown that this technique can achieve a high level of PLS in the presence of an eavesdropper, without introducing significant added complexity.

4.2.3.1 System Characterization

In the CathLab, a patient has an IVUS catheter inserted, which is connected to a Patient Interface Module (PIM). This module will be located in the doctor's hand, and is responsible for wirelessly transmitting the images obtained from the IVUS to a receiver, which is installed in the stretcher where the patient is laying down or close to it. Consider a MIMO system where the PIM's transmitter front-end is equipped with T antennas and the receiver in the stretcher is equipped with R antennas. The maximum number of individual data streams that can be sent over the channel is $C = \min(T, R)$. The sender and receiver will henceforth be referred to as Alice and Bob, or A and B for short, respectively. Additionally, the presence of a third user Eve, or E for short, who is trying to eavesdrop the wireless signal is considered. Eve is located outside of the room and will employ the same receiving techniques as Bob. A diagram of the three user scenario is shown in Fig. 4.24.

In a real CathLab environment, the MIMO channels are not fully uncorrelated, which can be explained by the poor multipath environment of the CathLab room. Therefore, the theoretical channel capacity associated to MIMO schemes might not be achieved in practice, even when the antenna separation at the receiver, d_R, is much larger than half of the carrier wavelength (i.e., $d_R > \lambda/2$). A more accurate channel model of this particular environment was proposed in [121], which takes into account the room geometry and uses ray tracing techniques to derive the CIR. This model was used to generate the CIR in

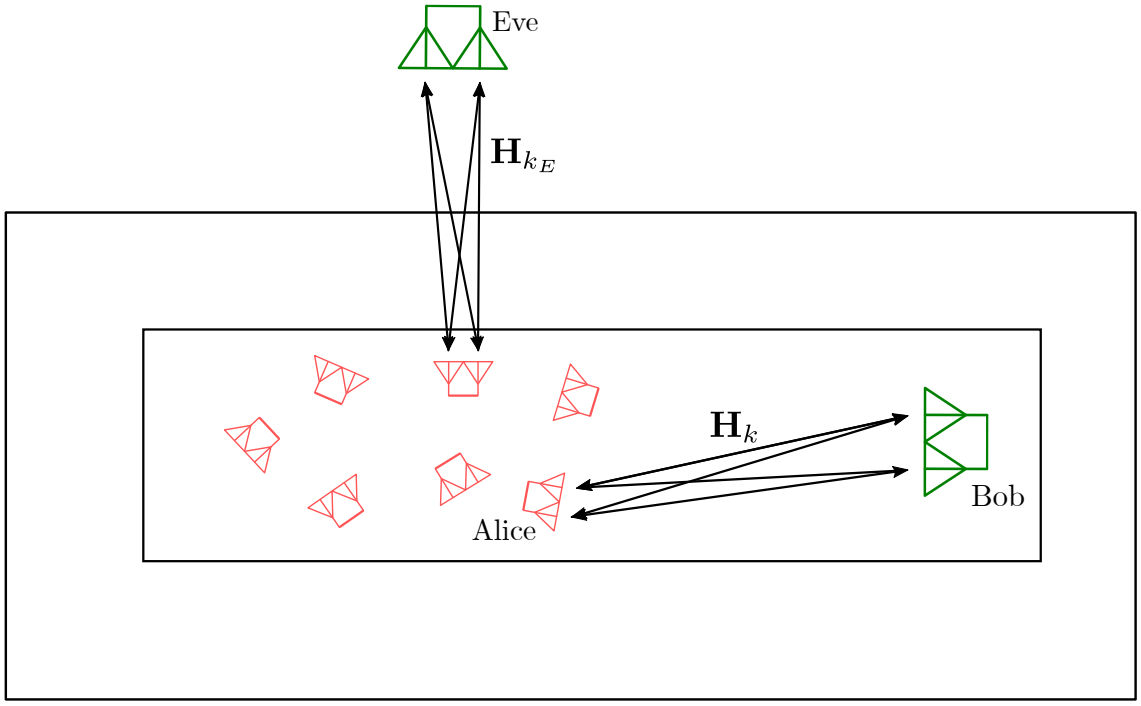

Figure 4.24: Diagram of a stretcher inside a room, with the 2×2 three user system, where Eve is located outside the room with the machine. The red antennas represent various positions where the PIM can be located.

this scenario, defining the channel frequency response at the kth subcarrier, $\mathbf{H}_k$, as

$$\mathbf{H}_k = \begin{bmatrix} H_k^{(1,1)} & H_k^{(1,2)} & \cdots & H_k^{(1,T)} \\ H_k^{(2,1)} & H_k^{(2,2)} & \cdots & H_k^{(2,T)} \\ \vdots & \vdots & \ddots & \vdots \\ H_k^{(R,1)} & H_k^{(R,2)} & \cdots & H_k^{(R,T)} \end{bmatrix}. \tag{4.13}$$

An interleaved SVD scheme was used to separate the different data streams.

4.2.3.2 Simulation Results

The system performance system was evaluated by simulation considering OFDM blocks with $N = 120$ subcarriers. For each OFDM block, a CathLab channel realization with $N_{ray} = 5$ multipath components is generated. Unless otherwise stated, the antenna separation at the receiver is $d_R = 2.5\lambda$.

Fig. 4.25 presents the BER of the proposed system for MIMO scenarios with size 2×2 and 4×4. As can be noted from the figure, the performance for each stream is strongly dependent on the power of the corresponding singular value. For a target BER of 10^{-4} in all streams, an $\frac{E_b}{N_0}$ greater than 35 dB would be required for 4×4. This performance can be greatly improved by performing a bit interleaving operation, which has the added benefit of improving the error correcting capability of the decoder.

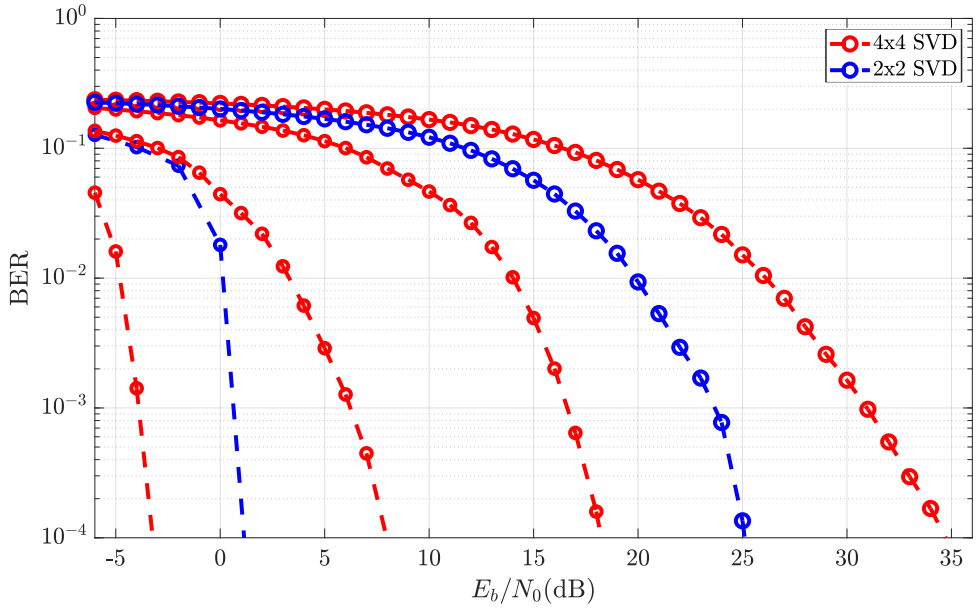

Figure 4.25: BER for different MIMO configurations, with $d_R = 2.5\lambda$.

Fig. 4.26 presents the BER for the interleaved system, considering different antenna separations. As can be observed, for the same target BER of 10^{-4}, this implementation

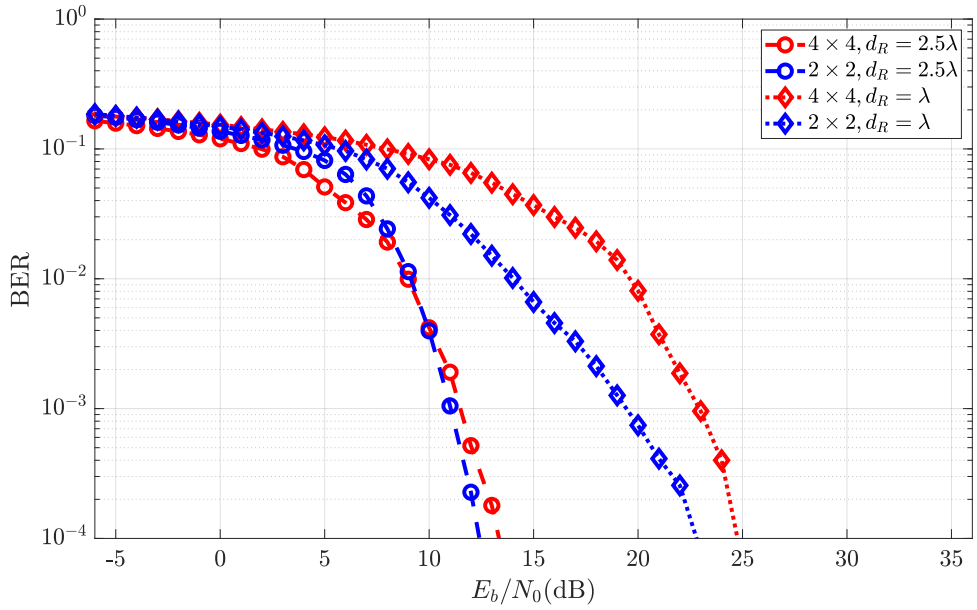

Figure 4.26: BER with bit interleaving for different antenna spacements.

requires an $\frac{E_b}{N_0}$ below 14 dB for both MIMO scenarios. Moreover, it can be observed that, for the same target BER of 10^{-4}, an increase of 1.5λ in d_R can boost performance by about

11 dB. In particular, the 4×4 system achieves a greater performance increase than the 2×2, due to the higher performance gain for the weaker singular values.

4.2.3.3 Secrecy Rate

The secrecy rate of the system is shown in Fig. 4.27, for the scenarios of 2×2 and 4×4. From the figure, it can be observed that for low values of ρ_E, the secrecy rate is proportional to the number of antennas, offering a good security performance. Moreover, it can be noted that the achievable secrecy rate is higher for larger values of d_R, particularly for the 4×4 MIMO configuration. If the existence of the additional error due to the channel differences

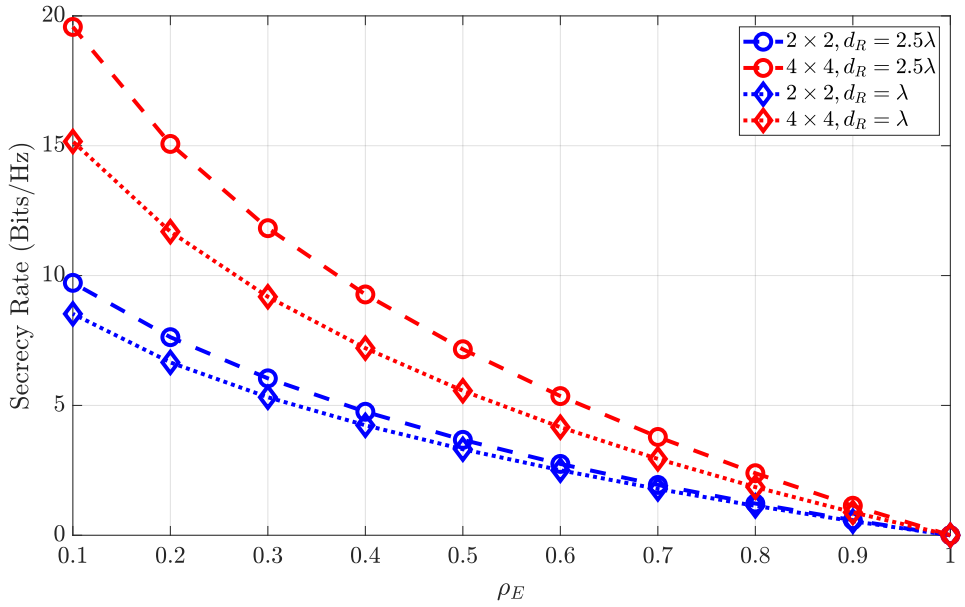

Figure 4.27: Secrecy rate considering 2×2 and 4×4 MIMO configurations and different values of ρ_E and d_R.

is considered, then the achievable secrecy rates will increase, as shown in Fig. 4.28, where it can be observed that even for higher ρ_E values, the secrecy rate is significantly higher than the one obtained in the scenario of Fig. 4.27.

Fig. 4.29 shows the same scenario for the 4×4 system. From the figure, it can be concluded that the potential secrecy rate gains are relatively higher when compared to the 2×2 MIMO configuration, since the interference degrades the channel capacity further for higher order systems.

4.2.4 SDR Prototype

The OFDM SVD system from the previous section was implemented using two Ettus USRP B210 devices, using the GNURadio framework [105]. Both devices are connected to a host computer, which is responsible for generating and streaming the complex data

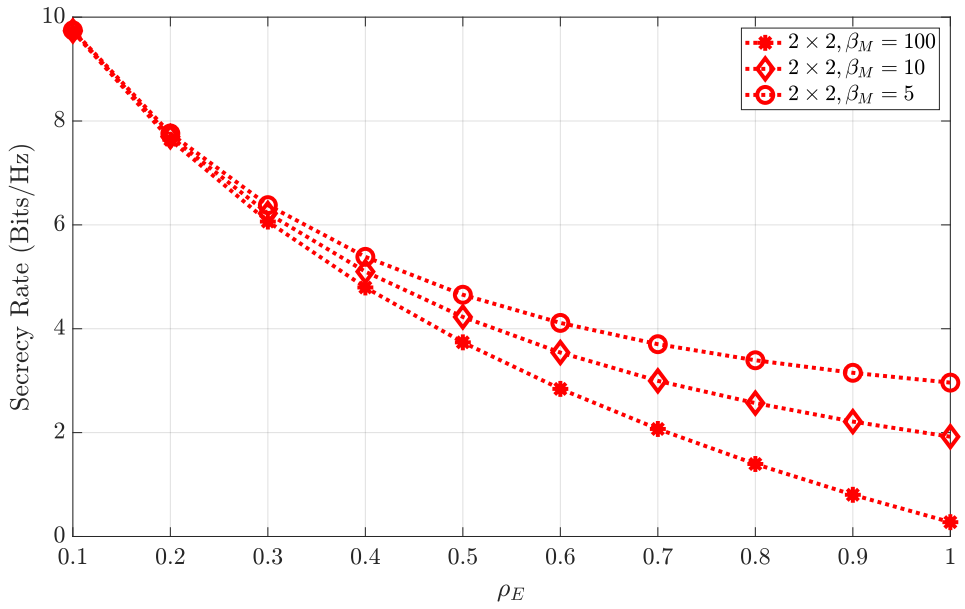

Figure 4.28: Secrecy rate of the 2×2 system with different levels of β and different values of ρ_E.

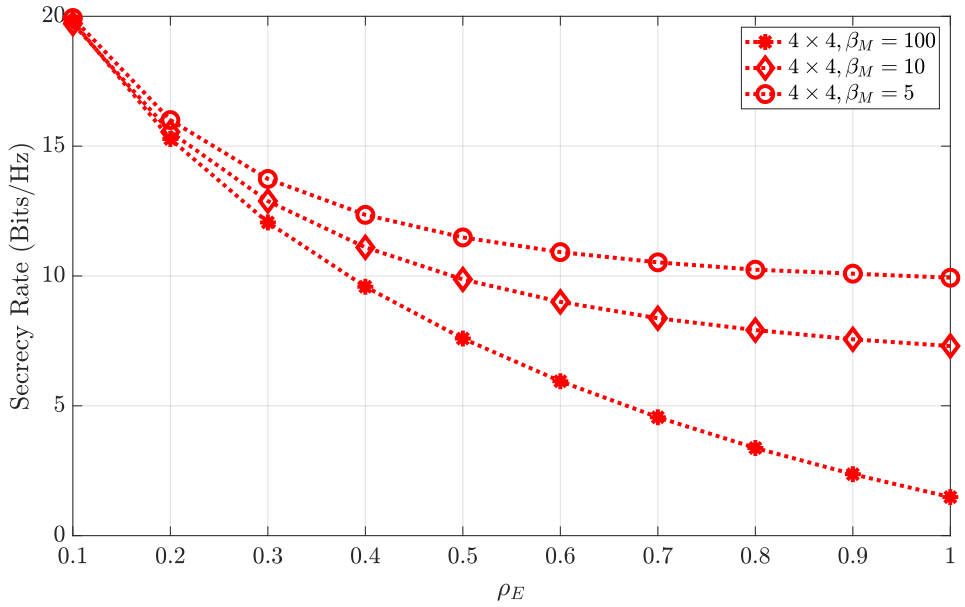

Figure 4.29: Secrecy rate of the 4×4 system with different levels of channel differences, for different values of ρ_E.

symbols to the USRPs. The signal processing tasks in GNURadio are defined using blocks that provide an interactive Python API for functions implemented in either Python or C++. The blocks are then inserted into a flowgraph, which contains the connections between all blocks. The flowgraph is then compiled into a python file, which when run initializes each blocks and begins the sample processing. This implementation utilizes $R = T = C = 2$ antennas at each device, and have split the data transmission into two distinct flowgraphs: one responsible for estimating the channel and generating the precoded symbols, shown in Fig. 4.30, a second responsible for the transmission of the precoded signal to the intended receiver, shown in Fig. 4.31. The interface with the SDR devices, namely with the RF transceivers, is done with the USRP source and sink blocks, for reception and transmission, respectively.

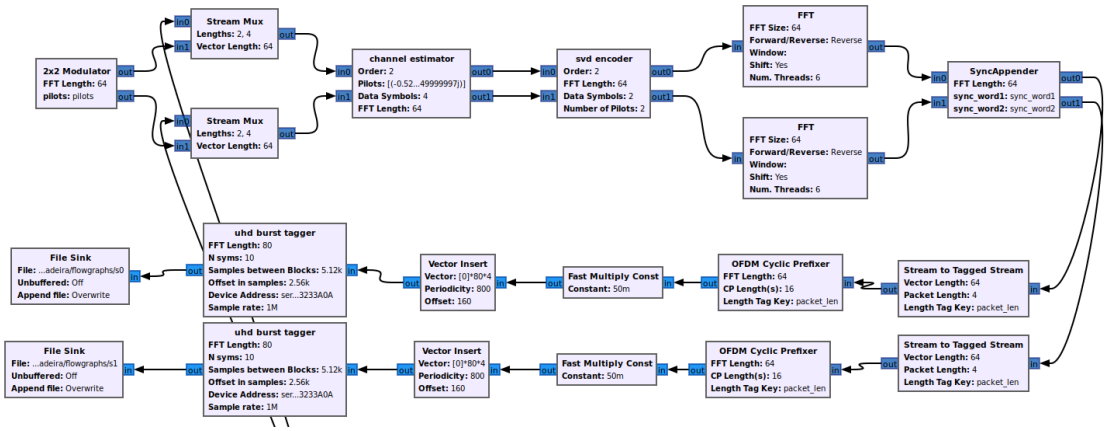

Figure 4.30: Gnuradio flowchart that implements the transmitting user.

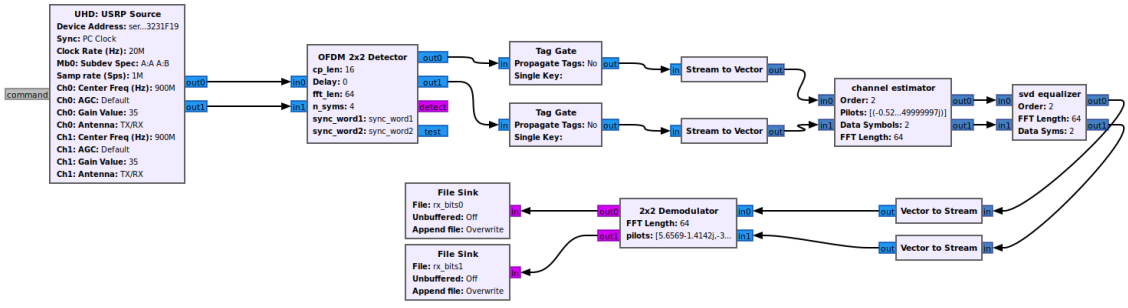

Figure 4.31: Gnuradio flowchart that implements the receiving user.

4.2.4.1 Blocks

These flowgraphs utilize several custom blocks to perform the signal processing functions of the proposed system. The blocks were implemented either as C++ code, or as "hier" blocks, which are blocks generated from a flowchart.

OFDM 2x2 Detector This hier block is responsible for detecting the OFDM preamble in the input data and outputting the information contained in the OFDM block, correctly synchronized in the time domain, thereby ensuring that the FFT window of samples is correctly aligned. This block produces no samples until it detects a preamble, and the unused output ports are used for debugging purposes.

Channel Estimator C++ block responsible for obtaining the channel estimation from the OFDM symbol at its input. It multiplies the incoming pilot symbols by the inverse pilot matrix, defined as

$$\hat{\mathbf{H}}_k = \mathbf{Y}_k \mathbf{P}_k^{-1}, \tag{4.14}$$

where $\mathbf{P}_k$ is the invertible matrix containing the pilot symbols. The channel estimate is then passed on to the next blocks using a tag object, while the data symbol samples, without the pilots, are sent to the output.

2x2 Modulator and Demodulator The hier modulator and demodulator are responsible for generating the modulated complex samples and decoding the received symbols, respectively. Although in this work it is configured to support M-QAM, it can be used with other modulation schemes. The modulator also prepends the pilot symbols to the data symbol, considering the specified data-pilot ratio.

SVD Encoder and Equalizer The SVD algorithm is implemented by using two different C++ blocks, one for the transmitter and the other for the receiver. The transmitter utilizes the encoder to perform the SVD precoding operation on the data symbols, skipping over the pilot symbols in the OFDM block. The equalizer is used in the receiver to perform both the SVD decoding, as well as the ZF equalization using the singular value matrix. In both blocks, the SVD is computed using the channel estimate produced in the channel estimator block.

Sync Appender This is a simple hier block that appends the preamble to the OFDM block.

UHD Burst Tagger In order to set the USRPs to use TDD, it is necessary to tag each OFDM block with a start and end tags, as well as a transmit time tag. This block tags the data in the correct samples, as well as calculate the time when a block should be transmitted, to ensure it does not collide with an opposite direction transmission.

Synchronization The OFDM synchronization between the two users is achieved through the well-known Schmidl and Cox algorithm [41], which consists in transmitting a preamble before the OFDM symbols. The preamble is composed of two training symbols, $\mathbf{c}_1$ and $\mathbf{c}_2$, which are used for symbol timing and carrier frequency offset estimation. At the nth sample a symbol timing metric, $M(n)$, is computed for the cth stream as

$$M(n) = \frac{|P(n)|^2}{(R^2(n))}, \tag{4.15}$$

where $P(n)$ is the correlation between the two halves of incoming symbol, defined as

$$P(n) = \sum_{d}^{\frac{N}{2}-1} y_{n+d}^{(c)*} y_{n+d+\frac{N}{2}}^{(c)}, \tag{4.16}$$

and $R(n)$ is a normalization factor computed as

$$R(n) = \frac{1}{2} \sum_{d}^{N-1} |y_{n+d}^{(c)}|^2. \tag{4.17}$$

If the timing metric is above the detection threshold, i.e. $M(n) > m_{th}$, then a symbol is detected at sample n. For C different streams, each timing is computed separately and a symbol detected only if all metrics are above the detection threshold.

The carrier frequency offset estimate is defined as

$$\hat{\delta}_f = \frac{\hat{\phi}}{T_s \pi} + \frac{2\hat{g}}{T_s}, \tag{4.18}$$

where $\hat{\phi}$ is obtained by angle$(P(n))$, and $\hat{g}$ is chosen to maximise the expression

$$B(g) = \frac{\sum_{i \in I} Y_{i+2g}^{(c)*} V_i^* Y_{N+i+2g}^{(c)}}{2 \sum_{i \in I} |Y_{N+i}^{(c)}|^2}, \tag{4.19}$$

where I is the set of even subcarrier indices, $Y^{(c)}$ is the frequency domain counterpart of the detected preamble, and $\mathbf{V}$ is the differential sync word defined as $\sqrt{2}\frac{\mathbf{c}_2}{\mathbf{c}_1}$.

4.2.4.2 Performance Results

This implementation considers a $T = R = C = 2$ MIMO system, with a static two tap fading channel, where the interference between streams is constant. The interference is statically set by using an auxiliary matrix $\mathbf{L}_k$, with the equivalent channel being defined as $\mathbf{L}_k \mathbf{H}_k$. The number of subcarriers was fixed at $N = 64$, with all subcarriers carrying data. The carrier frequency was set to 900 MHz, which is an appropriate carrier for both LTE and 5G systems, while the bandwidth was set to 1 MHz due to the sample rate of the SDR. The USRPs utilize 20 MHz internal clock. The sync words were defined using a Zhadoff-Chu sequence with a certain seed s [123], $\mathbf{Z}_s$. The first sync word is defined as

$$c_{1,k} = \begin{cases} Z_1(\frac{k}{2}), & \text{mod } (k,2) < 1 \\ 0, & \text{mod } (k,2) \geq 1. \end{cases} \tag{4.20}$$

Table 4.1: Summary of the results from the prototype testing.

Parameter	A to B		A to E	
Carrier freq.	900 MHz			
Bandwidth	1 MHz			
USRP Clock	20 MHz			
Data Symbols	2			
Modulation	QPSK	16-QAM	QPSK	16-QAM
BER_0	0.89%	1.75%	38.3%	49.5%
BER_1	0.57%	5.47%	23.6%	35.9%
EVM_0	12.8%	13.8%	57.7%	70%
EVM_1	16.1%	20.8%	46.8%	67.5%

The second sync word was similarly defined as

$$c_{2,k} = \begin{cases} Z_7(\frac{k}{2}), & \text{mod } (k,2) < 1 \\ Z_{13}(\frac{k}{2}), & \text{mod } (k,2) \geq 1. \end{cases} \tag{4.21}$$

In the first scenario, $\mathbf{L}_k$ is defined as

$$\mathbf{L}_k = \begin{bmatrix} 1.3\exp(1j) & 0.5\exp(1.5j) \\ 0.9\exp(2.4j) & 0.8\exp(1j) \end{bmatrix}, \tag{4.22}$$

While the matrix for the eavesdropper, $\mathbf{L}_{k_E}$, was defined as

$$\mathbf{L}_{k_E} = \begin{bmatrix} 1.1e^{1.5j} & 0.8e^{0.5j} \\ 0.7e^{1.4j} & 1.1e^{1.5j} \end{bmatrix}, \tag{4.23}$$

and the equivalent eavesdropper channel is defined as $\mathbf{L}_{k_E}\mathbf{H}_{k_E}$. The BER and EVM were selected as metrics to evaluate the performance of the prototype.

Two different modulation schemes were considered: QPSK and 16-QAM. The legitimate and eavesdropped prototypes were tested using these settings, producing the BER and EVM results shown in Table 4.1.

The QPSK legitimate system achieved an average BER of 0.89% and 0.57%, with an EVM of 12.8% and 16.1%, for the first and second streams, respectively. The first stream is associated with a stronger singular value, which leads to a smaller EVM on that stream. The BER is higher due to symbol mapping of QPSK, which has only 2 adjacent symbols per symbol. In the case of 16-QAM, the average BER is 1.75% and 5.47%, while the EVM is 14.5% and 16.6%, for the first and second streams, respectively. The BER is noticeably worse, particularly for the second stream, which is associated with the weakest singular value. The EVM degradation is due to the reduced bit energy, E_b, of the larger constellation. The simulated BER of the system is shown in Fig. 4.32.

The measurements from the prototype are highlighted in the same figure for reference. It should be noted that the theoretical model does not account for imperfect channel

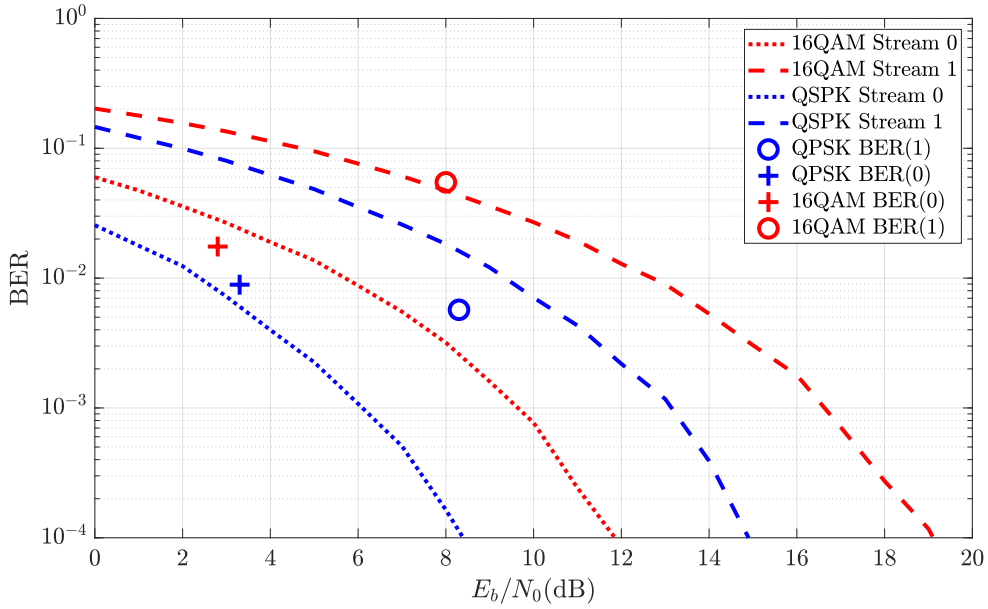

Figure 4.32: BER for the two chosen modulations, with markers for the BER of the prototype.

estimation and nonlinear effects in the RF chain, which can explain the discrepancy between simulated and measured results. The eavesdropper was tested by receiving the exact same signal as the legitimate receiver, albeit with a different equivalent channel. In the case of QPSK, the eavesdropper achieved an average BER of 38.3% and 23.6%, with an EVM of 57.7% and 46.8%, for the first and second streams, respectively. In contrast with the legitimate receiver, the BER is significantly higher, even for the largest singular value, which is confirmed by the large EVM. Due to the mismatch in the SVD decoding, the stream selected by the eavesdropper as having the highest singular value may not be the same as the one associated to the legitimate channel. Therefore, it would be difficult for the eavesdropper to decode any information in this system. If the system uses 16-QAM, then eavesdropping becomes even harder. The average BER in this case was 49.5% and 35.9%, with an EVM of 70% and 67.5%, for the first and second streams, respectively. In this scenario, the eavesdropper cannot decode any one of the streams at all, since BER is close to a 50%, while the other is significantly impaired. The EVM in this case is higher due to the residual interference between channels, which is worsened by the fact that 16-QAM has more amplitude levels than QPSK.

4.3 GAMP for PAPR Reduction

A novel application for GAMP receivers was developed to allow for low PAPR transmission in OFDM systems, with improved performance. This work was published in [15].

In this scenario, a clipping operation is applied independently to the in-phase and quadrature components is considered. This operation is denoted by $f(\cdot)$, and is defined as the soft clipping function shown in sec. 2.6.6.3, with clipping threshold s_{clip}. The clipped signal is defined as

$$x_n = f(\text{Re}\,(s_n)) + jf(\text{Im}\,(s_n)), \tag{4.24}$$

with a frequency domain counterpart X_k, obtained via DFT. It is considered that the clipped signal is amplified within the linear region of the PA, and so does not suffer from additional distortion.

The receiver employs GAMP to improve performance in the presence of nonlinear distortion. Since the nonlinearity is applied independently to the I and Q branches, then the lower complexity likelihood from sec. 3.3.1 can be calculated.

4.3.1 Simulation Results

The following BER simulation results consider the proposed receiver with $N = 2048$ data subcarriers, compared with an ideal receiver with no distortion, a conventional ZF receiver with a nonlinearity at the transmitter, and a BNC receiver. The received signal is oversampled by a factor of $O_s = 4$. The receivers were compared by the averaged BER, presented here as a function of the E_b/N_0, where E_b is the bit energy and N_0 is the noise PSD. The effect of the clipping operation is shown by the average PAPR of the transmitted signal, defined for each as

$$\text{PAPR} = 10\log_{10}\left(\frac{|x_n|^2}{\mathbb{E}[|x_n|^2]}\right) \tag{4.25}$$

Fig. 4.33 shows the BER for a 256-QAM system. All receivers employ the same parity matrix, which is used in the WiMax standard [124], with a code rate of $R_c = 1/2$ and a parity matrix of size $N_c = 960, K_c = 480$. The integration limit of the proposed GAMP receiver was set to $A_x = 2$, with a damping parameter $\beta = 0.75$. The chosen clipping threshold A_{clip} results in a significant 7.4dB PAPR reduction. Although excellent for amplification efficiency, it is clear that conventional receivers cannot detect this signal correctly. For such a strong clipping, the BNC receiver is also not powerful enough. The proposed GAMP receiver can successfully decode the signal, requiring only an additional 2dB in E_b/N_0.

Fig. 4.34 presents the BER results for a 1024-QAM system. In this scenario, the linear PAPR is only slightly higher due to the larger constellation, however, the sensitivity to distortion of higher order modulations is much greater. Therefore, reducing the clipping threshold obtains a PAPR of 3.23dB, 1dB higher than the 256-QAM scenario. Neither the conventional nor BNC receivers can recover the clipped signal, despite the lessened distortion. The GAMP receiver can recover the signal for only an additional 1.5dB of E_b/N_0.

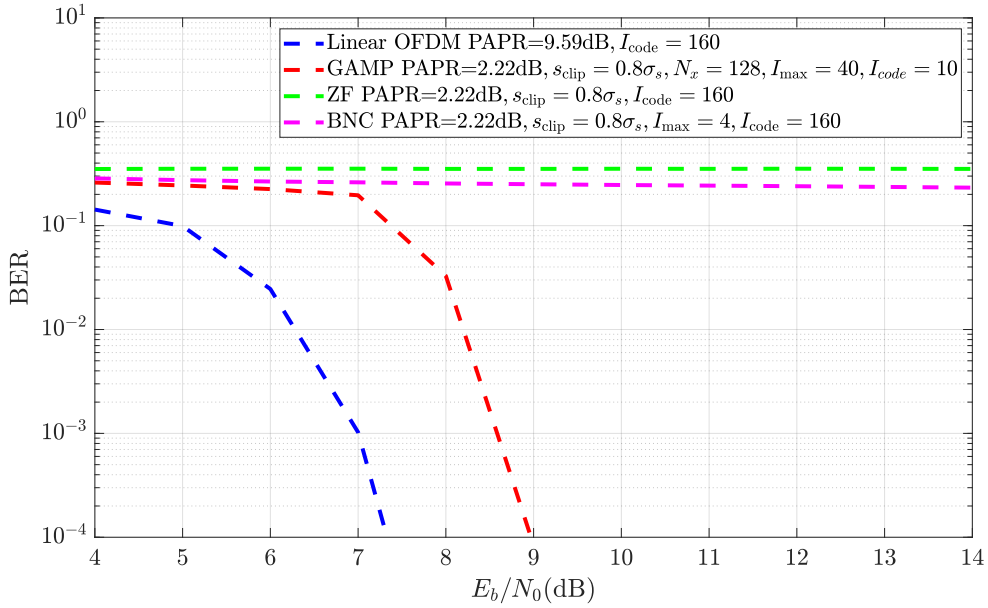

Figure 4.33: BER for 256-QAM, compared with a conventional receiver, BNC receiver, and GAMP.

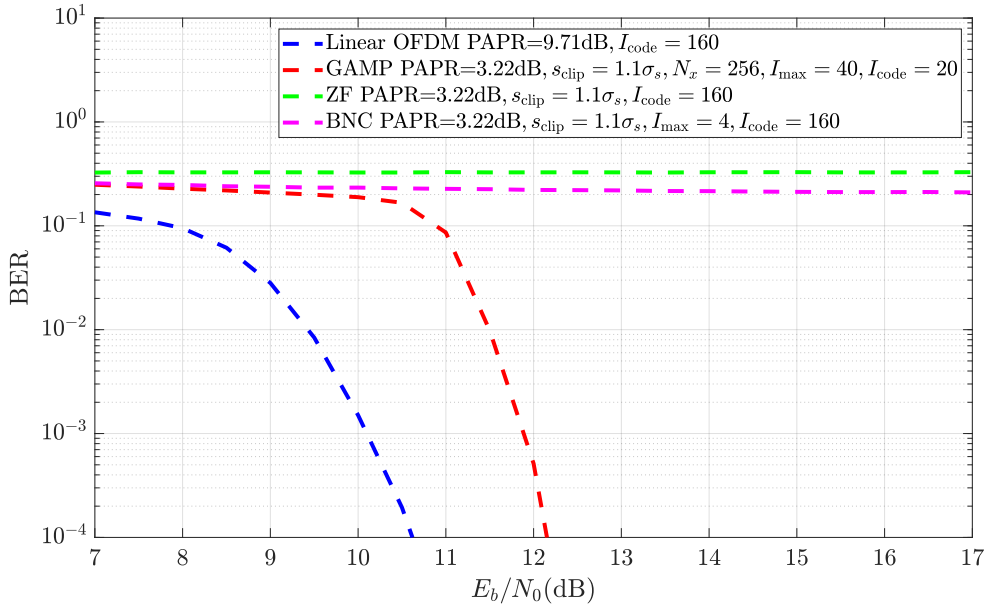

Figure 4.34: BER for 1024-QAM, compared with a conventional receiver, BNC receiver, and GAMP.

4.4 GAMP Receiver with Low-resolution ADC

Although nonlinearities in the transmitter are of more interest due to the possible nonlinear performance gains, the receiver may also introduce nonlinearities in the signal. In this case it is not possible to improve performance due to data processing inequality [125], however, the receiver can be made cheaper and more efficient. One such application is the use of low-resolution ADCs, which are cheaper and consume significantly less power than high-resolution ADCs [126], at the cost of more quantization noise in the signal.

A novel scheme that makes use of GAMP to recover the signal at the receiver was developed. Since GAMP can cope with nonlinear distortion, it becomes possible to use an ADC with a narrow input range, thereby decreasing the quantization noise. The additional nonlinear distortion that arise from the implicit clipping operation, is used by GAMP to decode the signal. A journal paper on this work was published in [16].

4.4.1 System Characterization

As was described in sec. 2.6.5, an ADC is an important component of RF receivers. The non-ideal behaviour of this component is a source of additional noise and distortion in the received signal. Ideally, the largest ADC resolution possible would be used, however, this would make these components exceedingly expensive and power hungry. Therefore, there is a need for receivers that can operate using cheaper non ideal ADCs.

In this scenario a nonlinear distortion at the receiver is considered, as opposed to the previous scenarios that considered a nonlinear transmitter. Fig. 4.35 shows a diagram of the nonlinear model considered in this scenario. Generally, this is not the optimum case since due to data processing inequality, a distortion at the receiver cannot be used to improve system performance.

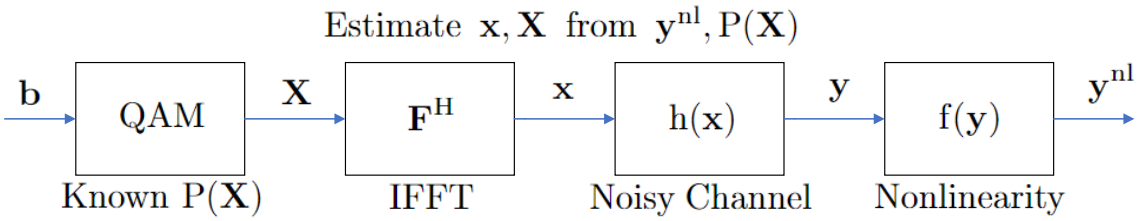

Figure 4.35: Block diagram of the general nonlinear model with a non-ideal ADC.

Although it is not the same proposed use case, it is possible to use BNC and GAMP receivers to increase performance, even in this scenario with a nonlinear distortion at the receiver. The BNC receiver can be used as it previously defined, whereas GAMP can be adjusted to take into account that the nonlinearity is placed after the channel. The updated GAMP algorithm for ADC nonlinearities is shown in Algorithm 3.

Algorithm 3 GAMP Receiver

Given a nonlinearly distorted received signal in the time domain, $\mathbf{y}$, produce an estimate, $\hat{\mathbf{X}}$, of the original transmitted data $\mathbf{X}$.

1) Initialization

$$i = 1, \hat{\mathbf{X}}(1) = \mathbf{0}_{NO_s,1}, \hat{\mathbf{s}}(0) = \mathbf{0}_{NO_s,1}, \mu^X(1) = \mathbf{1}_{NO_s,1}$$

2) Output linear step

$$\mu^p(i) = \frac{1}{NO_s} \sum_{k=0}^{NO_s-1} \mu_k^X(i)$$

$$\hat{p}_n(i) = \sum_{k=0}^{NO_s-1} \left(F_{n,k}^H \hat{X}_k(i) \right) - \mu^p(i) \hat{s}_n(i-1), \forall n$$

3) Output nonlinear step

$$\hat{s}_n(i) = \left(1-\beta\right) \hat{s}_n(i-1) + \beta g_{out}(\hat{p}_n(i), \mu^p(i), y_n), \forall n$$

$$\mu_n^s(i) = \left(1-\beta\right) \mu_n^s(i-1) - \beta \frac{\partial}{\partial \hat{p}_n} g_{out}(\hat{p}_n(i), \mu^p(i), y_n), \forall n$$

4) Input linear step

$$\tilde{X}_k(i) = (1-\beta)\tilde{X}_k(i-1) + \beta \hat{X}_k(i), \forall k$$

$$\mu_k^V(i) = \left(\frac{1}{NO_s} \sum_{n=0}^{NO_s-1} \mu_n^s(i) \right)^{-1}, \forall k$$

$$V_k(i) = \tilde{X}_k(i) + \mu_k^V(i) \sum_{n=0}^{NO_s-1} F_{n,k} \hat{s}_n(i), \forall k$$

5) Input nonlinear step

$$\hat{X}_k(i+1) = g_{in}(\hat{V}_k(i), \mu_k^V(i)), \forall k$$

$$\mu_k^X(i+1) = -\mu_k^V(i) \frac{\partial}{\partial \hat{V}_k} g_{in}(\hat{V}_k(i), \mu_k^V(i)), \forall k$$

The nonlinear step functions are the same as those defined in Sec. 3.4.2. It should be noted that there are implementations using GAMP that consider non-ideal ADCs [127, 128], however, they do not take into account the distortion due to low ADC saturation.

4.4.1.1 Performance Results

In the following results, the proposed GAMP-based receiver's performance is compared with an ideal receiver with infinite precision and no saturation effects, a conventional ZF equalization scheme with a non-ideal ADC, and a BNC receiver using $I_{\max}$ iterations. It is considered that all receivers operate with the same oversampling factor. The GAMP damping factor was set to $\beta = 0.7$ to improve convergence at the cost of more iterations, while N_x was set at 256 for 64-QAM, and 512 for 256-QAM. An ADCs with two values of A_{adc} and different resolutions is considered. The A_{adc} values were selected to assure the lower distortion level for a given ADC resolution.

Fig. 4.36 presents the BER performance of different receivers for a 64-QAM OFDM system with $N = 512$ and $O_s = 4$. The ADC is parameterized with $R_{\text{bit}} = 3$ bits of resolution and variable saturation levels. From the figure, it can be noted that the presence

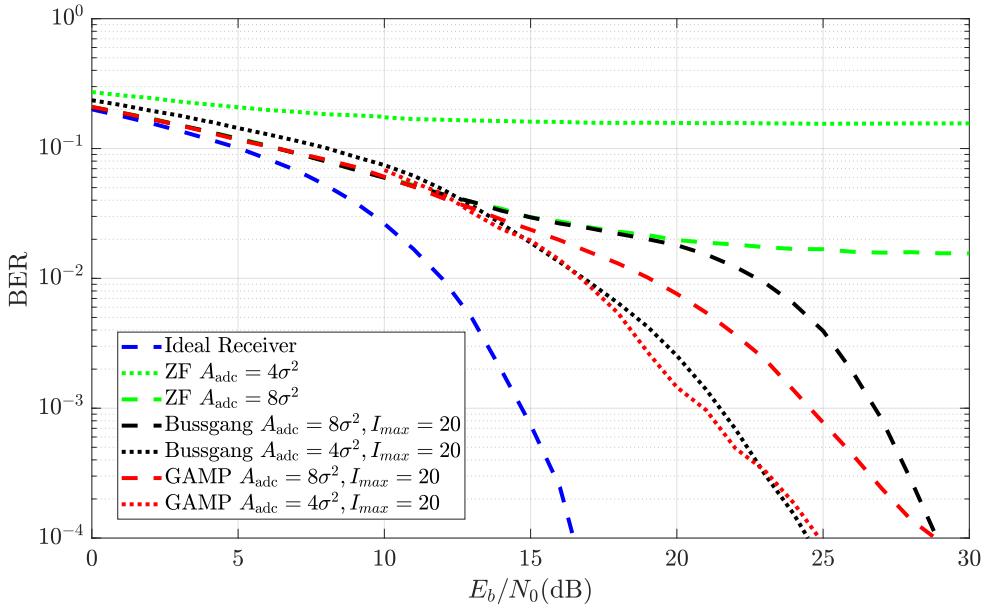

Figure 4.36: BER for 64-QAM OFDM system with $R_{\text{bit}} = 3$, compared with a conventional ZF, BNC receiver, and GAMP with $N_x = 256$.

of the imperfect ADC significantly degrades the detection performance of the conventional ZF receiver, regardless of the considered A_{adc}. For $A_{\text{adc}} = 8\sigma_s^2$, where $\sigma_s^2 = \text{var}[X_k]/2$, the ZF receiver presents a high BER floor. For a target BER of 10^{-4}, the performance loss of the GAMP and BNC receivers relatively to the ideal receiver is approximately 13 dB. For $A_{\text{adc}} = 4\sigma_s^2$, the nonlinear distortion due to signal clipping is larger, while the quantization

noise for the signal below A_{adc} is reduced, compared to the previous case. The BNC and GAMP receivers take advantage of this fact to improve performance, reaching a target BER of 10^{-4} at 9 dB of E_b/N_0 from the ideal receiver, i.e., a 4 dB reduction over using a larger A_{adc}. The similar performance of both receivers indicates that the nonlinear distortion present in the signal is being successfully mitigated.

Fig. 4.37 presents the BER results with $R_{\text{bit}} = 4$. From the figure, it is interesting to

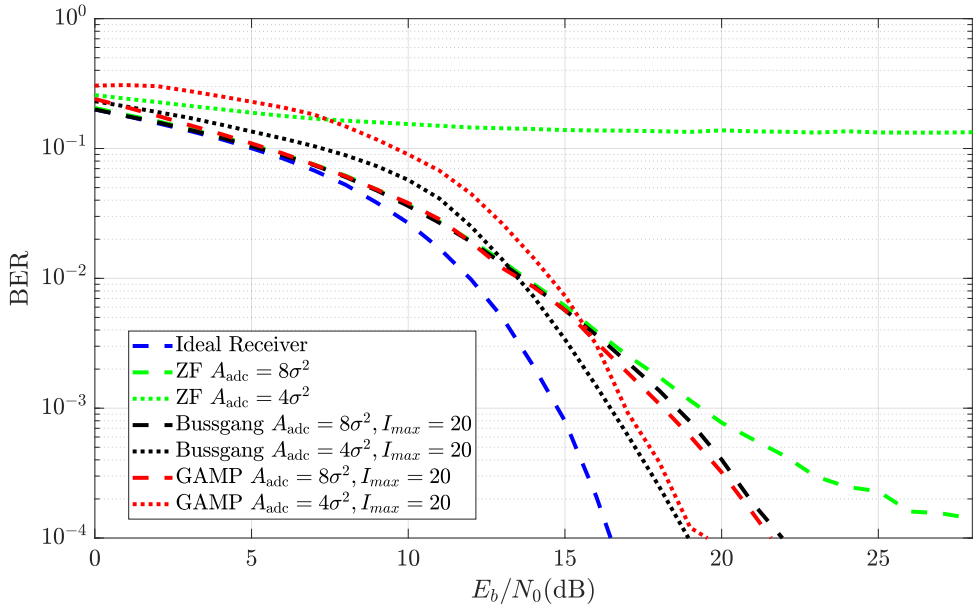

Figure 4.37: BER for 64-QAM with $R_{\text{bit}} = 4$, compared with a conventional ZF, BNC receiver, and GAMP with $N_x = 256$.

note how a single bit drastically affects the performance of all receivers. When $A_{\text{adc}} = 8\sigma_s^2$, the ZF receiver achieves a BER floor close to 10^{-4}, while the BNC and GAMP receivers significantly outperform it, achieving the target BER of 10^{-4} at an additional 5 dB of E_b/N_0, compared to the linear case. For $A_{\text{adc}} = 4\sigma_s^2$, the conventional receiver cannot recover the signal at all, whereas BNC and GAMP perform only 3 dB worse than the ideal receiver. In this situation, there is no clear advantage to using GAMP over BNC, however, this is not the case for higher-order modulation.

Fig. 4.38 shows the BER performance for 256-QAM with $R_{\text{bit}} = 4$. When $A_{\text{adc}} = 8\sigma_s^2$, the BNC and GAMP receivers can achieve a target BER of 10^{-4} at the cost of approximately 12 dB in E_b/N_0. However, for the lower saturation value $A_{\text{adc}} = 4\sigma_s^2$, BNC receiver does not reach the target BER, while GAMP can achieve the target, while requiring only 6 more dB of E_b/N_0 than the ideal receiver, making this receiver a more effective option for this scenario. The poor performance of BNC is due to its limited distortion cancellation performance for large constellations, as it relies on estimating the transmitted signal.

The following results consider a Rayleigh fading channel, which degrades performance,

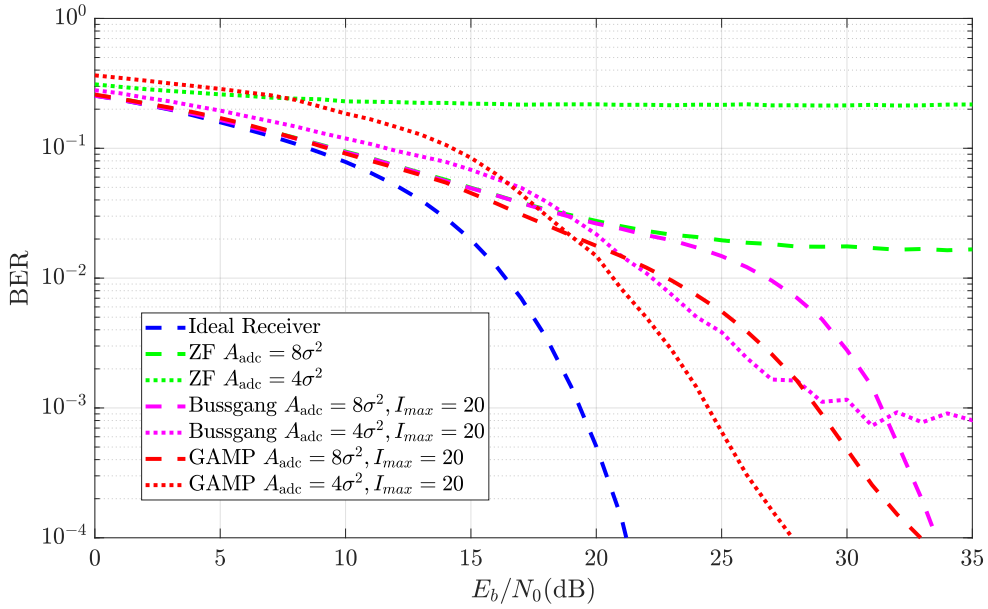

Figure 4.38: BER for 256-QAM with $R_{\text{bit}} = 4$, compared with a conventional ZF, BNC receiver, and GAMP with $N_x = 1024$.

and a larger set of subcarriers $N = 1024$. To cope with this channel, the system employs a $R_{\text{code}} = 1/2$ rate LDPC code with $N_P = 2016$ and $K_P = 1008$ is used to cope with the selective channel [124], where coded bits are interleaved randomly within each OFDM symbol. Due to the code gain of the LDPC, the GAMP damping parameter was increased to $\beta = 0.85$, and N_x was set to 256. The SER, which is defined as the probability that an OFDM symbol has at least 1 incorrect bit, is selected as the performance metric. For these simulations, a target SER of 10^{-2} was chosen. Fig. 4.39 presents the SER of different reception schemes considering an ADC with $R_{\text{bit}} = 3$ bits of resolution. As can be observed from the figure, the addition of channel coding allows the conventional receiver to perform adequately even for $R_{\text{bit}} = 3$. In this case, the code gain is sufficient to compensate for the nonlinearity, except in the case of low A_{adc}, where only GAMP can achieve an acceptable SER.

In Fig. 4.40 is presented the SER considering $R_{\text{bit}} = 2$. From the figure, the GAMP performance benefits are clear, since the GAMP receiver presents a much better performance than the BNC receiver. The ZF receiver was omitted due to its SER being 1 for all E_b/N_0 in this scenario. For $A_{\text{adc}} = 4\sigma_s^2$, only the GAMP receiver achieves the target SER of 10^{-2} at an E_b/N_0 of 12 dB, which is a loss of only 6 dB relatively to the ideal receiver. For $A_{\text{adc}} = 8\sigma_s^2$, neither receiver can achieve an SER lower than 1 due to the higher quantization noise.

Fig. 4.41 presents the SER for a 256-QAM system, using $R_{\text{bit}} = 4$.

The coding gain allows the conventional receiver to perform well with only $R_b = 4$ bits of ADC resolution. The GAMP receiver can recover the signal even for low A_{adc}, though

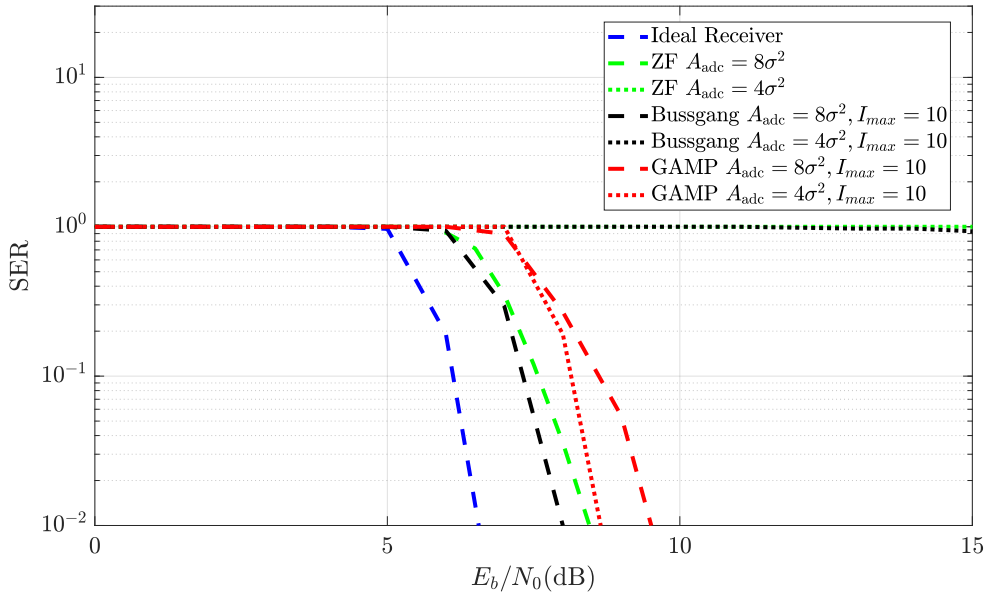

Figure 4.39: SER for 64-QAM with $R_{\text{bit}} = 3$, for BNC and GAMP receivers with $N_x = 64$ and $\beta = 0.85$.

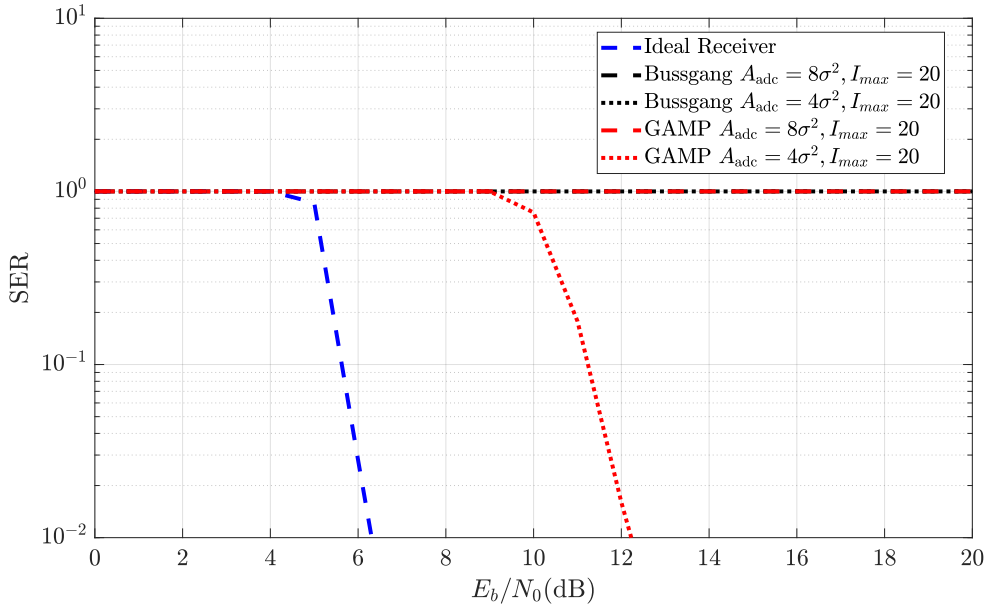

Figure 4.40: SER for 64-QAM with $R_{\text{bit}} = 2$, for BNC and GAMP receivers with $N_x = 64$ and $\beta = 0.85$.

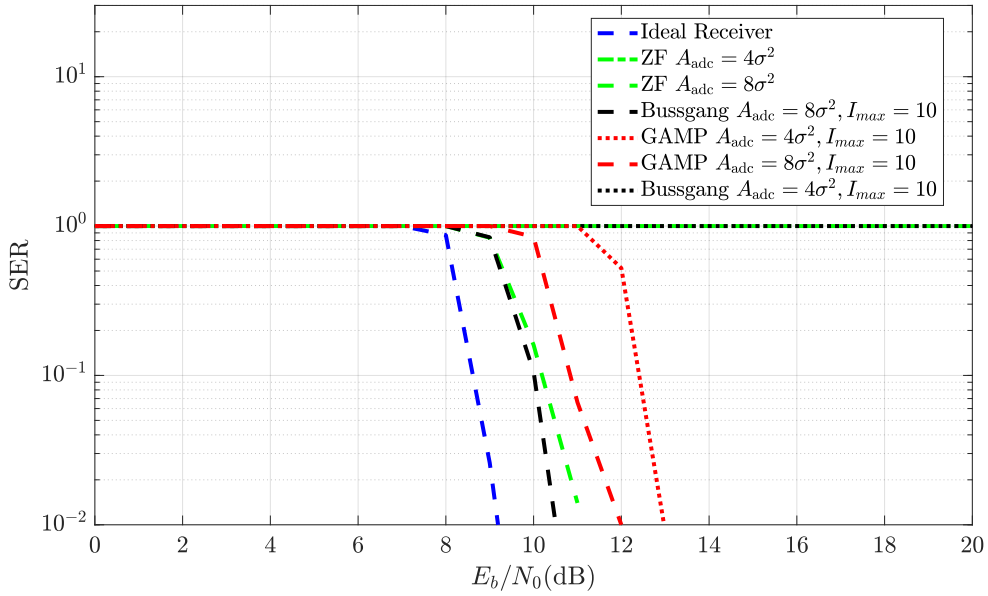

Figure 4.41: SER for 256-QAM with $R_{\text{bit}} = 4$, for BNC and GAMP receivers with $N_x = 256$ and $\beta = 0.85$.

it performs worse for higher A_{adc}. Fig. 4.42 shows the SER considering $R_{\text{bit}} = 3$. The

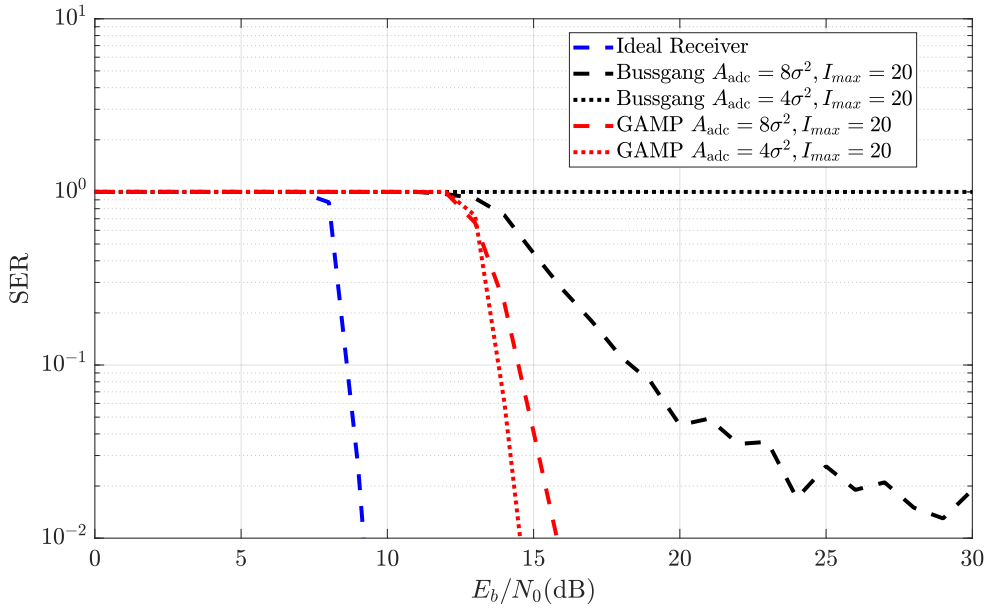

Figure 4.42: SER for 256-QAM with $R_{\text{bit}} = 3$, compared with a BNC receiver, and GAMP with $N_x = 256$ and $\beta = 0.85$.

performance of the ZF receiver was omitted for clarity, as the SER was 1 for all E_b/N_0. In the

uncoded case, it was necessary to increase the ADC resolution to maintain performance. With the LDPC, however, BNC shows a modest improvement, though it cannot reach an SER below 10^{-2}. The GAMP receiver can achieve a much better performance, reaching the target SER of 10^{-2} at only 5 and 6 dB of E_b/N_0 from the linear receiver, with $A_{\text{adc}} = 4\sigma_s^2$ and $A_{\text{adc}} = 8\sigma_s^2$. As was seen in previous results, GAMP performs better when the saturation value is lower due to the increased clipping.

An additional benefit of combining the LDPC decoding within GAMP iterations is the reduced number of iterations necessary for convergence. Table 4.2 compares the median number of iterations for both receivers considering the various simulated scenarios.

Table 4.2: Comparison of the median number of iterations required for convergence, considering different system configurations.

System parameters	Median Number of Iterations
64-QAM@25dB $O_s = 4$	9
LDPC 64-QAM@15dB $O_s = 4$	4
256-QAM@28dB $O_s = 4$	14
LDPC 256-QAM@17dB $O_s = 4$	6

The addition of LDPC decoding can reduce the necessary iterations by up to 56%, greatly reducing the total complexity of iterative GAMP over uncoded implementations.

4.4.1.2 Imperfect CSI

This section considers the impact of inaccurate CSI on the performance of the system. The imperfect CSI is modelled as

$$\hat{H}_k = \rho H_k + \epsilon_k, \tag{4.26}$$

where $\rho \in [0, 1]$ is a correlation factor with the real channel, and ϵ_k is an error term that follows a Gaussian distribution $\mathcal{N}\left(0, 1 - \rho^2\right)$. For convenience, the error variance is expressed in dB as

$$\sigma_E = 10 \log_{10}\left(1 - \rho^2\right). \tag{4.27}$$

Fig. 4.43 presents the SER of 64-QAM for $R_{\text{bit}} = 2$ and imperfect CSI. From the figure, it can be observed that for $\sigma_E = -24$ dB, GAMP's performance is only about 1.5 dB worse than the ideal CSI scenario. For $\sigma_E = -21$ dB, results in a performance degradation of approximately 4 dB, assuming a target SER of 10^{-2}. With $\sigma_E = -18$ dB, the SER is significantly higher, and the target SER of 10^{-2} is not achieved within the simulated E_b/N_0 range.

Fig. 4.44 shows the SER for 256-QAM with $R_{\text{bit}} = 3$ and imperfect CSI. From the figure, it can be observed that a higher-order constellation shows a higher sensitivity to CSI errors. For $\sigma_E = -24$ dB, there is a slight degradation of approximately 1.5 dB in E_b/N_0 for the target SER 10^{-2}. At $\sigma_E = -22$ dB, the degradation is significantly high, at approximately 5

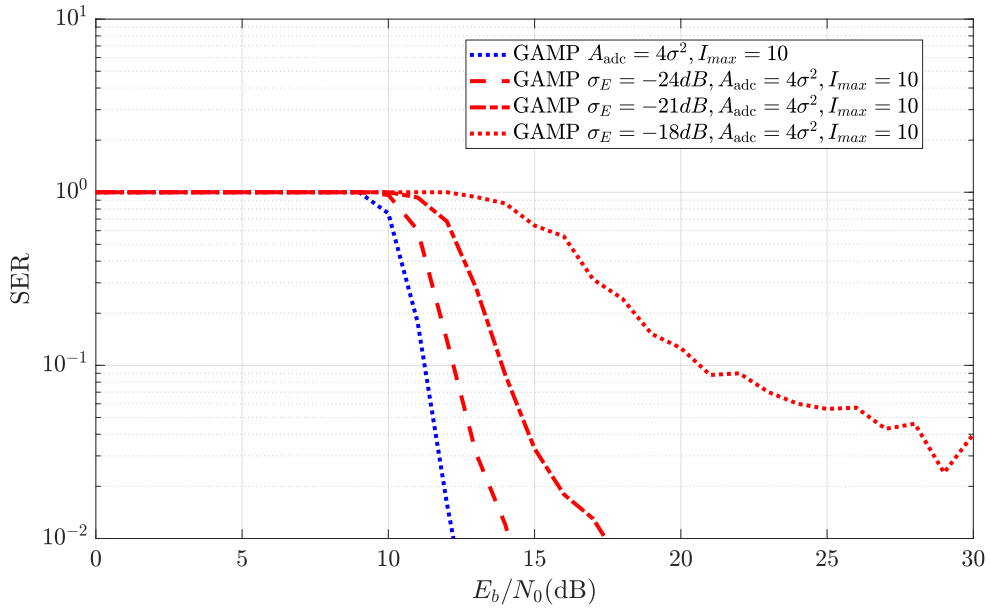

Figure 4.43: SER for imperfect CSI 64-QAM with $R_{\text{bit}} = 2$ of GAMP with $N_x = 64$ and $\beta = 0.85$.

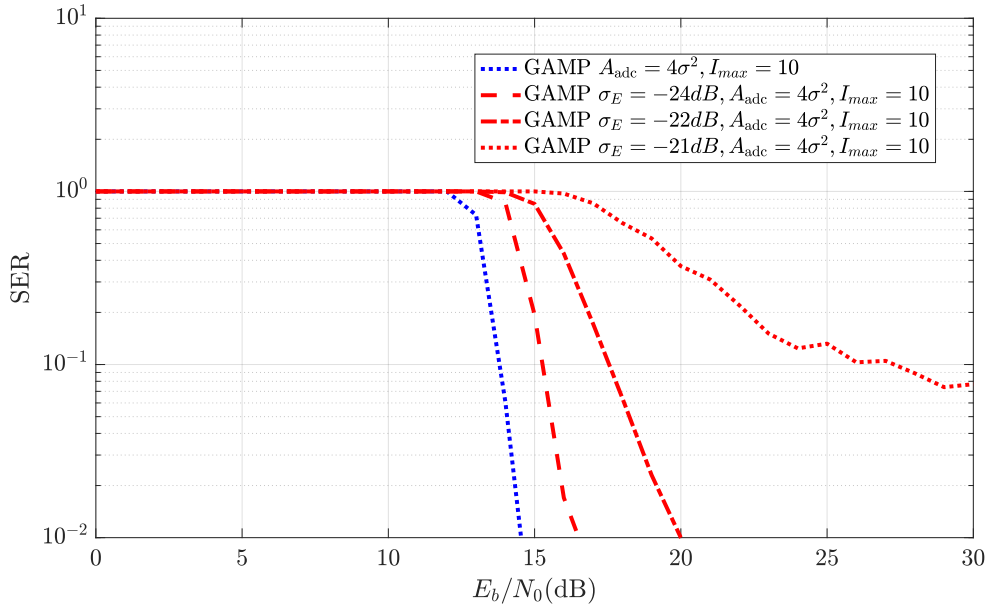

Figure 4.44: SER for imperfect CSI 256-QAM with $R_{\text{bit}} = 3$, of GAMP with $N_x = 256$ and $\beta = 0.85$.

dB of E_b/N_0, for the same target. For CSI error variances $\sigma_E \geq -21$ dB, the receiver does not reach the target SER.

4.5 Retransmission Schemes

This section covers novel retransmission schemes that aim to increase retransmission reliability in wireless systems. The work developed in this section was published in [13, 17, 18]. A journal paper was submitted for publication at "IEEE Transactions in Communications".

4.5.1 LDPC Concatenation HARQ

Type II HARQ schemes rely on transmitting new information after a failed transmission, to increase the likelihood of a successful reception. This can be done by using a low code rate base coding scheme and then puncturing the parity bits [31, 129], and then sending the punctured bits in the following retransmissions. However, finding an optimum puncturing rule for a specific code is non-trivial. Therefore, a novel scheme that relies on concatenated LDPC matrices was developed and shown to achieve excellent results and efficient scalability.

4.5.1.1 System characterization

Let us consider a Rician fading channel that is defined by two terms: a LoS term that does not have fading and a multipath composed by N_{ray} multipath components. It is assumed that the transmit power P is enough to guarantee the required SNR for the underlying application. However, there can be blockages of the LoS component that lead to a significant degradation of the received signal power, which decreases to $P(1-K)$. It can be assumed that for the first channel realization, there is a probability γ_{LOS} of having the LoS component. It is also reasonable to admit that if there is a blockage and the LoS component is lost, that loss spans over n_{down} channel realizations. After n_{down} realizations, the next n_{up} realizations will have the LoS component. After n_{up} realizations, the next channel realizations will again be dependent on the value of γ_{LOS}. Also, it is considered that the transmitter cannot anticipate the change in the channel or its duration, and can only be made aware of the wireless link degradation after transmitting at least one block during the state without LoS.

The average channel power across all subcarriers for the channel between the rth and tth antennas, $\mathbb{E}(|H_k^{(r,t)}|^2)$, is shown in Fig. 4.45 for 1000 channel realizations, considering $K = 0.75$, $\gamma_{LOS} = 0.05$ and $n_{down} = n_{up} = 20$. Fig. 4.46 presents the PDF of the absolute value of $H_k^{(r,t)}$ was obtained with 10000 channel realizations, for the same parameters as the previous figure.

It should be noted that when a block is transmitted in the no LoS scenario, there is a high probability that the received reconstructed codeword cannot be decoded by the

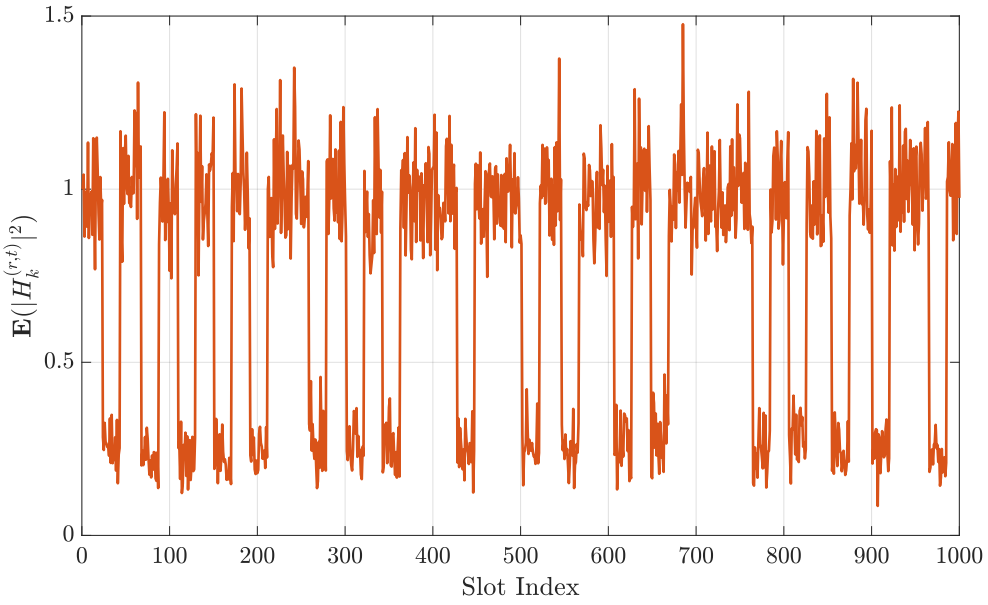

Figure 4.45: Average channel power considering 1000 channel realizations with $K = 0.75$, $\gamma_{LOS} = 0.05$ and $N_{down} = n_{up} = 20$.

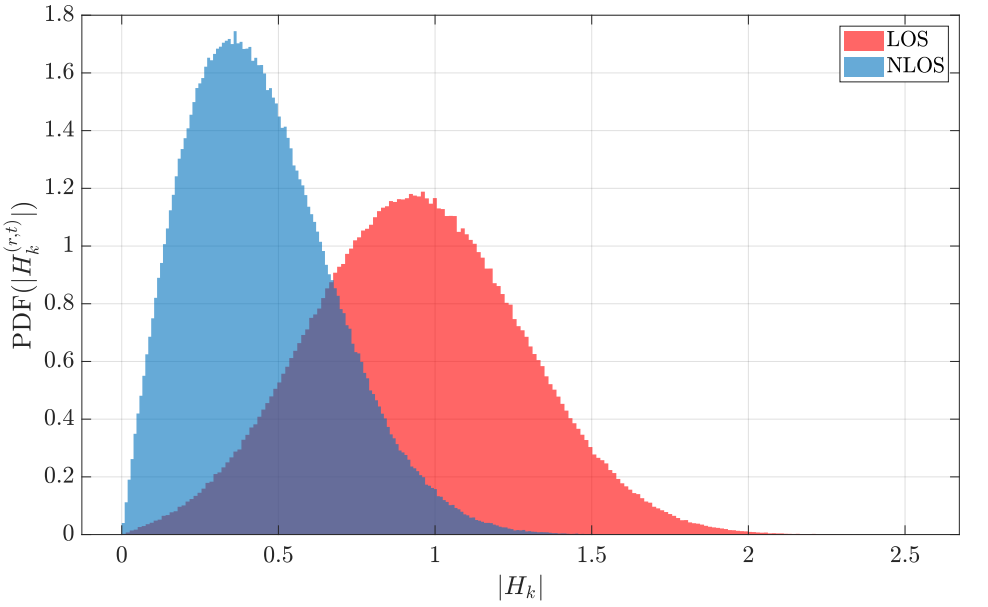

Figure 4.46: PDF of $|H_k^{(r,t)}|$ over 10000 channel realizations, with $K = 0.75$, $\gamma_{LOS} = 0.05$ and $n_{down} = n_{up} = 20$.

LDPC decoder. In this case, the iterative decoder will perform the maximum number of allowed iterations, and if the final codeword does not pass the parity check, the receiver will request retransmission using a Negative Acknowledgement (NAK). The transmitter can then use one of the types of HARQ in order to achieve a successful transmission. It is considered that the retransmissions are performed within the coherence time interval of the channel, which means that the channel does not recover during the retransmission phase.

Concatenated LDPC code HARQ is a retransmission scheme wherein each retransmission contains the parity bits obtained by encoding the previously transmitted codeword with a larger LDPC code, which must satisfy:

$$N_v^{r-1} = N_v^r - K_p^r, \tag{4.28}$$

where N_v^r and K_p^r represent the number of variable and check nodes of the rth parity matrix, respectively, and $N_v^0 = N_v$. In this case, the code rates for the successive codes can be fine tuned for the desired use-case. The larger parity matrices can be obtained using random generation [130], and can be defined using the same parity check distributions as the first LDPC parity matrix. The pre-processed parity matrix, [33], associated with the rth coded retransmission is referred to as $\mathbf{H}_p^r$, while the rth generator matrix is referred to as $\mathbf{G}^r$. If the maximum number of retransmissions, r_{tr}, is larger than the number of different retransmission LDPC codes, r_p, then the transmitter can loop around and transmit the original coded block, followed by, if necessary, the parity bits of the successive codes.

The codeword for the rth retransmission is defined as

$$\mathbf{p}^r = \begin{cases} \mathbf{p}^{r-1}\mathbf{G}^r, & r \leq r_p \\ \mathbf{p}^{r \mod r_p}, & r > r_p, \end{cases} \tag{4.29}$$

where $\mathbf{p}^r$ is the rth codeword that will be transmitted, and p^0 is the codeword of the first transmission. The additional encoding is only performed when a retransmission is requested, which results in no overhead processing for successful transmissions, requiring only additional memory to store the generator matrices. The concatenation of the LDPC codes results in an equivalent code rate that is the product of all individual code rates, which for the rth transmission is given by

$$R_{code}^r = \prod_{r'=0}^{r} \frac{(N_v^{r'} - K_p^{r'})}{N_v^{r'}}. \tag{4.30}$$

At the receiver, the equalization is performed separately for each re-transmitted block, while the BP decoding can be computed using $r+1$ LDPC decoders, one for the initial code and r for the retransmission codes. In the first step, the decoder for the larger parity matrix decodes the soft decided coded bits, $\mathbf{L}$, and the output soft decoded bits are then used as the input for the decoder associated with the second largest parity matrix, repeating until it decodes the initial code. In order to maximise the performance of this approach,

the resulting soft decoded bits would have to be re-encoded using the $r+1$ LDPC codes, and then decoded using the same process. This is to enable the sharing of information between all decoders.

Alternatively, it is possible to construct a parity matrix that represents the relationship between all codes and has a code rate equal to the product of all code rates. The parity matrix can be defined using the following expression

$$\mathbf{H}_p^{de} = \begin{bmatrix} \mathbf{H}_p^{(0,0)} & \dots & \mathbf{H}_p^{(0,K_p)} & \dots & 0 \\ & & \dots & & \\ \mathbf{H}_p^{(N_v,0)} & \dots & \mathbf{H}_p^{(0,K_p)} & \dots & 0 \\ \mathbf{H}_p^{1,(0,0)} & \dots & \mathbf{H}_p^{1,(0,\frac{K_p^1}{2})} & \dots & 0 \\ & & \dots & & \\ \mathbf{H}_p^{r_p,(N_v^{r_p},0)} & & \dots & & \mathbf{H}_p^{r_p,(N_v^{r_p},K_p^{r_p})} \end{bmatrix}, \tag{4.31}$$

where $\mathbf{H}_p^r$ is the parity matrix for the rth re-encoded transmission, with size $K_p^r \times N_v^r$. This decoding process also allows scaling the coding scheme further by using increasingly larger LDPC codes without significantly changing the decoding process at the receiver. Since the decoding parity matrix can be constructed by combining the matrices of each individual code, the total required storage capacity at the receiver will be lower than if using a different code for each retransmission.

4.5.1.2 Throughput and Goodput

In order to evaluate the effectiveness of the proposed system the throughput, T_{tp}, and goodput, T_{gp}, metrics are used, both defined in Bits-per-Second (bps). The throughput of a system refers to the rate of correctly received bits, being defined in this scenario as

$$T_{tp} = \frac{\log_2(M)\min(T,R)}{t_{tx}}, \tag{4.32}$$

where t_{tx} is the time necessary for a symbol to be correctly received, which will depend on the additional retransmissions. The goodput of the system refers to the correctly received information bits, and is defined as

$$T_{gp} = \frac{\log_2(M)\min(T,R)R_{code}^0}{t_{tx}}, \tag{4.33}$$

since it depends on the rate of the LDPC code selected. It should be noted that each retransmission will reduce the value of both of these metrics.

4.5.1.3 Simulation Results

In the following simulation results, unless otherwise stated, the average channel gain between two antennas with LoS is unitary, the bandwidth in use is 20 MHz, and the

number of antennas is $T = R = 4$. The number of data subcarriers is $N = 240$ and the FFT size is 256. The data symbols are selected from a 256-QAM constellation, which means that each transmitted block can contain up to $C_{bits} = 1920$ coded bits, with the amount of information bits being dependent on the chosen code rate. The LDPC coder is set to potentially perform up to $I = 30$ decoding iterations. It is assumed that the first transmission is always encoded by an LDPC with rate $R^0_{code} = \frac{1}{2}$, $N_v = 960$ and $K_p = 480$, while the re-encoded transmission only scales up once, $r_p = 1$, using a code with $N^1_v = 1920$ and $K^1_p = 960$. The maximum number of retransmissions is set at $r_{tr} = 3$.

First, an analysis on the throughput of different retransmission techniques under stable channel conditions, i.e., considering a scenario with $\gamma_{LOS} = 1$. Fig. 4.47 presents the evolution of the throughput considering different values of r_{tr}. From the figure, it can be

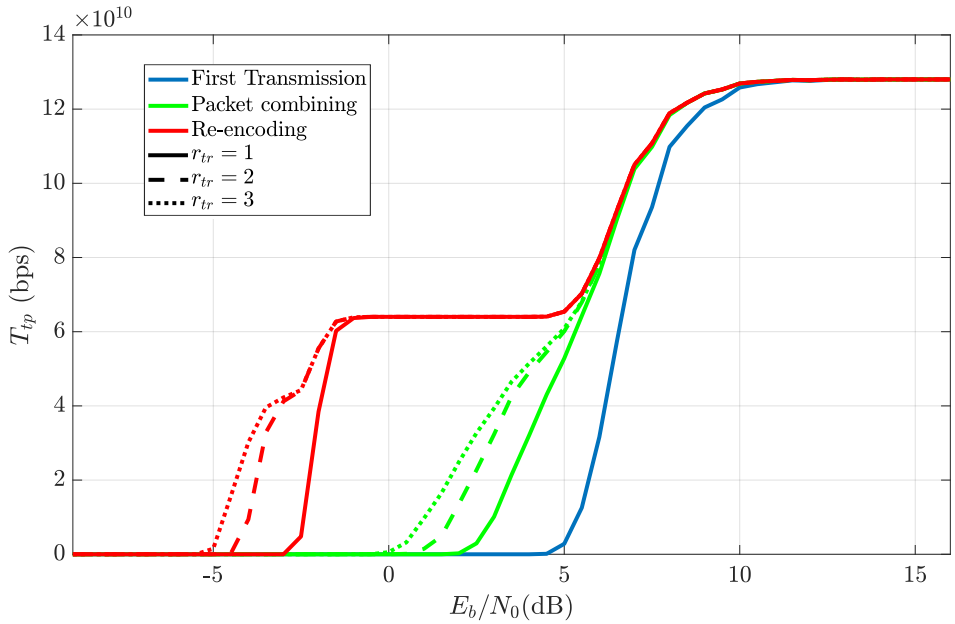

Figure 4.47: Throughput of the system as a function of the E_b/N_0, for various numbers of retransmissions.

concluded that for a system with a target throughput of $T_{tp} = 12.8$ Gbps, an E_b/N_0 of 10 dB is enough. In this scenario, the use of retransmissions raises the throughput at lower values of E_b/N_0. In fact, it can be observed that the first retransmission with packet combining results in an increase of the throughput to around $T_{tp} = 5$ Gbps, at 5 dB. However, additional performance gains associated to the execution of more retransmissions (i.e., $r_{tr} > 1$) are marginal, since these retransmissions are performed within the channel coherence time and the transmission power is kept constant. In the same conditions, the proposed re-encoding retransmission scheme can achieve a throughput of $T_{tp} = 6.4$ Gbps with just one retransmission. This is the case even at 0 dB, resulting in a much more energy efficient transmitter.

Fig. 4.48 shows the BER results for the initial transmission, as well as the packet combining and proposed LDPC re-encoding techniques. In this scenario, the LoS component was considered to be $K = 75\%$ of the total channel power, along with a channel state that spans over $n_{down} = n_{up} = 20$ OFDM symbols, and $\gamma_{LOS} = 0.05$. From the figure, it can

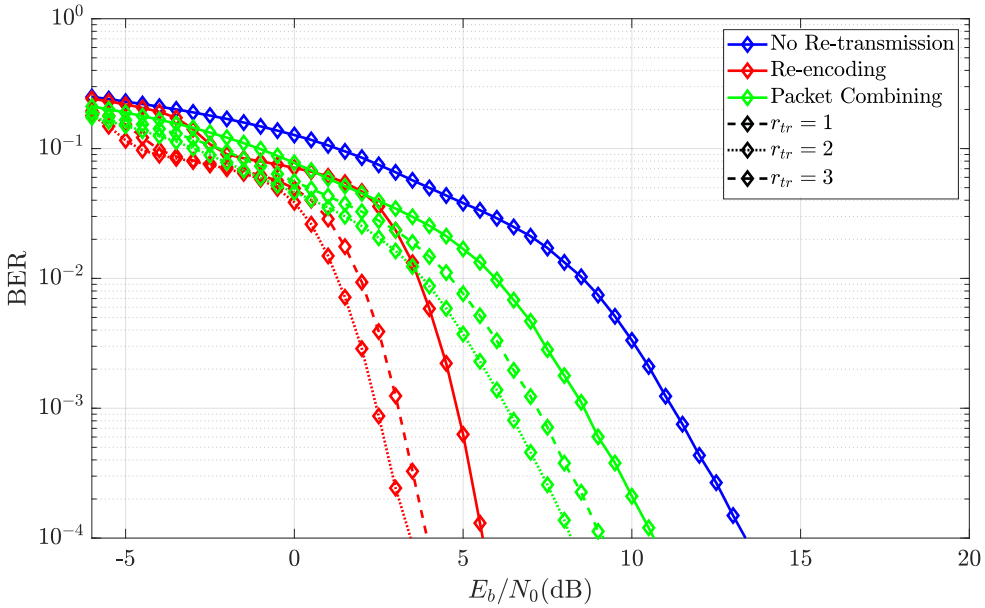

Figure 4.48: BER of the proposed system considering different retransmission strategies.

be noted that employing retransmissions greatly decreases the BER. Once again, it can be observed that the maximum performance gain is obtained in the first retransmission, thanks to the fact that the next successive retransmissions have the same length and are transmitted with the same power as the first transmission, their potential performance gain is lower. Moreover, it can be observed that the proposed re-encoding scheme can achieve a significantly lower BER than the conventional packet combining scheme, even after $r_{tr} = 3$ retransmissions.

Consider a wireless channel where the LoS component has $K = 90\%$ of the total channel power, and a channel downtime of $n_{down} = n_{up} = 20$ OFDM symbols. Fig. 4.49 shows the achievable goodput in that situation.

From the figure, it is clear that the system with no retransmissions requires a significantly higher E_b/N_0 in order to cope with the channel downtimes. In the results two different thresholds can be observed for the initial transmission, the first between approximately 10 dB and 15 dB, and the second beyond 20 dB. The first threshold occurs when the E_b/N_0 is high enough to recover all the transmissions during the LoS channel, while the second threshold occurs when the E_b/N_0 is high enough to also recover the transmissions when there is no LoS. Each PC retransmission decreases the required E_b/N_0 to reach this threshold, while the re-encoded retransmissions increase the goodput at the

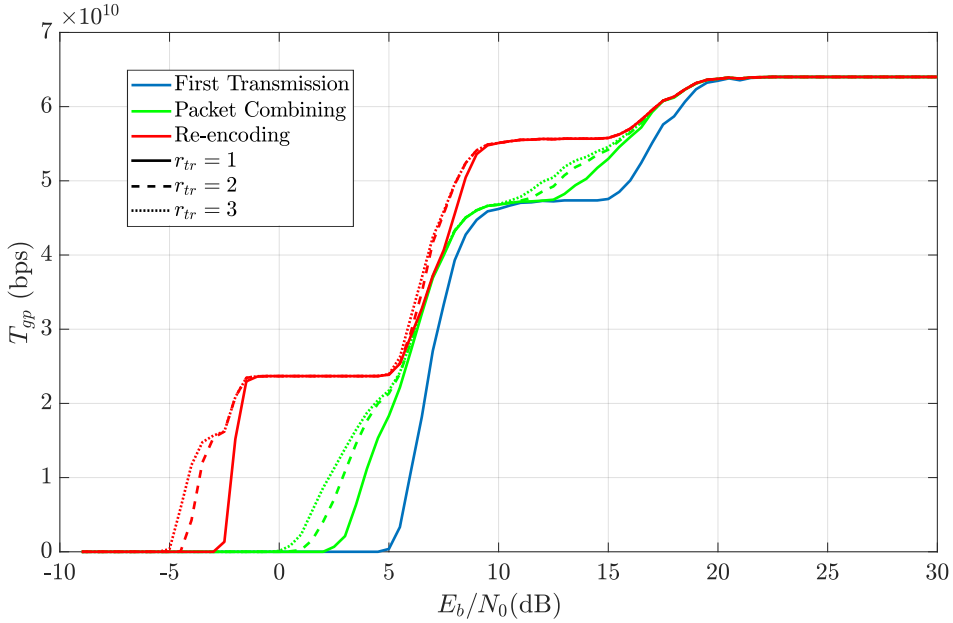

Figure 4.49: Goodput of the system as a function of the E_b/N_0, for various numbers of retransmissions, with an LOS component power of 0.9.

first threshold, as well as create a new threshold at a lower E_b/N_0, namely between -2 dB and 5 dB, which is due to the greater error correcting capabilities of the second LDPC code.

Fig. 4.50 shows the simulated outage probability for the proposed system with $r_{tr} = 3$. In this figure three scenarios are shown, namely: (i) a scenario where $\gamma_{LOS} = 1$, (ii) a scenario where $\gamma_{LOS} = 0$ and lastly, (iii) a scenario where the channel randomly loses LoS with $K = 0.9$ and $n_{down} = n_{up} = 20$. It can be concluded that re-encoding scheme can significantly reduce the outage probability of the system, allowing the system to operate at a much lower E_b/N_0 for this scenario, with low outage probability.

4.5.2 Nonlinearity-Aided Retransmission

A novel technique was developed in this work to increase the efficiency and reliability of retransmissions using nonlinearly distorted signals. A clipping scheme is used to reduce the PAPR of retransmitted signals, at the cost of introducing nonlinear distortion. Consequently, a GAMP based receiver takes advantage of the distortion to improve performance, balancing the disadvantage of the clipping scheme. Although GAMP receivers for nonlinearities can require many iterations, the initial linear transmission can be used to drastically improve convergence speed, reducing the associated complexity.

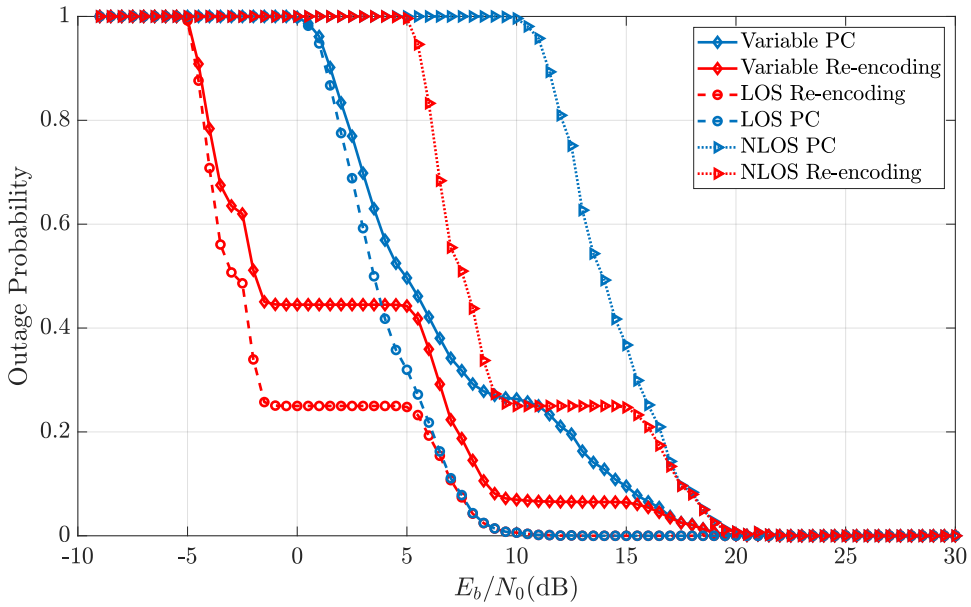

Figure 4.50: Outage probability of the proposed scheme considering $r_{tr} = 3$ and a LOS component with $K = 0.9$.

4.5.2.1 NL-ARQ

Consider a set of functions **f**, that are applied to the in-phase and quadrature components of the signal before transmission. This process is defined as

$$x_n = f_r\left(\mathrm{Re}\left(s_n\right)\right) + f_r\left(\mathrm{Im}\left(s_n\right)\right), \tag{4.34}$$

where r refers to the rth retransmission attempt, and x_n has a frequency domain counterpart denoted by X_k. In this case, the received signal is written as

$$Y_k = H_k X_k + N_k. \tag{4.35}$$

The first function of the set is defined to be the identity function, written as

$$f_0(x) = x, \tag{4.36}$$

which ensures that the initial transmission ($r = 0$) is not distorted. For $r > 0$, a nonlinear function is applied, written as

$$f_r(x) = f_{clip}(x), \quad r > 0, \tag{4.37}$$

where f_{clip} is the soft clipping function defined in sec. 2.6.6.3.

When a retransmission is requested, the transmitter computes (4.34) using $f_r(\cdot)$ where r is the current retransmission attempt. Although this analysis is focused on this particular nonlinear clipping function, this work can easily be extended to other nonlinear functions.

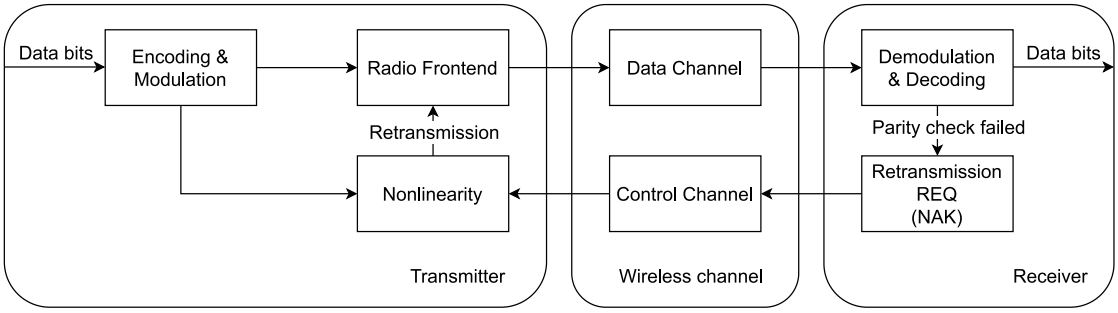

Figure 4.51: Diagram of the proposed nonlinearity-aided HARQ scheme. The receiver's radio frontend is omitted for simplicity.

Fig. 4.51 shows a diagram of the proposed nonlinearity-aided ARQ scheme. Applying the soft clipping function in (2.124) produces an output signal with much lower PAPR, proportional to the clipping threshold s_{clip}. In a real system, the energy efficiency of the PA is maximised if the amplifier is operating in the saturation region. However, amplifying in this region introduces severe nonlinear distortion in the output, which negatively impacts performance. For that reason PAs are operated in the less efficient linear region, to ensure that the input signal does not reach saturation. The relationship between the amplification efficiency of the rth transmission attempt and PAPR can be approximated as

$$E_r \approx \frac{1}{\text{PAPR}}. \tag{4.38}$$

This approximation holds as long as it is considered that the input signal is fully within the linear region of the PA, to minimize nonlinear distortion in the amplification process. Since the first transmission is always linear, then it is important to quantify the efficiency, taking into account all retransmissions. The average efficiency of a system is defined as

$$T_E = \frac{1}{R}\sum_{r=0}^{R-1} E_r. \tag{4.39}$$

Fig. 4.52 displays the efficiency of the proposed clipping scheme, considering different values of R. The first transmission is always linear, and therefore is not impacted by the proposed scheme. For $R > 1$, the initial transmission is considered to have a PAPR of 8.9dB, which corresponds to an OFDM signal with $N = 512$ subcarriers and 1024-QAM, while the retransmissions's PAPR is visible in the x-axis. As shown in the figure, a lower PAPR in retransmissions can achieve a significant power efficiency improvement over conventional high PAPR signals.

Alternatively, the transmitter can opt to increase transmitter power in proportion to the PAPR reduction. Although only applicable in scenarios where there is a margin to increase transmitter power, increasing retransmission reliability can be an effective option to reduce system delay. This scheme is referred to as Nonlinear ARQ with Enhanced Power (NL-ARQ-EP)/Nonlinear HARQ with Enhanced Power (NL-HARQ-EP).

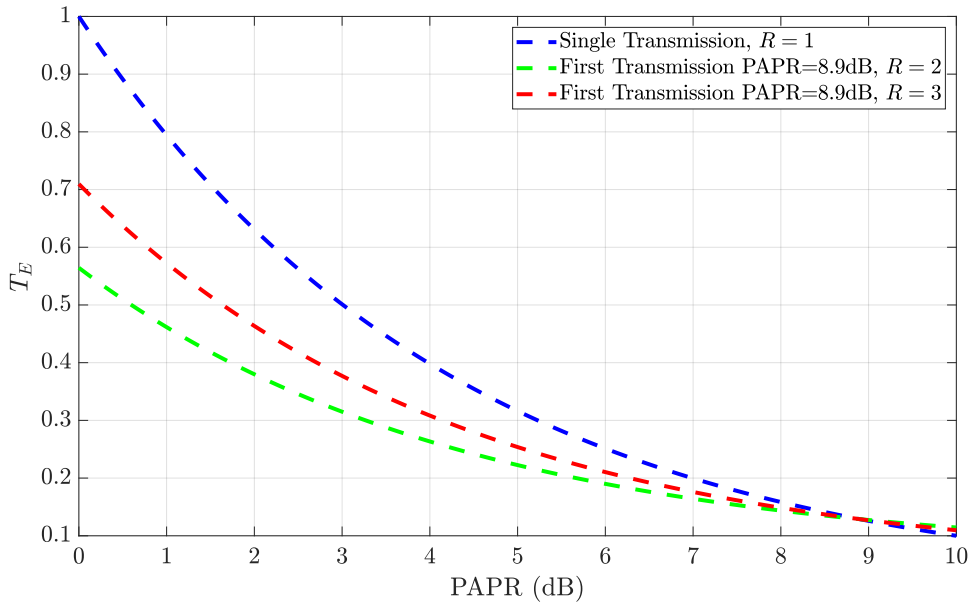

Figure 4.52: Average transmission efficiency considering different values of R, where retransmissions have a different PAPR from the original transmission.

The distorted retransmission, which in most cases would be detrimental, can actually be recovered using GAMP, as was shown in the previous sections. This requires rewriting the expectations in (3.52)-(3.55) and (3.56) to take into account the previously transmitted signals, resulting in the following expressions.

$$\begin{aligned}\mathrm{E}[z|\hat{p},\mathbf{y}_n,\mu^p] =& \frac{1}{\mathrm{Re}\,(C)}\int_{-\infty}^{\infty} x\exp\left(-\frac{|\mathrm{Re}\,(\hat{p})-x|^2}{2\mu^p}-\sum_{j=0}^{r}\frac{\left|\mathrm{Re}\,\left(y_{(n,j)}\right)-f_r(x)\right|^2}{2\sigma^2_{N,r}}\right)\mathrm{d}x+\\ &\frac{j}{\mathrm{Im}\,(C)}\int_{-\infty}^{\infty} xj\exp\left(-\frac{|imag(\hat{p})-x|^2}{2\mu^p}-\sum_{j=0}^{r}\frac{\left|\mathrm{Im}\,\left(y_{(n,j)}\right)-f_r(x)\right|^2}{2\sigma^2_{N,r}}\right)\mathrm{d}x\end{aligned} \tag{4.40}$$

$$\begin{aligned}\mathrm{var}[z|\hat{p},\mathbf{y}_n,\mu^p] =& \frac{1}{\mathrm{Re}\,(C)}\int_{-\infty}^{\infty} |x|^2\exp\left(-\frac{|\mathrm{Re}\,(\hat{p})-x|^2}{2\mu^p}-\sum_{j=0}^{r}\frac{\left|\mathrm{Re}\,\left(y_{(n,j)}\right)-f_r(x)\right|^2}{2\sigma^2_{N,r}}\right)\mathrm{d}x+\\ &\frac{j}{\mathrm{Im}\,(C)}\int_{-\infty}^{\infty} |x|^2 j\exp\left(-\frac{|\mathrm{Im}\,(\hat{p})-x|^2}{2\mu^p}-\sum_{j=0}^{r}\frac{\left|\mathrm{Im}\,\left(y_{(n,j)}\right)-f_r(x)\right|^2}{2\sigma^2_{N,r}}\right)\mathrm{d}x-\mathrm{E}[z|\hat{p},\mathbf{y}_n,\mu^p]\end{aligned} \tag{4.41}$$

$$C = \int_{-\infty}^{\infty} \exp\left(-\frac{|\mathrm{Re}\,(\hat{p}) - x|^2}{2\mu^p} - \sum_{j=0}^{r} \frac{\left|\mathrm{Re}\,\left(y_{(n,j)}\right) - f_r(x)\right|^2}{2\sigma_{N,r}^2}\right) \mathrm{d}x + \\ j \int_{-\infty}^{\infty} \exp\left(-\frac{|\mathrm{Im}\,(\hat{p}) - x|^2}{2\mu^p} - \sum_{j=0}^{r} \frac{\left|\mathrm{Im}\,\left(y_{(n,j)}\right) - f_r(x)\right|^2}{2\sigma_{N,r}^2}\right) \mathrm{d}x. \tag{4.42}$$

In this case, r denotes the current retransmission attempt, and $r = 0$ is the initial transmission when GAMP is not used. The fact that the initial transmission is not distorted is very beneficial to GAMP, as it significantly accelerates convergence.

The following simulation results consider an AWGN channel, with GAMP variables set to $N_X = 512, A_X = 6\sigma_s, \beta = 0.85$. Fig. 4.53 compares the BER of ARQ and Nonlinear ARQ (NL-ARQ), with 1024-QAM, considering no oversampling, i.e. $O_s = 1$.

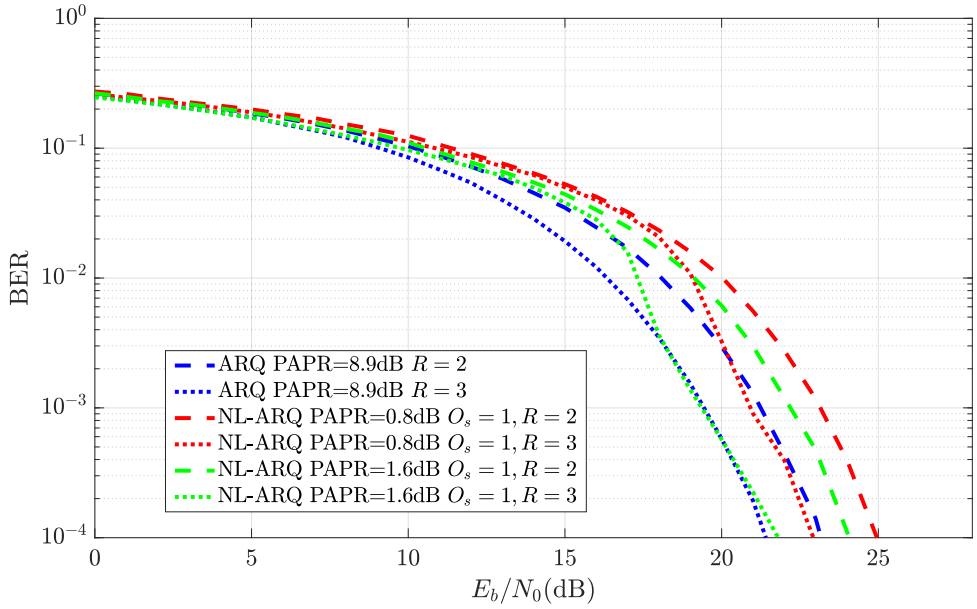

Figure 4.53: BER of 1024-QAM OFDM comparing conventional ARQ with NL-ARQ, for an AWGN channel.

From the figure the benefits of NL-ARQ are clear. Using a clipping operation that reduces the OFDM signal PAPR from 8.9dB to 1.6dB, results in a 1dB performance degradation at $R = 2$, and no degradation for $R = 3$. This is a substantial reduction in PAPR, which increases retransmission amplification efficiency to 69%, with an average efficiency of 41% and 50% for $R = 2$ and $R = 3$, respectively. Lowering the PAPR further to 0.8dB has a noticeable impact in performance, with a degradation of 2-3dB compared to conventional ARQ. In this case the retransmission effiency is 83%, and the total efficiency is 48% and 60%, for $R = 2$ and $R = 3$, respectively. This makes the PAPR of 1.6dB an appropriate design choice for NL-ARQ. Fig. 4.54 shows the BER results considering

NL-ARQ with $O_s = 4$.

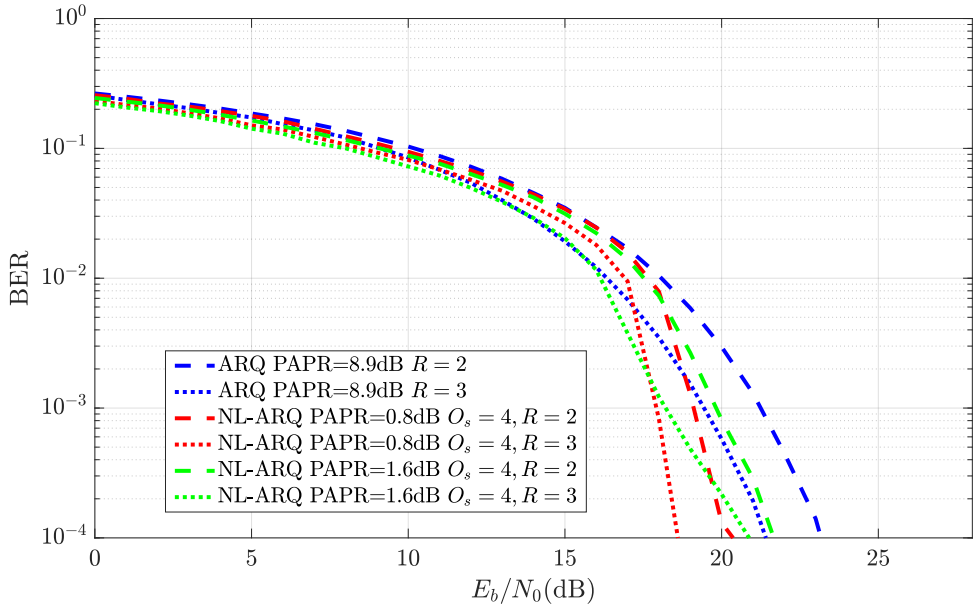

Figure 4.54: BER of 1024-QAM OFDM comparing conventional ARQ with NL-ARQ, for an AWGN channel, considering $O_s = 4$.

The increased oversampling results in considerable gains due to the reduced aliasing within the signal bandwidth from the clipping nonlinearity. In this case, for $R = 2$ employing a PAPR of 1.6dB results in a performance gain over conventional ARQ of approximately 3dB, whereas a PAPR of 0.8dB produces a smaller gain of around 1.5dB. This is a significant performance boost, in comparison to conventional ARQ, while requiring much less transmission power. For $R = 3$, the signal with PAPR of 1.6dB shows a performance improvement of about 3dB, whereas the signal with the PAPR of 0.8dB shows a minor performance improvement of 0.5dB. This result reinforces the potential of NL-ARQ, showing that the potential gain scales with retransmission attempts. In fact, a single retransmision of NL-ARQ, $R = 2$, outperforms conventional ARQ with $R = 3$. Fig. 4.55 compares the performance of conventional ARQ with NL-ARQ-EP, where the improved power efficiency of NL-ARQ is used to increase retransmission power.

In this scenario, the performance is maximised to improve reliability. The best performance was obtained for a signal with a PAPR of 1.6dB. With $O_s = 1$, NL-ARQ-EP achieves a performance gain of 4.5dB over conventional ARQ. With a higher oversampling of $O_s = 4$, the performance gain is 7dB over conventional ARQ. In both oversampling scenarios, NL-ARQ-EP with $R = 2$ outperforms ARQ with $R = 3$, resulting in less retransmissions overall. Fig. 4.56 shows the goodput of the system considering $R = 3$, which is the amount of correctly received bits per OFDM symbol, divided by the number of transmissions, considering a bandwidth of 120 MHz. An OFDM symbol with incorrect

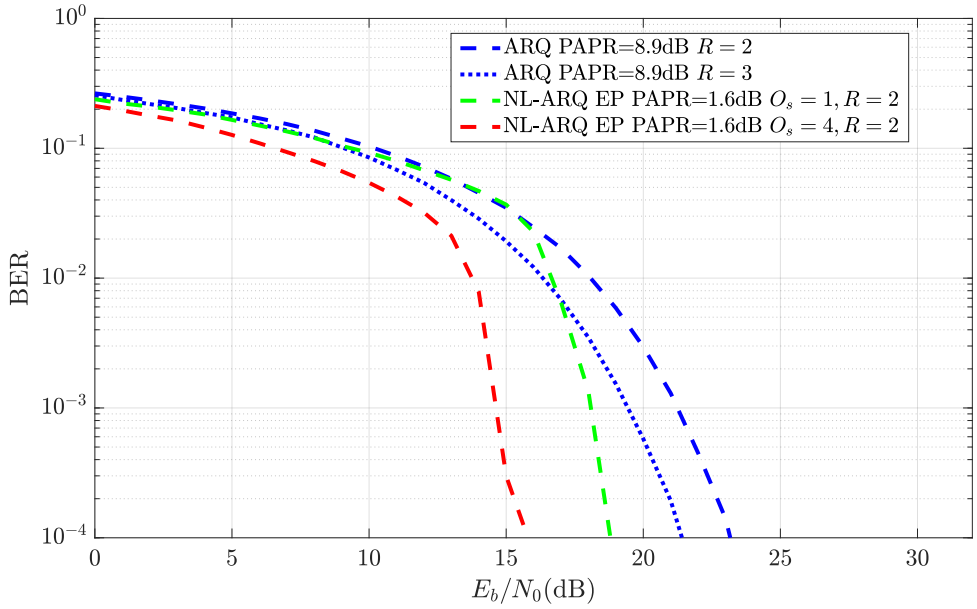

Figure 4.55: BER of 1024-QAM OFDM comparing conventional ARQ with NL-ARQ, for an AWGN channel, with enhanced transmission power.

bits is treated as a failed transmission, and a retransmission is requested.

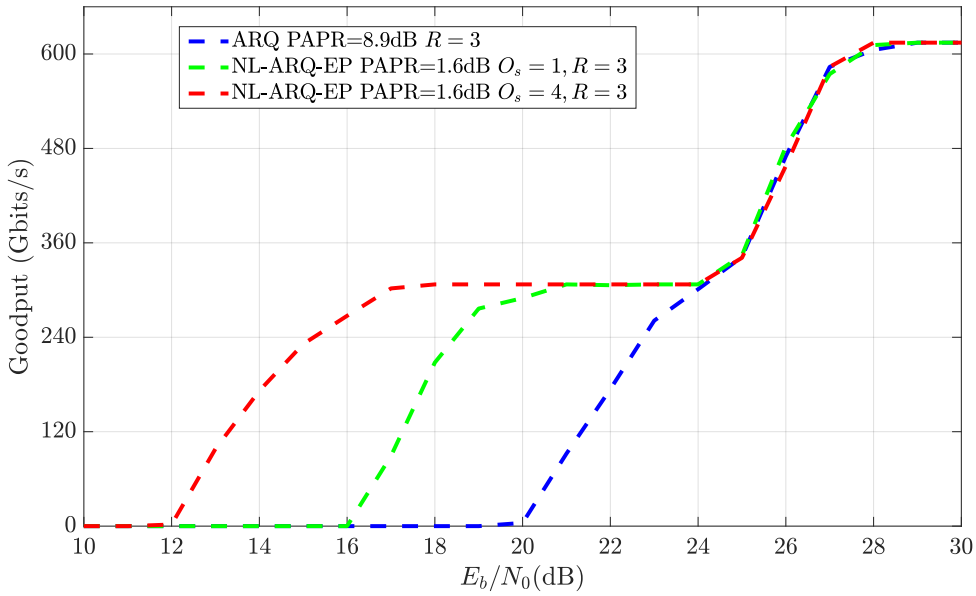

Figure 4.56: Goodput comparison between NL-ARQ-EP and ARQ for 1024-QAM and $N = 512$ subcarriers.

In conventional ARQ, there is a visible slope that is proportional to the E_b/N_0. For

larger values of R, the slope would be less steep, as the additional retransmissions salvage the goodput for lower E_b/N_0. For NL-ARQ-EP, there is a noticeable plateau at half the goodput, which is associated with the symbols that are correctly recovered with a single retransmission due to the nonlinearity decoding, similar to using FEC. For $O_s = 1$, this plateau starts at 21dB, which is a significant improvement over ARQ that has a much lower goodput at that E_b/N_0. For $O_s = 4$, the plateau starts at 17dB, which is a remarkable improvement over ARQ, as its goodput was 0 for the same E_b/N_0. For E_b/N_0 below the plateau region, there is a chance of retransmissions not being successful.

4.5.2.2 NL-HARQ

This section presents the performance of Nonlinear HARQ (NL-HARQ), using the LDPC HARQ scheme from the NR specification, and $N = 512$ subcarriers. First, consider Type I HARQ, which consists in retransmitting the same signal. Figure 4.57 shows the SER of a system using a clipping nonlinearity only on retransmissions. From the figure it can be

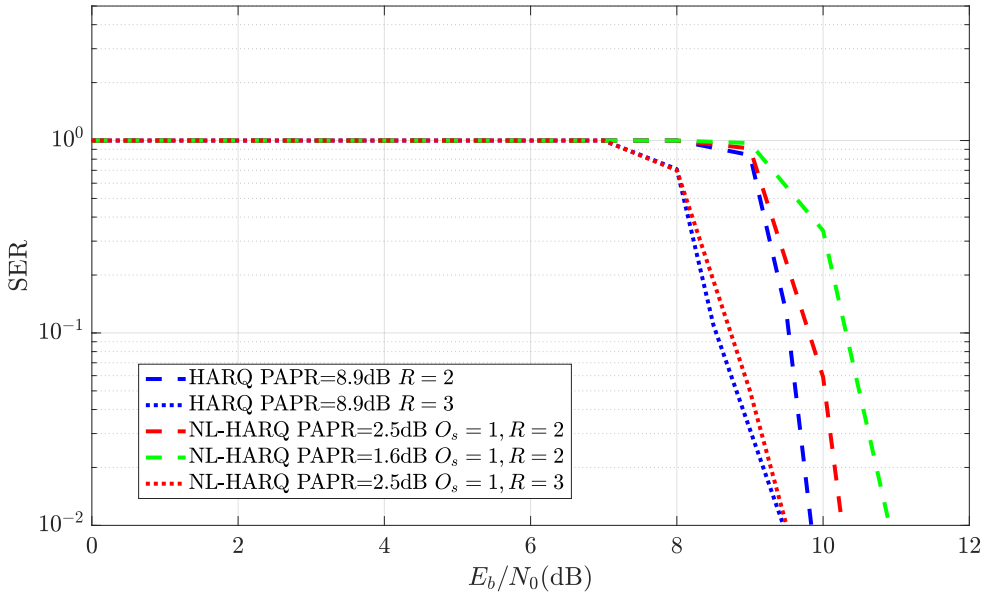

Figure 4.57: SER of 1024-QAM OFDM comparing conventional HARQ with NL-HARQ, for an AWGN channel.

seen the clipped signals boast a much lower PAPR than a conventional signal. For $R = 2$, that is 1 retransmission, with a PAPR of 2.5dB, NL-HARQ has slightly worse SER than the ideal HARQ system, whereas at PAPR 1.6dB there is a noticeable 1dB degradation for a SER of 10^{-2}. This reduction in PAPR can increase average efficiency to 34%, at a PAPR of 2.5dB. For $R = 3$, that is 2 retransmissions, for a PAPR of 2.5dB, NL-HARQ performs nearly the same as conventional HARQ, with an average efficiency of 42%. Table 4.3 compares the E_b/N_0+PAPR necessary to achieve a target SER of 1% for AWGN channels.

Table 4.3: Comparison of the necessary E_b/N_0+PAPR to achieve a target SER of 1%.

Scheme	PAPR	R	O_s	E_b/N_0	E_b/N_0+PAPR
HARQ	8.9dB	2	1	9.8dB	18.7dB
HARQ	8.9dB	3	1	9.5dB	18.4dB
NL-HARQ	1.6dB	2	1	11dB	12.6dB
NL-HARQ	2.5dB	2	1	10.2dB	12.7dB
NL-HARQ	2.5dB	3	1	9.5dB	12dB
NL-HARQ	0.2dB	2	4	11dB	11.2dB
NL-HARQ	0.8dB	2	4	10dB	10.8dB
NL-HARQ	0.8dB	3	4	9.1dB	9.9dB

For $O_s = 1$, NL-HARQ can achieve the lowest E_b/N_0+PAPR of 12dB, with a PAPR of 2.5dB and $R = 3$, an improvement of 6.4dB over HARQ. With oversampling, $O_s = 4$, the gain is noticeable higher, where the lowest E_b/N_0+PAPR to achieve the target is 9.9dB, with a PAPR of 0.8dB and $R = 3$, an improvement of 8.5dB over HARQ. These results confirm the high energy efficiency of NL-HARQ, over HARQ. Fig. 4.58 shows the SER for NL-HARQ-EP, with $O_s = 1$.

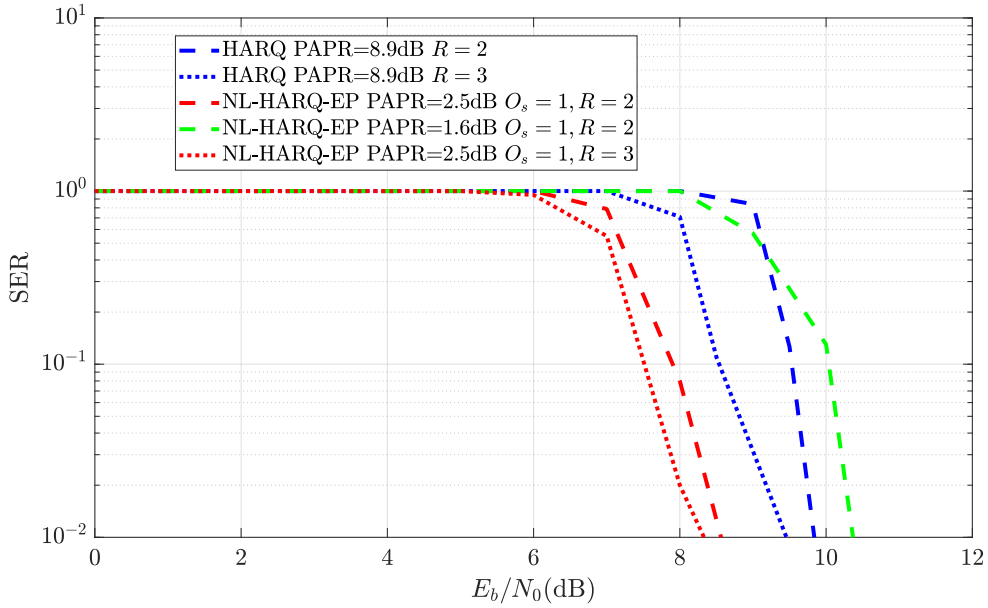

Figure 4.58: SER of 1024-QAM OFDM comparing conventional HARQ with NL-HARQ, for an AWGN channel, with enhanced transmission power.

Table 4.4: Comparison of the necessary E_b/N_0 to achieve a target SER of 1%.

Scheme	PAPR	R	O_s	E_b/N_0
HARQ	8.9dB	2	1	9.8dB
HARQ	8.9dB	3	1	9.5dB
NL-HARQ-EP	1.6dB	2	1	10.2dB
NL-HARQ-EP	2.5dB	2	1	8.6dB
NL-HARQ-EP	2.5dB	3	1	8.3dB
NL-HARQ-EP	0.2dB	2	4	6.6dB
NL-HARQ-EP	0.8dB	2	4	6.5dB
NL-HARQ-EP	0.8dB	3	4	5.5dB

The increased retransmission power results in a noticeable SER improvement. Considering $R = 2$, NL-HARQ-EP with a PAPR of 2.5dB outperforms ideal HARQ even at $R = 3$, by a margin of almost 1.5 dB in E_b/N_0. There is a limit, however, as the lower PAPR of 1.6dB actually performs worse than ideal HARQ, due to the additional distortion. For $R = 3$, there isn't a significant decrease in the SER, similar to ideal HARQ. Table 4.4 compares the E_b/N_0 necessary to achieve a target SER of 1% for AWGN channels. In this case, the reduced PAPR is used to increase transmission power, with higher efficiency.

From the table there is a clear improvement in required E_b/N_0 for the NL-HARQ-EP scheme. With $O_s = 1$ and $R = 2$, NL-HARQ-EP requires 1.2dB less E_b/N_0 to achieve the target PER of 1%, with the same result for $R = 3$, which highlights how NL-HARQ-EP scales well with further retransmissions. With oversampling of $O_s = 4$, the gains are significantly higher, achieving the target SER requiring 3.3dB and 4.5dB less E_b/N_0 than HARQ, for $R = 2$ and $R = 3$, respectively. Fig. 4.59 compares the goodput of HARQ and NL-HARQ-EP.

From the figure there is a clear improvement in goodput. For $O_s = 1$, the goodput of NL-HARQ-EP is about two times greater than HARQ, in the E_b/N_0 range between 6dB and 10dB. For $O_s = 4$, the goodput reaches half of the maximum at 7dB of E_b/N_0, an improvement of 3dB over HARQ. Between 3dB and 7dB, NL-HARQ-EP can achieve a significant goodput, in contrast with the 0 goodput of HARQ. Table 4.5 compares the E_b/N_0 necessary to achieve a target SER of 1% for a Rician channel with $K = 0.8$.

The channel fading has a negative impact in performance, as can be seen by the higher E_b/N_0 required to reach 1% SER. Without oversampling, there is only a significant gain for $R = 3$, where NL-HARQ-EP requires 0.8dB less E_b/N_0 to reach the target SER. With an oversampling of $O_s = 4$, the results are much better with a reduction in required E_b/N_0 of 1.4dB and 1.7dB for $R = 2$ and $R = 3$, respectively. Fig. 4.60 shows the goodput considering a Rician channel.

Compared to the AWGN scenario, the goodput improvement of NL-HARQ-EP over

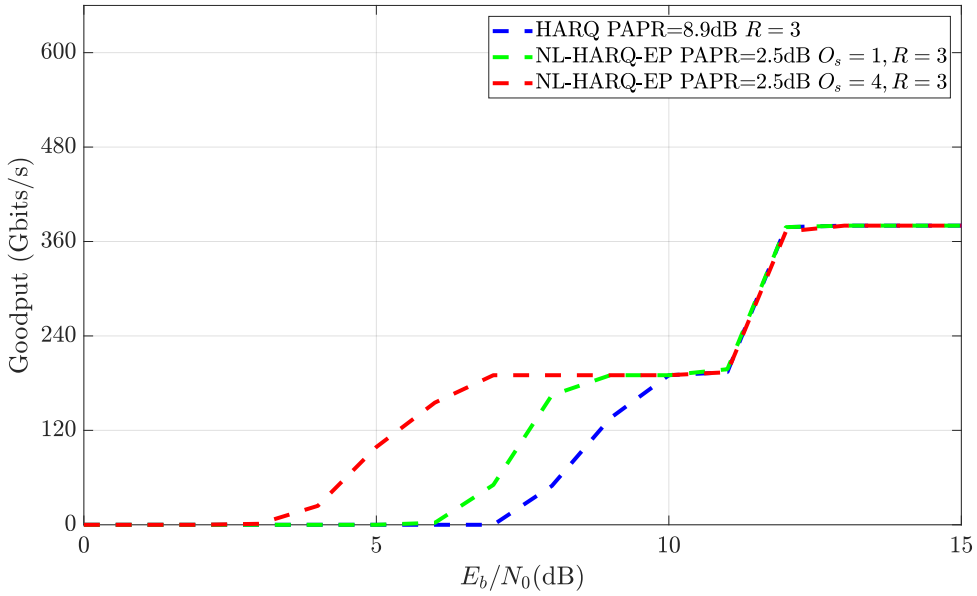

Figure 4.59: Goodput comparison between NL-HARQ-EP and HARQ for 1024-QAM and $N = 512$ subcarriers.

Table 4.5: Comparison of the necessary E_b/N_0 to achieve a target SER of 1%, considering a Rician channel with $K = 0.8$.

Scheme	PAPR	R	O_s	E_b/N_0
HARQ	8.9dB	2	1	10.2dB
HARQ	8.9dB	3	1	8.9dB
NL-HARQ-EP	3.5dB	2	1	10.2dB
NL-HARQ-EP	4.6dB	2	1	10.1dB
NL-HARQ-EP	4.6dB	3	1	8.1dB
NL-HARQ-EP	1.6dB	2	4	9dB
NL-HARQ-EP	2.5dB	2	4	8.8dB
NL-HARQ-EP	2.5dB	3	4	7.2dB

HARQ is lower. For $O_s = 1$, NL-HARQ-EP reaches half the maximum goodput at 1dB less of E_b/N_0 than HARQ. With $O_s = 4$, NL-HARQ-EP requires 2dB less E_b/N_0 to reach half the maximum goodput than HARQ.

4.5.2.3 NL-HARQ Type II

The standard scheme for NR Release 17 is HARQ Type II, which consists in transmitting the parity bits that were punctured from the original codeword. The bits are selected

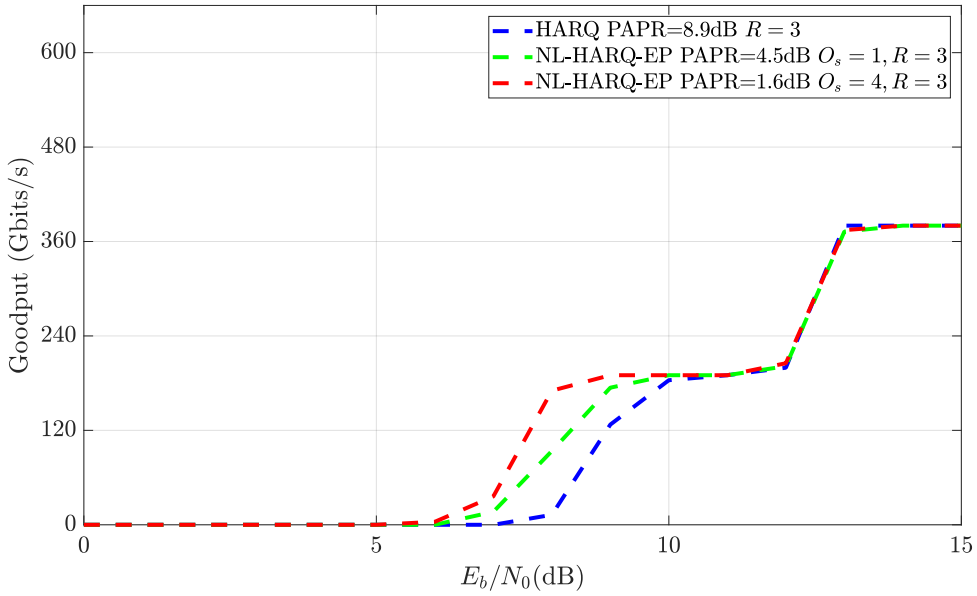

Figure 4.60: Goodput comparison between NL-HARQ-EP and HARQ for 1024-QAM and $N = 512$ subcarriers, for a Rician channel with $K = 0.8$.

to fill the OFDM symbol based on 4 different starting points in the codeword, named $rv_0 - rv_3$. rv_0 is the starting point for the initial transmission, and retransmissions follow a repeating pattern $rv_0, rv_2, rv3, rv1$ (including the initial transmission). Depending on bit space available in an OFDM symbol, there may be overlap between transmitted bits, with rv_0 and rv_2 contain the least possible overlap. The less overlap there is, the lower the rate of the code at the receiver, which is why rv_2 is a good choice for the first retransmission.

In this scenario, the combination of different signals is done at bit level as part of the decoding by combining the LLRs between transmissions. Since each retransmission uses a different rv, it contains different information, at least until the rv loops back to rv_0 after 4 retransmissions. Therefore, GAMP cannot use the previously received signals in the calculations. Therefore, the previous expressions are modified as follows.

$$\begin{aligned}\mathrm{E}[z|\hat{p},\mathbf{y}_n,\mu^p] =& \frac{1}{\mathrm{Re}\,(C)}\int_{-\infty}^{\infty} x\exp\left(-\frac{|\mathrm{Re}\,(\hat{p})-x|^2}{2\mu^p}-\frac{\left|\mathrm{Re}\,\left(y_{(n,r)}\right)-f_r(x)\right|^2}{2\sigma^2_{N,r}}\right)\mathrm{d}x+\\ &\frac{j}{\mathrm{Im}\,(C)}\int_{-\infty}^{\infty} xj\exp\left(-\frac{|\mathrm{Im}\,(\hat{p})-x|^2}{2\mu^p}-\frac{\left|\mathrm{Im}\,\left(y_{(n,r)}\right)-f_r(x)\right|^2}{2\sigma^2_{N,r}}\right)\mathrm{d}x\end{aligned} \tag{4.43}$$

$$\begin{aligned}\mathrm{var}[z|\hat{p},\mathbf{y}_n,\mu^p] =& \frac{1}{\mathrm{Re}\,(C)}\int_{-\infty}^{\infty} |x|^2\exp\left(-\frac{|\mathrm{Re}\,(\hat{p})-x|^2}{2\mu^p}-\frac{\left|\mathrm{Re}\,\left(y_{(n,r)}\right)-f_r(x)\right|^2}{2\sigma^2_{N,r}}\right)\mathrm{d}x+\\ &\frac{j}{\mathrm{Im}\,(C)}\int_{-\infty}^{\infty} |x|^2 j\exp\left(-\frac{|\mathrm{Im}\,(\hat{p})-x|^2}{2\mu^p}-\frac{\left|\mathrm{Im}\,\left(y_{(n,r)}\right)-f_r(x)\right|^2}{2\sigma^2_{N,r}}\right)\mathrm{d}x-\mathrm{E}[z|\hat{p},\mathbf{y}_n,\mu^p]\end{aligned} \tag{4.44}$$

$$C = \int_{-\infty}^{\infty} \exp\left(-\frac{|\mathrm{Re}\,(\hat{p}) - x|^2}{2\mu^p} - \frac{\left|\mathrm{Re}\,\left(y_{(n,r)}\right) - f_r(x)\right|^2}{2\sigma^2_{N,r}}\right) \mathrm{d}x + j\int_{-\infty}^{\infty} \exp\left(-\frac{|\mathrm{Im}\,(\hat{p}) - x|^2}{2\mu^p} - \frac{\left|\mathrm{Im}\,\left(y_{(n,r)}\right) - f_r(x)\right|^2}{2\sigma^2_{N,r}}\right) \mathrm{d}x. \tag{4.45}$$

Fig. 4.61 shows the SER for AWGN 1024-QAM.

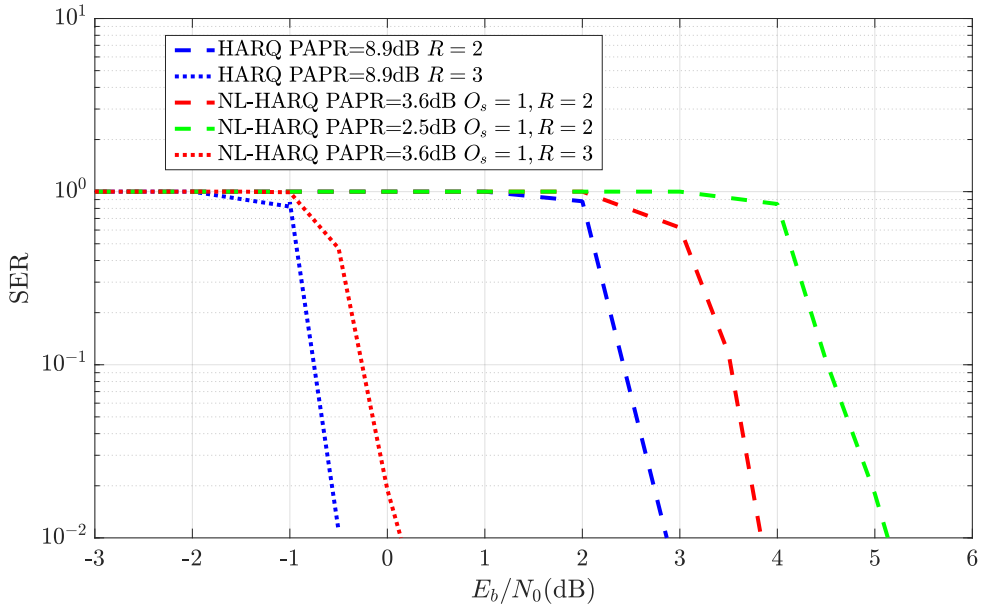

Figure 4.61: SER of 1024-QAM OFDM comparing conventional HARQ Type II with NL-HARQ Type II, for an AWGN channel.

From the figure it is clear how HARQ Type II is significantly more powerful than HARQ Type I. For $R = 2$, NL-HARQ with PAPR 3.6dB and 2.5dB performs about 1 and 2 dB worse than ideal HARQ, respectively. The average energy efficiency for these scenarios is 28% and 34%, respectively. Therefore, the lower PAPR of 2.5dB is not as beneficial as a PAPR of 3.6dB. At $R = 3$, NL-HARQ-EP performs only 0.5 dB worse, with a average efficiency of 34%. Table 4.6 summarizes the E_b/N_0+PAPR necessary for a target SER of 1%, for AWGN channels.

From the table there is a remarkable improvement in E_b/N_0+PAPR for NL-HARQ Type II, over conventional HARQ Type II. For $O_s = 1$, a PAPR of 3.6dB can be supported to enable required E_b/N_0+PAPR decreases of 4.3dB and 4.7dB over conventional HARQ, for $R = 2$ and $R = 3$, respectively. Oversampling by $O_s = 4$ reduces the necessary E_b/N_0+PAPR to 6.7dB and 7.5dB, for $R = 2$ and $R = 3$, respectively. Fig. 4.62 shows the performance of NL-HARQ-EP with $O_s = 1$.

In this scenario, at $R = 2$, NL-HARQ-EP outperforms ideal HARQ by 1dB, with a PAPR of 4.3dB. A lower PAPR of 3.6dB has a negative impact on performance. However, at $R = 3$ there is remarkable improvement of NL-HARQ-EP with a PAPR of 4.3dB, over

Table 4.6: Comparison of the necessary E_b/N_0+PAPR to achieve a target SER of 1%.

Scheme	PAPR	R	O_s	E_b/N_0	E_b/N_0+PAPR
HARQ Type II	8.9dB	2	1	2.9dB	11.8dB
HARQ Type II	8.9dB	3	1	-0.5dB	8.4dB
NL-HARQ Type II	2.5dB	2	1	5.1dB	7.6dB
NL-HARQ Type II	3.6dB	2	1	3.9dB	7.5dB
NL-HARQ Type II	3.6dB	3	1	0.1dB	3.7dB
NL-HARQ Type II	0.8dB	2	4	4.5dB	5.3dB
NL-HARQ Type II	1.6dB	2	4	3.5dB	5.1dB
NL-HARQ Type II	1.6dB	3	4	-0.7dB	0.9dB

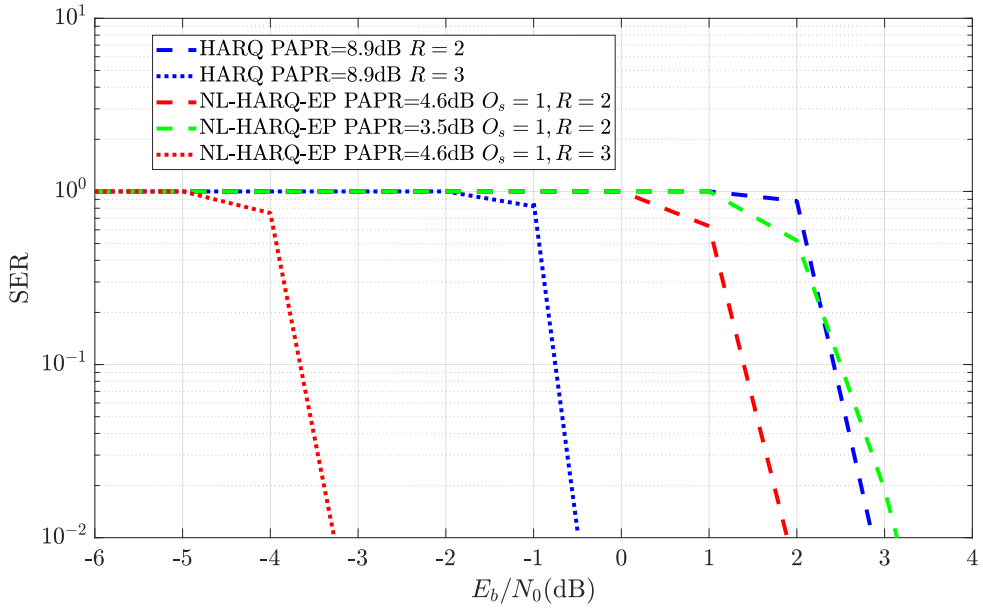

Figure 4.62: SER of 1024-QAM OFDM comparing conventional HARQ Type IIwith NL-HARQ Type II, for an AWGN channel, with enhanced transmissin power.

ideal HARQ. This can be justified by the fact that by the second retransmission attempt, a significant portion of the codeword was transmitted with higher power, which greatly improves GAMP's convergence. This allows NL-HARQ-EP to be much more effective in applications that expect highly volatile propagation characteristics. Table 4.7 summarises the necessary E_b/N_0 to reach a SER of 1%, for different system configurations, considering an AWGN channel.

With no oversampling, the proposed NL-HARQ-EP scheme achieves decreases of 1dB and 2.9dB in E_b/N_0 over standard HARQ, for $R = 2$ and $R = 3$, respectively. With

Table 4.7: Comparison of the necessary E_b/N_0 to achieve a target SER of 1%.

Scheme	PAPR	R	O_s	E_b/N_0
HARQ Type II	8.9dB	2	1	2.9dB
HARQ Type II	8.9dB	3	1	-0.5dB
NL-HARQ-EP Type II	3.5dB	2	1	3.2dB
NL-HARQ-EP Type II	4.6dB	2	1	1.9dB
NL-HARQ-EP Type II	4.6dB	3	1	-3.4dB
NL-HARQ-EP Type II	0.8dB	2	4	2.5dB
NL-HARQ-EP Type II	1.6dB	2	4	1dB
NL-HARQ-EP Type II	1.6dB	3	4	-4.7dB

oversampling, $O_s = 4$, the decreases in required E_b/N_0 are higher, with 1.9dB and 4.2dB for $R = 2$ and $R = 3$, respectively. These results showcase the potential of NNL-HARQ-EP to increase retransmission reliability, as it requires less E_b/N_0 than conventional schemes. Fig. 4.63 compares the goodput of NL-HARQ-EP Type II and HARQ Type II.

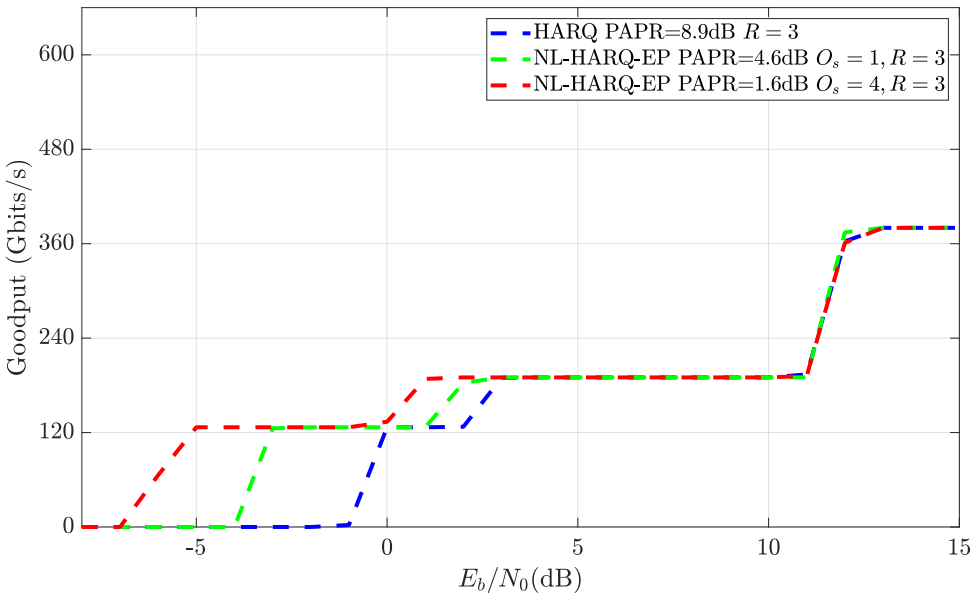

Figure 4.63: Goodput comparison between NL-HARQ-EP Type II and HARQ Type II for 1024-QAM and $N = 512$ subcarriers.

For $O_s = 1$, NL-HARQ-EP reaches half the maximum goodput while requiring 1dB less of E_b/N_0 than HARQ. Increasing oversampling to $O_s = 4$ improves this result by a further 1dB. At one third of the maximum goodput there is a visible plateau due to the

Table 4.8: Comparison of the necessary E_b/N_0 to achieve a target SER of 1%, considering a Rician channel with $K = 0.8$.

Scheme	PAPR	R	O_s	E_b/N_0
HARQ Type II	8.9dB	2	1	3.8dB
HARQ Type II	8.9dB	3	1	0.2dB
NL-HARQ-EP Type II	4.6dB	2	1	3.5dB
NL-HARQ-EP Type II	5.7dB	2	1	3.1dB
NL-HARQ-EP Type II	5.7dB	3	1	-1.5dB
NL-HARQ-EP Type II	1.6dB	2	4	2.8dB
NL-HARQ-EP Type II	2.5dB	2	4	2.5dB
NL-HARQ-EP Type II	2.5dB	3	4	-4.2dB

third transmission attempt. In this case, NL-HARQ-EP with $O_s = 1$ and $0_s = 4$ achieve this goodput while requiring 3dB and 5dB less E_n/N_0 than HARQ, respectively. Table 4.8 summarises the required E_b/N_0 for a target SER of 1%, considering a Rician fading channel with $K = 0.8$.

With no oversampling, NL-HARQ-EP requires 0.7dB and 1.7dB less E_b/N_0 than HARQ, for $R = 2$ and $R = 3$, respectively. The decrease in E_b/N_0 is smaller than the AWGN scenario due to the fading effects impacting GAMP convergence. With oversampling of $O_s = 4$, the required E_b/N_0 by NL-HARQ-EP is 1.3dB and 4.4dB lower compared to HARQ, for $R = 2$ and $R = 3$, respectively. Performance is much better with oversampling, as it allows lower clipping values to increase retransmission power. Fig. 4.64 compares the goodput considering a Rician fading channel.

The introduction of fading has a noticeable impact in NL-HARQ-EP goodput. The proposed NL-HARQ-EP achieves half the maximum goodput at 1dB less of E_b/N_0, compared to HARQ. The increased oversampling of $O_s = 4$ has a smaller impact in this case, and does not allow NL-HARQ-EP to reach half goodput with less E_b/N_0. On the other hand, NL-HARQ-EP with $O_s = 4$ achieves one third maximum goodput while still requiring 5dB less of E_b/N_0 over HARQ. With $O_s = 1$, this margin becomes 2dB, lower than the AWGN scenario.

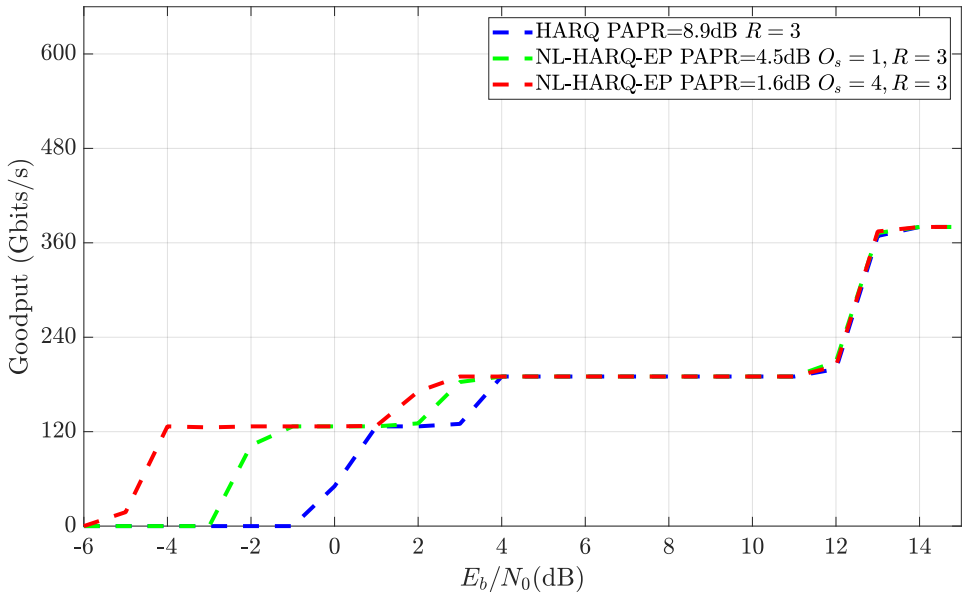

Figure 4.64: Goodput comparison between NL-HARQ-EP Type II and HARQ Type II for 1024-QAM and $N = 512$ subcarriers, for a Rician channel with $K = 0.8$.

5

Conclusions and Future Work

The main goal of this thesis was to design efficient and secure receiving algorithms for modern wireless standards, taking into account non-ideal hardware and challenging propagation conditions. The use of SC modulations was proposed as a way to achieve PLS in MIMO schemes, due to the use of SVD functioning as a pseudo encryption technique at the physical level. This analysis was extended for scenarios with power domain NOMA, and suboptimal propagation conditions. Three algorithms were proposed to handle nonlinear distortion in the received signal, namely BNC, GAMP and GTurbo. Each of these was analysed using Monte Carlo simulations due to the high complexity in deriving analytical expressions for their performances. It was shown that integrating these receivers with FEC can significantly increase performance, allowing the use of cheaper and more efficient hardware. In fact, it was shown that GAMP and GTurbo receivers can be suboptimum receivers for nonlinearly distorted signals, exceeding the performance of linear systems. The original work of this thesis was published in the following papers [9–16].

Chapter 2 characterized the wireless system model that was considered in this thesis, including SC and MC transmission techniques. A reference model for different hardware impairments was developed, which measured the impact of each impairment in the system's achievable EVM. These results highlighted the importance of linear hardware in high order constellations for modern standards. It was shown how the PLS of a system can be measured using the SR, which can be analytically derived from the channel capacity. A review of the literature of several different techniques to mitigate the impact of these impairments and wireless PLS showcased the research interest in these areas.

Chapter 3 characterized receivers for SC and MC systems. A novel IB-DFE receiver was developed to support power domain NOMA schemes, taking advantage of the inherent iterative interference cancellation. Receivers with BNC were defined for MIMO-SVD SC, and OFDM schemes to reduce the ICI due to nonlinear distortion. A GAMP-based receiver was proposed that can, for certain nonlinearities, outperform linear systems. A different approach based on GTurbo was also studied for the same goal, and achieved a similar performance to GAMP. The analysis of these receivers was extended to combine

FEC decoding operations in receiver iterations. This dramatically increased iterative gain, allowing these receivers to support stronger nonlinearities.

Chapter 4 presented several applications based on the algorithms characterized in Chapter 3. The PLS features of the proposed power-domain NOMA IB-DFE scheme were shown to be quite high. Different eavesdropper configurations were studied to provide an accurate assessment of the PLS potential of this technique. Even in non ideal propagation conditions, such as the CathLab scenario, it was shown that the SR of an OFDM-SVD was still significantly high. A Proof-of-Concept (POC) prototype was developed using an SDR platform, which showed promising results for a 2×2 MIMO SVD system. A novel PAPR reducing scheme for very high order QAM was also proposed, making use of the distortion decoding capabilities of GAMP. This receiver achieved excellent performance, enabling significant PA power savings due to the reduced PAPR. The performance of GAMP with a non-ideal ADC was characterized via simulation. It was shown how it can enable high order QAM with very low bit resolutions, by making use of the inherent clipping in the ADC input range. Lastly, a novel nonlinearity-aided ARQ scheme was developed that used GAMP only on retransmissions. This technique showed very promising results, even when compared with the 3GPP Release 17 HARQ scheme.

5.1 Future Work

Wireless systems that can support non-ideal hardware continues to be a highly relevant topic in wireless communication research. The algorithms that were proposed in this thesis were shown to perform promisingly in scenarios with current standards, though there is still work to be done in extending these algorithms to MIMO scenarios. Another key issue is lowering the complexity of nonlinear decoding algorithms such as GAMP and GTurbo, especially for very high order constellations. Low complexity nonlinear receivers for PA nonlinearities are currently a highly sought after solution. As previously mentioned, these are suboptimum receivers for nonlinearities, and cannot reach ideal performance. Currently, significant research is being done to find an optimum receiver with reasonable complexity.

The research area of PLS has grown significantly, and is expected to continue as it becomes possible to use more sophisticated and complex techniques in the PHY layer. This thesis demonstrated how SVD schemes can be an effective option with minimal overhead, in various scenarios. In fact, nonlinearity decoders can also be considered in PLS scenarios, due to their reliance on accurate nonlinear function information. As more research is done into these decoders, this option becomes increasingly realistic.

Bibliography

[1] J. M. Lourenço. *The NOVAthesis LaTeX Template User's Manual*. NOVA University Lisbon. 2021. URL: https://github.com/joaomlourenco/novathesis/raw/main/template.pdf (cit. on p. i).

[2] M. H. C. Garcia et al. "A Tutorial on 5G NR V2X Communications". In: *IEEE Communications Surveys & Tutorials* 23.3 (2021), pp. 1972–2026. DOI: 10.1109/COMST.2021.3057017 (cit. on p. 1).

[3] D.-J. Deng, K.-C. Chen, and R.-S. Cheng. "IEEE 802.11ax: Next generation wireless local area networks". In: *10th International Conference on Heterogeneous Networking for Quality, Reliability, Security and Robustness*. 2014, pp. 77–82. DOI: 10.1109/QSHINE.2014.6928663 (cit. on p. 1).

[4] A. I. Ali et al. "ZigBee and LoRa based Wireless Sensors for Smart Environment and IoT Applications". In: *2019 1st Global Power, Energy and Communication Conference (GPECOM)*. 2019, pp. 19–23. DOI: 10.1109/GPECOM.2019.8778505 (cit. on p. 1).

[5] H. Yu, T. Kim, and H. Jafarkhani. "Wireless Secure Communication With Beamforming and Jamming in Time-Varying Wiretap Channels". In: *IEEE Transactions on Information Forensics and Security* 13.8 (2018), pp. 2087–2100. DOI: 10.1109/TIFS.2018.2809695 (cit. on p. 2).

[6] L. Dai et al. "Non-orthogonal multiple access for 5G: solutions, challenges, opportunities, and future research trends". In: *IEEE Communications Magazine* 53.9 (2015), pp. 74–81. DOI: 10.1109/MCOM.2015.7263349 (cit. on p. 2).

[7] G. Auer et al. "How much energy is needed to run a wireless network?" In: *IEEE Wireless Communications* 18.5 (2011), pp. 40–49. DOI: 10.1109/MWC.2011.6056691 (cit. on p. 3).

[8] A. Israr, Q. Yang, and A. Israr. "Power consumption analysis of access network in 5G mobile communication infrastructures — An analytical quantification model". In: *Pervasive and Mobile Computing* 80 (2022), p. 101544. ISSN: 1574-1192. DOI: 10.1016/j.pmcj.2022.101544. URL: https://www.sciencedirect.com/science/article/pii/S1574119222000049 (cit. on p. 3).

[9] J. Madeira et al. "On the Physical Layer Security Characteristics for MIMO-SVD Techniques for SC-FDE Schemes". In: *Sensors* 19.21 (2019). ISSN: 1424-8220. DOI: 10.3390/s19214757. URL: https://www.mdpi.com/1424-8220/19/21/4757 (cit. on pp. 4, 81, 109, 117, 171).

[10] J. Madeira, J. Guerreiro, and R. Dinis. "Iterative frequency-domain detection and compensation of nonlinear distortion effects for MIMO systems". In: *Physical Communication* 37 (2019), p. 100869. ISSN: 1874-4907. DOI: 10.1016/j.phycom.2019.100869. URL: https://www.sciencedirect.com/science/article/pii/S1874490719301739 (cit. on pp. 4, 67, 171).

[11] J. Madeira et al. "A Physical Layer Security Technique for NOMA Systems with MIMO SC-FDE Schemes". In: *Electronics* 9.2 (2020). ISSN: 2079-9292. DOI: 10.3390/electronics9020240. URL: https://www.mdpi.com/2079-9292/9/2/240 (cit. on pp. 4, 109, 171).

[12] J. Madeira, J. Guerreiro, and R. Dinis. "Physical Layer Security for High Data Rate Communications in the CathLab Environment". In: *2021 IEEE 94th Vehicular Technology Conference (VTC2021-Fall)*. 2021, pp. 1–5. DOI: 10.1109/VTC2021-Fall52928.2021.9625416 (cit. on pp. 4, 109, 171).

[13] J. Madeira et al. "A Scalable LDPC Coding Scheme for Adaptive HARQ Techniques". In: *2022 IEEE 95th Vehicular Technology Conference: (VTC2022-Spring)*. 2022, pp. 1–6. DOI: 10.1109/VTC2022-Spring54318.2022.9860855 (cit. on pp. 4, 109, 148, 171).

[14] J. Madeira, J. Guerreiro, and R. Dinis. "A Software Defined Radio Implementation of Physical Layer Security Using MIMO-SVD". In: *2022 International Young Engineers Forum (YEF-ECE)*. 2022, pp. 75–79. DOI: 10.1109/YEF-ECE55092.2022.9850114 (cit. on pp. 4, 109, 171).

[15] J. Madeira et al. "LDPC assisted GAMP for PAPR reduction in Super-QAM OFDM". In: *2023 8th International Conference on Frontiers of Signal Processing (ICFSP)*. 2023, pp. 1–4. DOI: 10.1109/ICFSP59764.2023.10372912 (cit. on pp. 4, 103, 109, 136, 171).

[16] J. Madeira et al. "Receiver Design for OFDM Schemes With Low-Resolution ADCs". In: *IEEE Open Journal of Vehicular Technology* 5 (2024), pp. 632–642. DOI: 10.1109/OJVT.2024.3390204 (cit. on pp. 4, 109, 139, 171).

[17] J. Madeira et al. "Nonlinearity-Aided Hybrid ARQ for Satellite Communications". In: *2024 IEEE 100th Vehicular Technology Conference (VTC2024-Fall)*. 2024, pp. 1–6. DOI: 10.1109/VTC2024-Fall63153.2024.10757736 (cit. on pp. 5, 148).

[18] J. Viana et al. "Increasing Reliability on UAV Fading Scenarios". In: *IEEE Access* 10 (2022), pp. 30959–30973. DOI: 10.1109/ACCESS.2022.3149588 (cit. on pp. 5, 109, 148).

[19] Z. Mokhtari et al. "A Least Squares Approach for Estimating Non-linearity Parameters for OFDM Signals with Bussgang Receivers". In: *2023 IEEE 97th Vehicular Technology Conference (VTC2023-Spring)*. 2023, pp. 1–6. DOI: 10.1109/VTC2023-Spring57618.2023.10199316 (cit. on pp. 5, 58).

[20] D. Dinis et al. "Quasi-Optimum Detection of Nonlinear OFDM: Performance Bounds and Receiver Design". In: *IEEE Transactions on Communications* (2024), pp. 1–1. DOI: 10.1109/TCOMM.2024.3439433 (cit. on p. 5).

[21] C. E. Shannon. "A mathematical theory of communication". In: *The Bell System Technical Journal* 27.3 (1948), pp. 379–423. DOI: 10.1002/j.1538-7305.1948.tb01338.x (cit. on p. 9).

[22] A. Goldsmith and P. Varaiya. "Capacity of fading channels with channel side information". In: *IEEE Transactions on Information Theory* 43.6 (1997), pp. 1986–1992. DOI: 10.1109/18.641562 (cit. on p. 10).

[23] N. Benvenuto et al. "Single Carrier Modulation With Nonlinear Frequency Domain Equalization: An Idea Whose Time Has Come—Again". In: *Proceedings of the IEEE* 98.1 (2010), pp. 69–96. DOI: 10.1109/JPROC.2009.2031562 (cit. on p. 15).

[24] S. Lin, D. J. Costello, and M. J. Miller. "Automatic-repeat-request error-control schemes". In: *IEEE Communications Magazine* 22.12 (1984), pp. 5–17. DOI: 10.1109/MCOM.1984.1091865 (cit. on p. 18).

[25] E. Modiano. "An adaptive algorithm for optimizing the packet size used in wireless ARQ protocols". In: *Wireless Networks* 5 (1999), pp. 279–286. DOI: 10.1023/A:1019111430288 (cit. on p. 18).

[26] T. Richardson and R. Urbanke. *Modern coding theory*. Cambridge university press, 2008. ISBN: 9780521852296 (cit. on pp. 18, 21).

[27] E. Berlekamp, R. McEliece, and H. van Tilborg. "On the inherent intractability of certain coding problems (Corresp.)" In: *IEEE Transactions on Information Theory* 24.3 (1978), pp. 384–386. DOI: 10.1109/TIT.1978.1055873 (cit. on p. 20).

[28] A. Viterbi. "Error bounds for convolutional codes and an asymptotically optimum decoding algorithm". In: *IEEE Transactions on Information Theory* 13.2 (1967), pp. 260–269. DOI: 10.1109/TIT.1967.1054010 (cit. on pp. 20, 21).

[29] L. Bahl et al. "Optimal decoding of linear codes for minimizing symbol error rate (Corresp.)" In: *IEEE Transactions on Information Theory* 20.2 (1974), pp. 284–287. DOI: 10.1109/TIT.1974.1055186 (cit. on p. 21).

[30] "IEEE Standard for Air Interface for Broadband Wireless Access Systems". In: *IEEE Std 802.16-2017 (Revision of IEEE Std 802.16-2012)* (2018), pp. 1–2726. DOI: 10.1109/IEEESTD.2018.8303870 (cit. on p. 21).

[31] 3GPP. *Multiplexing and channel coding*. Technical Specification (TS) 38.212. Version 17.4.0. 3rd Generation Partnership Project (3GPP), 2023-01. URL: https://portal.3gpp.org/desktopmodules/Specifications/SpecificationDetails.aspx?specificationId=3214 (cit. on pp. 21–23, 148).

[32] R. Gallager. "Low-density parity-check codes". In: *IRE Transactions on Information Theory* 8.1 (1962), pp. 21–28. DOI: 10.1109/TIT.1962.1057683 (cit. on p. 21).

[33] T. Richardson and R. Urbanke. "Efficient encoding of low-density parity-check codes". In: *IEEE Transactions on Information Theory* 47.2 (2001), pp. 638–656. DOI: 10.1109/18.910579 (cit. on pp. 21, 150).

[34] H. Weingarten, Y. Steinberg, and S. Shamai. "The Capacity Region of the Gaussian Multiple-Input Multiple-Output Broadcast Channel". In: *IEEE Transactions on Information Theory* 52.9 (2006), pp. 3936–3964. DOI: 10.1109/TIT.2006.880064 (cit. on p. 24).

[35] G. J. Foschini and M. J. Gans. "On limits of wireless communications in a fading environment when using multiple antennas". In: *Wireless personal communications* 6.3 (1998), pp. 311–335. DOI: 10.1023/A:1008889222784 (cit. on pp. 24, 127).

[36] E. Telatar. "Capacity of Multi-antenna Gaussian Channels". In: *European Transactions on Telecommunications* 10.6 (1999), pp. 585–595. DOI: https://doi.org/10.1002/ett.4460100604. eprint: https://onlinelibrary.wiley.com/doi/pdf/10.1002/ett.4460100604. URL: https://onlinelibrary.wiley.com/doi/abs/10.1002/ett.4460100604 (cit. on p. 24).

[37] G. Lebrun, J. Gao, and M. Faulkner. "MIMO transmission over a time-varying channel using SVD". In: *IEEE Transactions on Wireless Communications* 4.2 (2005), pp. 757–764. DOI: 10.1109/TWC.2004.840199 (cit. on p. 26).

[38] 3GPP. *NR; Base Station (BS) radio transmission and reception*. Technical Specification (TS) 38.104. Version 17.5.0. 3rd Generation Partnership Project (3GPP), 2022-04. URL: https://portal.3gpp.org/desktopmodules/Specifications/SpecificationDetails.aspx?specificationId=3202 (cit. on p. 29).

[39] M. Morelli and U. Mengali. "An improved frequency offset estimator for OFDM applications". In: *1999 IEEE Communications Theory Mini-Conference (Cat. No.99EX352)*. 1999, pp. 106–109. DOI: 10.1109/CTMC.1999.790246 (cit. on p. 29).

[40] J. Armstrong. "Analysis of new and existing methods of reducing intercarrier interference due to carrier frequency offset in OFDM". In: *IEEE Transactions on Communications* 47.3 (1999), pp. 365–369. DOI: 10.1109/26.752816 (cit. on p. 29).

[41] T. M. Schmidl and D. C. Cox. "Robust frequency and timing synchronization for OFDM". In: *IEEE Transactions on Communications* 45 (12 1997), pp. 1613–1621. ISSN: 00906778. DOI: 10.1109/26.650240 (cit. on pp. 30, 46, 134).

[42] A. Garcia Armada. "Understanding the effects of phase noise in orthogonal frequency division multiplexing (OFDM)". In: *IEEE Transactions on Broadcasting* 47.2 (2001), pp. 153–159. DOI: 10.1109/11.948268 (cit. on p. 30).

[43] A. Pitarokoilis, E. Bjornson, and E. G. Larsson. "Performance of the Massive MIMO Uplink With OFDM and Phase Noise". In: *IEEE Communications Letters* 20 (8 2016-08), pp. 1595–1598. ISSN: 1089-7798. DOI: 10.1109/LCOMM.2016.2581169 (cit. on pp. 30, 64).

[44] P. Pedrosa et al. "Joint frequency domain equalisation and phase noise estimation for single-carrier modulations in doubly-selective channels". In: *IET Communications* 9.8 (2015), pp. 1138–1146. DOI: 10.1049/iet-com.2014.0900 (cit. on pp. 31, 50).

[45] T. Pollet, M. V. Bladel, and M. Moeneclaey. "BER sensitivity of OFDM systems to carrier frequency offset and Wiener phase noise". In: *IEEE Transactions on Communications* 43 (2/3/4 1995-02), pp. 191–193. ISSN: 0090-6778. DOI: 10.1109/26.380034 (cit. on p. 32).

[46] A. Demir, A. Mehrotra, and J. Roychowdhury. "Phase noise in oscillators: a unifying theory and numerical methods for characterization". In: *IEEE Transactions on Circuits and Systems I: Fundamental Theory and Applications* 47 (5 2000-05), pp. 655–674. ISSN: 10577122. DOI: 10.1109/81.847872 (cit. on p. 33).

[47] D. Petrovic, W. Rave, and G. Fettweis. "Effects of Phase Noise on OFDM Systems With and Without PLL: Characterization and Compensation". In: *IEEE Transactions on Communications* 55 (8 2007-08), pp. 1607–1616. ISSN: 0090-6778. DOI: 10.1109/TCOMM.2007.902593 (cit. on pp. 33, 34).

[48] T. Lee and A. Hajimiri. "Oscillator phase noise: a tutorial". In: *IEEE Journal of Solid-State Circuits* 35 (3 2000-03), pp. 326–336. ISSN: 0018-9200. DOI: 10.1109/4.826814 (cit. on p. 33).

[49] J. Tubbax et al. "Compensation of IQ imbalance in OFDM systems". In: *IEEE International Conference on Communications, 2003. ICC '03.* Vol. 5. 2003, 3403–3407 vol.5. DOI: 10.1109/ICC.2003.1204086 (cit. on p. 34).

[50] M. O'Droma, S. Meza, and Y. Lei. "New modified saleh models for memoryless nonlinear power amplifier behavioural modelling". In: *IEEE Communications Letters* 13.6 (2009), pp. 399–401. DOI: 10.1109/LCOMM.2009.090222 (cit. on p. 39).

[51] T. Araujo and R. Dinis. "On the Accuracy of the Gaussian Approximation for the Evaluation of Nonlinear Effects in OFDM Signals". In: *IEEE Transactions on Communications* 60 (2 2012-02), pp. 346–351. ISSN: 0090-6778. DOI: 10.1109/TCOMM.2011.102011.110151 (cit. on p. 40).

[52] D. Dardari, V. Tralli, and A. Vaccari. "A theoretical characterization of nonlinear distortion effects in OFDM systems". In: *IEEE Transactions on Communications* 48 (10 2000), pp. 1755–1764. ISSN: 00906778. DOI: 10.1109/26.871400 (cit. on p. 40).

[53] T. Araújo and R. Dinis. *Analytical evaluation of nonlinear distortion effects on multicarrier signals*. CRC Press, 2015. ISBN: 9780429171543 (cit. on pp. 40, 41).

[54] H. Moazzen, A. Mohammadi, and M. Majidi. "Performance Analysis of Linear Precoded MU-MIMO-OFDM Systems With Nonlinear Power Amplifiers and Correlated Channel". In: *IEEE Transactions on Communications* 67.10 (2019), pp. 6753–6765. DOI: 10.1109/TCOMM.2019.2922197 (cit. on p. 40).

[55] J. J. Bussgang. "Crosscorrelation functions of amplitude-distorted Gaussian signals". In: (1952) (cit. on p. 40).

[56] H. E. Rowe. "Memoryless Nonlinearities With Gaussian Inputs: Elementary Results". In: *Bell System Technical Journal* 61 (7 1982-09), pp. 1519–1526. ISSN: 00058580. DOI: 10.1002/j.1538-7305.1982.tb04356.x (cit. on p. 41).

[57] O. T. Demir and E. Bjornson. "The Bussgang Decomposition of Nonlinear Systems: Basic Theory and MIMO Extensions [Lecture Notes]". In: *IEEE Signal Processing Magazine* 38 (1 2021-01), pp. 131–136. ISSN: 1053-5888. DOI: 10.1109/MSP.2020.3025538 (cit. on p. 41).

[58] J. Guerreiro, R. Dinis, and P. Montezuma. "Massive MIMO with Nonlinear Amplification: Signal Characterization and Performance Evaluation". In: *2016 IEEE Global Communications Conference (GLOBECOM)*. 2016, pp. 1–6. DOI: 10.1109/GLOCOM.2016.7841975 (cit. on pp. 41, 55, 71).

[59] C. Rapp. "Effects of HPA-Nonlinearity on a 4-DPSK/OFDM-Signal for a Digital Sound Broadcasting System." In: (1991). LIDO-Berichtsjahr=1991, pages=6, pp. 179–184. URL: https://elib.dlr.de/33776/ (cit. on p. 42).

[60] G. Santella and F. Mazzenga. "A model for performance evaluation in M-QAM-OFDM schemes in prescence of nonlinear distortions". In: *1995 IEEE 45th Vehicular Technology Conference. Countdown to the Wireless Twenty-First Century*. Vol. 2. 1995, 830–834 vol.2. DOI: 10.1109/VETEC.1995.504984 (cit. on p. 42).

[61] S. Teodoro et al. "Theoretical Analysis of Nonlinear Amplification Effects in Massive MIMO Systems". In: *IEEE Access* 7 (2019), pp. 172277–172289. ISSN: 2169-3536. DOI: 10.1109/ACCESS.2019.2956596 (cit. on p. 42).

[62] A. Saleh. "Frequency-Independent and Frequency-Dependent Nonlinear Models of TWT Amplifiers". In: *IEEE Transactions on Communications* 29.11 (1981), pp. 1715–1720. DOI: 10.1109/TCOM.1981.1094911 (cit. on p. 43).

[63] A. Tusha, S. Dogan, and H. Arslan. "Performance Analysis of Frequency Domain IM Schemes under CFO and IQ Imbalance". In: IEEE, 2019-09, pp. 1–5. ISBN: 978-1-5386-8110-7. DOI: 10.1109/PIMRC.2019.8904248 (cit. on pp. 46, 52).

[64] S. Shaboyan et al. "Frequency and Timing Synchronization for In-Band Full-Duplex OFDM System". In: IEEE, 2017-12, pp. 1–7. ISBN: 978-1-5090-5019-2. DOI: 10.1109/GLOCOM.2017.8254928 (cit. on p. 47).

[65] K. Chang and S. Lee. "Robust OFDM-Based Synchronization Against Very High Fractional CFO and Time-Varying Fading". In: *IEEE Systems Journal* 14 (3 2020-09), pp. 4047–4058. ISSN: 1932-8184. DOI: 10.1109/JSYST.2020.2964816 (cit. on p. 47).

[66] Y. Meng et al. "Blind Fast CFO Estimation and Performance Analysis for OFDM". In: *IEEE Transactions on Vehicular Technology* 69 (10 2020-10), pp. 11501–11514. ISSN: 19399359. DOI: 10.1109/TVT.2020.3012968 (cit. on p. 47).

[67] W. Zhang and F. Gao. "Blind Frequency Synchronization for Multiuser OFDM Uplink With Large Number of Receive Antennas". In: *IEEE Transactions on Signal Processing* 64 (9 2016-05), pp. 2255–2268. ISSN: 1053-587X. DOI: 10.1109/TSP.2016.2516963 (cit. on p. 48).

[68] S. Wu and Y. Bar-Ness. "OFDM Systems in the Presence of Phase Noise: Consequences and Solutions". In: *IEEE Transactions on Communications* 52 (11 2004-11), pp. 1988–1996. ISSN: 0090-6778. DOI: 10.1109/TCOMM.2004.836441 (cit. on p. 48).

[69] Q. Zou, A. Tarighat, and A. H. Sayed. "Compensation of Phase Noise in OFDM Wireless Systems". In: *IEEE Transactions on Signal Processing* 55 (11 2007-11), pp. 5407–5424. ISSN: 1053-587X. DOI: 10.1109/TSP.2007.899583 (cit. on p. 49).

[70] Q. Zou, A. Tarighat, and A. Sayed. "Joint compensation of IQ imbalance and phase noise in OFDM wireless systems". In: *IEEE Transactions on Communications* 57 (2 2009-02), pp. 404–414. ISSN: 0090-6778. DOI: 10.1109/TCOMM.2009.02.060526 (cit. on pp. 50, 53).

[71] R. A. Casas, S. Biracree, and A. Youtz. "Time domain phase noise correction for OFDM signals". In: *IEEE Transactions on Broadcasting* 48 (3 2002-09), pp. 230–236. ISSN: 0018-9316. DOI: 10.1109/TBC.2002.803711 (cit. on p. 51).

[72] A. Leshem and M. Yemini. "Phase Noise Compensation for OFDM Systems". In: *IEEE Transactions on Signal Processing* 65.21 (2017), pp. 5675–5686. DOI: 10.1109/TSP.2017.2740165 (cit. on p. 51).

[73] V. Syrjala et al. "Pilot Allocation and Computationally Efficient Non-Iterative Estimation of Phase Noise in OFDM". In: *IEEE Wireless Communications Letters* 8 (2 2019-04), pp. 640–643. ISSN: 2162-2337. DOI: 10.1109/LWC.2018.2890665 (cit. on p. 51).

[74] M. Chung, L. Liu, and O. Edfors. "Phase-Noise Compensation for OFDM Systems Exploiting Coherence Bandwidth: Modeling, Algorithms, and Analysis". In: *IEEE Transactions on Wireless Communications* 21 (5 2022-05), pp. 3040–3056. ISSN: 1536-1276. DOI: 10.1109/TWC.2021.3117782 (cit. on p. 52).

[75] X. Cheng, K. Xu, and S. Li. "Compensation of Phase Noise in Uplink Massive MIMO OFDM Systems". In: *IEEE Transactions on Wireless Communications* 18 (3 2019-03), pp. 1764–1778. ISSN: 1536-1276. DOI: 10.1109/TWC.2019.2897089 (cit. on p. 52).

[76] Q. Shi et al. "Factor Graph Based Message Passing Algorithms for Joint Phase-Noise Estimation and Decoding in OFDM-IM". In: *IEEE Transactions on Communications* 68 (5 2020-05), pp. 2906–2921. ISSN: 15580857. DOI: 10.1109/TCOMM.2020.2973080 (cit. on p. 52).

[77] R. P. F. Hoefel. "IEEE 802.11ax: Joint Effects of Power Control and IQ Imbalance Mitigation Schemes on the Performance of OFDM Uplink Multi-User MIMO". In: IEEE, 2017-09, pp. 1–6. ISBN: 978-1-5090-5935-5. DOI: 10.1109/VTCFall.2017.8288241 (cit. on pp. 52, 54).

[78] A. Tarighat, R. Bagheri, and A. H. Sayed. "Compensation schemes and performance analysis of IQ imbalances in OFDM receivers". In: *IEEE Transactions on Signal Processing* 53 (8 2005-08), pp. 3257–3268. ISSN: 1053-587X. DOI: 10.1109/TSP.2005.851156 (cit. on pp. 52, 54).

[79] A. Tarighat and A. H. Sayed. "MIMO OFDM receivers for Systems with IQ imbalances". In: *IEEE Transactions on Signal Processing* 53 (9 2005-09), pp. 3583–3596. ISSN: 1053-587X. DOI: 10.1109/TSP.2005.853148 (cit. on p. 52).

[80] F. Shu et al. "Pilot Optimization, Channel Estimation, and Optimal Detection for Full-Duplex OFDM Systems With IQ Imbalances". In: *IEEE Transactions on Vehicular Technology* 66 (8 2017-08), pp. 6993–7009. ISSN: 0018-9545. DOI: 10.1109/TVT.2017.2667686 (cit. on p. 53).

[81] M. Sandell et al. "Estimation of Wideband IQ Imbalance in MIMO OFDM Systems with CFO". In: *IEEE Transactions on Wireless Communications* 20 (9 2021-09), pp. 5821–5830. ISSN: 15582248. DOI: 10.1109/TWC.2021.3070387 (cit. on p. 54).

[82] N. Tang et al. "IQ Imbalance Compensation for Generalized Frequency Division Multiplexing Systems". In: *IEEE Wireless Communications Letters* 6 (4 2017-08), pp. 422–425. ISSN: 2162-2337. DOI: 10.1109/LWC.2017.2699961 (cit. on p. 54).

[83] Y. Liang et al. "Channel Compensation for Reciprocal TDD Massive MIMO-OFDM With IQ Imbalance". In: *IEEE Wireless Communications Letters* 6 (6 2017-12), pp. 778–781. ISSN: 2162-2337. DOI: 10.1109/LWC.2017.2740936 (cit. on p. 54).

[84] Y. Chen et al. "IQ Imbalance Aware Receiver for Uplink Massive MIMO-OFDM with Adjustable Phase Shift Pilots". In: IEEE, 2019-12, pp. 1–6. ISBN: 978-1-7281-0962-6. DOI: 10.1109/GLOBECOM38437.2019.9014285 (cit. on p. 54).

[85] P. P. Ann and R. Jose. "Comparison of PAPR reduction techniques in OFDM systems". In: IEEE, 2016-10, pp. 1–5. ISBN: 978-1-5090-1065-3. DOI: 10.1109/CESYS.2016.7889995 (cit. on p. 55).

[86] Y. A. Jawhar et al. "A Review of Partial Transmit Sequence for PAPR Reduction in the OFDM Systems". In: *IEEE Access* 7 (2019), pp. 18021–18041. ISSN: 2169-3536. DOI: 10.1109/ACCESS.2019.2894527 (cit. on p. 56).

[87] M. Kim, W. Lee, and D.-H. Cho. "A Novel PAPR Reduction Scheme for OFDM System Based on Deep Learning". In: *IEEE Communications Letters* 22 (3 2018-03), pp. 510–513. ISSN: 1089-7798. DOI: 10.1109/LCOMM.2017.2787646 (cit. on p. 56).

[88] D. R. Morgan et al. "A Generalized Memory Polynomial Model for Digital Predistortion of RF Power Amplifiers". In: *IEEE Transactions on Signal Processing* 54 (10 2006-10), pp. 3852–3860. ISSN: 1053-587X. DOI: 10.1109/TSP.2006.879264 (cit. on p. 56).

[89] C. D. Presti et al. "A 25 dBm Digitally Modulated CMOS Power Amplifier for WCDMA/EDGE/OFDM With Adaptive Digital Predistortion and Efficient Power Control". In: *IEEE Journal of Solid-State Circuits* 44 (7 2009-07), pp. 1883–1896. ISSN: 0018-9200. DOI: 10.1109/JSSC.2009.2020226 (cit. on p. 56).

[90] R. Zayani, H. Shaiek, and D. Roviras. "Ping-Pong Joint Optimization of PAPR Reduction and HPA Linearization in OFDM Systems". In: *IEEE Transactions on Broadcasting* 65 (2 2019-06), pp. 308–315. ISSN: 0018-9316. DOI: 10.1109/TBC.2018.2855664 (cit. on p. 56).

[91] P. Fernandes et al. "On the Capacity of Nonlinear Massive MIMO-OFDM Systems". In: IEEE, 2016-09, pp. 1–5. ISBN: 978-1-5090-1701-0. DOI: 10.1109/VTCFall.2016.7881117 (cit. on p. 57).

[92] J. Guerreiro, R. Dinis, and P. Montezuma. "Analytical Performance Evaluation of Precoding Techniques for Nonlinear Massive MIMO Systems With Channel Estimation Errors". In: *IEEE Transactions on Communications* 66 (4 2018-04), pp. 1440–1451. ISSN: 0090-6778. DOI: 10.1109/TCOMM.2017.2782321 (cit. on p. 57).

[93] C. Li, A. Raghunathan, and N. K. Jha. "Hijacking an insulin pump: Security attacks and defenses for a diabetes therapy system". In: *2011 IEEE 13th International Conference on e-Health Networking, Applications and Services*. 2011, pp. 150–156. DOI: 10.1109/HEALTH.2011.6026732 (cit. on p. 60).

[94] R. Melki et al. "A survey on OFDM physical layer security". In: *Physical Communication* 32 (2019), pp. 1–30. ISSN: 1874-4907. DOI: 10.1016/j.phycom.2018.10.008. URL: https://www.sciencedirect.com/science/article/pii/S1874490718302817 (cit. on pp. 60, 127).

[95] H. Sharma, N. Kumar, and R. Tekchandani. "Physical layer security using beamforming techniques for 5G and beyond networks: A systematic review". In: *Physical Communication* 54 (2022), p. 101791. ISSN: 1874-4907. DOI: 10.1016/j.phycom.2022.101791. URL: https://www.sciencedirect.com/science/article/pii/S1874490722001094 (cit. on p. 60).

[96] N. Romero-Zurita, M. Ghogho, and D. McLernon. "Outage Probability Based Power Distribution Between Data and Artificial Noise for Physical Layer Security". In: *IEEE Signal Processing Letters* 19.2 (2012), pp. 71–74. DOI: 10.1109/LSP.2011.2178067 (cit. on p. 62).

[97] C. Gong et al. "Enhancing Physical Layer Security With Artificial Noise in Large-Scale NOMA Networks". In: *IEEE Transactions on Vehicular Technology* 70.3 (2021), pp. 2349–2361. DOI: 10.1109/TVT.2021.3057661 (cit. on p. 62).

[98] X. Zhou, B. Maham, and A. Hjorungnes. "Pilot Contamination for Active Eavesdropping". In: *IEEE Transactions on Wireless Communications* 11.3 (2012), pp. 903–907. DOI: 10.1109/TWC.2012.020712.111298 (cit. on p. 62).

[99] T. M. Hoang et al. "Cell-Free Massive MIMO Networks: Optimal Power Control Against Active Eavesdropping". In: *IEEE Transactions on Communications* 66.10 (2018), pp. 4724–4737. DOI: 10.1109/TCOMM.2018.2837132 (cit. on p. 62).

[100] Z. Liu et al. "Covert Wireless Communications in IoT Systems: Hiding Information in Interference". In: *IEEE Wireless Communications* 25.6 (2018), pp. 46–52. DOI: 10.1109/MWC.2017.1800070 (cit. on p. 62).

[101] T. M. Hoang, N. M. Nguyen, and T. Q. Duong. "Detection of Eavesdropping Attack in UAV-Aided Wireless Systems: Unsupervised Learning With One-Class SVM and K-Means Clustering". In: *IEEE Wireless Communications Letters* 9.2 (2020), pp. 139–142. DOI: 10.1109/LWC.2019.2945022 (cit. on p. 62).

[102] C. Liu, J. Lee, and T. Q. S. Quek. "Safeguarding UAV Communications Against Full-Duplex Active Eavesdropper". In: *IEEE Transactions on Wireless Communications* 18.6 (2019), pp. 2919–2931. DOI: 10.1109/TWC.2019.2906177 (cit. on p. 63).

[103] B. Duo et al. "Joint trajectory and power optimization for securing UAV communications against active eavesdropping". In: *China Communications* 18.1 (2021), pp. 88–99. DOI: 10.23919/JCC.2021.01.008 (cit. on p. 63).

[104] R. Bustin et al. "An MMSE approach to the secrecy capacity of the MIMO Gaussian wiretap channel". In: *EURASIP Journal on Wireless Communications and Networking* 2009 (2009), pp. 1–8. DOI: 10.1155/2009/370970 (cit. on p. 63).

[105] *GNU Radio – the Free and Open Software Radio Ecosystem*. URL: github.com/gnuradio/gnuradio (cit. on pp. 64, 130).

[106] K. S. Ryland. "Software-Defined Radio Implementation of Two Physical Layer Security Techniques". PhD thesis. Virginia Tech, 2018 (cit. on p. 64).

[107] H. Yan et al. "Software Defined Radio Implementation of Carrier and Timing Synchronization for Distributed Arrays". In: *2019 IEEE Aerospace Conference*. 2019, pp. 1–12. DOI: 10.1109/AERO.2019.8742232 (cit. on p. 65).

[108] J. Madeira, J. Guerreiro, and R. Dinis. "Iterative Frequency-Domain Detection for MIMO Systems with Strong Nonlinear Distortion Effects". In: *2018 10th International Congress on Ultra Modern Telecommunications and Control Systems and Workshops (ICUMT)*. 2018, pp. 1–5. DOI: 10.1109/ICUMT.2018.8631239 (cit. on pp. 67, 109).

[109] S. Rangan. "Generalized approximate message passing for estimation with random linear mixing". In: *2011 IEEE International Symposium on Information Theory Proceedings*. 2011, pp. 2168–2172. DOI: 10.1109/ISIT.2011.6033942 (cit. on p. 83).

[110] S. V. Zhidkov. "Detection of Nonlinearly Distorted OFDM Signals via Generalized Approximate Message Passing". In: (2017). DOI: 10.48550/arXiv.1703.01562. arXiv: 1703.01562 [cs.IT]. URL: https://arxiv.org/abs/1703.01562 (cit. on pp. 84, 88).

[111] S. V. Zhidkov and R. Dinis. "Belief Propagation Receivers for Near-Optimal Detection of Nonlinearly Distorted OFDM Signals". In: *2019 IEEE 89th Vehicular Technology Conference (VTC2019-Spring)*. 2019, pp. 1–6. DOI: 10.1109/VTCSpring.2019.8746319 (cit. on p. 85).

[112] S. Rangan et al. "On the Convergence of Approximate Message Passing With Arbitrary Matrices". In: *IEEE Transactions on Information Theory* 65.9 (2019), pp. 5339–5351. DOI: 10.1109/TIT.2019.2913109 (cit. on p. 85).

[113] T. Liu et al. "Generalized turbo signal recovery for nonlinear measurements and orthogonal sensing matrices". In: *2016 IEEE International Symposium on Information Theory (ISIT)*. 2016, pp. 2883–2887. DOI: 10.1109/ISIT.2016.7541826 (cit. on p. 92).

[114] Y. Guan, K. Xu, and X. Cheng. "Accurate Wideband Localization in Massive MIMO Systems With Low-Resolution ADCs". In: *IEEE Transactions on Vehicular Technology* 73.2 (2024), pp. 2830–2835. DOI: 10.1109/TVT.2023.3312258 (cit. on p. 92).

[115] H. Wang et al. "Optimal data detection for OFDM system with low-resolution quantization". In: *2016 IEEE International Conference on Communication Systems (ICCS)*. 2016, pp. 1–6. DOI: 10.1109/ICCS.2016.7833583 (cit. on p. 92).

[116] H. Wang, C.-K. Wen, and S. Jin. "Bayesian Optimal Data Detector for mmWave OFDM System With Low-Resolution ADC". In: *IEEE Journal on Selected Areas in Communications* 35.9 (2017), pp. 1962–1979. DOI: 10.1109/JSAC.2017.2720978 (cit. on p. 92).

[117] P. Carvalho et al. *A method and an apparatus for physical layer in noma based wireless communication systems*. 2021 (cit. on p. 109).

[118] A. Katouzian et al. "A State-of-the-Art Review on Segmentation Algorithms in Intravascular Ultrasound (IVUS) Images". In: *IEEE Transactions on Information Technology in Biomedicine* 16.5 (2012), pp. 823–834. DOI: 10.1109/TITB.2012.2189408 (cit. on p. 126).

[119] H. Sharei et al. "Data Communication Pathway for Sensing Guidewire at Proximal Side: A Review". In: *Journal of Medical Devices* 11.2 (2017-05), p. 024501. ISSN: 1932-6181. DOI: 10.1115/1.4035545. eprint: https://asmedigitalcollection.asme.org/medicaldevices/article-pdf/11/2/024501/6240090/med_011_02_024501.pdf. URL: https://doi.org/10.1115/1.4035545 (cit. on p. 126).

[120] P. Viegas et al. "A Highly-Efficient Amplification Scheme for OFDM Signals". In: *2021 IEEE 93rd Vehicular Technology Conference (VTC2021-Spring)*. 2021, pp. 1–5. DOI: 10.1109/VTC2021-Spring51267.2021.9449004 (cit. on p. 126).

[121] J. Guerreiro, R. Dinis, and L. Campos. "On the Achievable Capacity of MIMO-OFDM Systems in the CathLab Environment". In: *Sensors* 20.3 (2020). ISSN: 1424-8220. DOI: 10.3390/s20030938. URL: https://www.mdpi.com/1424-8220/20/3/938 (cit. on p. 127).

[122] A. Goldsmith et al. "Capacity limits of MIMO channels". In: *IEEE Journal on Selected Areas in Communications* 21.5 (2003), pp. 684–702. DOI: 10.1109/JSAC.2003.810294 (cit. on p. 127).

[123] *CommPy: Digital Communication with Python*. 2021-06. URL: github.com/veeresht/CommPy (cit. on p. 134).

[124] "IEEE Standard for Air Interface for Broadband Wireless Access Systems". In: *IEEE Std 802.16-2017 (Revision of IEEE Std 802.16-2012)* (2018), pp. 1–2726. DOI: 10.1109/IEEESTD.2018.8303870 (cit. on pp. 137, 143).

[125] T. M. Cover and J. A. Thomas. *Elements of Information Theory (Wiley Series in Telecommunications and Signal Processing)*. USA: Wiley-Interscience, 2006. ISBN: 0471241954 (cit. on p. 139).

[126] R. Walden. "Analog-to-digital converter survey and analysis". In: *IEEE Journal on Selected Areas in Communications* 17.4 (1999), pp. 539–550. DOI: 10.1109/49.761034 (cit. on p. 139).

[127] C. Cao, H. Li, and Z. Hu. "An AMP based decoder for massive MU-MIMO-OFDM with low-resolution ADCs". In: *2017 International Conference on Computing, Networking and Communications (ICNC)*. 2017, pp. 449–453. DOI: 10.1109/ICCNC.2017.7876170 (cit. on p. 141).

[128] X. Song et al. "On Robust Millimeter Wave Line-of-Sight MIMO Communications With Few-Bit ADCs". In: *IEEE Transactions on Wireless Communications* 21.12 (2022), pp. 11164–11178. DOI: 10.1109/TWC.2022.3190243 (cit. on p. 141).

[129] M. El-Khamy et al. "HARQ Rate-Compatible Polar Codes for Wireless Channels". In: *2015 IEEE Global Communications Conference (GLOBECOM)*. 2015, pp. 1–6. DOI: 10.1109/GLOCOM.2015.7417429 (cit. on p. 148).

[130] *LDPC-codes*. URL: github.com/radfordneal/LDPC-codes (cit. on p. 150).

2024 Receiver Design for Reliable and Secure Wireless Communications João Madeira